ZEOLITE MEMBRANE WATER VAPOR SEPARATION

FOR BUILDING AIR-CONDITIONING AND VENTILATION SYSTEMS

A Dissertation

by

OLEKSANDR TANSKYI

Submitted to the Office of Graduate and Professional Studies of
Texas A&M University
in partial fulfillment of the requirements for the degree of

DOCTOR OF PHILOSOPHY

Chair of Committee,	David E. Claridge
Co-Chair of Committee,	Michael B. Pate
Committee Members,	Charles H. Culp
	Juan-Carlos Baltazar-Cervantes
Head of Department,	Andreas A. Polycarpou

August 2015

Major Subject: Mechanical Engineering

Copyright 2015 Oleksandr Tanskyi

ABSTRACT

This dissertation presents the findings of a microporous molecular sieve zeolite composite membrane experimental study for dehumidification in building ventilation and air-conditioning systems. The dependence of membrane water and air permeance from inlet airflow parameters (flow rate, humidity, temperature), and permeate total pressure was experimentally studied. Based on the obtained results, the membrane dehumidification system and the membrane air-conditioning system's annual energy efficiency were estimated in an actual building located in a hot and humid climate.

Membrane dehumidification process application was considered in three main areas: an energy recovery ventilation (ERV) system, an outdoor air dehumidification for dedicated outdoor air system (DOAS), and an air-conditioning system that combines an evaporative cooling and the membrane dehumidification system. Application of the membrane separation process for building air-conditioning provides several advantages: improvement of an occupant's health and comfort due to better ventilation rate, better energy efficiency, operation without fluorocarbon refrigerant, capability to collect pure water from the airstream during dehumidification process, no condensation during dehumidification provides mold resistant system, and separate control of sensible and latent load.

The experimental data revealed, that with the existing technology studied zeolite membrane average effective air permeance does not exceed (3±0.5)E-9 kmol/(kPa-m²-s), and average effective water permeance is at least (5±2)E-6 kmol/kPa-m²-s that provides a membrane selectivity coefficient above 1500.

The analytical model of the membrane ERV systems showed that at the design conditions, the ERV system can provide 0.78 cross-flow enthalpy effectiveness with a membrane area of 0.25 m²/cfm (0.42 m²/ (m³/h)).

The application of the membrane dehumidification system in a typical office building can provide an increase in dehumidification process energy efficiency from

coefficient of performance of 4.1 to 7.4. This change in the coefficient of performance will provide energy savings between 6% and 10% for a conventional HVAC system.

The membrane air-conditioning system analysis show that the system operating in actual weather conditions of College Station, Texas can provide annual energy efficiency of 0.98 kW/TR with further possibility to reduce energy consumption to 0.62 kW/TR (COP 5.7).

DEDICATION

To my Mother who has supported and encouraged me throughout my life and provided an exceptional model for me to follow as a researcher that continues to inspire me.

ACKNOWLEDGEMENTS

The experimental test membrane dehumidification system and the membrane air-conditioning system construction were completed with help from Francesco Nima Schaff and consultation from Dr. Michael Pate, Dr. David Claridge, Dr. Charles Culp, Dr. Jeff S. Haberl, and Dr. Wei Liu. The research was done at Texas A&M University in cooperation with the Pacific Northwest National Laboratory and Advance Materials Products, Inc.

I would like to thank my academic adviser, Dr. Claridge, and my committee members: Dr. Pate, Dr. Culp, and Dr. Baltazar-Cervantes, for their guidance throughout the course of this research.

Thanks also go to Mathew Zinke, Mitchell Paulus, and my friends, faculty and staff at the Riverside Energy Efficiency Laboratory and Energy Systems Laboratory of Texas A&M University, for their help and friendship in the past several years during my study.

I am grateful for the financial support from two research projects:

1. U.S. Department of Energy and Advance Materials Products, Inc. Project DE-AR0000138 “High-efficiency, on-line membrane air dehumidifier enabling sensible cooling for warm and humid climates”.
2. Naval Facilities Engineering Command (NAVFAC), Pacific Northwest National Laboratory (PNNL), and Advanced Research Projects Agency – Energy (ARPA-E) from the ARPA-E portfolio “Building Energy Efficiency Through Innovation Thermodevices” (BEETIT). Project DE-FOA-0000752 “Novel Membrane Dehumidification-Enabled Air Cooling”.

The views, opinions, and conclusions stated here are not necessarily those of the Texas A&M University, or the Pacific Northwest National Laboratory, or any other mentioned organization.

NOMENCLATURE

Symbols

Symbol	Name	Typical units
A	Area	m^2
a	Thermodynamic activity	-
C	Heat capacity rate	W/K
C_p	Specific heat	J/kg-K
c	Molar concentration	mol/m^3
D	Fick's diffusion coefficient (diffusivity)	m^2/s
$\mathfrak{D}$	Maxwell–Stefan diffusion coefficient	m^2/s
D_{AB}	Mass diffusivity of water	m^2/s
d	Hydraulic diameter	m
E	Electric potential	V
f	Darcy friction factor	-
$\mathcal{F}$	Faraday constant	C/mol
F	Force	N
h	Enthalpy	J/mol
h	Convection heat transfer coefficient	W/m^2-K
h_m	Convection mass transfer coefficient	m/s
J	Mass diffusion flux	$kmol/m^2$-s
k	Thermal conductivity	W/m-K
k_D	Darcy's hydraulic permeability	m^2
k_m	Mass transfer coefficient	m/s
L	Length	m
M	Molar mass	kg/kmol
$\dot{m}$	Mass flow rate	kg/s
m	Mobility	m^2-mol/J-s

$\dot{N}$	Molar flow rate	kmol/s
Nu	Nusselt number	-
P	Pressure	Pa
$P_{AB_{Air}}$	Effective air permeance	kmol/m²-s-kPa
$P_{AB_{Water}}$	Effective water permeance	kmol/m²-s-kPa
Pr	Prandtl number	-
$\dot{q}$	Heat flux	W/m²
R	Ideal gas constant	J/mol-K
$\Re$	Retention rate	-
Re	Reynolds number	-
S	Solubility	mol/m³-Pa
$s_{A/B}$	Selectivity coefficient	-
Sc	Schmidt number	-
Sh	Sherwood number	-
T	Temperature	K
U_m	Mass transfer conductivity	s/m
u_m	Mean fluid velocity	m/s
V	Molar volume	m³/mol
$\dot{V}$	Volumetric flow rate	m³/s
W	Power	W
x	Mole fraction	kmol/kmol
z	Valency	-
α	Thermal diffusivity	m²/s
$\alpha_{A/B}$	Separation factor	-
γ	Activity coefficient	-
ε	Effectiveness	-
η	Efficiency	-
μ	Dynamic (shear) viscosity	N-s/m²

$\boldsymbol{\mu}$	Chemical potential	J/mol
$\mathcal{P}$	Permeability	mol-m/m²-s-Pa
ν	Kinematic viscosity	m²/s
ξ	Local friction coefficient	-
ρ	Density	kg/m³
Ψ	Electric potential	V
ω	Humidity ratio	kg/kg

U.S. customary and other measure units

Unit	**Name**	**SI equivalent**
Barrer	Barrer	3.344E-16 (mol-m/m²-s-Pa)
Btu	British thermal unit	1,055 (J)
cfm	Cubic foot per minute	4.72E-4 (m³/s)
fpm	Feet per minute	5.08E-3 (m/s)
ft²	Square foot	9.29E-2 (m²)
in w.g.	Inches of water gage	249.2 (Pa)
lpm	Liter per minute	1.67E-5 (m³/s)
TR	Ton of refrigeration	3,517 (W)

Acronyms

ARPA-E	Advanced Research Projects Agency – Energy
ASHRAE	The American Society of Heating, Refrigerating, and Air-Conditioning Engineers
BEETIT	Building Energy Efficiency Through Innovation Thermodevices
COP	Coefficient of performance
DOAS	Dedicated outdoor air system
EES	Engineering Equation Solver
ERV	Energy recovery ventilation
FS	Full scale

HRV	Heat recovery ventilator
HVAC	Heating, ventilating, and air-conditioning
NAVFAC	Naval Facilities Engineering Command
NIST	National Institute of Standards and Technology
NREL	National Renewable Energy Laboratory
NTU	Number of transfer units
OA	Outdoor air
PC	Polycarbonate
PDMS	Polydimethylsiloxane
PE	Polyethylene
PES	Polyethersulphone
PNNL	Pacific Northwest National Laboratory
PSF	Polysulfone
PVDF	Polyvinylidenefluoride
RH	Relative humidity
SF	Separation factor
STP	Standard conditions for temperature and pressure

TABLE OF CONTENTS

Page

LIST OF FIGURES

Page

LIST OF TABLES

Page

1 INTRODUCTION

1.1 Background

Improvements in the development of membrane materials have created opportunities for the expansion of membrane gas separation process applications in various industries, including building heating, air-conditioning, and ventilation (HVAC) systems. Applications of membrane gas separation processes for building air-conditioning allows for the development of systems that operate with no direct environmental pollution (e.g. fluorocarbon refrigerant leaks or CO_2 emissions). At the same time, the proposed systems can exceed the energy efficiency of conventional vapor compression systems.

Another advantage of this system is the separation of the sensible and latent loads. The separate control of the dehumidification load does not cause overcooling of the supply airflow and makes the reheat system an unnecessary component. Separate management of the cooling and dehumidification load increases the control over indoor air conditions and overall system efficiency.

Since 1980, membrane gas separation has been a competitive technology that can replace conventional systems (e.g. building air-conditioning) that operate based on a phase change (water condensation) principle or adsorption processes (e.g. ERV). One of the most common examples of a successful membrane separation technology application is seawater desalination for freshwater supply, where membrane separation systems have demonstrated low operation costs and minimum environmental impact in comparison to alternative technologies [1].

The cooling load from ventilation air dehumidification is a major contributor to the cooling energy requirements and chiller capacity requirements of commercial buildings, particularly in hot and humid climates. For example, the 25,000 ft² (2,323 m²) building occupied by the Energy Systems Laboratory in College Station, Texas has a peak cooling load of 286,000 Btu/h (83.8 kW). According to a calibrated DOE-2

simulation [2], ventilation air contributes 47% to the building peak cooling load. A heat recovery ventilator (HRV) with 80% effectiveness would reduce the required air-conditioning capacity by 19%, while an energy recovery ventilator with 80% sensible and 80% latent effectiveness can decrease the required air conditioner size by 38%. The annual cooling energy savings from this ERV would be approximately eight times that of the cooling savings from the HRV in the humid climate of College Station, Texas. The difference between energy savings is reasonable because about 87% of the cooling load due to outside air is a latent load in this climate.

The most commonly used type of ERV today is a rotating desiccant wheel. However, ERVs are not widely used due to the cost and significant maintenance requirements related to the rotating wheel.

Membrane separation applications in air-conditioning and ventilation systems are not limited to energy recovery ventilation. The membrane dehumidification system, with a partial vacuum on the permeate side of the membrane and building supply airflow on the other, creates a dehumidification system that can operate independently from exhaust airflow availability. With further system improvements by a direct/indirect evaporative cooling component, the membrane dehumidification system can replace a conventional refrigerant vapor compression air-conditioning system.

The preliminary theoretical research study of the zeolite membrane dehumidification system was done by Bynum [3]. His dissertation shows that the combination of multiple evaporative coolers and membrane dehumidification components could achieve a maximum coefficient of performance (COP) of 3.73 (with the design membrane properties assumption), which exceeded the ARPA-E target value of 3.58 for dehumidifying 90°F air at 90% relative humidity (RH) to a humidity ratio of 0.0047.

The membrane separation experimental research study was done using six zeolite membrane modules. They were connected to the experimental system and tested in different system configurations at various inlet conditions representing humid climates. A zeolite membrane on a porous nickel substrate used in the tested modules was

developed by Liu [4] at Pacific Northwest National Laboratory. Experimental results of this research were included in the energy analysis modeling to estimate new system energy efficiency.

The application of this new technology is novel and disruptive, with unknown reliability compared to the standard HVAC systems. This creates some level of market risk for investors. The new system will require design and manufacturing of some special parts that are not yet on the market. Design and installation of the new system will also require training for all personnel involved. At the same time, direct expansion air-conditioning has been optimized for more than 100 years and is at the threshold of cost and practical limits of thermodynamic efficiency's. If the above mentioned risks can be mitigated, the membrane dehumidification system for building air-conditioning has strong market potential.

1.2 Purpose and objectives

The purpose of this study is to investigate opportunities for applications of the membrane separation process based on non-organic zeolite membrane material for the dehumidification process in building air-conditioning and ventilation systems. This study targets technology applications in warm and hot climates and is limited by outdoor air wet-bulb temperatures between 40-85°F (4-30°C) and dry-bulb temperatures between 40-120°F (4-49°C).

Theoretical analysis combined with the experimental data is used to estimate the effect of different variables (design parameters and operation conditions) on the performance and energy efficiency of the dehumidification and the air-conditioning system.

This research considers three main application targets for the zeolite membrane dehumidification process in building air-conditioning and ventilation systems. The first application is energy recovery ventilation. The second application is outdoor air dehumidification, as part of a dedicated outdoor air system (DOAS). The third application is the membrane air-conditioning system that combines an evaporative cooling and membrane dehumidification system.

This research targets the analysis of the zeolite membrane separation performance and the impact of the separation performance on whole system energy efficiency.

The objectives of this research include:

- Development of a thermodynamic and heat transfer analytical model of a zeolite membrane ERV device for cross-flow and counter-flow configurations.
- Estimation of theoretical energy effectiveness of an energy recovery ventilation system operating with the zeolite membrane.
- Design and construction of a proof-of-concept experimental model of membrane dehumidification system and membrane-air-conditioning system.
- Investigation of the physical properties of the zeolite membrane separation process as a function of inlet conditions (airflow rate, temperature, humidity) and permeate pressure.
- Development of a thermodynamic and heat transfer analytical model of the membrane dehumidification system and air-conditioning system based on the experimental data.
- Estimation of the energy efficiency of DOAS with zeolite membrane dehumidification in comparison to a conventional HVAC system.
- Estimation of the energy efficiency of a membrane air-conditioning system that combines the evaporative cooling and membrane dehumidification process.

1.3 Significance of the work

The work provides analysis of zeolite membrane performance in different conditions that can occur during the membrane dehumidification operation as part of a building air-conditioning and ventilation system. Based on the experimental results obtained, the new system's energy efficiency was estimated. This work is also a proof of concept that the membrane air-conditioning and dehumidification systems can provide

the required cooling and dehumidification of the airstream with system energy consumption that does not exceed the energy consumption of a modern conventional HVAC system. The combination of high energy efficiency, compact size, and no direct emissions from system operation or fluorocarbon leakage is an important advantage over conventional systems.

Investigation results of this work can be extrapolated from specific membrane materials and climate conditions to the application of other membrane materials with high selectivity.

The experimental results and analysis provided in this work will be valid in many regions of the world, especially those with hot and humid climates or hot climates with access to fresh water for evaporative cooling, including the southern United States, South America, the Middle East, and Southeast Asia.

1.4 Limitations of the work

This research is limited to one type of membrane material developed by the Pacific Northwest National Laboratory (PNNL). Detailed information about the zeolite membrane material and the membrane module construction is considered confidential and exempt from public disclosure in this manuscript. All investigations in this work are limited to weather conditions above freezing. Though systems described in this research have many components (e.g. vacuum water condenser, intermediate compressor, vacuum pump), the detailed analysis provided in the manuscript is limited to the membrane module performance only, and does not include other system components. Membrane ERV system analysis includes only theoretical modeling, due to cost limitations of the research project.

2 LITERATURE REVIEW

The literature review section is separated into two main subsections. The first subsection describes application of industrial technologies related to the work described in the dissertation. The second subsection describes fundamentals of mass transfer, membrane classification and separation principle.

2.1 Related technologies application

The following literature review subsection is divided into three individual areas related to the proposed research field. The first part addresses the applications of the zeolite membrane gas separation for the building airflow dehumidification process and the application of membrane separation using zeolite membrane. The second part discusses the variety of membrane separation process applications for energy recovery between building outdoor airflow and exhaust air flow. The third part covers applications of direct and indirect water evaporative cooling of building supply airflow.

2.1.1 Zeolite membrane for gas separation and membrane dehumidification

The membrane gas separation process was originally developed for hydrogen recovery to replace cryogenic distillation. At present, the main application of the gas separation process is: production of nitrogen and oxygen enriched gases, hydrogen recovery from refinery streams, and CO_2 separation from natural gas [1, 5, 6]. Organic polymers as asymmetric nonporous membranes based on solution-diffusion transport mechanisms are generally used for gas separation [1].

In this research, the application of the microporous molecular sieve inorganic zeolite composite membrane material with Ni-support for building air-conditioning and ventilation systems is analyzed.

Zeolites are crystalline inorganic framework structures that have uniform, molecular-sized pores and are deposited on porous supports [6, 7]. The application of the zeolite membrane, in comparison to organic membranes, improves the system's ability

to withstand mechanical stress, aggressive chemicals, as well as high temperatures. The separation performance of zeolite membranes is highly dependent on operating conditions, such as chemical composition, total pressure and temperature of the gas [8, 9].

Zeolite membranes are capable of separating mixtures based on several parameters: adsorption properties, component size, and shape [7, 10-12]. The zeolite membrane separation model is similar to the solubility-diffusion model developed for dense organic polymer membranes, and can be described by a combination of the mixture adsorption equilibrium and the mixture diffusion process [1, 7]. When the zeolite pore size distribution falls between the molecular sizes of the feed components, a size exclusion mechanism can dominate the separation process [6].

Mass transfer modeling of the zeolite membrane using the Maxwell–Stefan theory and the bi-modal pore diffusion is not appropriate for the air dehumidification systems, in which water vapor is a strongly-adsorbing component and air (O_2 and N_2) is a weakly-adsorbing component [12]. Future research is required to develop mass transfer models of the zeolite membrane for water vapor separation based on the Maxwell–Stefan theory.

The key parameter for the membrane separation process energy efficiency is high membrane selectivity (relative permeability of the membrane for the target feed species) that is a result of the membrane formation process. For the membrane surface formation, two groups of zeolite membrane preparation methods can be used: one-step methods and seeding technique methods [13].

In one-step methods (in situ) of membrane formation, zeolite crystals are grown inside of macroporous support pores (pore plugging synthesis) from an alkaline solution containing the zeolite precursors that provides a defect-free and very robust membrane, but at the same time membrane permeance for the dominant species is low [7, 14, 15].

Application of the seeding technique method allows decoupling of zeolite nucleation from crystal growth that increases ability to optimize conditions of each process [16]. The first step of the seeding technique is deposition of the crystal seeds on

the membrane support surface [1]. The crystals are deposited with precise control, over which the crystallographic axis is oriented perpendicular to the support [6, 7]. The second step, during the hydrothermal treatment, is when crystal growth occurs. This technique provides the possibility to orient seed crystals and increase the permeation flux [17]. At the same time the risk of defects, such as non-zeolitic pore formation, also increases. Formation of non-zeolitic pores creates intercrystalline pathways larger than zeolite pores, which reduces membrane selectivity [1, 7]. The seeding technique provides the membranes with higher permeance but lower selectivity. Transport through non-zeolite pores that are larger than zeolite pores has contributions from both surface diffusion and Knudsen diffusion, and it might also have viscous flow contributions [7].

Membrane selectivity can be improved if one of the mixture components (e.g. water molecules) swells the crystals [18]. Absorbed molecules cause adsorption-induced expansion of the crystals. This expansion shrinks the size of the defect and as a result improves membrane selectivity [19].

The optimum thickness of the zeolite film is another component that increases selectivity but reduces membrane permeance for the dominant component (i.e. water vapor). According to van de Graaf et al. [9], selectivity of the membrane increases with an increase of the preferentially separated component in the feed content. Membrane selectivity based on the adsorption process also decreases with temperature.

The effect of concentration on pure component diffusivities in zeolites was described by Chen and Yang [20]. The solution provided is based on the irreversible thermodynamics kinetic approach to calculate the Fickian diffusivity matrix for surface diffusion of multicomponent systems. The article showed that the use of a single-component diffusion formulation can cause large errors for the binary diffusion process. The article introduced a blocking parameter that represents the extent of the blocking of the pore by coadsorbed molecules and generalized Maxwell-Stefan equations for multicomponent diffusion.

Increase of the membrane permeance in exchange for some loss of selectivity is an important factor, considering the current high cost of the membrane manufacturing

process around $3000/m² - $4000/m² [1, 12]. The high cost is a result of the fact that most of the zeolite membranes are now fabricated in lab scale sizes and quantities [6]. With the increase of mass production this cost should decrease below $1000/m². At that point the zeolite membrane will be able to compete with other membranes in both cost and performance [1, 7]. The cost of $800/m² [21] for Dupont's ion exchange membrane Nafion (commercially used for compressed air drying devices) is an example of how commercial scale manufacturing decreased cost. A more recent publication suggests the cost of zeolite membrane material could decrease below $50/m² in a membrane module packaged form [12]. The possibility of reducing cost of membrane material manufacturing with large-scale production was also stated by Zhang and Niu [22].

A common application for the zeolite membrane separation process is in the natural gas and chemical industries [5]. Van de Graaf et al. [8] reported membrane separation of ethane/methane and propane/methane mixtures at a total hydrocarbon pressure up to 425 kPa and temperature between 273-373 K. The article states that selectivity of the membrane is highly dependent on operating conditions (composition, total pressure, and temperature). The mass transfer process is described by the generalized Maxwell-Stefan equation, which is based on the separately determined single-component adsorption and diffusion parameters and adsorbate-adsorbate interaction terms. Modeling results were confirmed by the experimental data.

The industrial application of the air/nitrogen and water vapor separation process is limited and exists in compressed air [23] and nitrogen dehumidification [24]. One of the commercially available membrane separation systems is Air Products' PRISM membrane system, which provides dried, compressed air or nitrogen as a system output for food preservation during transportation [23].

Several publications [12, 21, 25-31] and United States patents [32-36] are dedicated to membrane gas separation for air-conditioning and dehumidification systems.

Early publications (1970-1980) in the membrane air dehumidification systems analysis ignored the resistance to gas transport in the gas feed and/or in the gas permeate

[26]. This was justified for membranes with low permeance but needs to be adjusted for advanced membrane materials.

A publication by Asaeda from Hiroshima University [27] in 1986 describes experimental performance of a ceramic membrane (silica-alumina) with coarse porous support for air dehumidification. The analytical calculations made in the article, based on Knudsen's flow assumption, were not capable to predict experimental performance. Experimental data showed decrease of apparent permeability of water with the increase of relative humidity and a similar result for the apparent permeability of air. Experimental data showed that the tested membrane water to air selectivity coefficient was above 1,000 at the stagnant gas condition on the feed side, with a small airflow rate at 50% RH and a temperature of 40 °C (104 °F). At these conditions the effective water permeance was 5.6E-6 kmol/kPa-m²-s and the effective air permeance was 2.7E-9 kmol/kPa-m²-s [27].

In 1992, Ray at al. published a research paper [29] analyzing the ventilation airflow dehumidification system in a microgravity environment. The analyzed device was called a water recovery heat exchanger and was designed to remove water droplets and water vapor from an air stream by separation through a hollow fiber membrane. The proposed device was a shell and tube condensing heat exchanger, constructed from hydrophilic regenerated cellulose tubes with a total area of 1m². The cooling water was circulated by a small circulation pump in the fiber lumens at a pressure below ambient. Water vapor condensed on the lumen surface and was absorbed through the membrane.

Another 1992 publication describes a hollow fiber membrane module for air dehumidification with a reported selectivity coefficient of water over air above 4,000 [26]. The publication showed the importance of the mass transfer resistance consideration in the feed and permeate airflow relative to the membrane mass transfer resistance. It also proposed to recycle some of the retentate gas as a sweep stream on the permeate side. The analysis was done with the assumption of constant membrane permeability independent from pressure and temperature as well as gas concentration.

A recent publication by Xing et al. [12] describes a zeolite membrane application for building air-conditioning and ventilation systems in a hot and humid climate. According to Xing et al. [12], the potential energy efficiency gain over the conventional vapor compression system is more than 50% when the membrane separation factor is above 200. However, currently available membranes do not meet all required criteria to achieve a high energy efficiency in combination with an affordable cost [12].

One of the main concerns in the membrane gas separation for air-conditioning dehumidification system is the reduction of oxygen concentration during the dehumidification process. Experimental results of Xing et al. [12] showed that the membrane separation factor O_2/N_2 is always close to 1.0 and the membrane dehumidification process will not have a measurable effect on retentate oxygen concentration.

Membrane dehumidification in combination with an indirect/direct evaporative cooling system was analyzed by El-Dessouky et al. [25] for the summer weather data of Kuwait. The proposed membrane unit of the analyzed system consists of cellulose acetate and polysulfone tubular hollow fibers that provide a water nitrogen separation factor of 403. Several options to create a partial pressure difference across the membrane were considered. One of the alternative methods to create a driving force is the creation of a vacuum on the permeate side, at a total absolute pressure of 10 kPa.

Another approach for a membrane module operation is the application of a liquid desiccant instead of a vacuum on a permeate side of the membrane [28]. The experimental study was made with cross flow microfiber polyethylene membrane dehumidification in a non-isothermal cyclic process. In this research, the liquid desiccant reactivation was achieved at relatively low temperatures of 37-57 °C.

Dehumidification of air by a hygroscopic liquid membrane packaged in a small flat-type membrane cell with airflow rate of 50–70 cm^3/min was described by Ito [37]. The article shows selectivity of water vapor with respect to air over 2,000. In this study, the humidity of the feed airstream is successfully removed under a vacuum (<0.2 kPa)

on the permeate side. In the experimental setup humidity was measured by a dew point meter with an aluminum oxide sensor calibrated to the dew point accuracy of ± 0.2 K.

2.1.2 Membrane energy recovery ventilation

Energy consumption by HVAC systems in many industrialized countries accounts for 30% of total energy consumption. Conditioning of fresh ventilation air can consume 20 - 40% of the total HVAC energy in hot and humid regions and up to 60% in cold climates [38, 39].

To reduce energy required for dehumidification and cooling/heating of outdoor air, enthalpy exchangers, or Energy Recovery Ventilator (ERV) systems can be used. The literature review by Zhang et al. [38] shows that before 2008, parallel-plate membrane ERV systems have not been studied in open literature. Some of the main concerns in membrane energy recovery ventilation (ERV) systems research are: high cost of membrane material, high pressure drop across the energy recovery ventilation system, and insufficient experimental work in membrane research related to the ERV systems.

Analysis of an air-to-air ERV system operation in Texas climates showed that ERV cost-effectiveness is largely dependent upon the type of building and location (i.e., climate conditions) as well as outside air fraction [40]. This system can save roughly $1.00 to $1.50 per cfm of outside air during a one year period at 2009 energy prices. The ERV system payback time is below 3 years for systems operating with 100% outside air (OA) and about 5 years for systems with 10% OA (e.g. office buildings) located in the humid climates of Dallas - Ft. Worth or San Antonio, Texas.

The air-conditioning system with an enthalpy exchanger, which pre-cools the fresh air before it is supplied to a refrigeration system for air dehumidification, was analyzed by Zhang et al. [30]. The proposed system is a combination of an enthalpy exchanger and refrigeration system with R134a refrigerant and a compressor operating with 0.75 isentropic efficiency. The conducted analysis shows that the analyzed system has COP between 2.5 and 6.5 when evaporator temperature increases from -10 to 25°C,

at a fixed condenser temperature of 45 °C. At an evaporator temperature of 12.8°C (55°F), the system COP is 4.5 [30]. The hourly simulation showed a system energy savings potential of 33%.

Parallel-plate enthalpy exchangers with novel membrane materials (common paper, cross-linked cellulose acetate membrane, and a modified cellulose acetate membrane) were analyzed by Zhang et al. [38]. A parallel-plate enthalpy exchanger with a surface area of 3.9 m² had a 2 mm channel height, which provided 43 Pa (0.17 in w.g.) of measured pressure head losses at the frontal air velocity of 0.55 m/s (108 fpm).

The experimental results for a modified cellulose acetate membrane show latent effectiveness of 0.75, independent from the fresh air relative humidity and temperature. The experimental results showed a decrease of latent effectiveness from 0.8 to 0.7 when the volumetric air flow rate changed between 0.37 and 0.74 m/s frontal air velocities (100-200 m³/h).

The effect of membrane properties on the performance of the membrane based ERV system was analytically studied by Min and Su [41]. The analysis shows that the membrane properties have negligible effect on the sensible heat transfer (less than 10% of the total thermal resistance) while affecting water vapor mass transfer (65-90% of total mass transfer resistance). For the analysis, a numerical computation method was used. The design channel height was 4 mm (2 mm from the membrane to the symmetry line) and 550 Reynolds number. For validation of the analysis results, the NTU method was used.

The following publication by Min et al. [42] describes an experimental study, and the numerical analysis of moisture permeation through polyvinylidenefluoride (PVDF) and polyethersulfone (PES) membranes. The experiments were conducted with an airflow rate of 3-5 lpm. Airflow humidity was measured by humidity/temperature sensors installed in the chambers (Rotronic AG Company, Model: Hygrolog NT-3) with measuring accuracy of 1.5% for relative humidity and 0.3°C for temperature. The experimental moisture diffusivity uncertainties were estimated to be 26.4–41.1% for the PVDF membrane and 23.8–35.6% for the PES membrane. The results show that the

water diffusivities in the PVDF and PES membranes are in the range of 10E-6 kg/m-s [42].

Another publication analyzes annual energy consumption of an air-conditioning system coupled with an enthalpy Z-flow configuration flat plate membrane heat exchanger constructed from 98μm thick 60g/m² Kraft paper [43]. The article showed that a savings of up to 8% in annual energy consumption can be achieved when a membrane heat exchanger is used with a conventional HVAC system in tropical climates and 4% in moderate climates. The experimental temperature measurements were made with multiple t-type thermocouples. The air velocity was measured by averaging the values of multiple hot-wire anemometers. The experimental error margin was below 9%. Experiments were conducted with the air face velocity ranging from 0.3 m/s to 2.89 m/s. The measured pressure drop across the heat exchanger was 400 Pa or 1.6 in w.g. at the feed air face velocity of 2 m/s and 250 Pa (1.0 in w.g.) at the air face velocity of 1.5 m/s. Energy performance was modeled with the enthalpy heat exchanger inlet stream face area of 3.3 m² and the air face velocity in the heat exchanger of 0.3 m/s. The estimation for the enthalpy exchanger sensible, total and latent effectiveness is 0.71, 0.66 and 0.61 respectively. Estimation was made for an air face velocity of 0.3 m/s.

Analysis of the membrane ERV system was conducted for the Hong Kong climate by Zhang and Niu [22]. Energy analysis showed that for Hong Kong weather conditions most of the energy is used in ventilation for dehumidification rather than for sensible cooling. The energy consumption of a heating system in Hong Kong weather conditions was negligible. Application of the membrane ERV system can save up to 58% of the energy used for air-conditioning of fresh air while a sensible heat exchanger provides only 10% energy savings. Comparison with the Beijing cold and dry climate conditions shows that the annual energy savings for the ERV system is 23.5% while the sensible heat recovery ventilation system can provide the annual energy savings of 18%. This shows that the application of ERV system should be more successful in humid climates. In Hong Kong climate conditions, the analyzed membrane ERV system with channel height of 2.5 mm provides average annual latent effectiveness of 0.6 [22].

Another analysis of the membrane ERV system performance was conducted by Zhou et al. [44] for the Shanghai and Beijing climates using EnergyPlus. The simulation results showed that the application of the ERV system in Beijing is uneconomical during the summer for an indoor temperature setpoint above 24 °C (75 °F).

An energy recovery ventilation system based on hollow fiber and flat sheet membranes with an interfacially polymerized coating of polyamide was analyzed by Kistler and Cussler [45]. The theoretically estimated latent energy recovery effectiveness of this system was up to 60%.

The effects of the membrane spacing and thickness on the ERV system performance was analytically investigated by Min and Su [46]. The results show that for a fixed fan power, as the channel height increases from 1.58 to 2.9 mm, the total heat transfer rate initially increases, however after reaching the maximum at a certain channel height, begins to decrease. For a fixed fan power, as the channel height increases, the airflow rate increases, which increases the total heat transfer rate, whereas the total heat transfer surface area decreases, which reduces the total heat transfer rate. These two effects interact and make the total heat transfer rate initially increase to the maximum and then decrease [46].

The other theoretical study by Min and Su shows that in hot weather, the sensible effectiveness barely changes with the outdoor temperature but decreases gently with increasing outdoor humidity [47]. At the same time, the latent effectiveness decreases slightly with increasing outdoor temperature but increases rapidly with increasing outdoor humidity.

The high energy cost and cold climate conditions have created a large market for residential sector ventilation heat recovery systems in Sweden and Germany. Cold climate conditions create system design requirements that are very different from the previously discussed systems. One of the largest differences is a negative building pressurization requirement in cold climate to avoid water condensation in walls. In Sweden, ventilation heat recovery systems became popular in 1979. The German building energy code after the year 2000 requires well insulated and tight buildings so

the energy demand for heating from ventilation air tends to reach about 60% of the building's total annual energy consumption [39]. These conditions make an energy recovery system one of the required building components. The article [39] shows that one of the most effective systems in a cold climate (COP change between 5 and 3 for the outside air temperature -10 °C to 14°C) is a heat pump combined with an air-to-air heat exchanger.

2.1.3 Evaporative cooling systems (desert/R 718 cooling systems)

The analysis of a desiccant enhanced advanced indirect evaporative air conditioner that combines liquid desiccant and evaporative cooling technologies into an innovative "cooling core" is described by the National Renewable Energy Laboratory (NREL) technical report [48] and related journal publication [49]. Simple indirect evaporative coolers can achieve a supply air temperature that approaches the dew point of the ambient air without adding moisture, but they do not provide dehumidification. To provide dehumidification, a combination of the desiccant-based dehumidification and indirect evaporative cooling can be used. The combination of two separate systems has significant limitations due to the equipment size and complexity. Application of liquid desiccant (strong lithium chloride (LiCl) and calcium chloride ($CaCl_2$) salt water solutions) in a combined system is one of the ways to avoid these problems.

Modeling conducted in the National Renewable Energy Laboratory (NREL) showed that the yearly combined source energy for the thermal and electrical energy required to operate this system is expected to be 30%–90% less than the state-of-the-art direct expansion cooling (function of climate humidity) [48].

Application of an indirect operating evaporative air-conditioning system, based on the evaporation of water (R718), was analyzed for application in actual large building systems located in relatively dry climates [50]. The analyzed system operates as an indirect adiabatic evaporative cooling system that includes a spraying chamber and a cross-stream heat exchanger. In the system described, the feed building airstream is cooled through the heat exchanger to a temperature that can be below the outside air

wet-bulb temperature. The heat exchanger is cooled with processed air that passes through an evaporative cooler and is a mixture of an outside airflow and one third of a feed airflow separated after the heat exchanger. The processed air exiting the heat exchanger is rejected into the ambient air.

Packing material plays an important role in the cost of direct evaporative coolers, since it accounts for 10-20% of the system cost [25]. At the same time, increasing the packing thickness improves the cooling efficiency of direct evaporative coolers, because of the increase in the air residence time inside the packing material. In the direct evaporative cooler system described by El-Dessouky et al. [25], the water can be delivered through spray nozzles that generate a conical pattern of fine mist. The nozzles are arranged in a square or triangular pitch with proper spacing that gives complete wetting of the packing surface. An alternative for the spray nozzles is a simple tray distributor where a continuous stream of fine water droplets flows over the top surface of the packing block from the perforated base of simple tray distributor.

Application of an evaporative cooler with natural zeolite desiccant in a rotary dehumidifier was analyzed by Kanoglu et al. [51] for building ventilation systems. The proposed system combines a zeolite wheel with a counter-flow sensible heat exchanger (rotary regenerator) and evaporative cooling system. Exergy destruction and energy efficiency analyses of the system showed a COP of 0.35 and reversible COP of 3.11. In the proposed system, desiccant can be regenerated with a low-grade heat airflow at a temperature of about 60-95°C (140-203°F).

2.2 Membrane separation fundamentals

This literature review subsection describes membrane type classification, fundamentals of the water diffusion process, convection mass transfer mechanisms, and separation physical principles.

2.2.1 Membrane types classification

A membrane can be defined as a thin film separating two phases and acting as a selective barrier (functional material) to the transport of matter based on physical and/or

chemical properties [52]. A mass flow through the membrane depends on the nature of the elements contained in the two phases and on the driving force that is applied. The main advantages of membrane separation are:

- Separation at ambient temperatures without phase change. This reduces the amount of energy required to complete the process. (cooling is not required in the air dehumidification process),
- Separation taking place without accumulation of products inside the membrane. No regeneration cycle is required and a system can operate continuously,
- Easy scale-up and combination with other processes.

The main drawbacks are:

- Membrane fouling,
- Low membrane lifetime,
- Low selectivity.

Synthetic (non-biological) passive membrane classification can be based on the following parameters: driving force, separation mechanism, membrane structure, phases in contact, or the chemical nature of materials used [52].

The main driving forces are pressure gradients, activity (partial pressure, temperature, concentration), or electrical potential.

The separation mechanism is based on a difference in: size (sieve effect), vapor pressure (membrane distillation), affinity (adsorption, absorption), solubility and diffusivity of materials in the membrane (solution-diffusion mechanism), the electrical charges of the species (electrochemical effect), or the chemical nature (liquid membranes). Three main classes can be defined based on the separation mechanism: porous membranes (sieve effect), dense membranes (solution-diffusion mechanism), and electrically charged membranes (ion-exchange membranes).

Three membrane classes can be defined based on the membrane structure: isotropic, asymmetric (anisotropic membranes prepared from the same material), and composite (anisotropic membranes with layers of different materials). In composite

membranes the top layer determines the transport rate and a porous sublayer from a different material provides mechanical support. Due to reverse dependence of the flux and active membrane layer thickness (0.1 to 0.5 μm), composite membranes can provide a higher flux than isotropic membranes with thicknesses of 10-200 μm [53]. Membrane geometry can be flat or cylindrical.

Phases in contact can be liquid-to-liquid (microfiltration, ultrafiltration, hyperfiltration, osmosis, dialysis, and membrane distillation), liquid-to-gas (pervaporation) or gas-to-gas (gas separation).

Membranes can be divided into two classes according to the chemical nature of the materials used: organic (polymeric or liquid) and inorganic (ceramic, metals, glasses, etc.). The most common types of organic membranes are cellulose, polyamides, polysulfone (PSF), polyethersulphone (PES), polyethylene (PE), polycarbonate (PC) and others. The main advantage of inorganic material is superior chemical, mechanical and thermal stability relative to polymers. The main disadvantage is higher cost and brittleness.

For gas separation two types of membranes can be used: dense membranes (solution and diffusion of species in the free volume between the macromolecular chains of the membrane material) and porous membranes (with pore radius below 2nm where Knudsen flow occurs). The main industrial applications of membrane gas separation occur in hydrogen recovery and separation of oxygen and nitrogen, and of methane and carbon dioxide with limited application in air-conditioning systems.

2.2.2 Membrane separation physical principles

During membrane operation, a feed stream is separated into two streams: a permeate stream containing a material, which passes through the membrane, and a retentate stream containing the nonpermeating species (Figure 1).

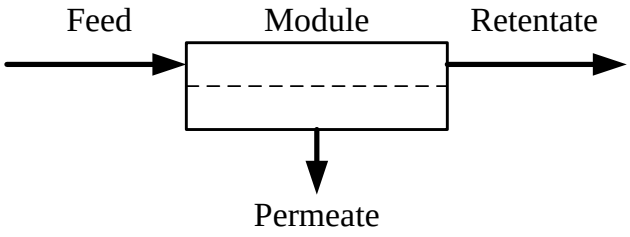

Figure 1. Membrane separation process

The flux through a membrane is a product of mobility, concentration and the driving force. The mobility can be defined as:

$$m = \mathrm{D}/\mathrm{RT}; \tag{1}$$

where: D - Fick's diffusion coefficient.

The concentration of the solute in the membrane varies with distance through the boundary layer and membrane.

The main local forces are the gradients of electrical potential $\mathrm{d}F/\mathrm{d}x$ or chemical potential $\mathrm{d}\mu/\mathrm{d}x$ of every component that can be transported [52]. Electrical potential, as well as other than concentration forms of potential (magnetic, centrifugal, gravity fields), will not be considered in this dissertation.

The change of chemical potential of component i can be expressed as a sum of terms under isothermal conditions:

$$d\boldsymbol{\mu} = RT \cdot dln\ a_i + V_i dP + z_i \mathcal{F} d\Psi; \quad (2)$$

where: a_i- thermodynamic activity;
P – pressure (acts on every component in proportion to its molar volume);
V_i - molar volume;
$\mathcal{F}$ - Faraday constant;
Ψ – electric potential (acts only on ionic species);
z_i – valency.

In this formula, the first component reflects a difference in composition, the second – a difference in pressure, and the last – a difference in electrical potential.

Absolute chemical potential can be expressed as:

$$\boldsymbol{\mu} = \boldsymbol{\mu}_i^o + RT \cdot lna_i + V_i P + z_i \mathcal{F} d\Psi; \quad (3)$$

where: $\boldsymbol{\mu}_\mathbf{i}^\mathbf{o}$ – constant.

Activity is directly proportional to component mole fraction:

$$a_i = \gamma_i \cdot x_i; \quad (4)$$

where: γ_i – activity coefficient;

x_i – mole fraction.

With the assumption of an ideal solution, the activity coefficient is equal to one and activity becomes equal to mole fraction or concentration [53]. This assumption is valid if the penetrant does not affect properties of a membrane (non-organic fluids). In polymer membranes, this assumption can be used for nitrogen or water vapor, but is not valid for gases interacting with the membranes (e.g. CO_2).

For ideal conditions chemical and electrical potential as a driving force can be expressed as:

$$F_i = \frac{RT}{L} \cdot \frac{\Delta x_i}{x_i} + \frac{\Delta V_i}{L} \Delta P + \frac{z_i \cdot \mathcal{F}}{L} \Delta E. \quad (5)$$

Multiplying this equation by L/RT $\left[\frac{\text{mol}}{\text{N}}\right]$, the driving force becomes dimensionless [53].

$$F_{i_{Dim}} = \frac{\Delta x_i}{x_i} + \frac{V_i}{RT} \Delta P + \frac{z_i \cdot \mathcal{F}}{RT} \Delta E; \quad (6)$$

or

$$F_{i_{Dim}} = \frac{\Delta x_i}{x_i} + \frac{\Delta P}{\text{P}^*} + \frac{\Delta E}{\text{E}^*}; \quad (7)$$

where: $\text{P}^* = \frac{R \cdot T}{V_i}$; $\text{E}^* = \frac{R \cdot T}{z_i \cdot \mathcal{F}}$.

For example, the chemical potential of water transfer through a membrane can be simplified as:

$$\Delta \boldsymbol{\mu}_\text{w} = \boldsymbol{\mu}_{\text{w}2} - \boldsymbol{\mu}_{\text{w}1} = \text{R} \cdot \text{T} \cdot (\ln \text{x}_2 - \ln \text{x}_1) + \text{V}_\text{w} \cdot (\text{P}_2 - \text{P}_1); \quad (8)$$

where subscript 2 refers to the permeate side and subscript 1 refers to the feed side.

The phenomenological relation between flux and force in the macroscopic transport process model, which considers the membrane as a black box, can be reflected in different ways (Table 1): a diffusion coefficient (D, Fick's law), permeability coefficient (k_m, Darcy's law) or by other relations (e.g. Fourier's law, Newton's law,

Ohm's law) [53]. This approach does not consider the membrane structure or chemical and physical effects on the transport process.

Table 1. Equations relating the driving force and flux

Flux	Relation	Law
Mass	$J_m = -D\frac{dc}{dx}$	Fick
Volume	$J_v = -k_m\frac{dP}{dx}$	Darcy
Thermal Energy	$J_t = -k\frac{dT}{dx}$	Fourier
Momentum	$J_n = -\nu\frac{dv}{dx}$	Newton
Electrical Energy	$J_i = -\frac{1}{R}\frac{dE}{dx}$	Ohm

In all cases the linear transport relation can be applied with the assumption of pure component permeation through a membrane. This assumption neglects coupling phenomena between components that permeate simultaneously.

To account for this interaction during multicomponent mixture permeation the Maxwell–Stefan model could be used. The Maxwell–Stefan steady state model for diffusion of multicomponent ideal gas systems in nonporous polymeric membrane [54-57] can be written:

$$\frac{\nabla \boldsymbol{\mu}_i}{R \cdot T} = \sum_{\substack{i=1 \\ j \neq i}}^{n} \frac{c_i c_j}{c^2 \mathfrak{D}_{ij}} \cdot \left(\frac{\vec{J_j}}{c_j} - \frac{\vec{J_i}}{c_i} \right); \quad (9)$$

where: $\nabla \mu_i$ - vector differential of chemical potential,

c_i - molar concentration of component i,

c - total molar concentration,

$\mathfrak{D}_{ij}$ - Maxwell–Stefan diffusion coefficient,

$\vec{J_i}$ - flux of component i.

A passive transport mechanism without coupling phenomena will move particles from a high potential to low potential. With no external forces applied, the system will reach equilibrium when the potential gradient is zero.

Another type of passive transport with coupling phenomena is a "carrier-mediated" mechanism [53]. In this case transport of a component across a membrane is affected by the presence of a mobile carrier (Figure 2). This additional mechanism affects free diffusion and accelerates the transport processes. The carrier-mediated mechanism also allows transport against the component chemical potential gradient and driven by the chemical potential gradient of the carrier.

The performance of a membrane can be described by its selectivity and the flux through the membrane. The flux (or permeation rate) is defined as the volume flowing through the membrane per unit area and time interval, and may be based on volume, mass or mole amount.

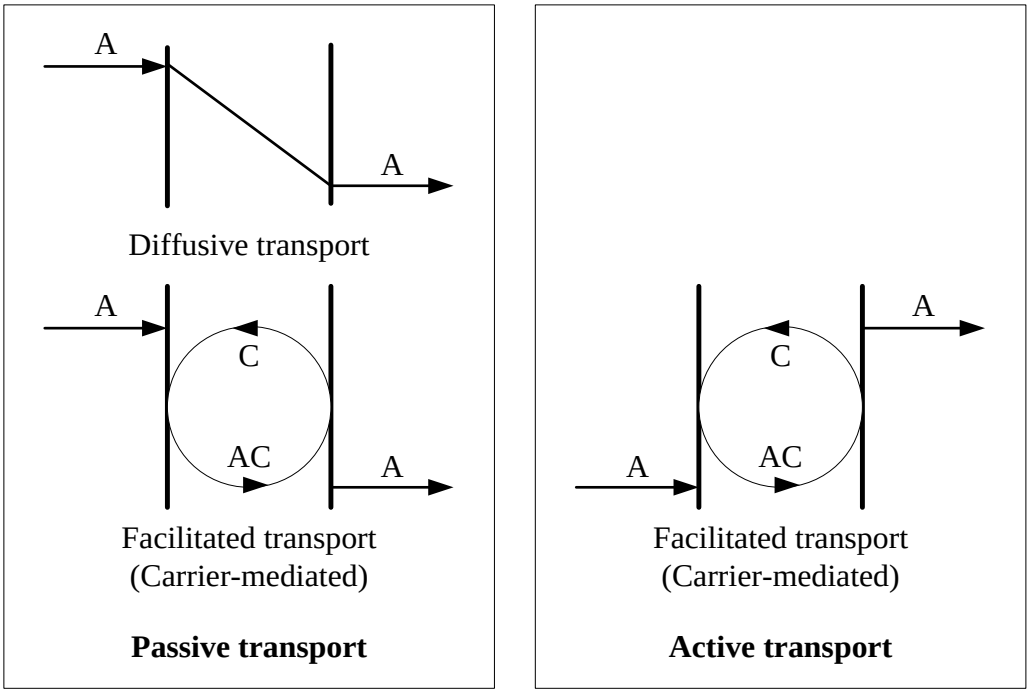

Figure 2. Main types of membrane mass transport (C is carrier and AC is carrier-solute complex)

The selectivity of a membrane can be expressed by retention rate, separation factor, or selectivity coefficient.

The retention rate is used for dilute aqueous mixtures consisting of a solvent (mostly water) and a solute, and is defined as:

$$\Re = \frac{c_f - c_p}{c_f}; \tag{10}$$

where: c_f - the solute concentration in the feed;
c_p - solute concentration in the permeate.

The separation factor is used for gas mixtures and is defined according to the equation (11) [15, 58, 59]:

$$\alpha_{A/B} = \frac{\left(\frac{c_A}{c_B}\right)_p}{\left(\frac{c_A}{c_B}\right)_f}; \quad (11)$$

where: c_A and c_B – concentrations of components A and B in the permeate (p) and in the feed (f).

Selectivity coefficient is used for gas mixtures and is defined as [58]:

$$s_{A/B} = \frac{\mathcal{P}_A}{\mathcal{P}_B}. \quad (12)$$

The concentration can be expressed as a mass concentration, molar concentration, weight fraction or volume fraction. The selectivity $s_{A/B}$ is defined in such a way that its value is greater than unity. If component B permeates preferentially the separation factor would be defined as $s_{B/A}$.

2.2.3 Water vapor diffusion and convection mass transfer mechanism

There are three main types of transport (mass diffusion) through a membrane for gas separation [53]:

- Viscous flow in wide pores (composite or asymmetric membranes),
- Knudsen flow in narrow pores,
- Dense membrane mass transfer.

The type of flow in pores (i.e. Knudsen or viscous) depends on pore size. For a pore with a radius greater than 10 μm, viscous flow occurs. Gas molecules in a viscous flow collide between each other and do not interact with a membrane. This does not provide separation and can occur in a composite membrane base layer.

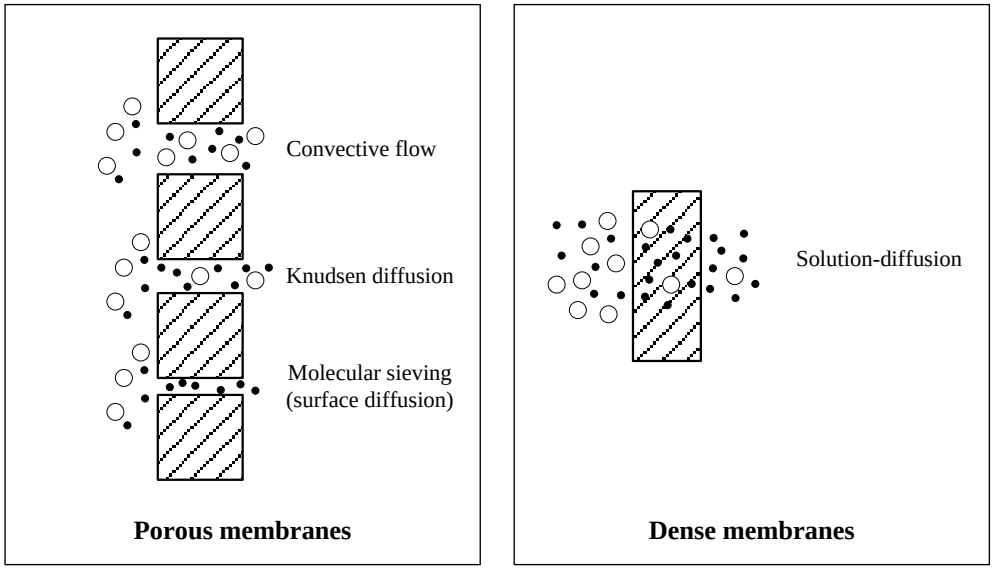

Figure 3. Mechanisms of gas permeation through porous and nonporous membranes

Knudsen diffusion occurs when pore size is reduced below 10 μm or with a decrease of gas pressure. In this case the mean free path of molecules exceeds the pore radius and a collision between molecules is less frequent than between molecules and membrane walls. Separation between different gases with Knudsen flow is possible if they have molecules with sizes differing by an order of magnitude (separation depends on the ratio of the square root of the gasses' corresponding molecular weight).

Molecular sieving occurs when the permeating specie exhibits a strong affinity for the membrane surface and absorb along the pore walls. In this case, separation occurs due to the difference in the amount of adsorption of the permeating species based on molecular shape, molecular size and pore size [5]. The pore size in this case is comparable with the molecular size. This process occurs in Zeolite membranes [5].

In dense membranes, molecular transport is possible only if a molecule dissolves in the membrane (solubility). The extent of solubility is determined by the affinity between membrane materials and permeate fluid.

The transport of gas, vapor or liquid through dense membranes can be described by the solution-diffusion model [5, 31, 53, 60]. The permeability coefficient defines the rate at which a penetrant traverses a membrane [5].

$$\mathcal{P} = S \cdot D \tag{13}$$

where: $\mathcal{P}$ – Permeability $\left[\frac{mol \cdot m}{m^2 \cdot s \cdot Pa}\right]$;
S – Solubility (thermodynamic parameter), $\left[\frac{mol}{m^3 \cdot Pa}\right]$;
D – Diffusivity (kinetic parameter), $\left[\frac{m^2}{s}\right]$.

Solubility is a thermodynamic parameter that reflects a measure of the amount of penetrant sorbed by the membrane under equilibrium conditions with a given pressure of the gas and given temperature [61]. Diffusivity is a kinetic parameter that indicates how fast a penetrant is transported through the membrane in the absence of obstructive sorption [5].

Henry's law describes dependence of a concentration of a fluid (solute) inside the membrane (solution) as a function of the applied partial pressure outside the membrane [60]:

$$c = S \cdot P \tag{14}$$

where: c - Concentration of the solute inside the membrane $\left[\frac{mol}{m^3}\right]$;
S – Solubility $\left[\frac{mol}{m^3 \cdot Pa}\right]$;
P - Partial pressure of the solute [Pa].

Partial pressure as a driving force can be considered as a simplified version of the more general case where **fugacity** plays the role of a driving force.

Diffusivity is a kinetic parameter of statistical molecular transport that indicates how fast a penetrant is transported through the membrane. Diffusivity can be described by Fick's first law [15, 60]:

$$J_i = -\frac{D}{R \cdot T}\frac{\partial(c_i \cdot \mu_i)}{\partial x}; \tag{15}$$

where: J_i – Mass diffusion flux $\left[\frac{mol}{m^2 \cdot s}\right]$;

D - Diffusion coefficient or diffusivity $\left[\frac{m^2}{s}\right]$.

For inorganic fluids in polymer membranes both solubility and diffusivity could be assumed independent of concentration, as well as time and place (relaxation phenomena) [53]. A combination of Henry's law and Fick's law integrated across the membrane leads to the definition of permeability coefficient $\mathcal{P}$ [53]:

$$J_m = S \cdot D \cdot \frac{dP}{dx} = \mathcal{P}\frac{dP}{dx}. \tag{16}$$

Based on this equation, the **permeability coefficient** can be defined as an intrinsic parameter in Barrer units $\left(1 \cdot 10^{-9}\,\frac{cm^3 O_2\,(STP) \cdot cm}{cm^2 \cdot s \cdot cmHg} = 0.76 \cdot 10^{-17}\,\frac{m^3 O_2\,(STP) \cdot m}{m^2 \cdot s \cdot Pa}\right)$ [53, 62, 63]. Based on the definition, permeability depends on the membrane thickness, area and the driving force. In this definition cm^3 (STP) is a reference to a molar quantity of oxygen rather than volume, which requires a molar mass correction factor to be applied for other chemical species (17).

$$1\ \text{Barrer} = \frac{29.882}{M}\left[1 \cdot 10^{-9}\frac{cm^3(STP) \cdot cm}{cm^2 \cdot s \cdot cmHg}\right] = \frac{1}{2.99 \cdot 10^{15}}\frac{kmol \cdot m}{m^2 \cdot s \cdot kPa} \tag{17}$$

Though this unit is widely used in industry [62], no official definition is available in NIST. According to ASTM E96/E 96M-05 **Permeability** can be defined only when

the test specimen is homogeneous and not less them 12.5 mm thick as a product of permeance and thickness [64].

Based on the definition of the permeability coefficient, a pressure gradient (fugacity) is considered a driving force for mass transfer. This definition is similar to Darcy's Law that describes a proportional relationship between the instantaneous discharge rate, viscosity of the fluid and pressure drop over a given distance in a porous medium.

$$J_m = \frac{-k_D}{\mu} \cdot \frac{dP}{dx} \tag{18}$$

where: J_m - fluid flux $\left[\frac{m^3}{m^2 \cdot s}\right]$;

k_D - hydraulic permeability of the medium $[m^2]$;

μ – Dynamic (shear) viscosity $\left[\frac{Pa}{s}\right]$.

To transfer permeability from pressure gradient to concentration gradient as a driving force, the following conversion can be performed based on the ideal gas relation:

$$J_m = \mathcal{P}\frac{dP}{dx} = \mathcal{P}\frac{d\left(\frac{R \cdot T \cdot c}{M}\right)}{dx} = \frac{\mathcal{P}}{M} \cdot \frac{d(R \cdot T \cdot c)}{dx} \tag{19}$$

With the assumption of an isothermal process through the membrane, this equation transforms to:

$$J_m = \frac{\mathcal{P} \cdot R \cdot T}{M} \cdot \frac{dc}{dx} \tag{20}$$

Another related coefficient is **permeance**, which is equal to permeability divided by the thickness of material. The most common units of permeance are:

1 *US* perm = 1 grain of water vapor per hour, per ft^2, per inHg

1 metric perm = 1 gram of water vapor per day, per m^2, per mmHg.

1 perm (0 °C) = 5.72135 E-11 kilogram per pascal second square meter $\left[\frac{kg}{Pa \cdot s \cdot m^2}\right]$;

1 perm (23 °C) = 5.74525 E-11 kilogram per pascal second square meter $\left[\frac{kg}{Pa \cdot s \cdot m^2}\right]$.

According to ASTM E96/E 96M-05, 1 perm is equal to 5.72 E-8 $\left[\frac{g}{Pa \cdot s \cdot m^2}\right]$.

Another unit from DIN 53122 [65] is WVTR (water vapor transmission rate) $\left[\frac{g}{m^2 \cdot day}\right]$ that corresponds to a difference in relative humidity of 85% at 23 °C between both sides. This unit is equal to (1/17.918) of a metric perm.

Water vapor has a relatively high permeability coefficient compared to other penetrants, due to a combination of a high mobility for water (diffusivity) and a high solubility [66].

Penetrant size has a linear effect on diffusivity. For water molecules with a kinetic diameter of 0.26nm (2.65Å) [12], the diffusion coefficient at infinite dilution is 1E-4 cm^2/s, which is much higher than 3.2E-5 cm^2/s for oxygen or nitrogen with a kinetic diameter of about 0.346nm (0.364 nm) [12, 66, 67]. In general, the diffusion coefficient at infinite dilution decreases with an increase of penetrant size. For comparison the size of a zeolite channel is 4.0 Å [12].

Solubility coefficient is directly proportional to the penetrant critical temperature. It can be interpreted as a measure for the condensability of the penetrant [66]. For example, in Polydimethylsiloxane (PDMS) at 35°C, the water solubility coefficient is 10E-1 cm^3(STP)/(cm^3-cmHg) (650 K critical temperature) which is more than an order of magnitude larger than the values of 1E-3 and 2E-3 cm^3(STP)/(cm^3-cmHg) for oxygen or nitrogen molecules with critical temperatures of 125 K and 150 K [66].

For binary gas mixtures of permeate gases, a high selectivity is often accompanied by a low permeability and vice versa. An exception to this rule is permeance of water vapor in a mixture with a permanent gas (Table 2) [66].

Table 2. Water vapor permeability and water vapor/nitrogen selectivity for various polymers at 30°C extrapolated to water vapor activity zero

Polymer	Abbreviation	H_2O Permeability (Barrer)	Selectivity (H_2O/N_2)
Polyethylene	(PE)	12	5.71
Polypropylene	(PP)	68	230
Polyvinylchloride	(PVC)	275	12,500
Polyacrylonitril	(PAN)	300	1,875,000
Polyimide (Kapton)	(PI)	640	5,333,300
Polystyrene	(PS)	970	400
Polycarbonate	(PC)	1,400	4,700
Polysulfone	(PSF)	2,000	8,000
Natural rubber	(NR)	2,600	300
Polyethersulfone	(PES)	2,620	10,480
Polyphenyleneoxide	(PPO)	4,060	1,070
Cellulose acetate	(CA)	6,000	24,000
Ethyl cellulose	(EC)	20,000	6,060
Polydimethylsiloxane	(PDMS)	40,000	140
Sulfonated polyetheretherketon	(SPEEK)	61,000	10,166,700

Many values of the permeability and selectivity listed in the Table 2 are obtained from pure gas permeabilities by calculating the ratio of the permeabilities for each species. In real gas mixtures, water will swell the membrane and might affect the transport rate of the other permeating species [66].

The high selectivity of water vapor transport through the membrane causes the gradient of solute distribution in the solvent (concentration polarization phenomena). The concentration polarization phenomena occur if the flux of solute (water vapor) through a membrane is larger than the flux of solute from the bulk of the feed to the membrane surface. This flux imbalance creates a concentration boundary layer across the membrane surface (Figure 4).

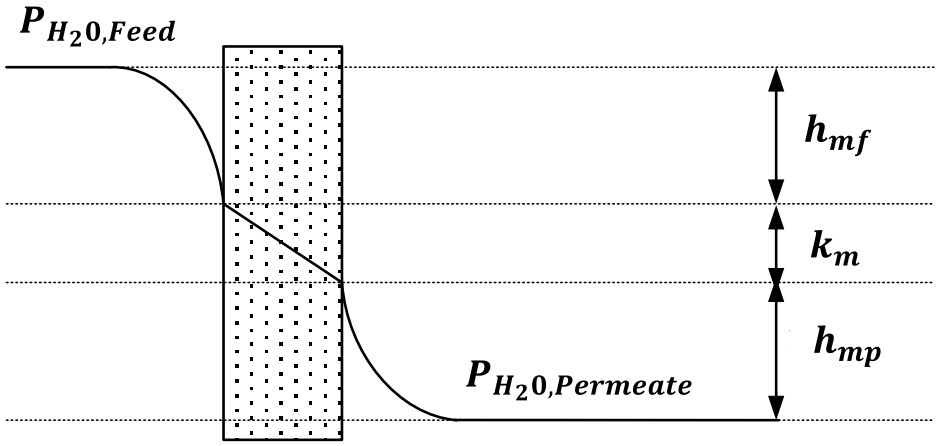

Figure 4. Schematic representation of the partial pressure profile for solute (water vapor) in solvent (air) and membrane material with respective mass transfer coefficients

In Figure 4, h_{mf} is the mass transfer coefficient in feed flow (adsorption from the bulk phase to the membrane external surface), k_m - in the membrane (diffusion from the surface to the inside of the zeolite channels, diffusion inside the zeolite channels, and diffusion from the zeolite channel to the external surface) and h_{mp} the mass transfer coefficient in the permeate flow (desorption from the external surface to the gas phase) [66]. The total resistance for mass transfer will be their series summation:

$$U_m = \frac{1}{k_\Sigma} = \frac{1}{\left(\frac{1}{h_{mf}} + \frac{1}{k_m} + \frac{1}{h_{mp}}\right)}; \quad (21)$$

where: U_m – total mass transfer conductivity for water vapor permeation $\left[\frac{s}{m}\right]$;

k_Σ – overall mass transfer coefficient for water vapor $\left[\frac{m}{s}\right]$.

The solute mass transfer coefficient in the solvent on both sides of the membrane is a function of the flow geometry and the hydrodynamic condition. The solute mass transfer can be described by the Sherwood relation [68]:

$$\mathrm{Sh} = Nu \cdot \left(\frac{Sc}{Pr}\right)^{1/3} \tag{22}$$

where: Sc – Schmidt number, ratio of momentum and mass diffusivities;

Nu – Nusselt number, dimensionless temperature gradient at the surface;

Pr – Prandtl number, ratio of the momentum and thermal diffusivities.

The Nusselt number is related to the heat transfer coefficient by the following equation (feed flow example):

$$Nu_f = \frac{h_f \cdot d_f}{k_f} \tag{23}$$

Where k_f – thermal conductivity of the feed stream fluid;

$\mathrm{d_f}$ – hydraulic diameter of feed flow.

The mass transfer coefficient is related to Sherwood number by the following equation (feed flow example) [69]:

$$\mathrm{Sh_f} = \mathrm{h_{mf}} \cdot \frac{\mathrm{d_f}}{D_{AB}} \tag{24}$$

Each of the Sherwood relation components is defined as follows:

$$\mathrm{Sc} = \frac{\nu}{D_{AB}} \tag{25}$$

$$\mathrm{Pr} = \frac{\nu}{\alpha} \tag{26}$$

where: $\nu = \frac{\mu}{\rho}$; $\alpha = \frac{k}{\rho \cdot c_p}$;

ν - kinematic viscosity $\left[\frac{m^2}{s}\right]$;

μ - Dynamic (shear) viscosity $\left[\frac{N \cdot s}{m^2}\right]$;
ρ – density $\left[\frac{kg}{m^3}\right]$;
α - thermal diffusivity $\left[\frac{m^2}{s}\right]$;
D_{AB} - mass diffusivity $\left[\frac{m^2}{s}\right]$;
k - thermal conductivity $\left[\frac{\mathrm{W}}{m \cdot K}\right]$;
C_p - specific heat $\left[\frac{\mathrm{J}}{kg \cdot K}\right]$.

The Nusselt number for turbulent flow in a circular tube can be found from the Gnilinski modification of the Petukhov equation [69]:

$$\overline{Nu}_D = \frac{(\mathrm{f}/8)\cdot(Re_D - 1000)\cdot Pr}{1+12.7\cdot(\mathrm{f}/8)^{1/2}\left(Pr^{2/3}-1\right)};\ 3000 < Re_D < 5 \cdot 10^6 \tag{27}$$

$$Re_D = \frac{u_m \cdot d}{\nu} \tag{28}$$

where: Re_D – Reynolds number, ratio of inertia and viscous force;
d - hydraulic diameter;
u_m - mean fluid velocity over the channel;
f – friction factor.

This Nusselt number definition is valid for following condition: 0.5<Pr<2000 and $3000 < \mathrm{Re_D} < 5 \cdot 10^6$. For internal fully developed laminar flow and the entry region in a flat channel (with uniform temperature surfaces and infinite sides ratio) the Nusselt number can be estimated using Equation (29) [70]. Without the thermal entrance length effect, the Nusselt number is equal to 7.54 [69-71].

$$\overline{Nu}_D = 7.54 + \frac{0.03\cdot\left(\frac{\mathrm{d}}{\mathrm{L}}\right)\cdot \mathrm{Re}_D \cdot \mathrm{Pr}}{1+0.016\cdot\left[0.03\cdot\left(\frac{\mathrm{d}}{\mathrm{L}}\right)\cdot \mathrm{Re}_D \cdot \mathrm{Pr}\right]^{\frac{2}{3}}};\ \mathrm{Re}_D \leq 2800 \tag{29}$$

where: L – Length of plates

The friction factor can be obtained from the numerically derived explicit equation proposed by Zigrang and Sylvester [72], which provides a higher accuracy than the Colebrook equation:

$$\frac{1}{\sqrt{f}} = -2.0 \cdot \log\left[\frac{\epsilon/D_h}{3.7} - \frac{5.02}{Re}\log\left[\frac{\epsilon/D_h}{3.7} - \frac{5.02}{Re}\right]\log\left[\frac{\epsilon/D_h}{3.7} + \frac{13}{Re}\right]\right] \quad (30)$$

where: ϵ/D_h - relative roughness.

This equation is valid for fully developed turbulent flow ($\mathrm{Re_D} > 2500$). For laminar flow, the Hagen-Poiseuille equation can be used for internal, fully developed laminar flow in a flat channel with uniform temperature surfaces and infinite channel length [69]:

$$f = 96/\mathrm{Re} \quad (31)$$

The mass diffusivity coefficient of water vapor in nitrogen at various pressures and temperatures used in equation (24) can be estimated based on the given pressure and temperature [66]:

$$D_{AB} = \mathrm{D_0} \cdot \left(\frac{\mathrm{P_0}}{\mathrm{P}}\right) \cdot \left(\frac{T}{\mathrm{T_0}}\right)^{1.81} \quad (32)$$

where: $\mathrm{D_0} = 2.19 \cdot 10^{-5}\left[\frac{\mathrm{m^2}}{\mathrm{s}}\right]$ - the diffusion coefficient of water in nitrogen at reference conditions ($\mathrm{P_0} = 101.3\ kPa$) and ($\mathrm{T_0} = 273.2°\mathrm{K}$).

The Nitrogen concentration has an uneven distribution in the flow due to a lower water vapor pressure near the membrane surface. This effect can be neglected, because the amount of water vapor in the feed is significantly smaller than the amount of nitrogen [66].

An alternative approach is to use a regression curve fit provided by Nellis and Klein [73]. For the ERV system design conditions the difference between these formulas is less than 3%.

$$D_{AB} = -2.775 \cdot 10^{-6}\left[\frac{m^2}{s}\right] + 4.479 \cdot 10^{-8}\left[\frac{m^2}{s \cdot K}\right] \cdot T + 1.656 \cdot 10^{-10}\left[\frac{m^2}{s \cdot K^2}\right] \cdot T^2 \quad (33)$$

The Schirmer's equation was proposed in 1938 and is used in many European standards to calculate the water vapor permeability in the still air layer [74-76]:

$$D_{AB} = \frac{2.306 \cdot 10^{-5}}{R_w T} \cdot \left(\frac{\mathrm{P}_0}{\mathrm{P}}\right) \cdot \left(\frac{T}{\mathrm{T}_0}\right)^{1.81}, \left[\frac{kg \cdot m}{m^2 \cdot s \cdot kPa}\right] \quad (34)$$

where: $\mathrm{P}_0 = 101.3\ kPa$;

$\mathrm{T}_0 = 273.2°\mathrm{K}$;

$R_w = 461.5 \frac{J}{K \cdot kg}$ - Individual gas constant for water.

2.2.4 Membrane material comparison

All analysis and experimental work described in this dissertation was done with the zeolite membrane prepared by the PNNL. To compare alternative membrane materials to the zeolite membrane several commercially available materials were considered (Tyvek, BlueskinVP, PDMS membranes). Their application was considered only for the ERV system. Membrane application for the proposed dehumidification and air-conditioning systems requires higher mechanical strength that needs to be considered during membrane design and generally makes ERV membranes not applicable for operation with a total pressure difference across the membrane approaching one atmosphere.

The PNNL composite zeolite membrane consists of a zeolite membrane film (< 2 μm) deposited on a thin, porous nickel metal sheet (~50μm). The metallic nature of the sheet provides mechanical strength and flexibility for packaging into a membrane

module that can withstand a pressure gradient above one atmosphere [12]. Design water vapor permeance of this membrane is $8 \cdot 10^{-6} \cdot \frac{\text{kmol}}{\text{s·m}^2\text{·kPa}}$ at a temperature of 90ºF (32.2ºC) with a design selectivity above 10, with a feed air stream of 50% RH at 30ºC. The target membrane product value is \$50/m².

If we assume that only the zeolite layer provides resistance to water transport, the membrane permeability can be estimated:

$$\mathcal{P}_{H_2O/\text{ZM}} = 8 \cdot 10^{-6} \cdot \frac{\text{kmol}}{m^2 \cdot s \cdot kPa} \cdot \frac{\text{Barrer}}{\frac{1}{2.99 \cdot 10^{15}} \frac{kmol \cdot m}{m^2 \cdot s \cdot kPa}} \cdot 2 \cdot 10^{-6} m = 47{,}840 \text{ Barrer} \quad (35)$$

The widely available DuPont™ Tyvek® HomeWrap and self-Adhered Water Resistive Air Barrier Membrane BlueskinVP™ 100 manufactured by Henry® Company were considered as alternatives for the ERV system due to good water permeability, but rejected due to higher air permeation rate.

Polydimethylsiloxane Membrane (PDMS) from Specialty Silicone Products, Inc. has permeability for oxygen of 50 Barrers, for Nitrogen of 25 Barrers, and for CO_2 of 270 Barrers. According to Metz [66], PDMS permeability for water vapor is 40,000 Barrers. With a smallest available membrane thickness of 0.003 in (76.2 μm) PDMS membrane permeance is:

$$\mathcal{P}_{H_2O/\text{PDMS}} = \frac{40{,}000}{2.99 \cdot 10^{15}} \cdot \frac{kmol \cdot m}{m^2 \cdot s \cdot kPa} \cdot \frac{\frac{39.37in}{1m}}{0.003\text{in}} = 0.1756 \cdot 10^{-6} \frac{kmol}{s \cdot m^2 \cdot kPa} \quad (36)$$

The polydimethylsiloxane Membrane water to nitrogen selectivity is 140 [66]. This is much lower than the expected selectivity of the zeolite membranes manufactured by the PNNL.

Analysis of the existing membrane materials and availability of the products for the experimental testing in combination with the research objectives resulted in selection of the PNNL zeolite membrane as the main membrane material for this research.

2.3 Conclusions

The literature review provided above shows the current state of research and market implementation of technology in different areas related to the membrane dehumidification system application for building air-conditioning and ventilation systems. It provides a membrane type classification, fundamentals of the water diffusion process, and a convection mass transfer mechanism.

The reviewed material also include membrane gas separation fundamentals, zeolite membrane specific characteristics and the impact of its formation process on the membrane selectivity and membrane water permeance, case study and energy efficiency analysis of related system application for building air-conditioning and ventilation systems.

The literature review shows that application of membrane separation for dehumidification of an air stream is a relatively new technology that became available after 1970 with advancement of membrane material manufacturing technology. Literature analysis shows that though the application of membrane separation for building dehumidification was considered before, no detailed annual energy efficiency analysis and energy savings estimation is available for membrane dehumidification and membrane air-conditioning systems on the whole system (building) level.

3 MEMBRANE ENERGY RECOVERY VENTILATION SYSTEM

This section describes results of the energy effectiveness analysis of the Energy Recovery Ventilation (ERV) system with zeolite inorganic membrane for the building air-conditioning systems applications.

The ERV system provides heat transfer and mass transfer of water vapor between two air streams. It is comprised of layers of water permeable membrane that provide selective water vapor mass transfer from a feed air stream to a sweep air stream. In a building application for a hot and humid climates, the incoming outside ventilation airflow is an example of a feed flow while the building exhaust air can be treated as the sweep air stream.

To analyze ERV operation, two independent models were developed based on the Effectiveness-NTU method. The first model analyzes the conduction and convection heat transfer through the membrane and from the feed air stream to the sweep air stream, while the second model analyzes the water vapor diffusion and convection mass transfer between the two air streams. These models consider the resistance of the membrane to heat and mass transfer, and the convection diffusion coefficient for heat and mass transfer with the air stream. The objective of these models is to estimate operational effectiveness of the ERV with the zeolite membrane operating in hot and humid climates.

The flat plate membrane ERV is analyzed for unmixed fluids with two configurations: counter-flow and cross-flow.

3.1 Energy recovery ventilation simulation model

Parallel-plate heat and mass exchangers are the most common stationary enthalpy exchangers to recover both sensible heat and moisture. This is due to their simple structure and large packing densities. The analyzed heat and mass exchanger is schematically shown in Figure 5. The membrane surfaces are positioned parallel to each other. An air stream is blown across each surface of the membrane. The difference in

partial pressure of water vapor across the membrane is the driving force for the water transport mechanism.

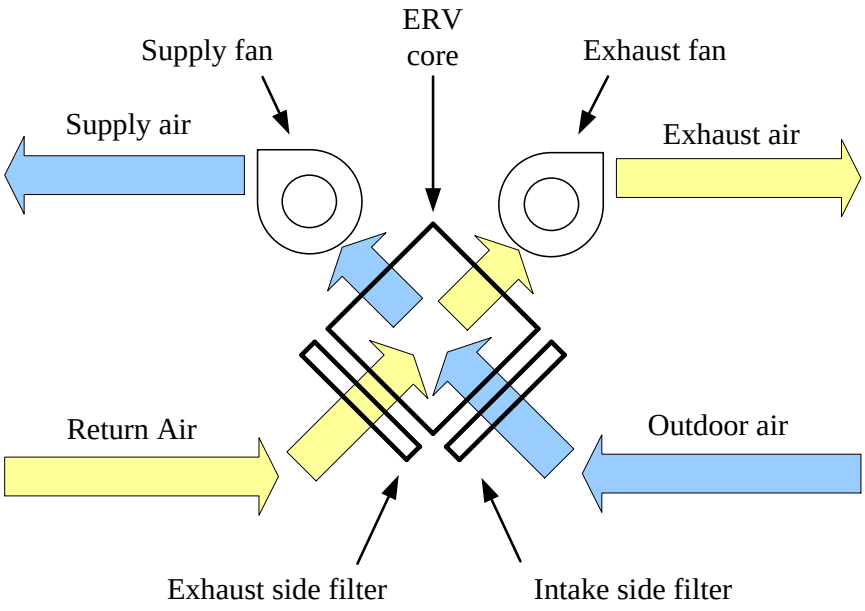

Figure 5. ERV system cross-flow flat-plate heat exchanger

The main assumptions for the model development are:

1. The height of feed and sweep channels are identical.
2. Heat and mass transfer is steady state, steady flow, and is assumed to be in one direction perpendicular to the surface of the membrane.
3. The velocity, temperature, and concentration profiles are assumed to be fully developed.
4. Both airflows are assumed to be unmixed.
5. Thermal and concentration profiles are a function of the velocity profile and do not affect each other.
6. The fouling factor is neglected since an air filter is assumed to remove any materials that would foul the system.
7. Heat transfer between the heat exchanger and surroundings is zero.

8. Kinetic and potential energy changes in the air streams are zero.
9. Friction factor is estimated by the Zigrang equation.
10. All heat transfer and thermodynamic properties are estimated at an average airflow temperature.
11. Water vapor diffusion in air is considered to be equal to the diffusion in pure nitrogen at the same conditions.

According to the Effectiveness-NTU method, the maximum possible heat transfer rate, through a counterflow heat exchanger with infinite length, will occur when one of the fluids experiences a maximum temperature difference [69]:

$$q_{max,T} = \min(\mathrm{C_h}; \mathrm{C_c}) \cdot \left(T_{h,i} - T_{c,i}\right), [kW]; \tag{37}$$

where: $\mathrm{C_h}; \mathrm{C_c}$ – heat capacity rate of each flow (mass flow times specific heat);

$T_{h,i}; T_{c,i}$ – inlet temperature of each airflow.

The corresponding governing equation for the maximum possible mass transfer rate through the counterflow heat exchanger is:

$$q_{max,m} = \min\left(\frac{\dot{\mathrm{m}}_\mathrm{c} \cdot \omega_{c,i}}{c_{c,i}}; \frac{\dot{\mathrm{m}}_\mathrm{h} \cdot \omega_{h,i}}{c_{h,i}}\right) \cdot \left(c_{h,i} - c_{c,i}\right), \left[\frac{kg}{s}\right]; \tag{38}$$

where: $c_{h,i}; c_{c,i}$ – molar concentration of water at the flow inlet, $\left[\frac{kmol}{m^3}\right]$;

$\dot{\mathrm{m}}_\mathrm{h}; \dot{\mathrm{m}}_\mathrm{c}$ – mass flow rate of humid air in each stream, $\left[\frac{kg}{s}\right]$;

$\omega_{c,i}; \omega_{h,i}$ – humidity ratio at the flow inlet.

Based on the maximum possible heat transfer rate, the thermal effectiveness can be defined as the ratio of the actual heat transfer for the heat exchanger to the maximum possible heat transfer rate:

$$\varepsilon_T \equiv \frac{q_T}{q_{max,T}} = \frac{C_h \cdot (T_{h,i} - T_{c,i})}{\min(C_h; C_c) \cdot (T_{h,i} - T_{c,i})}. \quad (39)$$

An equivalent equation for the mass transfer effectiveness can be defined in a similar way:

$$\varepsilon_m \equiv \frac{q_m}{q_{max,m}} = \frac{\frac{\dot{m}_h \cdot \omega_{h,i}}{c_{h,i}} \cdot (c_{h,i} - c_{h,o})}{\min\left(\frac{\dot{m}_c \cdot \omega_{c,i}}{c_{c,i}}; \frac{\dot{m}_h \cdot \omega_{h,i}}{c_{h,i}}\right) \cdot (c_{h,i} - c_{c,i})}. \quad (40)$$

To estimate heat transfer, an additional parameter can be defined as the number of heat transfer units (NTU_T):

$$NTU_T \equiv \frac{U_T \cdot A}{\min(C_h; C_c)}; \quad (41)$$

where: A – membrane area $[m^2]$;

U_T –total thermal conductivity (including convection and conduction coefficients) $\left[\frac{kW}{m^2 \cdot K}\right]$.

Number of mass transfer units:

$$NTU_m \equiv \frac{U_m \cdot A}{\min\left(\frac{\dot{m}_c \cdot \omega_{c,i}}{c_{c,i}}; \frac{\dot{m}_h \cdot \omega_{h,i}}{c_{h,i}}\right)}; \quad (42)$$

where: U_m – total mass transfer conductivity (including convection mass transfer coefficients and permeation coefficient through the membrane as given by Equation (21) $[m/s]$.

For a counter-flow heat exchanger, the relation between thermal effectiveness and NTU_T can be expressed by the following equation [69, 70, 77]:

$$\varepsilon_T = \frac{1-\exp\left(-NTU\cdot\left(1-C_{r,T}\right)\right)}{1-C_{r,T}\cdot\exp\left(-NTU\cdot\left(1-C_{r,T}\right)\right)}; \tag{43}$$

where: $C_{r,T}$ – heat capacity ratio.

$$C_{r,T} = \frac{\min(C_h;C_c)}{\max(C_h;C_c)}. \tag{44}$$

The analogous equations for mass transfer are:

$$\varepsilon_m = \frac{1-\exp\left(-NTU\cdot\left(1-C_{r,m}\right)\right)}{1-C_{r,m}\cdot\exp\left(-NTU\cdot\left(1-C_{r,m}\right)\right)}; \tag{45}$$

where: $C_{r,m}$ – mass capacity ratio.

$$C_{r,m} = \frac{\min\left(\frac{\dot{m}_c\cdot\omega_{c,i}}{c_{c,i}};\frac{\dot{m}_h\cdot\omega_{h,i}}{c_{h,i}}\right)}{\max\left(\frac{\dot{m}_c\cdot\omega_{c,i}}{c_{c,i}};\frac{\dot{m}_h\cdot\omega_{h,i}}{c_{h,i}}\right)} \tag{46}$$

The relation for a single-pass, cross-flow heat exchanger thermal effectiveness with both fluids unmixed can be expressed by the following equation [69, 70]:

$$\varepsilon_T = 1 - \exp\left[\frac{NTU_T^{0.22}}{C_{r,T}}\cdot\left[\exp\left(-C_{r,T}\cdot\left(NTU_T\right)^{0.78}\right)-1\right]\right] \tag{47}$$

The mass transfer effectiveness for a single-pass, cross-flow heat exchanger with both fluids unmixed has the same format with thermal coefficients replaced by mass coefficients.

To verify the calculation results, the overall thermal and mass balance can be used for each fluid. Heat transfer from one fluid to another can be described using the logarithmic mean temperature difference as the driving force:

$$q_T = U_T \cdot A \cdot \Delta T_{lm}\,; \tag{48}$$

$$\Delta T_{lm} = \frac{\Delta T_2 - \Delta T_1}{\ln(\Delta T_2/\Delta T_1)}. \tag{49}$$

Mass transfer from one fluid to another can be described by the logarithmic mean concentration difference as the driving force:

$$q_m = U_m \cdot A \cdot \Delta c_{lm} \cdot M, \left[\frac{kg}{m^3}\right] \tag{50}$$

where: M – molecular weight of water.

$$\Delta c_{lm} = \frac{\Delta c_2 - \Delta c_1}{\ln\left(\frac{\Delta c_2}{\Delta c_1}\right)}, \left[\frac{kmol}{m^3}\right] \tag{51}$$

For the counter-flow exchanger, the endpoint temperature difference is defined as:

$$\begin{cases} \Delta T_1 \equiv T_{h,i} - T_{c,o} \\ \Delta T_2 \equiv T_{h,o} - T_{c,i} \end{cases} \tag{52}$$

In this equation indices h and c describe hot and cold airflow, while i and o indicates the inlet and outlet condition. Rewriting the above equations for concentration:

$$\begin{cases} \Delta c_1 \equiv c_{h,i} - c_{c,o} \\ \Delta c_2 \equiv c_{h,o} - c_{c,i} \end{cases} \tag{53}$$

For the cross-flow heat exchanger, a correction factor needs to be applied to the counter-flow configuration:

$$\Delta T_{lm} = F \cdot \frac{\Delta T_2 - \Delta T_1}{\ln(\Delta T_2 / \Delta T_1)}. \quad (54)$$

The value of the correction factor can be found in Incropera and DeWitt [69].

The **total effectiveness** of a single pass heat exchanger is equal to the actual total energy transfer divided by the product of the minimum energy capacity rate and the enthalpy difference:

$$\varepsilon_{\Sigma} = \frac{m_h \cdot (h_{h,i} - h_{h,o})}{\min(m_h; m_c) \cdot (h_{h,i} - h_{c,i})}; \quad (55)$$

where: $h_{h,i}; h_{h,o}$ - enthalpy values of inlet and outlet hot air streams.

Another parameter used to estimate performance of the ERV is the **Recovery Efficiency Ratio (RER).** It is a ratio of energy recovered divided by energy expended in the energy recovery process, according to the ANSI/ASHRAE Standard 84-2008 [78].

$$RER = \frac{m_h \cdot (h_{h,i} - h_{h,o})}{\left(\Delta P_h \cdot \frac{Q_h}{\eta_{fh}} + \Delta P_c \cdot \frac{Q_c}{\eta_{fc}} + q_{aux}\right)}; \quad (56)$$

where: $\Delta P_h; \Delta P_c$ – the pressure drop across the hot and cold sides of the exchanger respectively;

$Q_h; Q_c$ – the hot and cold side volume flow rates;

$\eta_{fh}; \eta_{fc}$ – the hot and cold side air fan and drive total effectiveness;

q_{aux} – the auxiliary total power input to the exchanger (e.g. control system).

The pressure drop across the ERV system can be found [22]:

$$\Delta P = \left(f_i \frac{L}{d_e} + \xi \right) \cdot \frac{V^2}{2\rho_a} \quad (57)$$

where f_i – Darcy friction factor of flow channels;

ξ – local friction coefficient that reflects the entrance and exit losses;

V – mass flux of air, $\left[\frac{kg}{m^2 \cdot s}\right]$;

L – length of flow channels, $[m]$;

d_e – effective diameter of the rectangular channel, $[m]$.

For fully developed laminar flow in parallel plate channels with infinite width the friction factor can be defined by the formula:

$$f_i = \frac{96}{Re} \quad (58)$$

The ERV system simulation models were programmed in Engineering Equation Solver (EES) V9.195 based on the relations described above [79]. The program was verified with the methodology described in the dissertation of Kistler [80]. A distinctive characteristic of the EES software is the availability in the program of physical properties for solids, liquids and gases. Model input parameters include the inlet airflow velocity, temperature, and relative humidity for each air stream, as well as the membrane size, heat and mass transfer properties.

3.2 Flat plate membrane ERV simulation modeling results

The simulation models developed in EES were used to estimate the ERV operational effectiveness for different operational conditions in cross-flow and counter-flow configuration. All analysis was done for a single channel with design airflow of 5 cfm. Based on a single channel design the size of the heat exchanger can be scaled up

to the required capacity. The simulation parameters of the heat and moisture exchanger, used for the base case model are shown in Table 3.

Table 3. Design conditions of the ERV system simulation model

Name	Units	Value
Heat Exchanger length	m	1
Heat Exchanger width (variable for parametric study)	m	1.25
Membrane Area (variable for parametric study)	m^2	1.25
Membrane water permeability	$kmol/(kPa \cdot m^2 \cdot s)$	8E-6
Membrane thermal conductivity	$kW/(m^2 \cdot K)$	3650
Volumetric airflow of each stream	cfm	5
Channel height of the hot airflow side	mm	2
Channel height of the cold airflow side	mm	2
Hot Airflow Inlet Temperature	°C	38
Hot Airflow Inlet Pressure	kPa	101.325
Hot Airflow Inlet Relative Humidity	%	70
Cold Airflow Inlet Temperature	°C	24
Cold Airflow Inlet Pressure	kPa	101.325
Cold Airflow Inlet Relative Humidity	%	50

During the parametric study, the length of the heat exchanger and volumetric airflow of both channels were constant. Adjustments of the heat exchanger width in the simulation changed the velocity of the air in both streams and the membrane area.

Simulation results for the zeolite membrane cross-flow heat exchanger show that the maximum mass exchange effectiveness (Figure 6) and enthalpy effectiveness (Figure 7) exceed 0.8 for channel heights below 2 mm, when the membrane area is above 0.4 m^2/cfm. Figure 6 and Figure 7 show calculation results for the design airflow rate of 5 cfm per channel.

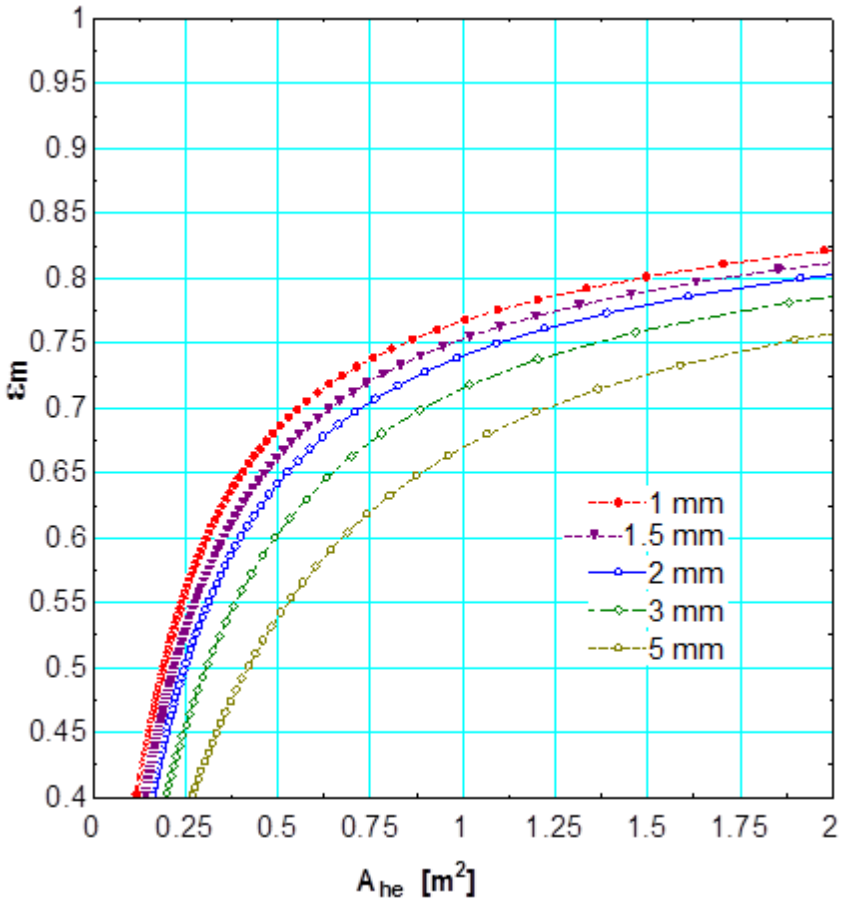

Figure 6. Mass exchange effectiveness of cross-flow ERV device, for different membrane channel heights as a function of membrane area

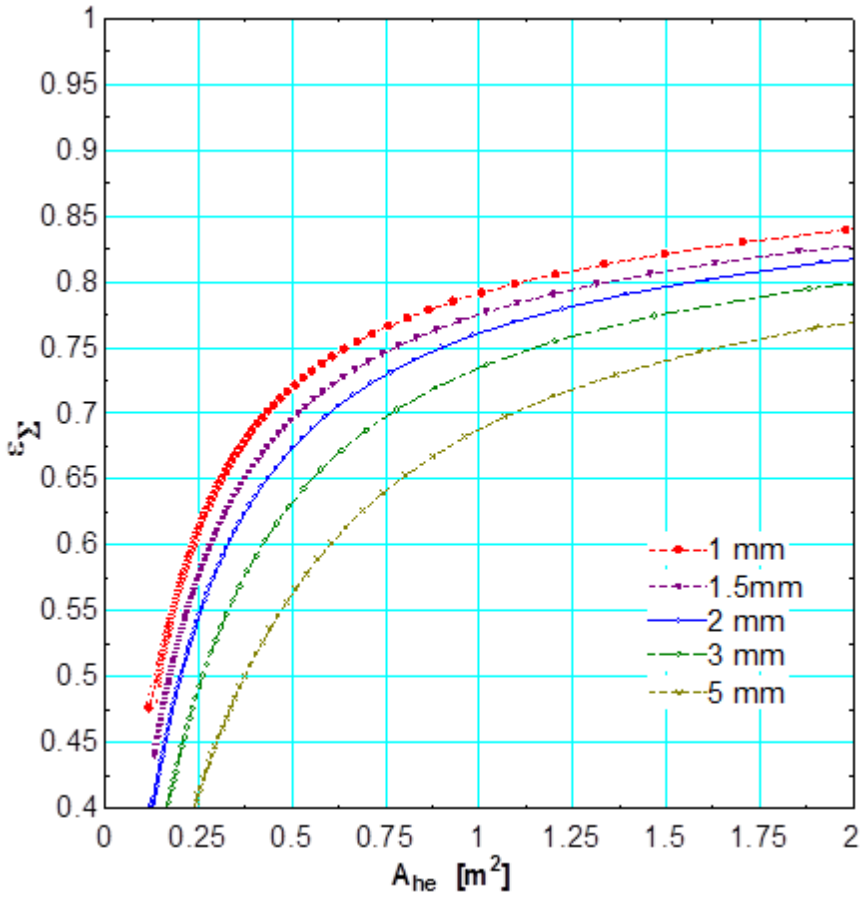

Figure 7. Enthalpy effectiveness of cross-flow ERV device for different membrane channel heights as a function of membrane area

The simulation results for pressure loss show that the membrane channel height of 2 mm provides pressure losses below 100 Pa (0.4 in w.g.) when the membrane area is above 0.15 m²/cfm (Figure 8).

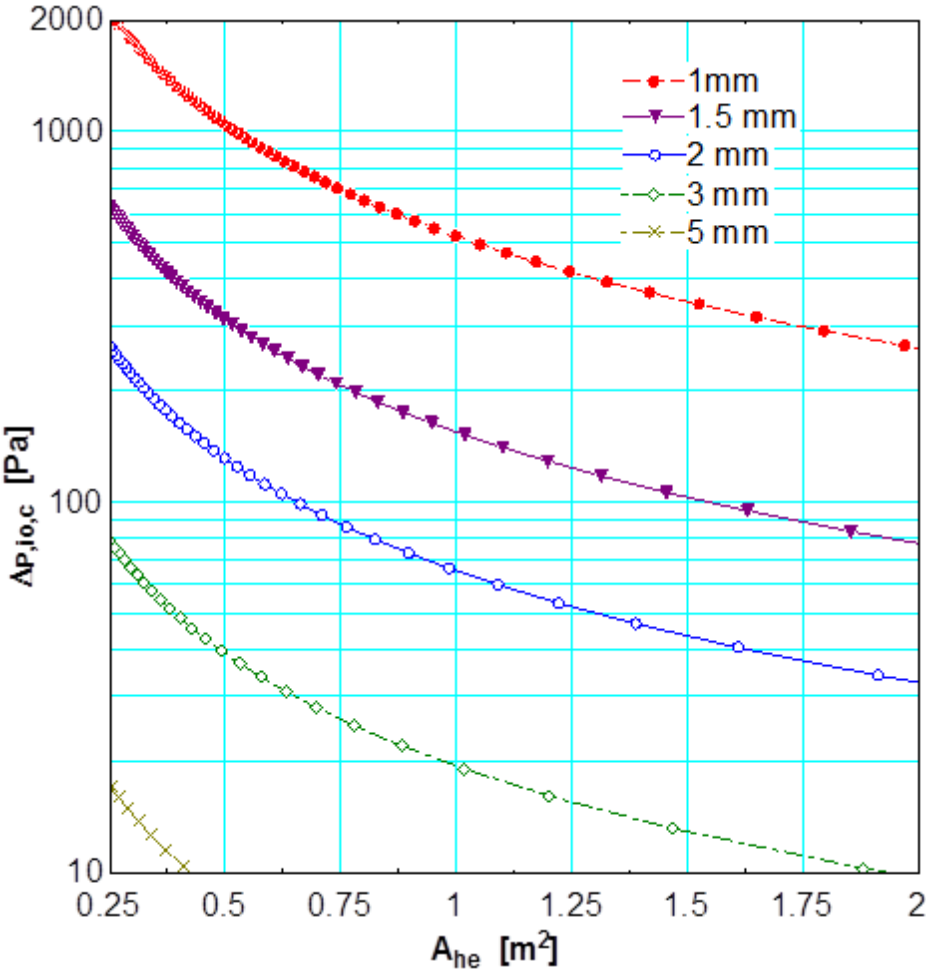

Figure 8. Pressure loss of cross-flow ERV device for different membrane channel heights as a function of membrane area

Another set of simulations was performed for a counter-flow heat exchanger based on the same parameters, properties, and assumptions as in the cross-flow heat exchanger simulation model. A comparison of mass exchange effectiveness for both configurations shows a higher maximum effectiveness of 0.95 for a counter-flow ERV system (Figure 9).

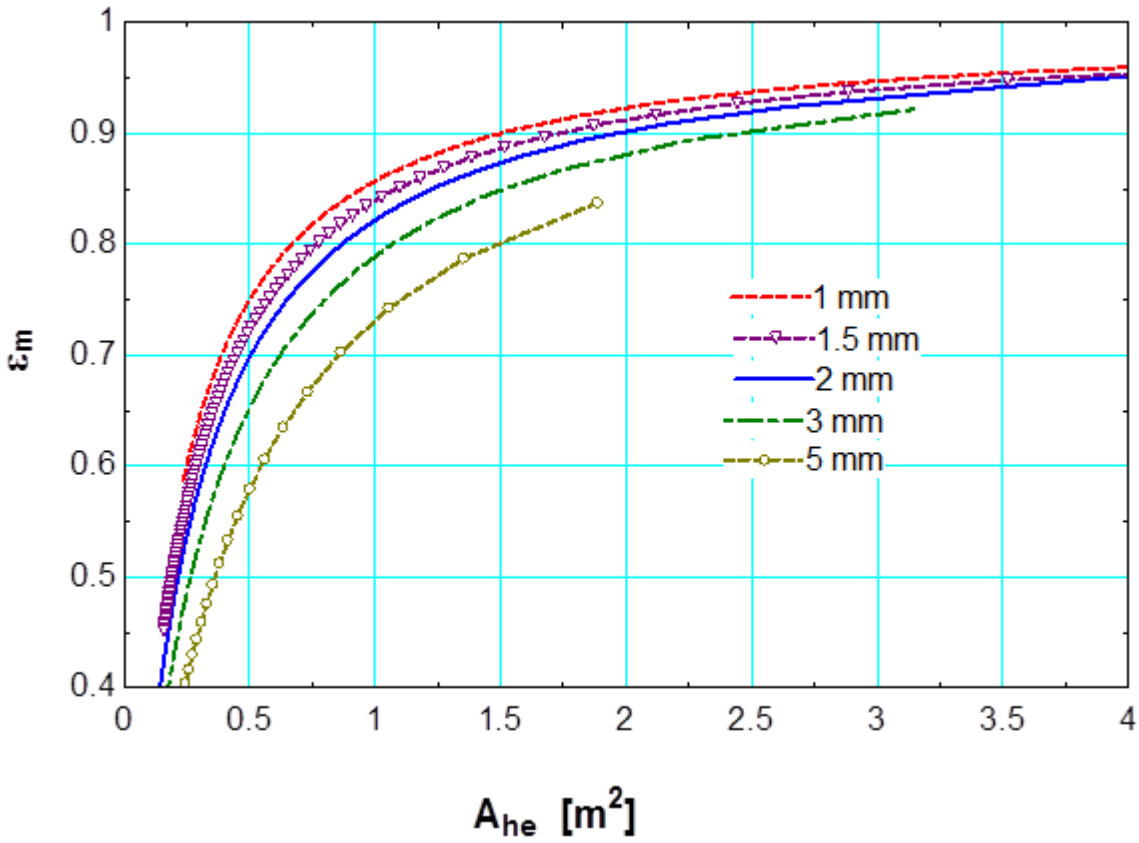

Figure 9. Mass exchange effectiveness of counter-flow ERV device for different membrane channel heights as a function of membrane

The corresponding enthalpy effectiveness of the counter-flow configuration also increased and exceeded 0.9 for a 2 mm channel height when the membrane area is above 2 m² per 5 cfm (Figure 10).

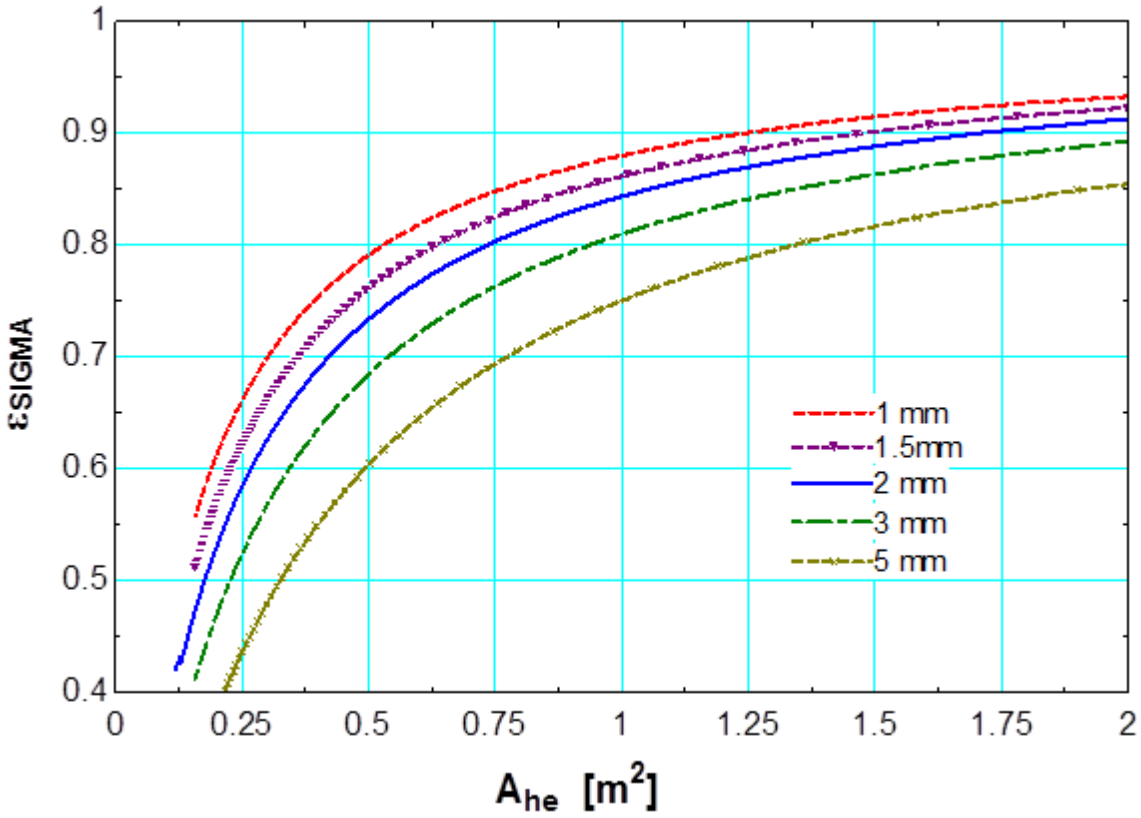

Figure 10. Enthalpy effectiveness of counter-flow ERV device for different membrane channel heights as a function of membrane area

Air pressure loss for both streams across the ERV is not affected by the change of direction and stayed at the same level (Figure 11).

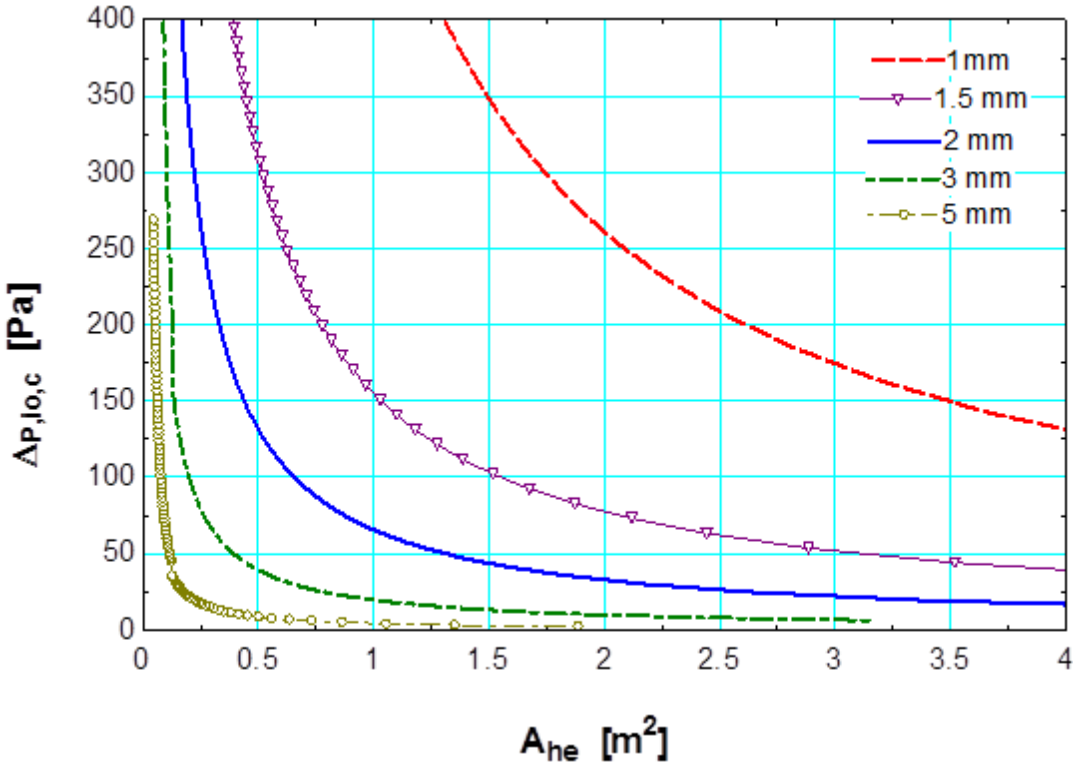

Figure 11. Pressure loss of counter-flow ERV device for different membrane channel heights as a function of membrane area

Based on the system design conditions (Table 3), the estimated enthalpy effectiveness of the zeolite membrane energy recovery ventilation system is around 0.8 (Table 4).

Table 4. Performance of zeolite membrane ERV with different configuration

Parameter	Cross-Flow	Counter-Flow
Effective membrane water permeance (kmol/kPa-s-m²)	8.0E-6	8.0E-6
Water mass transfer (kg/s-m²)	32.8E-6	36.8E-6
Energy transfer (W/m²)	107	119
Heat transfer effectiveness	0.831	0.935
Mass transfer effectiveness	0.764	0.852
Enthalpy (total) effectiveness	0.782	0.871

Heat and mass transfer resistances for the counterflow ERV system configuration are provided in Table 5.

Table 5. Heat and mass transfer resistance for the counter-flow ERV base case model with 2 mm channel height and air velocity 2 m/s (394 fpm)

Parameter	Cold Airflow	Membrane	Hot Airflow
Mass transfer coefficient, m/s	29.24E-3	20.05E-3	31.63E-3
Heat transfer coefficient, kW/m²-K	31.22E-3	3650	32.5E-3

Results of this theoretical analysis were used in the experimental work described in Rees [81].

3.3 Conclusions

The modeling has determined that a cross-flow ERV based on the assumptions in Table 3, having a membrane water permeance of 8E-6 kmol/(kPa·m²·s) and membrane spacing of 2 mm, would operate with a combined heat and mass transfer effectiveness of 0.8 for a membrane area of 0.25 m²/cfm.

The diffusion resistance and the membrane resistance are approximately equal for a flow velocity of 1 m/s and channel height of 3 mm when the membrane permeance to water vapor is 8E-6 kmol/(kPa·m²·s). Hence, for the example chosen, a higher membrane permeance will result in only a marginal increase in mass transfer effectiveness.

A 2 mm channel spacing normal to the membrane was determined to be the optimum spacing to maximize measurable mass and heat transfer through the membrane while not creating excessive pressure drop.

4 MEMBRANE DEHUMIDIFICATION SYSTEM

The experimental test membrane dehumidification system and the membrane air-conditioning system construction were completed with help from Francesco Schaff. More detailed information about the experimental system construction is provided in his thesis [82]. The membrane dehumidification system could be used as a building Dedicated Outdoor Air System (DOAS) that operates in humid climate conditions.

The design inlet condition to the experimental system was chosen to be an extreme condition of 90°F (32.2°C) dry-bulb temperature and 90% RH at a 30 cfm (51 m^3/h) airflow rate. The target design outlet conditions were also extreme at a dry-bulb temperature of 55°F (13°C) and 50% RH. In this experimental setup, the feed airflow is first dehumidified in an isothermal process using membrane separation with a permeate pressure below 2 kPa. After the airflow dehumidification process is completed, the air is cooled with a conventional chilled water coil, as in most commercial buildings operating in the U.S.

Application of the membrane dehumidification system in a hot and humid climate in a large commercial building was studied to estimate the proposed system energy efficiency.

4.1 Single stage system design

The experimental system design was separated into five major subsystems with their respective components: the inlet-air conditioning component (S0), the membrane module component (S1), the sensible cooling component (S2), the vacuum subsystem (S3), and the water rejection component (S4). An illustration of these individual subsystems and components is shown in Figure 12.

The major subsystems described above were designed to be isolated from the overall system for configuration change flexibility with their own control and measurement locations, which ensures that each subsystem is working appropriately and

accurately throughout operation. A brief description of the various sections is included below.

Section S0 is used to precondition the air stream of the membrane dehumidification ventilation system to achieve the required inlet airflow, dry-bulb temperature, and relative humidity conditions. This system component is also used to measure feed airflow rate using a nozzle chamber for flow measurements.

Section S1 is designed to provide dehumidification to the feed air stream by utilizing the membrane separation process. Temperature and relative humidity data loggers were used to determine the inlet and outlet humidity ratios, respectively. The difference between two measurements was used to estimate the feed airstream dehumidification rate.

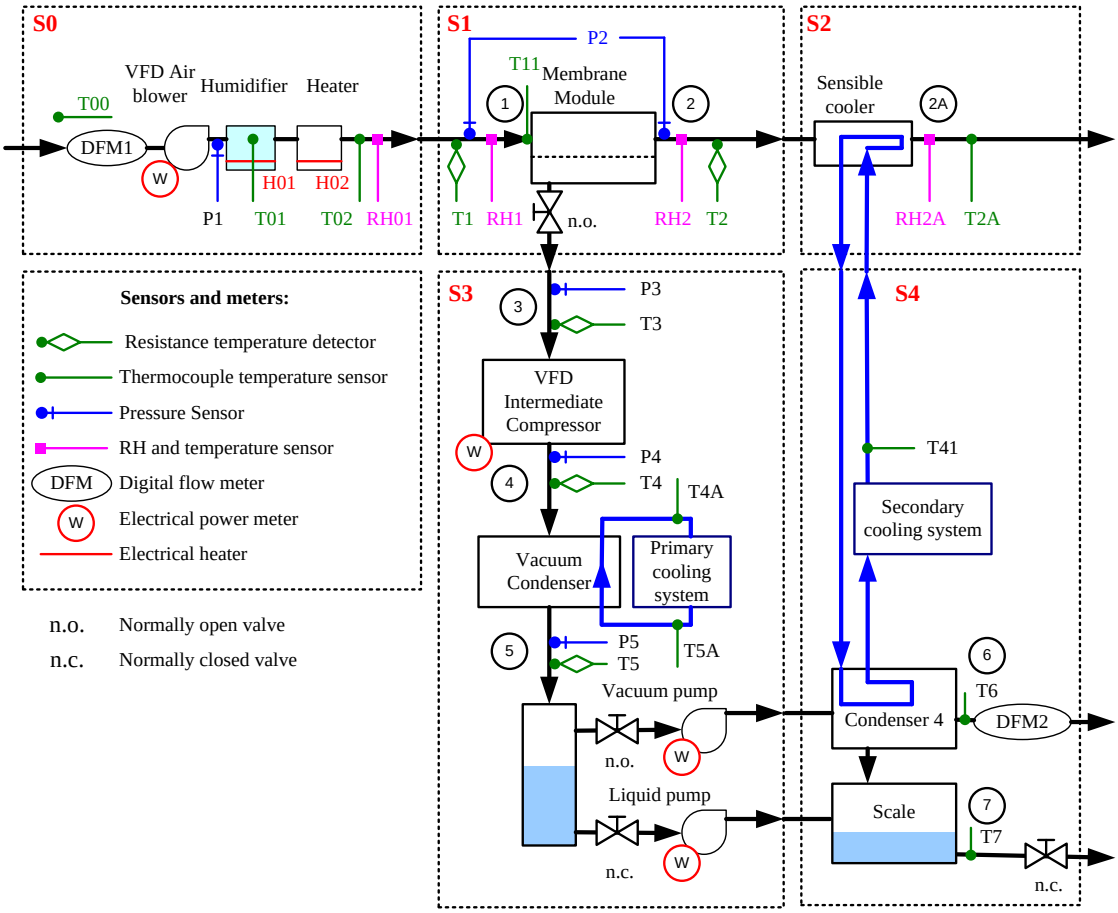

Figure 12. Membrane dehumidification system configuration

Section S2 includes the membrane outlet sensible cooler (operation based on refrigerant compression-evaporation cycle) and measurement system for monitoring the outlet temperature and humidity. Since the sensible cooling system operates at temperatures above the airflow dewpoint, measurement of the outlet airflow humidity ratio was a verification of the measurements at the exit of Section S1.

Section S3 is intended to provide the required vacuum pressure level on the permeate side of the membrane surface for dehumidification in Section S1. The first element is an intermediate compressor (VFD Roots blower) designed to increase the permeate pressure of the dehumidification system from a range of 0.5-2 kPa to a pressure above the water vapor saturation pressure of 4-8 kPa. Afterwards the intermediate compressor gas flow is subsequently cooled in a vacuum condenser using cooling water. The cooling water supply temperature is maintained above the inlet airflow wet-bulb temperature to simulate a cooling tower operation. Condensed water is rejected to the ambient air with a liquid pump while the vacuum pump rejects the rest of the noncondensable gas to the ambient air.

Section S4 is designed to provide measurements of the permeate airflow and extracted water during the dehumidification process. Since airflow temperature rejected from the vacuum pump is above the temperature operation range of the flowmeter, additional sensible cooling is used to cool the airflow before flow measurement.

The changes in the design airflow properties during the membrane dehumidification system operation are shown in Figure 13.

The first part of the air-conditioning process (Point 1-2) is isothermal dehumidification of the airstream from a humidity ratio of 0.02787 to 0.00456 that is done using the membrane separation process. The second part is a sensible cooling of the airflow from the design setpoint of 90°F to 55°F (Point 2 - 2A).

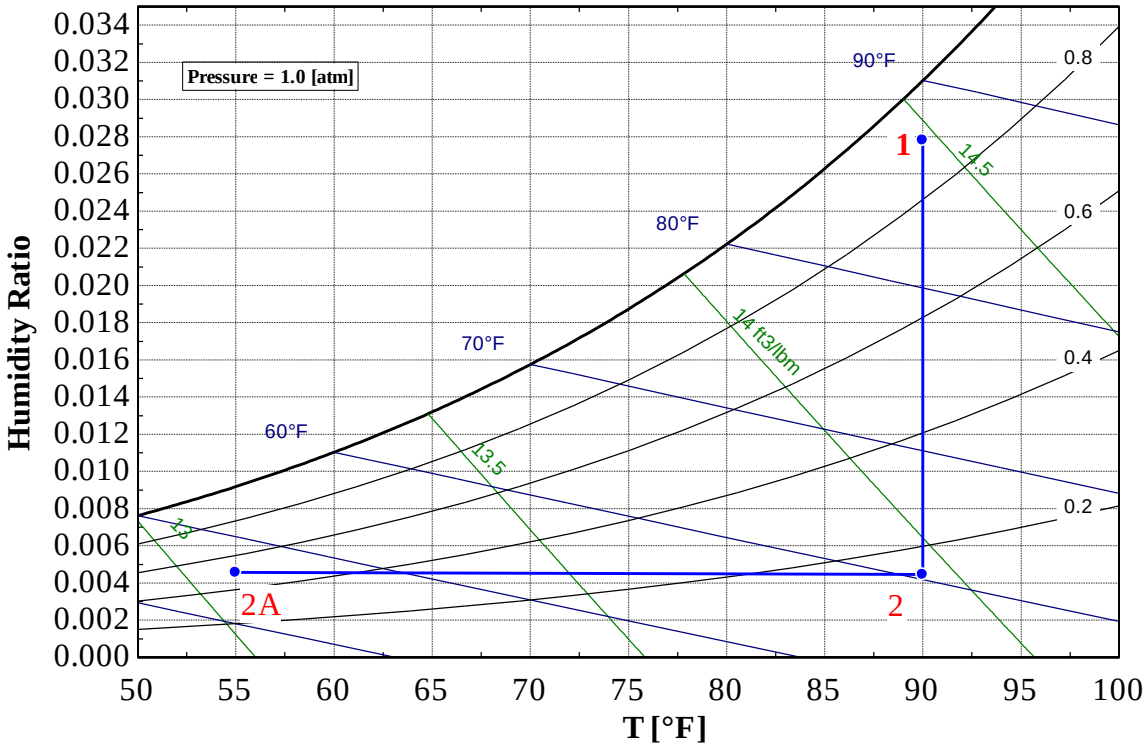

Figure 13. Membrane dehumidification system operation

4.2 Single stage experimental system configuration

Based on the experimental system design, five major subsystems were developed: the inlet-air conditioning component (S0), the membrane module component (S1), the sensible cooling component (S2), the vacuum subsystem (S3), and the water rejection subsystem (S4).

4.2.1 Inlet-air conditioning component (Section S0)

The inlet-air conditioning component is used to precondition the inlet air stream of the membrane dehumidification system to achieve the required airflow, dry-bulb temperature, and relative humidity conditions. This system component is also used to measure the feed airflow rate using a nozzle chamber for flow measurements.

The first part of the system is a nozzle chamber with a custom construction. Construction was made according to the configuration of "Figure 15 - inlet chamber setup-multiple nozzles in chamber" from ANSI/ASHRAE 51-07: Laboratory Methods of Testing Fans for Certified Aerodynamic Performance Rating [83]. The operation principle is based on airflow pressure drop measurement by a differential pressure sensor across the system of nozzles. Location of the nozzle chamber upstream of the supply air fan provided uniform airflow distribution and reduced the differential pressure of nozzle chamber relative to the ambient air. The configuration of the nozzle chamber included three nozzles with 0.375", 0.5", and 0.75" discharge diameters.

Based on Equation 7.22 from ASHRAE Standard 51-2007 [83], the volumetric airflow rate was calculated as a function of differential pressure drop:

$$\dot{V} = Y \cdot \sqrt{\frac{2 \cdot \Delta P}{\rho}} \cdot \sum_{i=1}^{3} (C_i \cdot A_i)\,, [\mathrm{m}^3/\mathrm{s}] \tag{59}$$

where: Y – expansion factor;
ΔP – pressure drop across nozzle system, [Pa];
ρ – density of feed airflow, $[\mathrm{kg}/\mathrm{m}^3]$;
C_i – discharge coefficient;
A_i – area of nozzle discharge cross section, $[\mathrm{m}^2]$.

The expansion factor can be found from:

$$Y = 0.452 \cdot \frac{\Delta P}{\rho \cdot \mathrm{R}_a \cdot T} \tag{60}$$

where: R_a – individual gas constant for air, $287.1\ \left[\frac{\mathrm{J}}{\mathrm{kg \cdot K}}\right]$;
T – airflow temperature, [K].

The nozzle discharge coefficient i can be found as:

$$C_i = 0.9986 - \left(\frac{7.006}{(Re_i)^{0.5}}\right) + \left(\frac{134.6}{Re_i}\right); \quad (61)$$

where: Re – Reynolds number

The Reynolds number can be found as:

$$Re_i = \frac{\sqrt{2}}{\mu} \cdot C_i \cdot D_{N_i} \cdot Y \cdot \sqrt{\Delta P \cdot \rho} \quad (62)$$

where: D_{N_i} – nozzle i discharge diameter, [m];
μ – dynamic air viscosity, $[kg/(m \cdot s)]$.

Based on the values obtained, conversion from the differential pressure across the nozzle system to the volumetric flow rates in the range of 0-35 cfm can be described with the power equation as (Figure 14):

$$\dot{V} = 19.994 \cdot \Delta P^{0.5091}, [\text{cfm}]; \quad (63)$$

where: ΔP – differential pressure across nozzles, [in w. g.].

Measurement of the differential pressure change were made using differential pressure transducers (Setra Model 264, 0.1-3 in w.g.) with a static standard accuracy of ±1.0% at a full scale in normal ambient temperature environments. Sensor operation is based on the electrical capacitance change due to stainless steel diaphragm movement with pressure change.

The next component of the subsystem is a VFD air blower used for air movement in the feed airstream (Figure 15). A Fuji single-stage ring compressor VFC400A-7W is used in the system, and is capable of providing airflow rates up to 98 cfm (2,775 lpm) and 54.5 in w.g. (13.6 kPa) of static pressure.

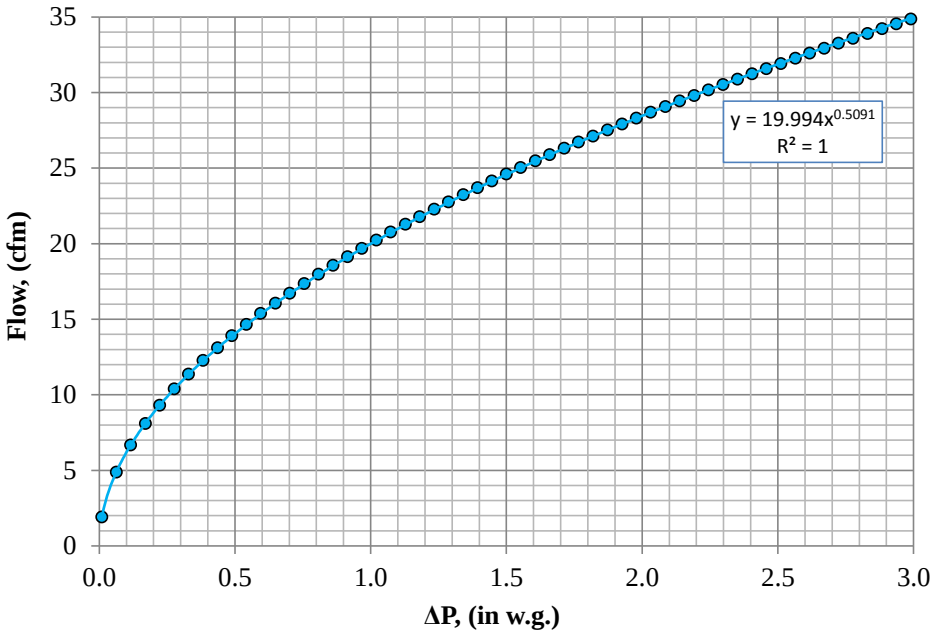

Figure 14. Air flow across the nozzle system at static pressure of 101 kPa and airflow temperature of 25°C (77°F)

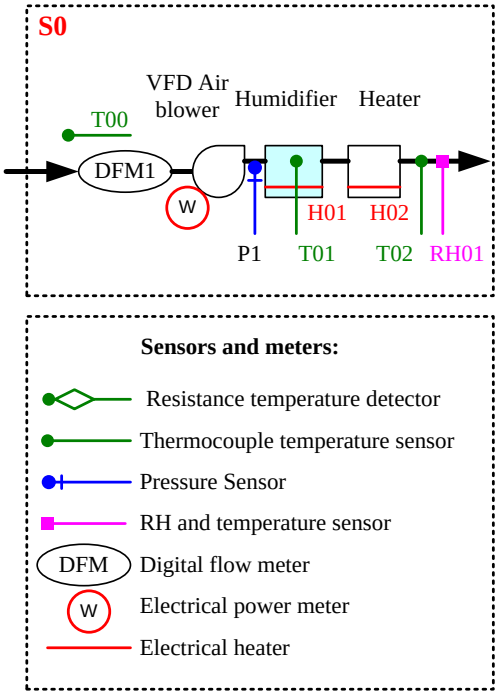

Figure 15. Inlet-air conditioning component (Section S0)

The next component is the air humidification system. It is designed to be capable of humidification of ambient air from 24 °C (75°F) and 50% RH to 32°C (90°F) and 90% RH at an airflow rate of 30 cfm (51 m³/h). This humidity change corresponds to the change of the humidity ratio from 0.009329 to 0.02754 and requires a heat input of 906 W. This is accomplished by passing the feed-air stream through the evaporative cooler medium constantly supplied with water recirculating through a water heater section. The supply water temperature to the evaporative cooler is regulated with a proportional-integral-derivative controller based on a given temperature setpoint for the supply airflow wet-bulb temperature.

After the required humidity ratio is obtained using the humidification system, the feed airflow is reheated to the required dry-bulb temperature with the heating stage. Outlet conditions of Section S0 is recorded using the Maxim Integrated iButton Hygrochron temperature/humidity logger with a temperature sensor accuracy of ±0.5 °C and capacitive polymer humidity sensor with a measurement accuracy of ±5% RH. In addition, exit temperature is recorded with a T-type thermocouple with sensor accuracy of ±1 °C.

4.2.2 Membrane module component (Section S1)

The main part of this section is a membrane module. Feed airflow temperature was measured with platinum resistance temperature detectors at the inlet (Point 1) and outlet of the module (Point 2). Hygrochron temperature/humidity loggers recording air temperature and humidity with a capacitive polymer humidity sensor were installed at the same location. A differential pressure sensor was used to measure static pressure drop of feed airflow across the membrane module (Figure 16).

To measure differential pressure across the membrane module, a low-pressure differential gauge with a measurement range of 0 to 5 in w.g. (0-1,245 Pa) and an accuracy of ±2.0% FS was used.

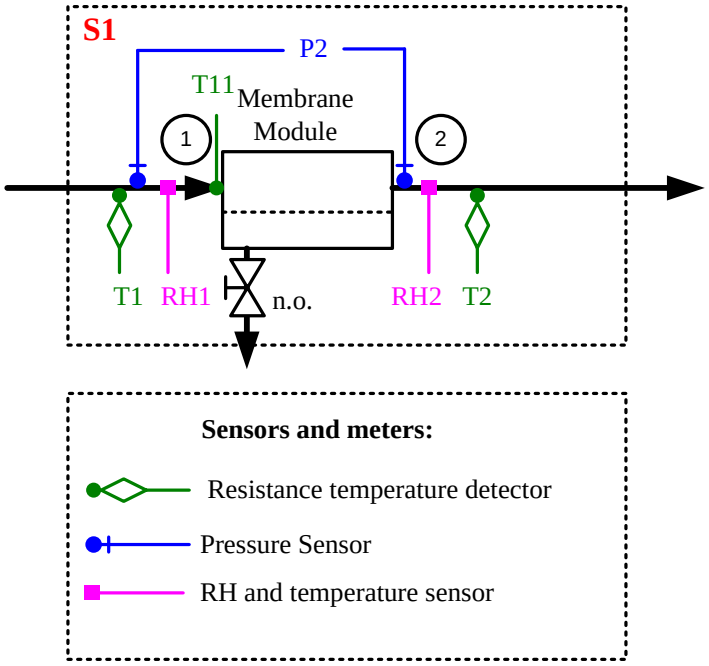

Figure 16. The membrane module component (Section S1)

This research includes experimental results obtained from six membrane modules developed by the PNNL with a similar construction and membrane surface area (Figure 17). The main differences between the membrane modules were improvements of the assembly technology. Each of the tested membrane modules was designed for a feed airflow rate of 30 cfm (51 m³/h). The membrane module was connected to a rigid rectangular metal duct with more than ten hydraulic diameters of the duct at the module's inlet and five hydraulic diameters at the module's outlet. The shape and area of the duct were the same as the cross section of the membrane module; this created a fully developed flow conditions at the membrane module inlet and minimized airflow entrance effects.

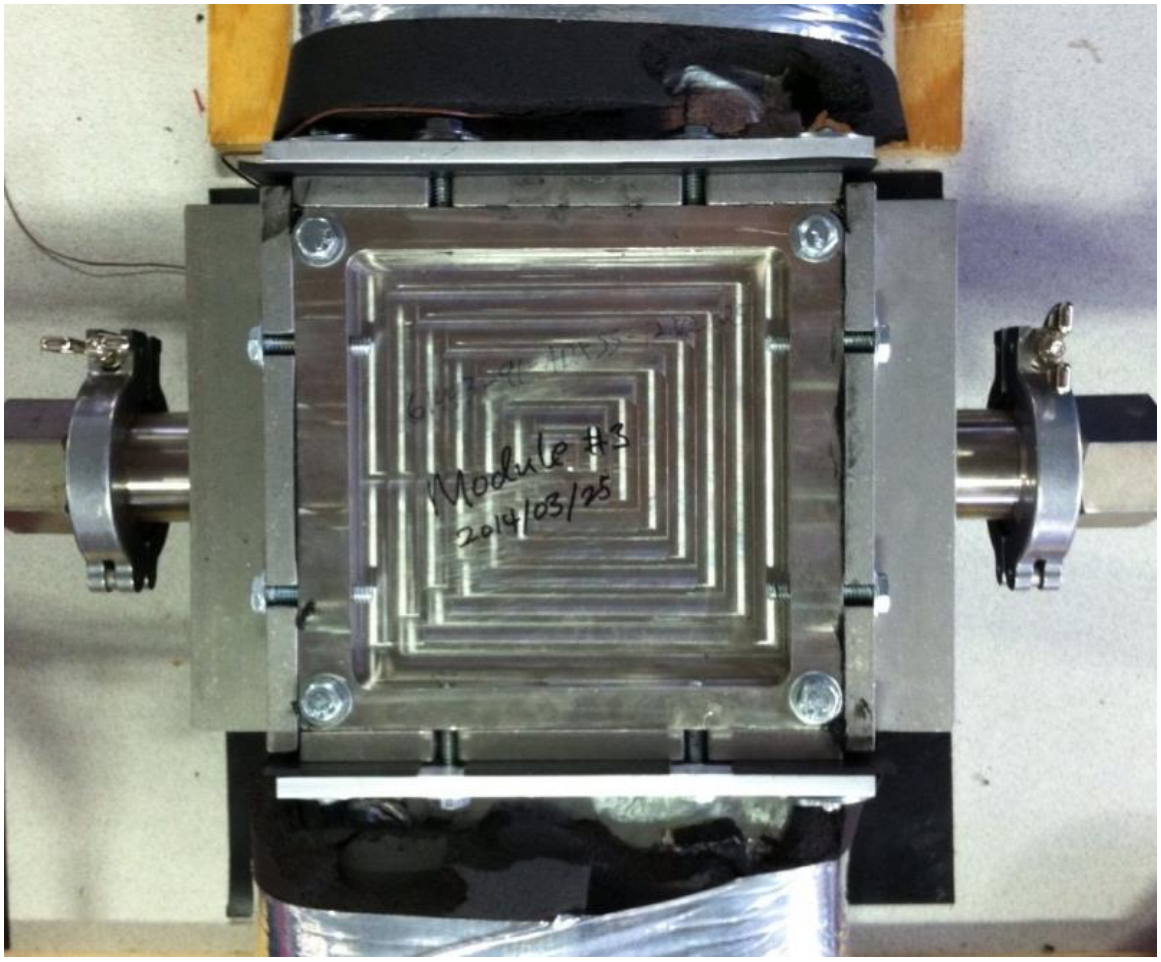

Figure 17. Membrane dehumidification module

The casing of the membrane module was constructed from stainless steel. Within the casing, each module contains membrane cassettes located parallel to each other. Each cassette has connections to the vacuum system on two opposite sides (left and right sides in Figure 18) and consists of two membrane sheets packed back-to-back with 5-mm spacing. The number of membrane plates is determined based on the membrane area requirement. Each membrane cassette has a zeolite membrane surface on each side (Figure 19).

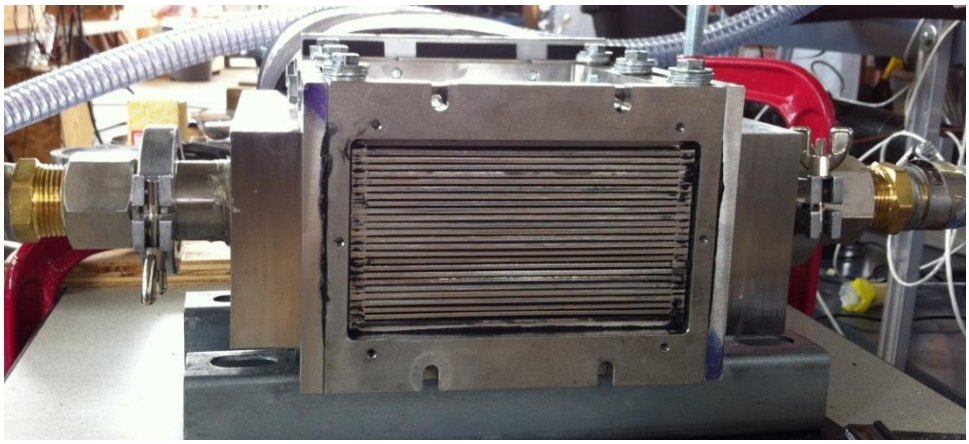

Figure 18. Membrane cassettes inside of the module (view from the feed airflow side)

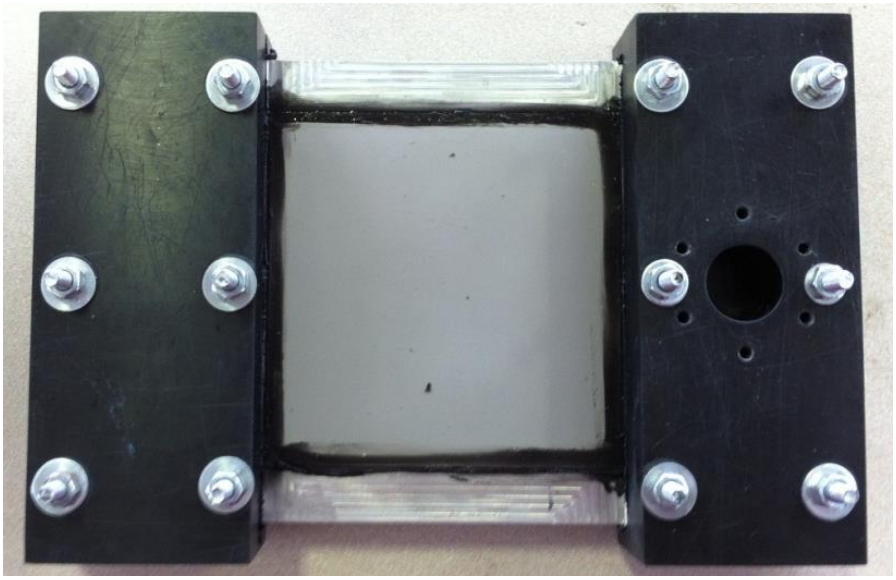

Figure 19. Zeolite membrane cassette mounted in the test frame

Composite membranes consist of an inorganic porous zeolite layer deposited on a porous metal substrate. A polymer material is located between two layers of porous metal substrate to provide increased mechanical strength and reduce water vapor vacuum flow resistance.

4.2.3 Sensible cooling component (Section S2)

The project design requires sensible cooling after the dehumidification process. The sensible cooling was provided by passing the feed air through a heat exchanger operating with chilled water for heat rejection (Figure 20).

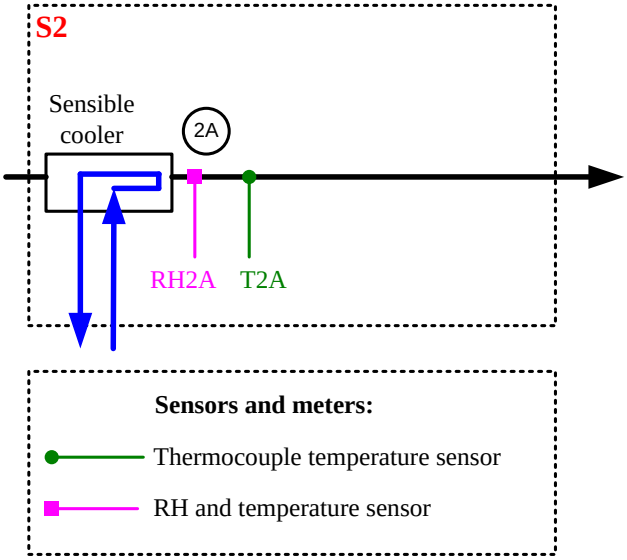

Figure 20. Sensible cooling component (Section S2)

The heat exchanger used in this study is water cooled shell and tube heat exchanger. The chilled water was supplied to the heat exchanger using a diaphragm water pump. The pump cycled water through a temperature-controlled reservoir, which was cooled by a custom-built refrigeration system. The cooling water temperature was measured by a T-type thermocouple located at the exit of the reservoir. This temperature sensor was used with a proportional-integral-derivative controller to control heat rejection by the refrigeration system. Airflow temperature and humidity were measured at the exit from the heat exchanger with a T-type thermocouple and iButton Hygrochron temperature/humidity logger.

4.2.4 Vacuum subsystem (Section S3)

Section S3 intends to provide the required vacuum pressure on the permeate side (0.5-2 kPa) of the membrane surface for dehumidification in Section S1 (Figure 21).

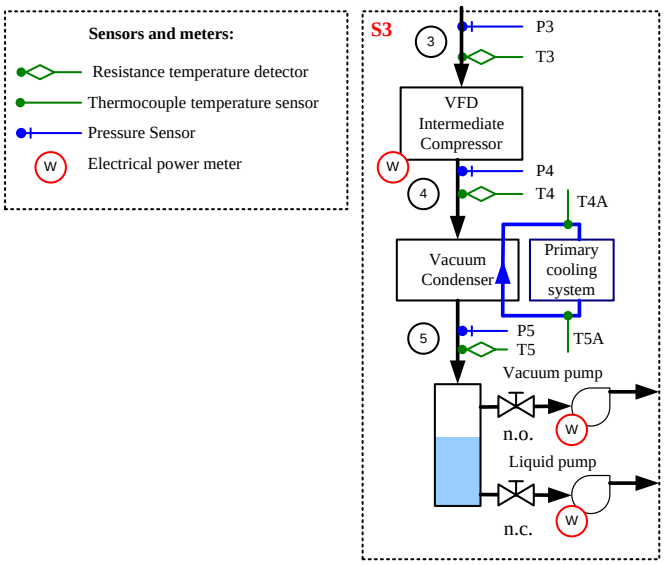

Figure 21. Vacuum subsystem (Section S3)

The first component of this subsystem is an intermediate compressor (VFD Roots blower) designed to increase the permeate pressure of the dehumidification system from a range of 0.5-2 kPa to a pressure above the water vapor saturation pressure of 4-8 kPa at condenser surface temperature of 30°C (86°F).

The inlet pressure is determined by the requirement to transfer water vapor from the feed air flow side to the permeate side. That means that the partial pressure of water vapor in the permeate airstream should be below the partial pressure of water in the retentate airflow stream. The intermediate compressor exit pressure is defined by the vacuum condenser temperature and area. The partial pressure of water vapor exiting the intermediate compressor should be above the saturation pressure of water at the temperature of the vacuum flow exiting the vacuum condenser. An Oerlikon-Leybold Roots Blower WA250 was used for the experimental setup.

The vacuum condenser is located after the intermediate compressor. The purpose of the vacuum condenser is to reduce the amount of water vapor rejected from the vacuum stream to the ambient air. This is one of the key components to achieve higher energy efficiency, since the energy required to increase the pressure of an incompressible liquid is much lower than required for the same mass of compressible gas. Dimensions of the condenser are limited by the maximum size and weight of the system. The condenser cooling water operating temperature is limited by cooling tower performance. In this work it was assumed that the temperature of the inlet cooling water to the condenser should be 2.7°C (5°F) above the feed airstream wet-bulb temperature. The vacuum condenser in the experimental system is a flat plate heat exchanger (Duda Diesel B3-36A-60ST) with a heat exchange area of 2.16 m² (Table 6). This heat exchanger operates in counterflow mode.

Table 6. Vacuum condenser (B3-36A-60ST) parameters

Parameter	Value
Length	465 mm (18.3 in)
Width	74 mm (2.9 in)
Height	2.24 mm/plate + 7 mm
Number of plates	120
Heat transfer area/plate	0.036 m²/plate
Thickness of plates	0.3 mm
Max design flow rate	66.6 L/min (17.6 gpm)
Channel capacities	0.05 L/channel
Design pressure	3.0 MPa
Test pressure	4.5 MPa
Design temperature	-195°C to +225°C
Refrigeration design capacity	4-15 kW (17,000-61,200 Btu/h)
Welding material	99.9% Copper
Plate material	Stainless Steel 304 (SS316L inner plates)

Condensed water in the vacuum condenser accumulates in the separation tank located after the vacuum condenser. This separation tank has two outlets. The upper outlet is used to reject remaining uncondensed water vapor and air, which permeates together with water vapor to the vacuum exhaust channel. A Pfeifer Duo 10M (dual stage high performance rotary vane pump with a pumping speed 10 m³/h when vacuum pressure is above 100 Pa) was used as a vacuum pump in the experimental system. The

lower outlet of the separation tank is used for condensed liquid water rejection by the water pump to the water storage system, which is kept at atmospheric pressure. The experimental system uses a compact dispensing water pump with a 1.4 gpm (5.3 lpm) flow rate.

The vacuum subsystem has three main measurement points: before and after the intermediate compressor and after the vacuum condenser. Each of them has platinum resistance temperature detectors connected to the centralized data acquisition system and capacitance manometers (Setra 730) for vacuum system measurements with a reading accuracy of ±0.5%.

4.2.5 Water rejection component (Section S4)

The water rejection component (Section S4) is designed to provide measurements of the permeate airflow and extracted water during the dehumidification process. To decrease temperature of the permeate flow and condense the remaining water vapor, Condenser 4 (flat-plate heat exchanger), is used after the vacuum pump exhaust (Figure 22).

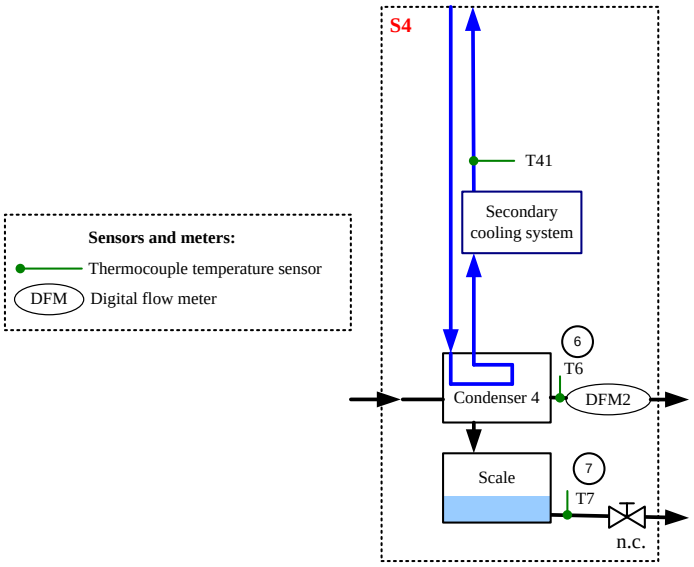

Figure 22. The water rejection component (Section S4)

The permeate flow temperature increases during the compression process in the vacuum pump to a level that exceeds 60°C (140°F). To reduce the permeate flow temperature to a temperature suitable for flow measurements, a flat plate heat exchanger is used. The flat plate heat exchanger used (Duda Diesel B3-12A 40) has a surface area of 0.48 m². The Condenser 4 cooling water inlet temperature is the same as the exiting cooling water temperature of the sensible cooler in Section S2.

The permeate airflow measurement is made by one of the three available flow meters connected at the exit of the flat plate heat exchanger:

- Pelton-type turbine wheel Omega FLR1006-D (1.0 – 5.0 lpm);
- Pelton-type turbine wheel Omega FLR1005-D (0.4 – 2 lpm);
- Diaphragm positive displacement flow meter
  Agilent ADM2000 (5E-4 – 1.0 lpm).

More information about the airflow meters used is given in APPENDIX A.

4.3 Mathematical model for experimental data analysis

To analyze the membrane separation process and system performance, a mathematical model was developed in Engineering Equation Solver based on the available experimental data. The main criteria for the energy efficiency analysis were: effective system COP, the membrane separation factor, and effective air and water permeances through the membrane surface and the airflow.

The key measured parameters for the analysis were:

- Temperature and relative humidity of feed airstream: at the system inlet at Point 01, before the membrane module inlet at Point 1, after the membrane module at Point 2, and after the sensible cooling system (system outlet) at Point 2A.
- Permeate vacuum flow temperatures and pressure: on the permeate side of the membrane module at Point 3, after the intermediate compressor at Point 4, and after the vacuum condenser at Point 5.
- Permeate airflow rate and temperature after the vacuum pump at Point 5.

- Pressure drop across the membrane module to estimate the power required to move the air.

The small scale of the system and the corresponding manufacturing limitations of several system components required development of assumptions about the potential energy efficiency of commercial system components:

- Supply air fan and electrical motor energy efficiency – 60%.
- Water pump and electrical motor – 80%.
- Vacuum pump and electrical motor – 60%.
- Intermediate compressor and electrical motor – 60%.

Another assumption made is saturation with water of the permeate airflow after it is cooled in Condenser 4. This assumption is valid for membranes with a relatively large selectivity coefficient.

System effective coefficient of performance (effective COP) was calculated based on the equation:

$$COP = \frac{\left(h_{Sys\ In} - h_{Sys\ out}\right) \cdot \dot{V} \cdot \rho_1}{W_{Total}} \tag{64}$$

where: h_x – feed airflow enthalpy at point x, [kJ/kmol];
$\dot{V}$ – feed airflow volumetric flow rate, [m^3/s];
ρ_1 – density of feed airflow, [kmol/m^3];
W_{Total} – system operation effective power consumption, [kW].

System operation effective power consumption can be found:

$$W_{Total} = 1.1 \cdot \left(\frac{1}{0.6} \cdot W_{sfan} + \frac{1}{0.8} \cdot W_{wp} + \frac{1}{0.6} \cdot W_{vp} + \frac{1}{0.6} \cdot W_{ic}\right), \text{[kW]} \tag{65}$$

where: W_{sfan} – power delivered by supply air fan to move feed airflow, [kW];
W_{wp} – power delivered by water pump between Point 5 and Point 7, [kW];
W_{vp} – power delivered by vacuum pump for gas compression between Point 5 and Point 6, [kW];
W_{ic} – power delivered by intermediate compressor for gas compression between Point 3 and Point 4, [kW].

In Equation (65), 10% of energy is reserved for operation of the control system and other supplemental system components.

Power delivered by the supply air fan to move feed airflow can be estimated based on the actual measured data:

$$W_{sfan} = \Delta P_{mm} \cdot \dot{V}, [kW] \tag{66}$$

where: ΔP_{mm} – static pressure drop of feed airflow across the membrane module, [kPa].

Power delivered by the water pump between Point 5 and Point 7 can be estimated with assumption of liquid water incompressibility:

$$W_{wp} = \frac{\dot{N}_{LiquidWater}}{\rho_{LiquidWater7}} \cdot (P_{atm} - P_5), [\text{kW}] \tag{67}$$

where: $\dot{N}_{LiquidWater}$ – molar flow rate of water condensed in the vacuum condenser, [kmol/s].

Power delivered by the vacuum pump between Point 5 and Point 6 was estimated for the isothermal process with the equation:

$$W_{vp} = \dot{N}_{Air6} \cdot R \cdot T_5 \cdot ln\left(\frac{P_6}{P_{a5}}\right) + \dot{N}_{Gas\,Water5} \cdot R \cdot T_5 \cdot ln\left(\frac{P_6}{P_{w5}}\right), [\text{kW}] \tag{68}$$

where: N_{Air6} – molar flow rate of air permeated through the membrane surface,[kmol/s];
R – universal gas constant, [kJ/(kmol · K)];
T_5 – gas mixture temperature at Point 5,[K];
P_{a5} – partial pressure of air at Point 5, [kPa];
$N_{Gas\,Water5}$ – molar flow rate of water leaving condenser as a vapor, [kmol/s];

P_{w5} – partial pressure of water vapor at Point 5, [kPa];
P_6 – total pressure of gas at Point 6, [kPa].

The power input required by the intermediate compressor in an ideal isothermal process between Point 5 and Point 6 is:

$$W_{ic} = \dot{N}_{w3} \cdot R \cdot T_4 \cdot ln\left(\frac{P_{w4}}{P_{w3}}\right) + \dot{N}_{a3} \cdot R \cdot T_4 \cdot ln\left(\frac{P_{a4}}{P_{a3}}\right), [\text{kW}] \quad (69)$$

The effective water permeance includes mass transfer conductivity for water vapor permeation through the bulk airflow, membrane surface and the permeate flow, and can be found as:

$$P_{AB_{Water}} = \frac{\dot{N}_{Water3}}{A_{membr} \cdot \Delta P_{water}}, \left[\frac{\text{kmol}}{\text{kPa} \cdot \text{m}^2 \cdot \text{s}}\right] \quad (70)$$

where: $\dot{N}_{Water3}$ – molar flow rate of water permeated through the membrane surface, [kmol/s];
A_{membr} – membrane surface area, [m^2];
ΔP_{water} – Log-mean water vapor partial pressure difference through the membrane, [kPa].

The molar flow rate of water permeating through the membrane surface can be measured based on the humidity ratio change in the feed airstream through the membrane module:

$$\dot{N}_{Water3} = \max\left(0, \dot{V} \cdot \rho_1 \cdot X_{w1} - \dot{N}_{a2} \cdot X_{relW2}\right), [\text{kmol/s}] \quad (71)$$

where: X_{w1} – water molar concentration at Point 1, $\left[\frac{\text{kmol}_\text{w}}{\text{kmol}_\text{total}}\right]$;

$\dot{N}_{a2}$ – molar flow rate of air on the retentate side at Point 2, $\left[\frac{\text{kmol}_\text{a}}{\text{s}}\right]$;

X_{relW2} – relative water molar fraction at Point 2, $\left[\frac{\text{kmol}_\text{w}}{\text{kmol}_\text{a}}\right]$.

The log-mean water vapor partial pressure difference through the membrane accounts for the change of partial pressure of the water profile along the membrane surface as:

$$\Delta P_{water} = \frac{P_{w1} - P_{w2}}{\ln\left(\frac{P_{w1} - P_{w3}}{P_{w2} - P_{w3}}\right)}, [\text{kPa}] \quad (72)$$

where: P_{w1} - Partial pressure of water vapor in the feed air stream at the membrane module inlet, [kPa];

P_{w2} - Partial pressure of water vapor in the retentate air stream at the membrane module outlet, [kPa];

P_{w3} - Partial pressure of water vapor in permeate gas flow, [kPa].

Effective air permeance can be found with the equation:

$$P_{AB_{Air}} = \frac{\dot{N}_{Air3}}{A_{membr} \cdot \Delta P_{Air}}, \left[\frac{\text{kmol}}{\text{kPa} \cdot \text{m}^2 \cdot \text{s}}\right] \quad (73)$$

where: $\dot{N}_{Air3}$ – molar flow rate of air permeated through the membrane surface, [kmol/s];

ΔP_{air} – Log-mean air partial pressure difference through the membrane, [kPa].

The log-mean air partial pressure difference through the membrane can be found as:

$$\Delta P_{Air} = \frac{P_{a1} - P_{a2}}{\ln\left(\frac{P_{a1} - P_{a3}}{P_{a2} - P_{a3}}\right)}, [\text{kPa}] \tag{74}$$

where: P_{a1} - Partial pressure of air in the feed air stream at the membrane module inlet (Point 1), [kPa];
P_{a2} - Partial pressure of air in the retentate air stream at the membrane module outlet (Point 2), [kPa];
P_{a3} - Partial pressure of air in permeate gas flow (Point 3), [kPa];

The **Separation Factor** of the membrane module can be found with [6]:

$$\alpha_{w/a} = \frac{\left(\frac{X_{w3}}{X_{a3}}\right)}{\left(\frac{X_{w1}}{X_{a1}}\right)} \tag{75}$$

where: X_{w3} – Water molar concentration in permeate stream, $\left[\frac{\text{kmol}_\text{w}}{\text{kmol}_\text{total}}\right]$;
X_{a3} – Air molar concentration in permeate stream, $\left[\frac{\text{kmol}_\text{Air}}{\text{kmol}_\text{total}}\right]$;
X_{w1} – Water molar concentration in feed air stream at the membrane module inlet, $\left[\frac{\text{kmol}_\text{w}}{\text{kmol}_\text{total}}\right]$;
X_{a1} – Air molar concentration in feed air stream at the membrane module inlet, $\left[\frac{\text{kmol}_\text{Air}}{\text{kmol}_\text{total}}\right]$.

Based on the previous calculations, the **Selectivity Coefficient** of water to air for the membrane module can be found from the membrane effective water and air permeances as:

$$\mathbf{s_{w/a}} = \frac{P_{AB_{Water}}}{P_{AB_{Air}}} \tag{76}$$

4.4 Membrane physical properties parametric analysis

The experimental membrane dehumidification system was tested with six zeolite membrane modules. All of the tested modules used in the experiments were built according to the same specification and have the same membrane surface area. The main differences between membrane modules were minor changes in the cassette and module assembly technology. The first generation of modules included Module #1, Module #2 and Module #3. The second generation used the same stainless steel casing, but with improved cassettes within the module and included Module #1A, Module #2A, and Module #3A. More than one hundred experiments were conducted under different conditions. The main goals for experimental tests were to determine pressure drop across the membrane module as a function of the airflow rate, and to determine effective water and air permeance as a function of airflow rate, feed airstream temperature, humidity ratio, and permeate total pressure.

4.4.1 Feed airflow rate and membrane module static pressure drop

The apparatus used for the static air pressure drop measurement across the feed side of the membrane module was the same as for the study of the membrane permeation and energy efficiency of the experimental system. The air feed duct was directly attached to the module in order for there to be no pressure drop associated with fittings. Sufficient length of the rectangular duct before and after the membrane module provided fully developed flow at the module inlet.

Module #1A and Module #2A were used to measure the feed airflow pressure drop across the membrane modules. Measurements were done at various airflow rates. A Fluke Pressure Calibrator 717 1G (uncertainty ±3.45 Pa) was used to measure the static pressure drop across the membrane module. The measurements for both modules were made under different conditions. In the first case, the membrane permeate side was not evacuated and kept at atmospheric pressure. In the second case, the permeate side was evacuated to an absolute pressure of 3.5 kPa. The fact that the permeate side was

evacuated had a strong impact on the pressure drop across the membrane module due to the changes of the cassette volumes as a result of membrane surface deflection caused by polymer material expansion inside each cassette (Figure 23, and Figure 24).

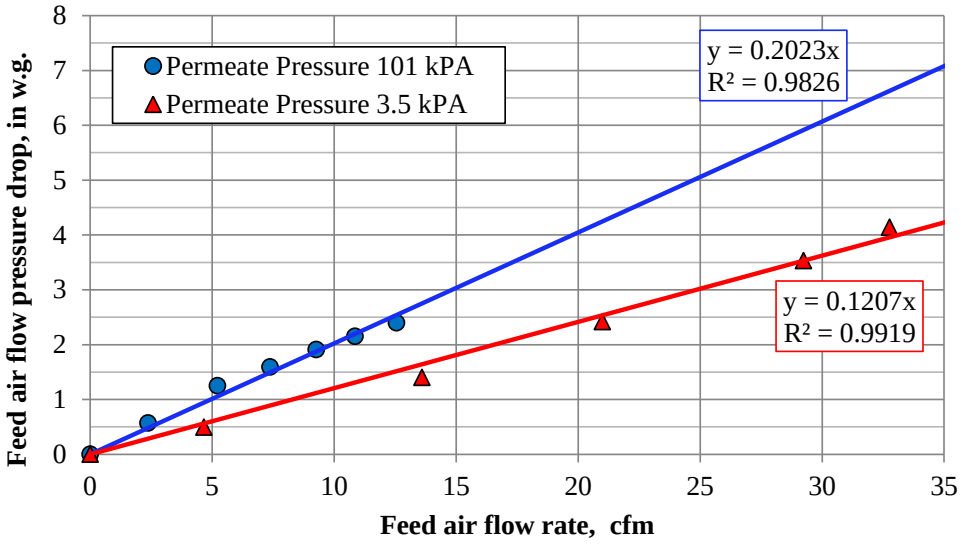

Figure 23. Module#1A measured feed airflow pressure drop

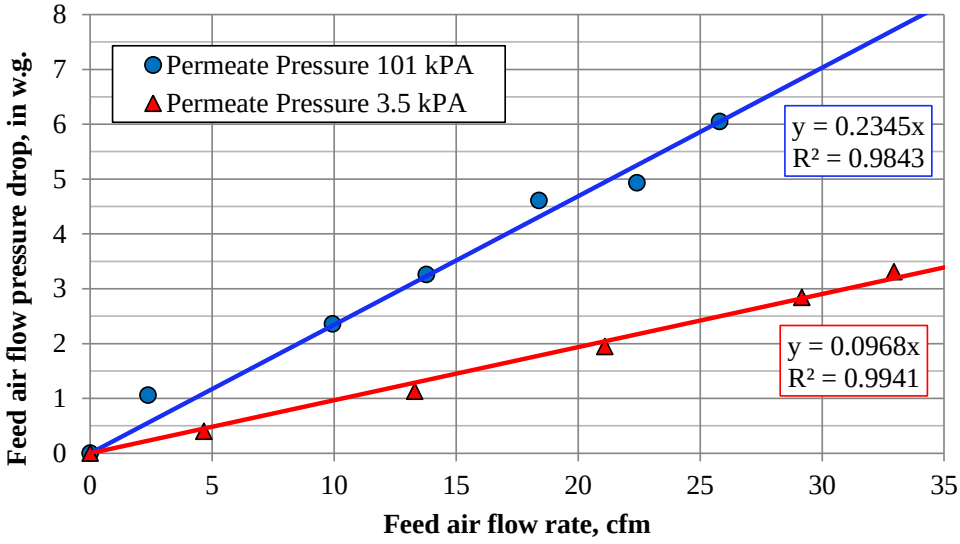

Figure 24. Module#2A measured feed airflow pressure drop

At the design airflow rate of 30 cfm (51 m³/h), the pressure drop across both tested modules exceeded the design level of 1 in w.g (249 Pa). Reduction of the static pressure drop across the feed air side of the membrane model requires future design adjustments. With the reduction of the membrane surface deflection and increase of the channel height membrane channel geometry can be improved that will decrease airflow static pressure drop.

4.4.2 Feed airflow rate and effective membrane permeance

A series of experiments were conducted by using the first generation modules (Module #1 and Module #2) and the second generation module (Module #3A) to investigate the effect of the feed airstream rate on the effective water and air permeance at the design inlet airflow temperature and humidity ratio. Experimental results are summarized in Table 7.

Table 7. Experimental data at different airflow rates and constant feed air properties

Test #	1	5	6	8	9	10	18	2M-7	2M-8
Membrane Module #	1	2	2	2	2	2	2	3A	3A
Feed air flow rate, cfm	23.7	14.5	9.1	5.0	5.0	3.5	30.1	30.0	13.2
Feed temperature, T1, °F	90.7	89.8	89.8	88.0	90.7	90.7	89.8	89.8	90.7
Feed humidity ratio, ω1	0.02527	0.02916	0.02980	0.02824	0.02867	0.02848	0.02719	0.02844	0.02980
Retentate temperature, T2, °F	88.0	88.0	87.1	86.2	85.3	84.4	88.0	88.9	89.8
Retentate humidity ratio, ω2	0.01186	0.00999	0.00692	0.00469	0.00510	0.00390	0.01445	0.01598	0.01297
Retentate relative humidity, RH2,%	42	35	25	18	20	16	51	54	43
Permeate air flow rate, lpm	0.860	0.864	0.960	3.700	5.300	5.850	1.030	0.457	0.512
Feed water flow, m_w1, kg/s-m²	417E-6	292E-6	185E-6	98E-6	98E-6	70E-6	568E-6	590E-6	270E-6
Permeate air flow, m_air3, kg/s-m²	23E-6	23E-6	26E-6	99E-6	142E-6	157E-6	28E-6	37E-6	163E-6
Permeate water flow, m_w3, kg/s-m²	222E-6	192E-6	142E-6	83E-6	81E-6	61E-6	267E-6	407E-6	234E-6
Permeate pressure, P3, kPa	1.21	1.09	0.95	1.059	1.270	1.20	1.500	1.286	1.426
PAB_air, kmol/(kPa-m²-s)	8.1E-9	8.2E-9	9.1E-9	35.0E-9	50.3E-9	55.5E-9	9.8E-9	4.3E-9	5.0E-9
PAB_water, kmol/(kPa-m²-s)	7.9E-6	6.5E-6	6.0E-6	4.1E-6	3.6E-6	2.8E-6	8.9E-6	6.9E-6	5.0E-6
Separation factor	380	284	185	29	20	14	355	389	48
Selectivity coefficient	968	798	665	116	71	51	907	1584	1003

All these experiments were conducted at the same feed airflow temperature and humidity setpoint. The change of the airflow rate with a constant permeate pressure was the reason for the difference in the retentate humidity ratio. All experiments were conducted at a feed airflow temperature above ambient. Even though the feed and retentate airstream had thermal isolation, energy loss occurred to the environment and airflow temperature decreased by 5°F (9°C) during dehumidification process due to reduced airflow rate (Figure 25).

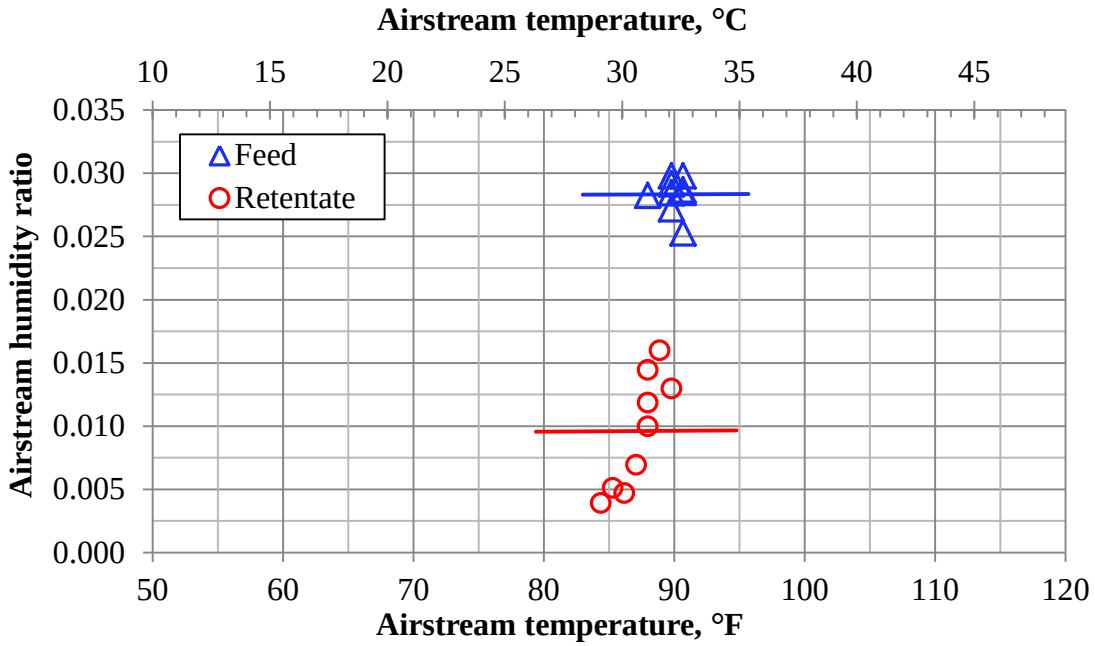

Figure 25. Airflow temperature and humidity for airflow rate impact study

Experimental data show that the decreases of the feed airflow rate result in an increase of effective air permeance (Figure 26) and a decrease of effective water permeance (Figure 27), if permeate pressure is relatively constant. This process is caused by a reduction of water vapor in the retentate stream and as a result, the average water concentration on the high pressure side of the membrane.

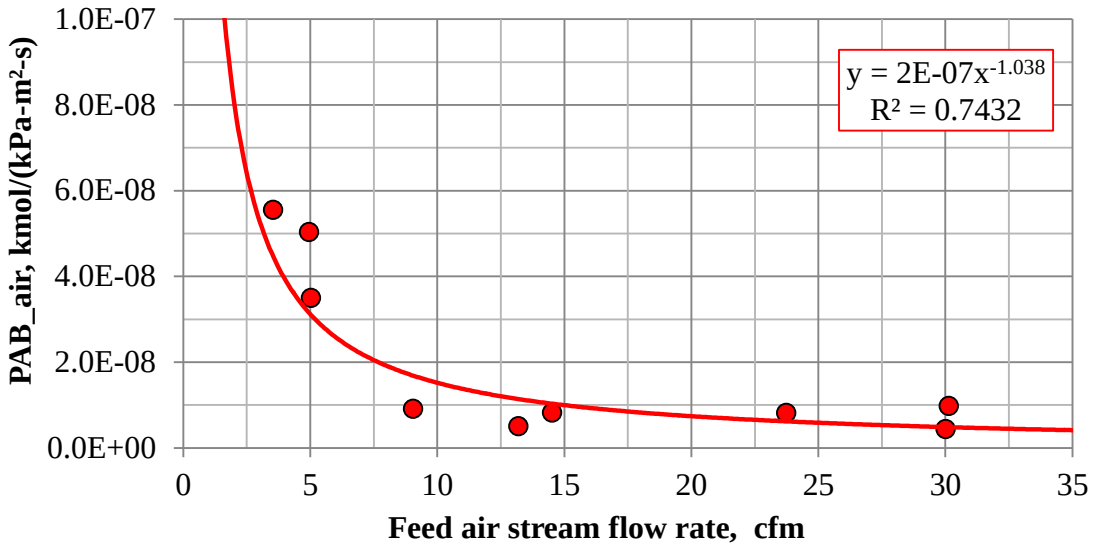

Figure 26. Effective air permeance at the design feed air stream conditions

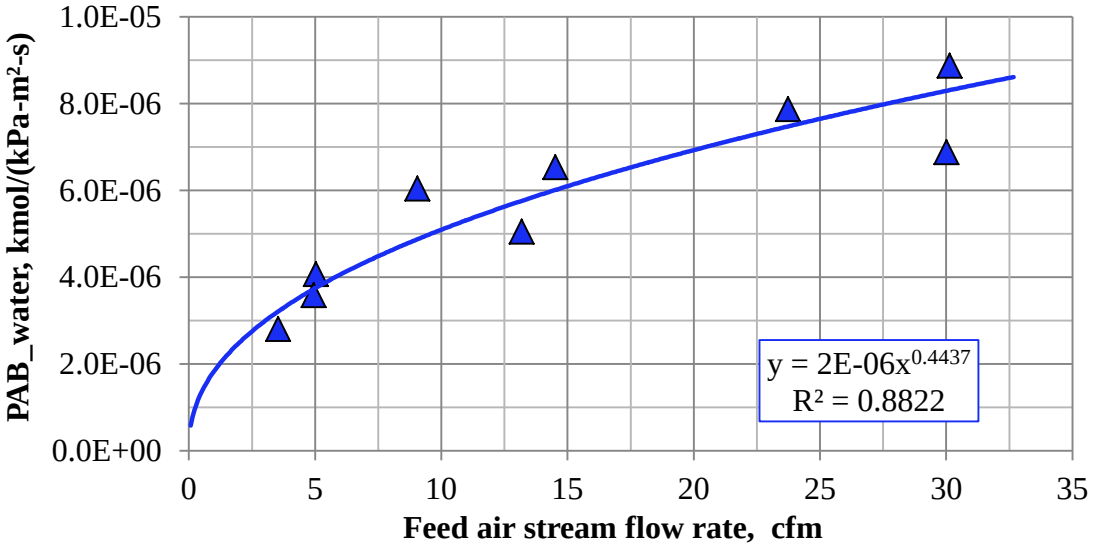

Figure 27. Effective water permeance at the design feed air stream conditions

The retentate relative humidity can be a more useful parameter for analysis of effective permeance change rather than feed airflow rate. When the feed airflow rate is reduced, retentate flow relative humidity also goes down since permeate pressure stays in the same range. Experimental data show that a humidity ratio of approximately 30%

can be considered a critical point that triggers a sudden increase of the effective air permeance (Figure 28) and decrease of effective water permeance (Figure 29).

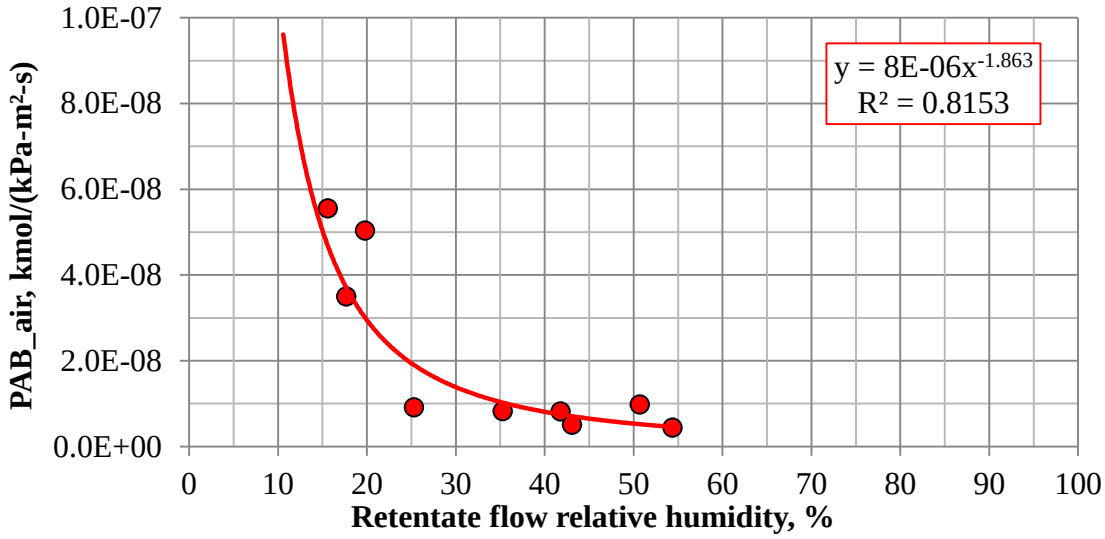

Figure 28. Retentate relative humidity impact on effective air permeance

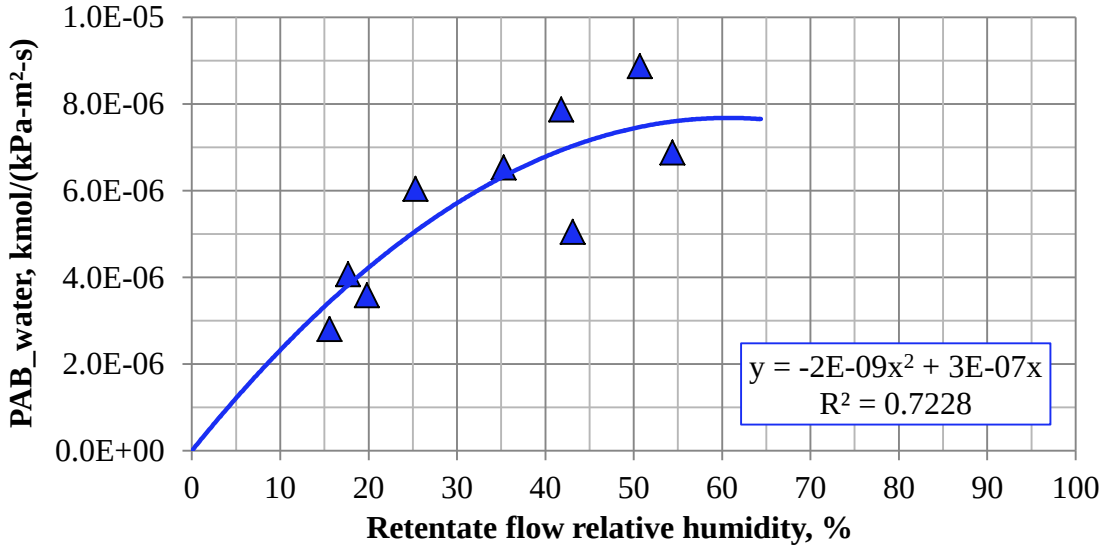

Figure 29. Retentate relative humidity impact on effective water permeance

The change of effective permeances, due to the retentate relative humidity change, impacts the membrane separation factor, which decreases when retentate relative humidity decreases. The series of experiments with different airflow rates shows that the separation factor is proportional to the feed airstream flow rate (Figure 30).

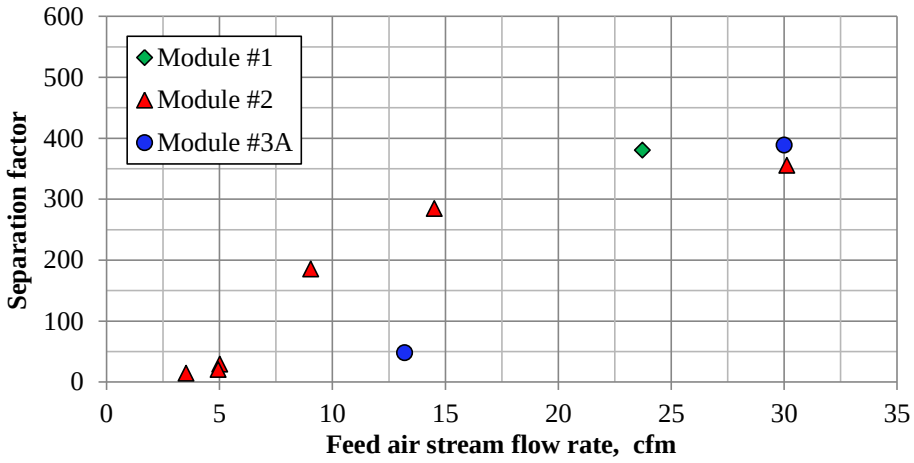

Figure 30. Separation factor at different feed airflow rates

The membrane selectivity coefficient has a similar dependence on the feed airflow rate, when permeate pressure stays constant (Figure 31).

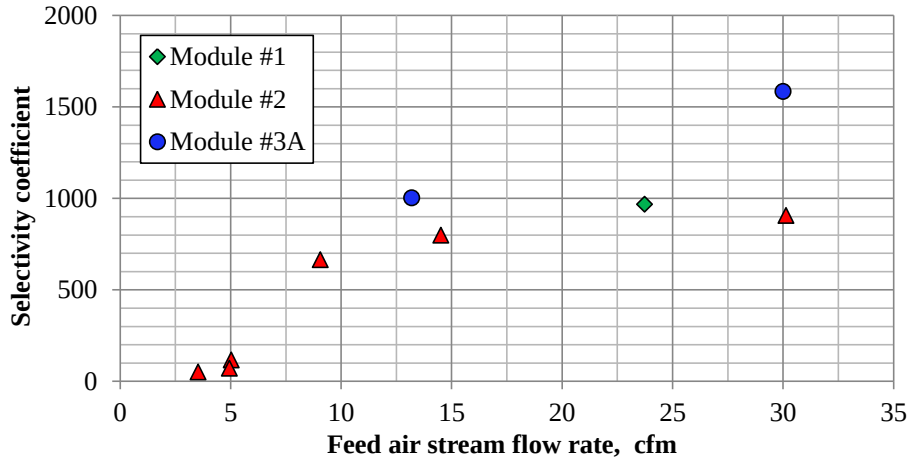

Figure 31. Selectivity coefficient at different feed airflow rates

The selectivity coefficient plotted versus retentate relative humidity for the same data points provides a clearer picture of this process (Figure 32).

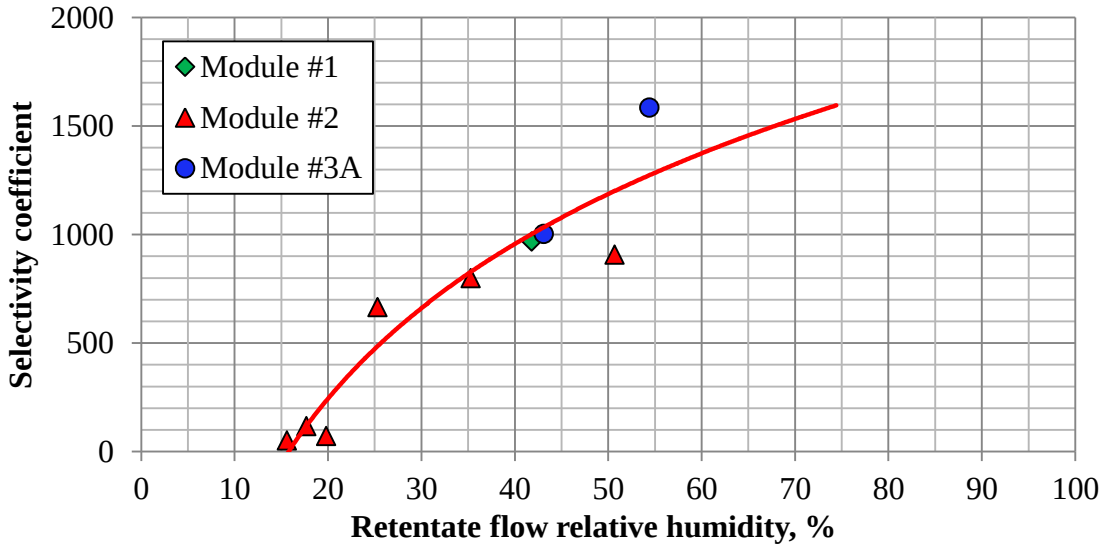

Figure 32. Selectivity coefficient as a function of retentate relative humidity

Experimental results show that the decrease of the feed airflow rate at a constant permeate pressure will cause reduction of the retentate relative humidity, and as a result, the membrane selectivity decreases. To maintain higher selectivity when the feed airflow rate is reduced, the dehumidification system control should increase the permeate pressure and keep the retentate relative humidity constant at the setpoint level above 30% RH for the current membrane manufacturing technology level. With improvement of membrane development technology, this limitation may be removed.

4.4.3 Feed airflow temperature and effective membrane permeance

A series of experiments was conducted with all six membrane modules to investigate the effect of a feed airstream temperature change on effective membrane water and air permeances, when the humidity ratio or the relative humidity is held constant.

The first part of this study included experiments conducted at a constant feed airflow rate of 30 cfm (51 m³/h) with the first generation (Module #2, Module #3) and the second generation of membrane modules (Module #1A). In this study, three constant feed airstream humidity ratio setpoints were chosen: 0.007, 0.009, and 0.015 (Table 8, Table 9).

Table 8. Experimental data at constant feed humidity setpoints (Module #1A, #2)

Test #	A1	A2	A3	13	14	16
Membrane Module #	1A	1A	1A	2	2	2
Feed airflow rate, cfm	30	30	30	30	30	30
Feed temperature, T1, °F	82	85	97	89	78	76
Feed relative humidity, RH1,%	42	32	25	22	31	31
Feed humidity ratio, ω1	0.0097	0.0083	0.0092	0.0069	0.0067	0.0064
Retentate temperature, T2, °F	80	84	93	87	77	75
Retentate relative humidity, RH2,%	25	19	16	13	18	17
Retentate humidity ratio, ω2	0.00532	0.00478	0.00519	0.00365	0.00350	0.00316
Permeate air flow, lpm	1.610	1.820	2.320	2.880	1.570	1.550
Feed water flow, m_w1, kg/s-m²	214 E-6	183 E-6	199 E-6	154 E-6	153 E-6	145 E-6
Permeate air flow, m_air3, kg/s-m²	44E-6	50E-6	63E-6	77E-6	42E-6	42E-6
Permeate water flow, m_w3, kg/s-m²	96E-6	77E-6	87E-6	73E-6	73E-6	73E-6
Permeate pressure, P3, kPa	0.694	0.701	0.771	0.736	0.584	0.573
PAB_air, kmol/(kPa-m²-s)	15E-9	17E-9	22E-9	27E-9	15E-9	14E-9
PAB_water, kmol/(kPa-m²-s)	9E-6	9E-6	9E-6	12E-6	12E-6	15E-6
Separation factor	227	189	150	137	259	277
Selectivity coefficient	590	507	390	443	856	1068

Table 9. Experimental data at constant feed humidity setpoints (Module #3)

Test #	21	22	23	24
Membrane Module #	3	3	3	3
Feed airflow rate, cfm	30	30	30	30
Feed temperature, T1, °F	70	74	81	92
Feed relative humidity, RH1,%	96	80	66	46
Feed humidity ratio, ω1	0.0155	0.0151	0.0154	0.0155
Retentate temperature, T2, °F	71	74	78	88
Retentate relative humidity, RH2,%	56	43	37	25
Retentate humidity ratio, ω2	0.00896	0.00760	0.00751	0.00693
Permeate air flow, lpm	0.725	0.690	0.705	0.730
Feed water flow, m_w1, kg/s-m²	347E-6	336E-6	338E-6	333E-6
Permeate air flow, m_air3, kg/s-m²	19E-6	19E-6	19E-6	20E-6
Permeate water flow, m_w3, kg/s-m²	147E-6	167E-6	173E-6	184E-6
Permeate pressure, P3, kPa	0.897	0.717	0.723	0.740
PAB_air, kmol/(kPa-m²-s)	6.8E-9	6.5E-9	6.6E-9	6.8E-9
PAB_water, kmol/(kPa-m²-s)	7.9E-6	9.0E-6	9.4E-6	10.9E-6
Separation factor	486	597	594	606
Selectivity coefficient	1159	1400	1422	1603

A humidity ratio of 0.009 could be considered as a critical point, since supply airflow in existing commercial systems is usually saturated with water at a temperature of 55°F (13°C) that corresponds to a humidity ratio of 0.009. The other two feed airflow humidity ratio setpoints were chosen above and below the setpoint of 0.009. The combination of experimental dehumidification ranges, shown in Figure 33, effectively covers the dehumidification process from 0.015 to 0.003 and the temperature range between 70-100°F (21-38°C).

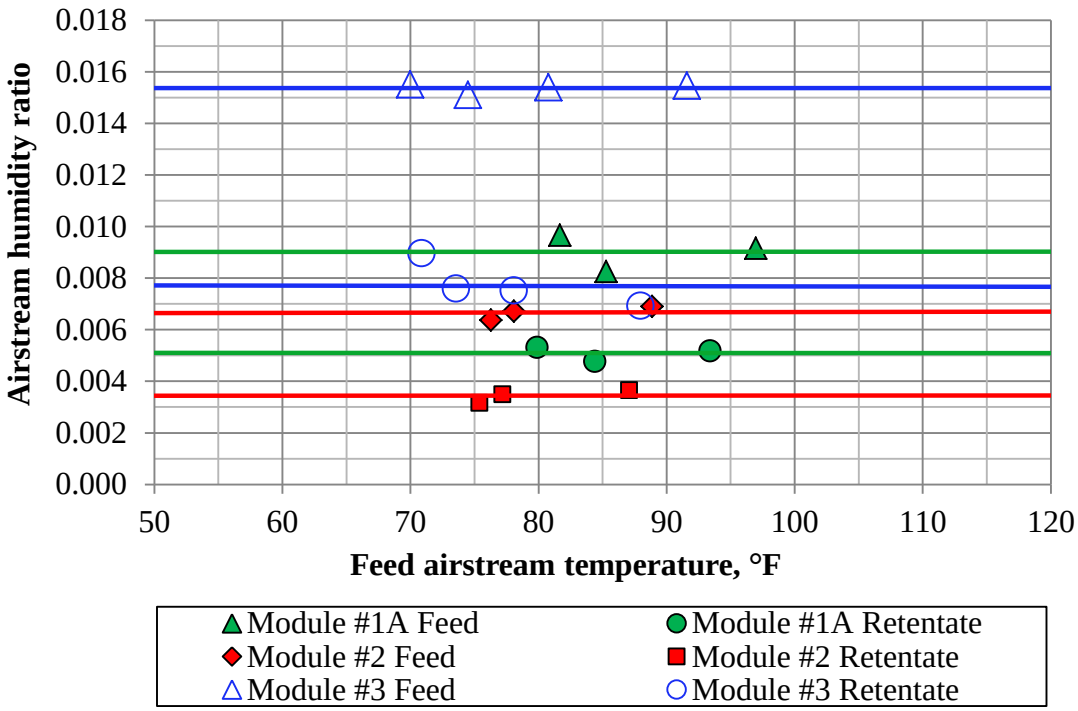

Figure 33. Feed and retentate airstream properties at three humidity ratio setpoints

Experimental results obtained with these three levels of the feed humidity ratio show different effective water permeance for a different feed airflow humidity ratio (Figure 34). Based on this experimental data, effective water permeance appears higher for a humidity ratio of 0.007 and is very similar for 0.009 and 0.015. This data set does not show a clear temperature dependence of the effective water permeance.

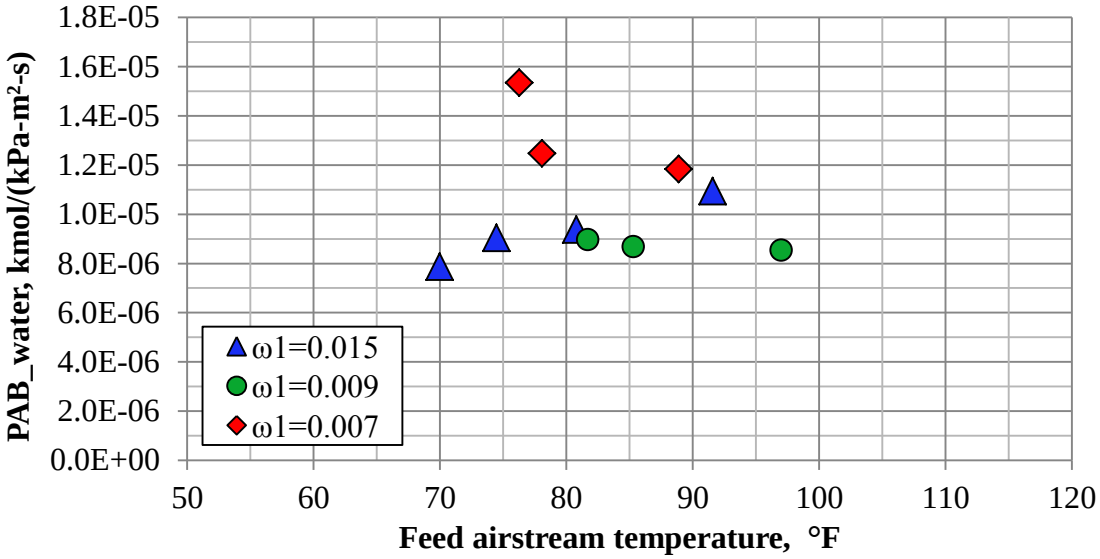

Figure 34. Effective membrane water permeance as a function of temperature

Better dependence can be seen if effective water permeance is analyzed as a function of retentate flow relative humidity (Figure 35).

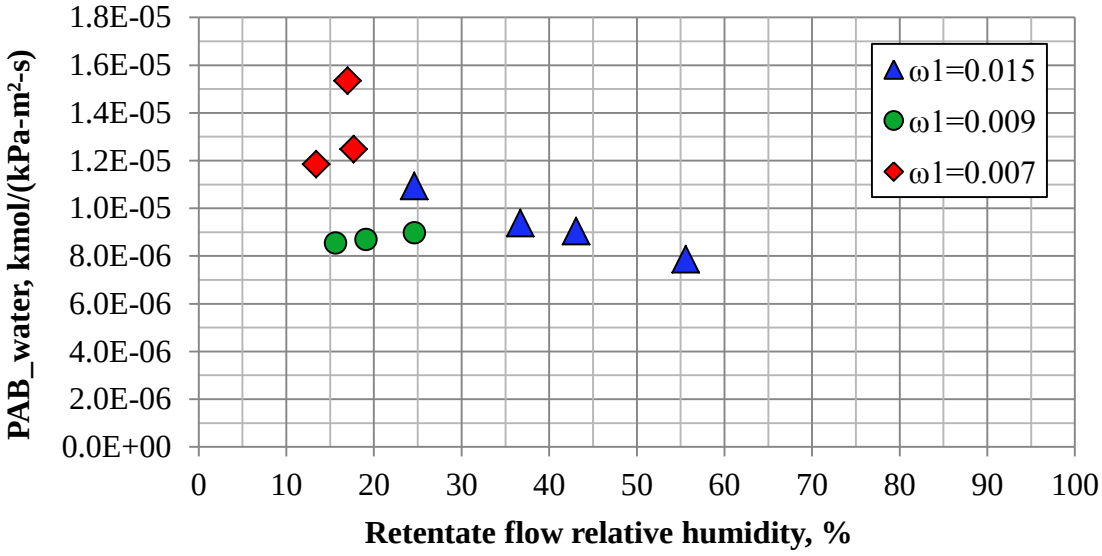

Figure 35. Effective membrane water permeance as a function of retentate flow relative humidity

Experimental data from the same tests show that the effective air permeance is not only a function of feed airstream temperature but also a function of airstream humidity ratio (Figure 36). At a higher humidity ratio, effective air permeance does not show temperature dependence (ω=0.015), while dryer air shows a strong temperature dependence (ω=0.007).

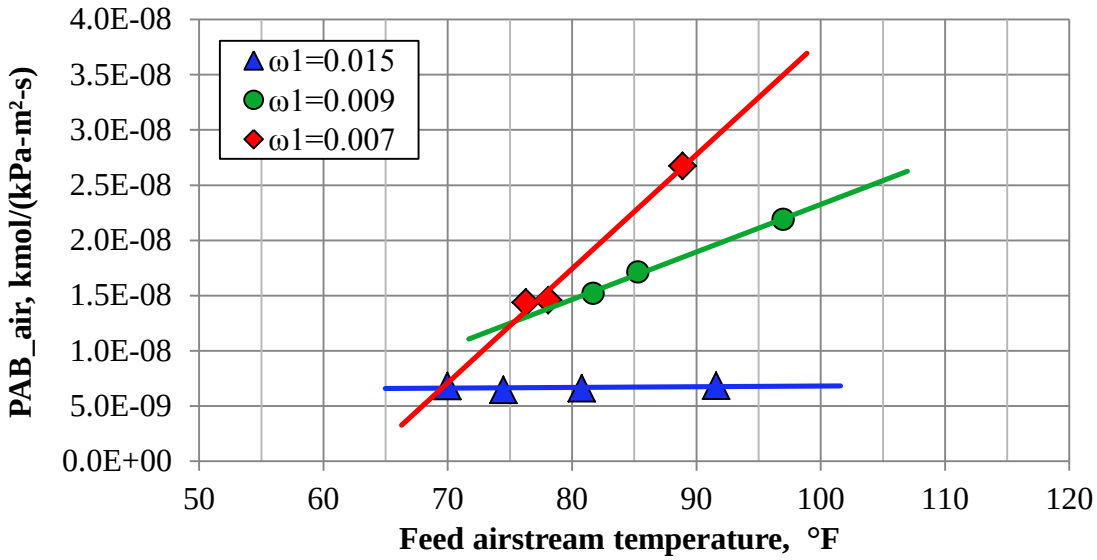

Figure 36. Effective membrane air permeance as a function of temperature

This phenomenon is better explained using a diagram of effective membrane air permeance plotted versus retentate flow relative humidity. In this case all three experimental series overlap and form one regression line (Figure 37).

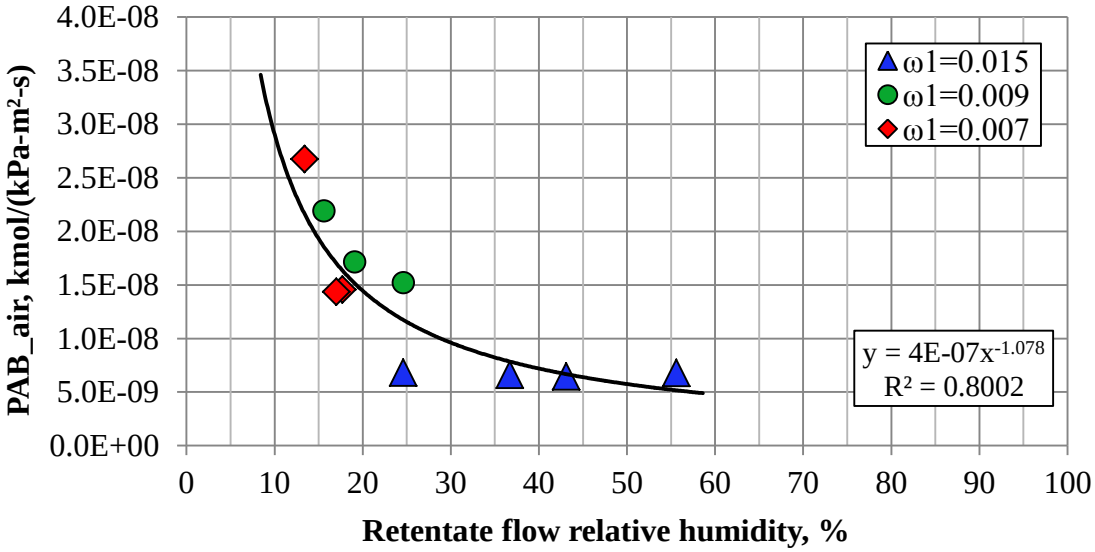

Figure 37. Effective membrane air permeance as a function of retentate flow RH

The regression line from Figure 37 shows a similar dependence as Figure 28. In both cases, the effective air permeance approaches 5E-9 kmol/(kPa·m²·s) for a retentate relative humidity above 30%, where a relatively constant effective membrane air permeance is observed. Also, when retentate relative humidity goes below 20%, the effective air permeance increases very rapidly with decreasing relative humidity. The dependence of effective air permeance on relative humidity, rather than temperature, creates two independent trend lines for the separation factor (Figure 38).

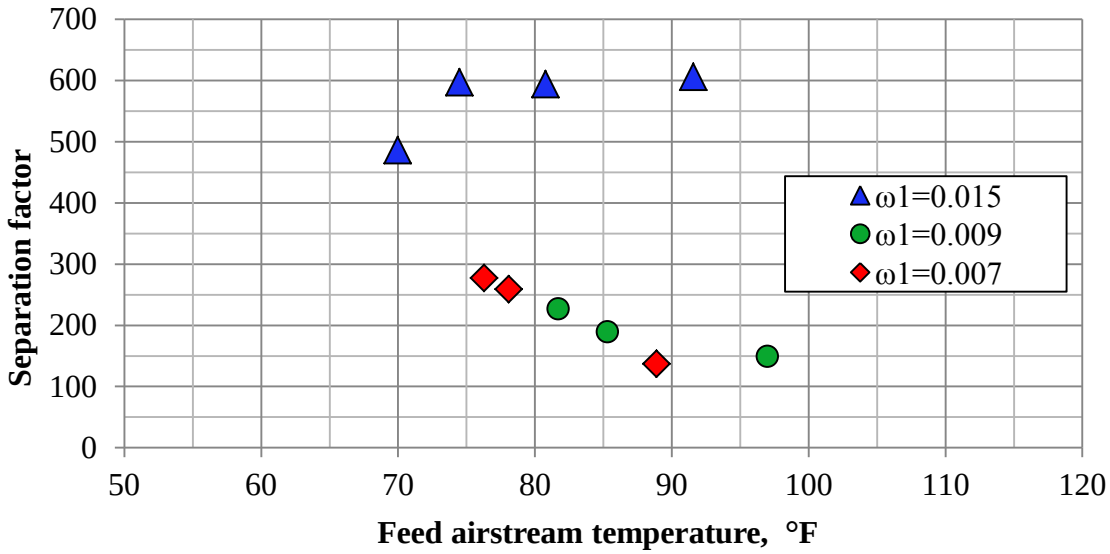

Figure 38. Separation factor as a function of airstream temperature

In the first case, when relative humidity is sufficiently high, the separation factor increases with temperature increase. When retentate flow relative humidity is low, the opposite effect is observed.

A higher humidity ratio and coincident higher retentate flow relative humidity (Figure 39) appears to be the reason why the obtained separation factor was the largest for the membrane Module #3 tested at a feed humidity ratio of 0.015.

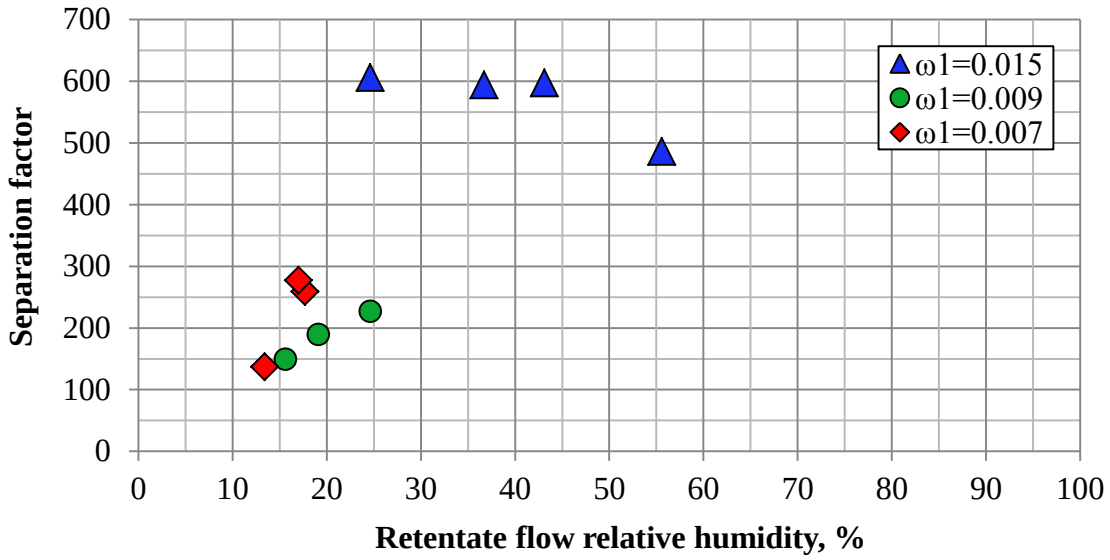

Figure 39. Separation factor as a function of retentate flow relative humidity

The second part of this study includes experiments conducted at a constant airflow rate of 30 cfm (51 m³/h) and feed air relative humidity approaching the saturation line (between 90% and 100%). This part of the study includes 40 experiments conducted with all six available membrane modules. The wet-bulb temperature of the feed airflow was changed between 60°F and 90°F (16-32°C).

The experimental results show different levels of the effective membrane water permeance plotted versus feed airstream temperature for different modules used in the experiment (Figure 40). In the tested temperature range, the effective water permeance is independent of the temperature and varies from 5E-6 to 9E-6 kmol/(kPa-m²-s) for different tests.

For all experiments described in Figure 40 retentate relative humidity was between 48% and 71%. The plot of effective water permeance as a function of the retentate flow relative humidity provides more useful information than the temperature dependence plot. In this case, all six groups of experiments form a single functional dependence that show a linear decrease of effective water permeance with a retentate flow relative humidity increase (Figure 41).

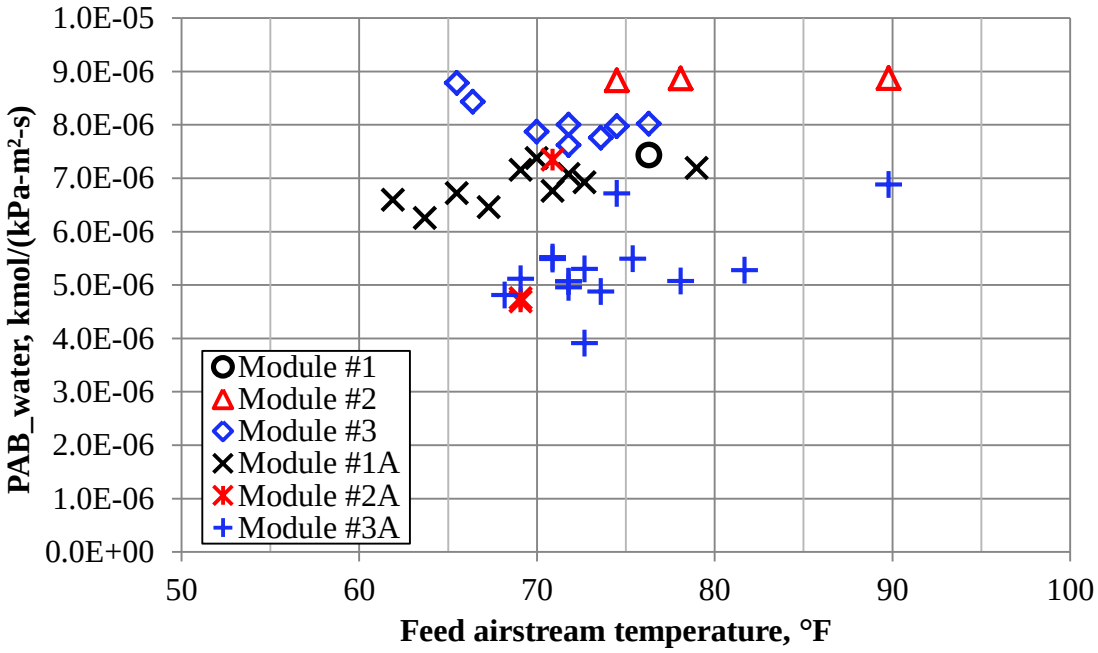

Figure 40. Effective water permeance as a function of temperature

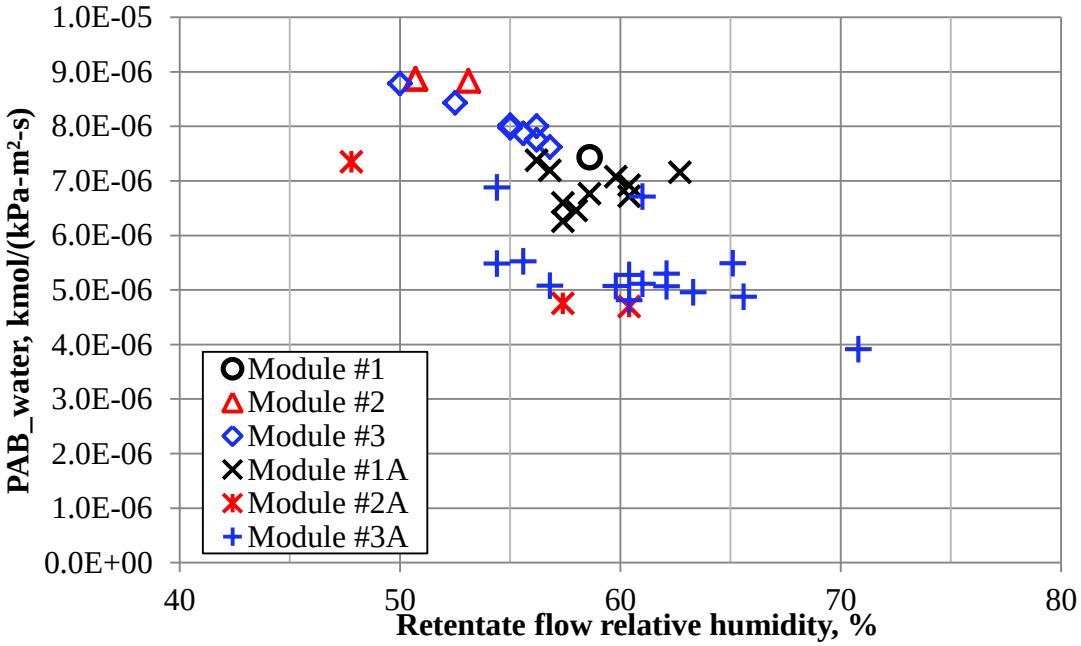

Figure 41. Effective water permeance as a function of relative humidity

The same experimental results were used to analyze effective air permeance as a function of temperature when feed airflow humidity conditions are close to saturation. Analysis shows that the effective air permeance has a positive dependence on temperature between 1.0E-9 and 9.5E-9 kmol/(K-kPa-m²-s). This was obtained based on the experimental data from Module #2, Module#3, Module #1A, and Module #3A (Figure 42).

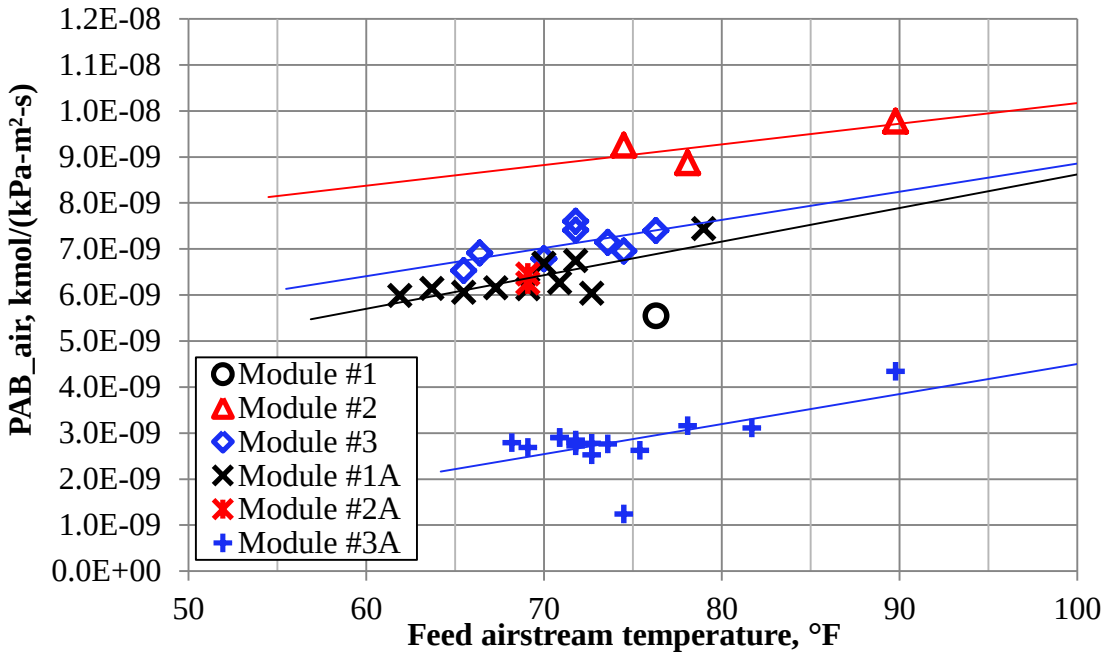

Figure 42. Effective air permeance at a constant airflow and relative humidity

At the same time there is no clear dependence of effective air permeance from retentate flow relative humidity (Figure 43) or the humidity ratio (Figure 44) for the retentate airflow relative humidity above 40%.

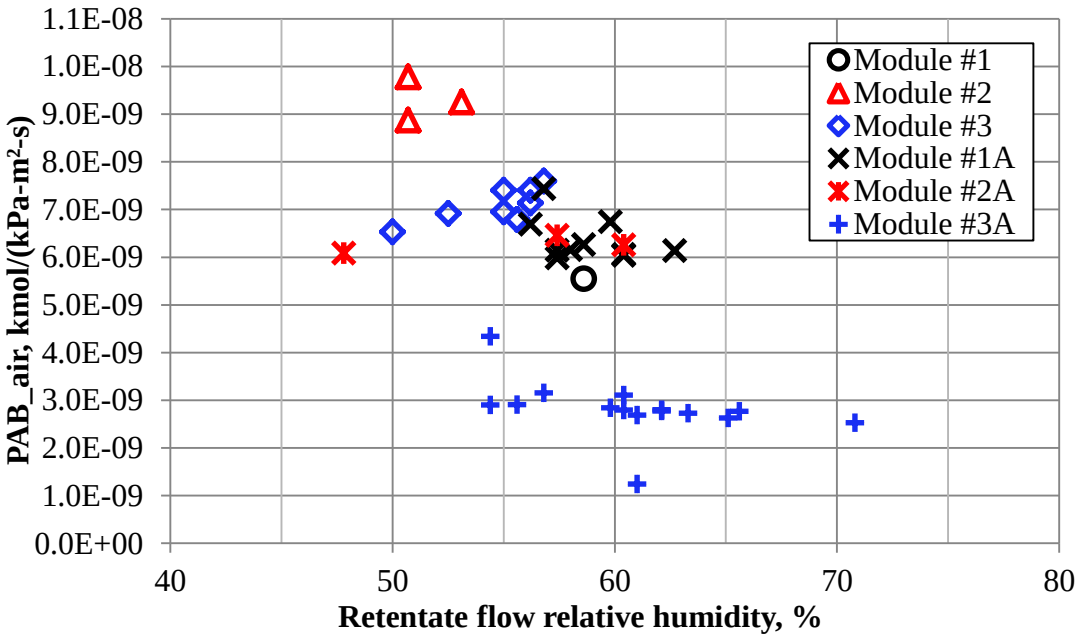

Figure 43. Effective air permeance as a function of retentate relative humidity

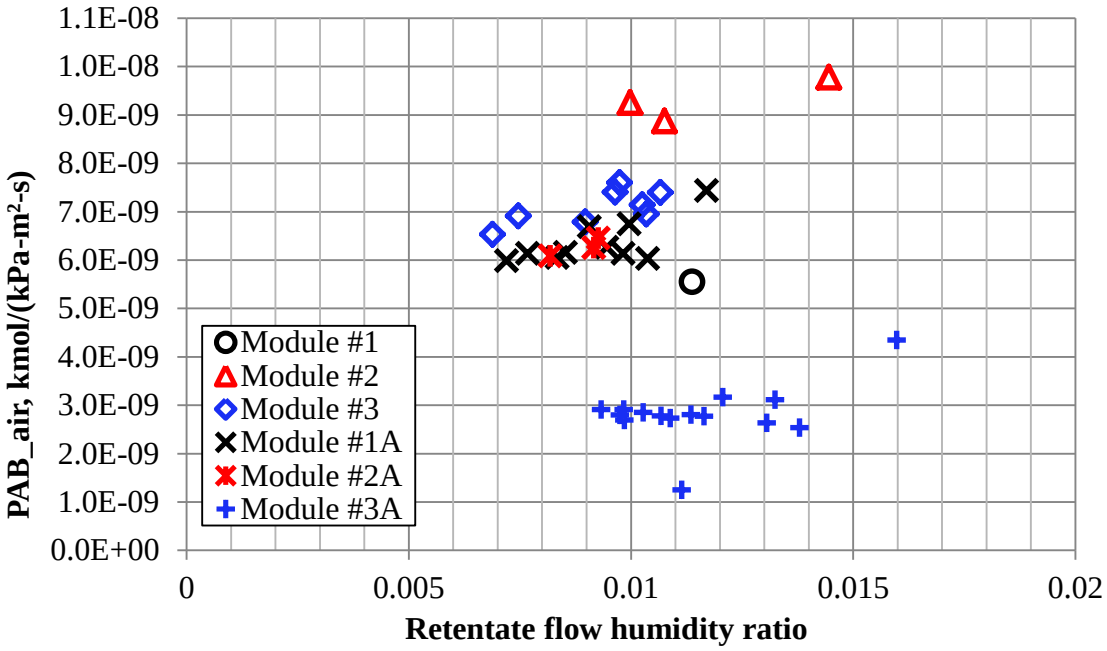

Figure 44. Effective air permeance as a function of retentate humidity ratio

Overall, all six membrane modules show similar performance. The lower effective air permeance of Module #3A improved the separation factor, to 1700 (Figure 45) and does not show temperature dependence.

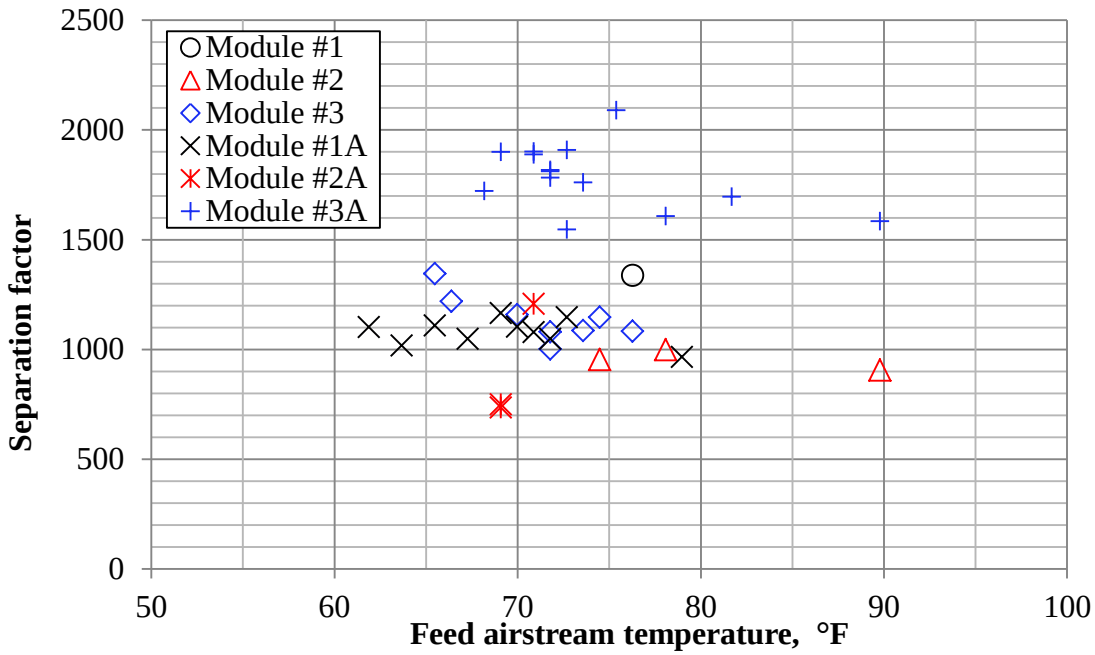

Figure 45. Separation factor as a function of airstream temperature

Experimental data demonstrate that for the feed airflow conditions close to saturation and retentate humidity above 50%, effective membrane water permeance decreases with an increase of retentate flow relative humidity and does not directly depend on feed airstream temperature. For dehumidification of a feed airflow between 100% RH and 50% RH, effective water permeance is 9E-6 kmol/(kPa-m²-s) (Figure 41). Effective air permeance is independent from retentate flow relative humidity above 50% and depends on the quality of the membrane surface.

4.4.4 Permeate total pressure and effective membrane permeance

A series of experiments was conducted with membrane Module #3A to investigate effective membrane permeance as a function of permeate pressure when feed airflow conditions stayed constant (Table 10).

Table 10. Membrane module #3A permeate total pressure effect

Parameter	Test S9	Test S10	Test S11	Test S12	Test S13
Feed air flow rate, cfm	30	30	30	30	30
Feed temperature, T1, °F	72.7	75.4	71.8	70.9	70.9
Feed relative humidity, RH1, %	89.3	89.8	90.8	90.8	91.8
Feed humidity ratio, ω1	0.015950	0.017600	0.015730	0.015240	0.014940
Retentate temperature, T2, °F	76.3	77.2	74.5	73.6	72.7
Retentate relative humidity, RH2, %	70.8	65.1	62.1	55.6	54.4
Retentate humidity ratio, ω2	0.013790	0.013050	0.011350	0.009834	0.009327
Permeate pressure, P3, kPa	1.820	1.440	1.100	0.763	0.634
Permeate temperature, T3, °C	26.1	26.3	25.7	25.6	25.4
Feed water flow, m_w1, kg/s-m²	255.0E-6	278.5E-6	252.0E-6	245.1E-6	240.9E-6
Permeate air flow, m_air3, kg/s-m²	5.2E-6	5.4E-6	5.8E-6	6.0E-6	6.0E-6
Permeate water flow, m_w3, kg/s-m²	34.6E-6	72.0E-6	70.2E-6	87.0E-6	90.6E-6
PAB_air, kmol/(kPa-m²-s)	2.5E-9	2.6E-9	2.8E-9	2.9E-9	2.9E-9
PAB_water, kmol/(kPa-m²-s)	3.9E-6	5.5E-6	5.1E-6	5.5E-6	5.5E-6
Separation factor	417	758	774	951	1010
Selectivity coefficient	1547	2089	1811	1901	1889
Effective COP	1.118	1.819	1.627	1.587	1.560

Experimental data show that a change in the absolute permeate pressure between absolute vacuum and pressure of 2 kPa result in an effective air permeance change of 20% (Figure 46), while the same change for effective water permeance corresponds to 40% (Figure 47). The change of absolute permeate pressure by 2 kPa has a much larger effect on the effective water permeance. The reason is because feed water partial pressure is below 2.5 kPa while feed air partial pressure is above 98 kPa. So the change of absolute permeate pressure has a smaller impact on effective partial pressure across the membrane for air in comparison with water vapor. The measurements uncertainty is 0.6E-9 kmol/(kPa-m²-s) for effective air permeance and 2.0E-6 kmol/(kPa-m²-s) for effective water permeance.

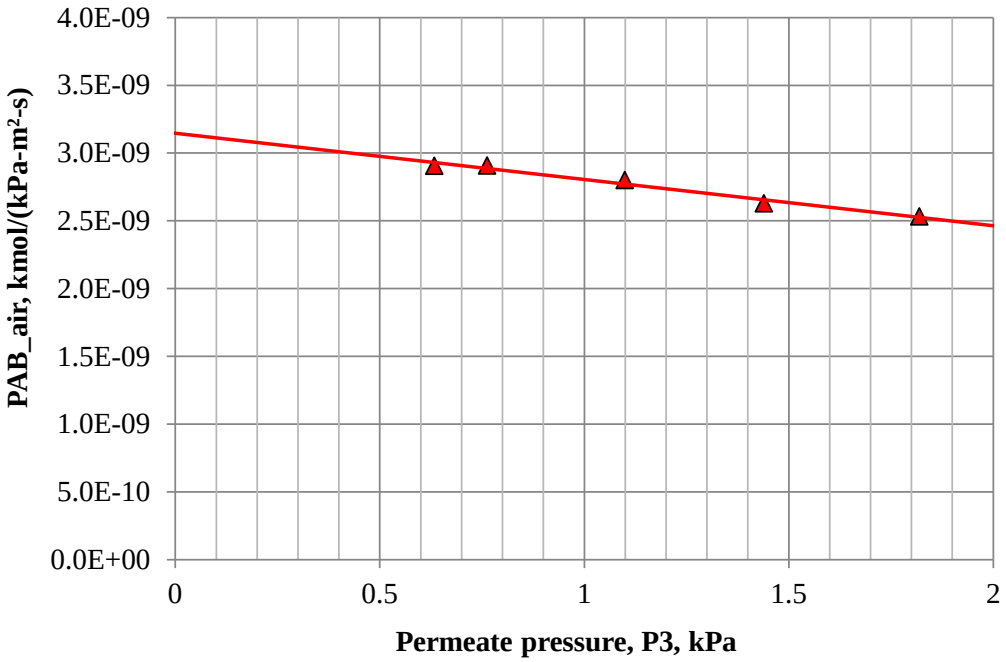

Figure 46. Effective air permeance as a function of total permeate pressure

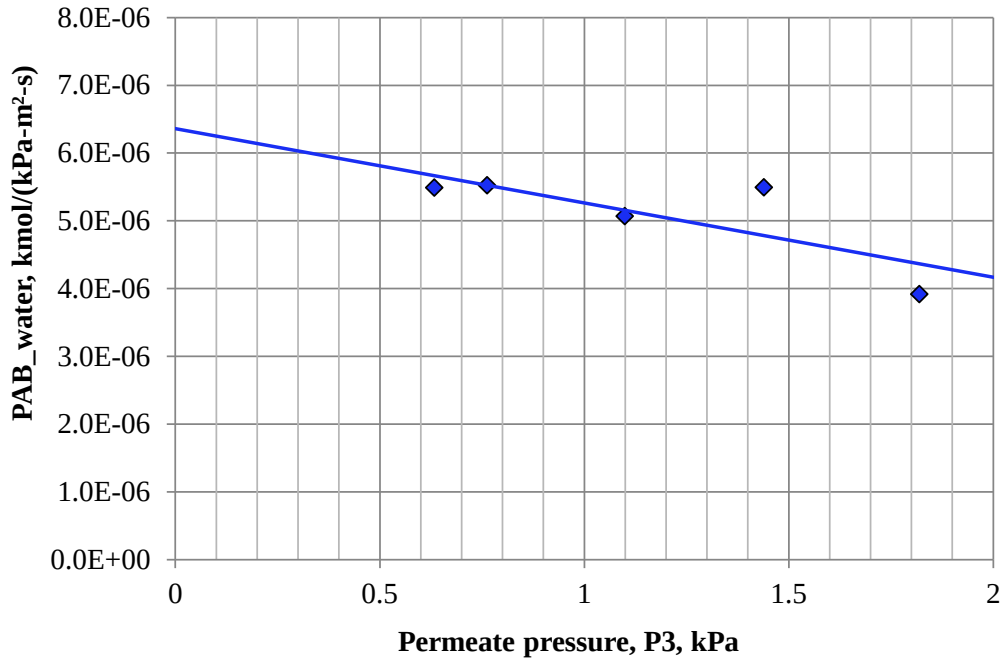

Figure 47. Effective water permeance as a function of total permeate pressure

The difference between the change of effective water and air permeance as a function of permeate pressure results in a relatively small decrease of the membrane selectivity coefficient by 12% (Figure 48).

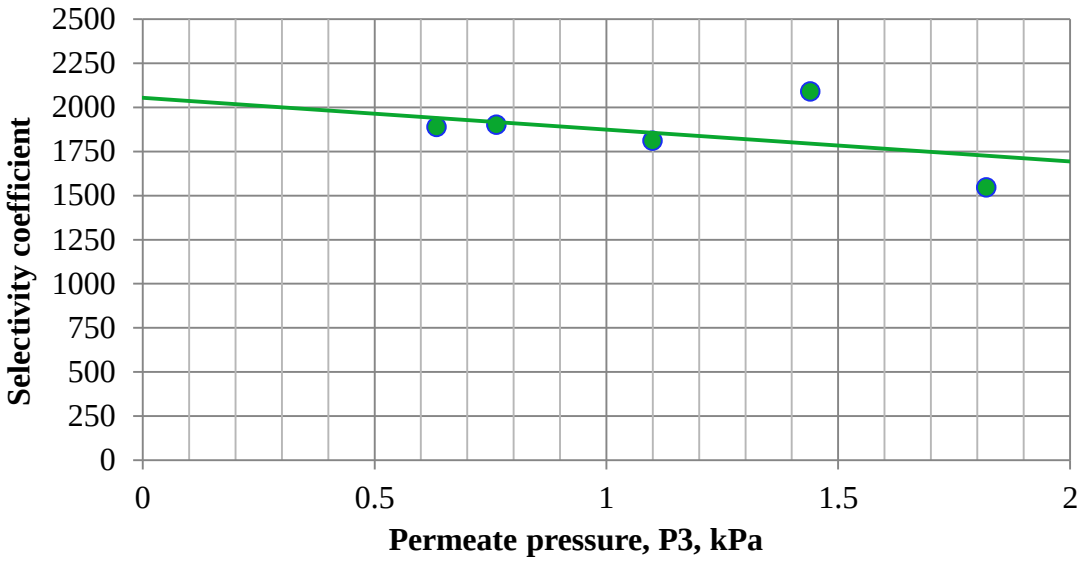

Figure 48. Selectivity coefficient as a function of permeate pressure

At the same time, the increase of absolute permeate pressure results in decrease of separation factor by 70% since much less water crosses the membrane due to the reduced pressure difference. This drastic change of separation factor with a change of permeate pressure shows the disadvantage of using the separation factor in membrane evaluation for air-conditioning systems.

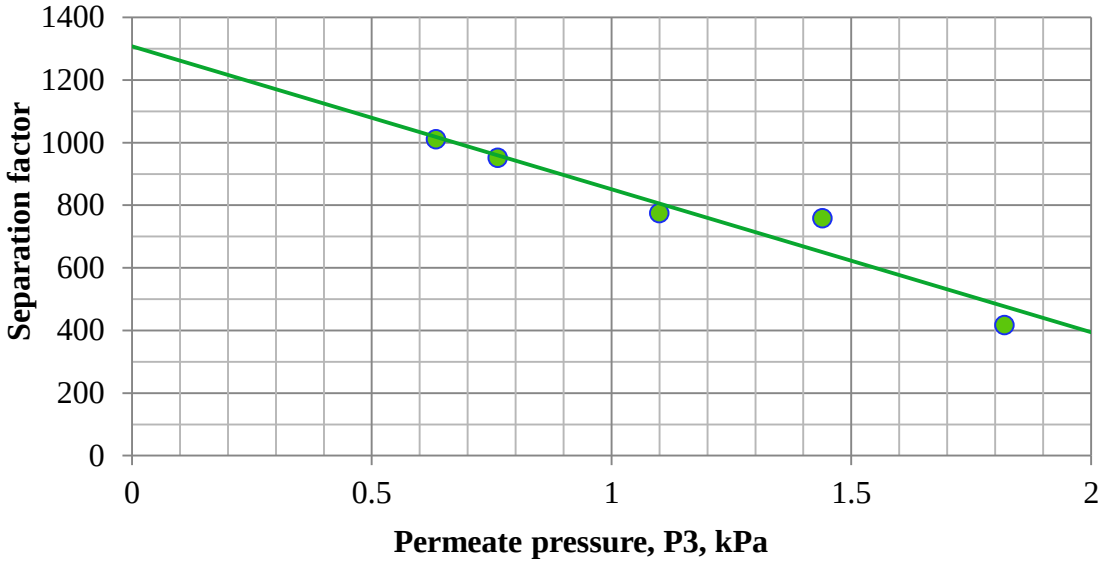

Figure 49. Separation factor as a function of permeate pressure

4.4.5 Effective membrane permeance summary

To summarize the results and conclusions described in the previous subsections, the complete experimental dataset was analyzed. Data came from experiments made at a feed airflow rate of 5-30 cfm, inlet air temperatures of 65-110°F, and feed airflow relative humidity levels of 22%-100%. Experiments were conducted with six experimental membrane modules. All of them had identical construction and the same type of zeolite non-organic membrane.

Analysis of data obtained shows that the effective water permeance does not depend on humidity when relative humidity is above 30%. Effective water permeance varies between 5E-6 and 15E-6 kmol/(kPa-m²-s) (Figure 50) for the membranes tested.

Effective water permeance increases with an increase of temperature (Figure 51). Effective water permeance dependence on temperature and permeate pressure can explain the wide data range of effective water permeance points at the same level of retentate air flow relative humidity shown in Figure 50.

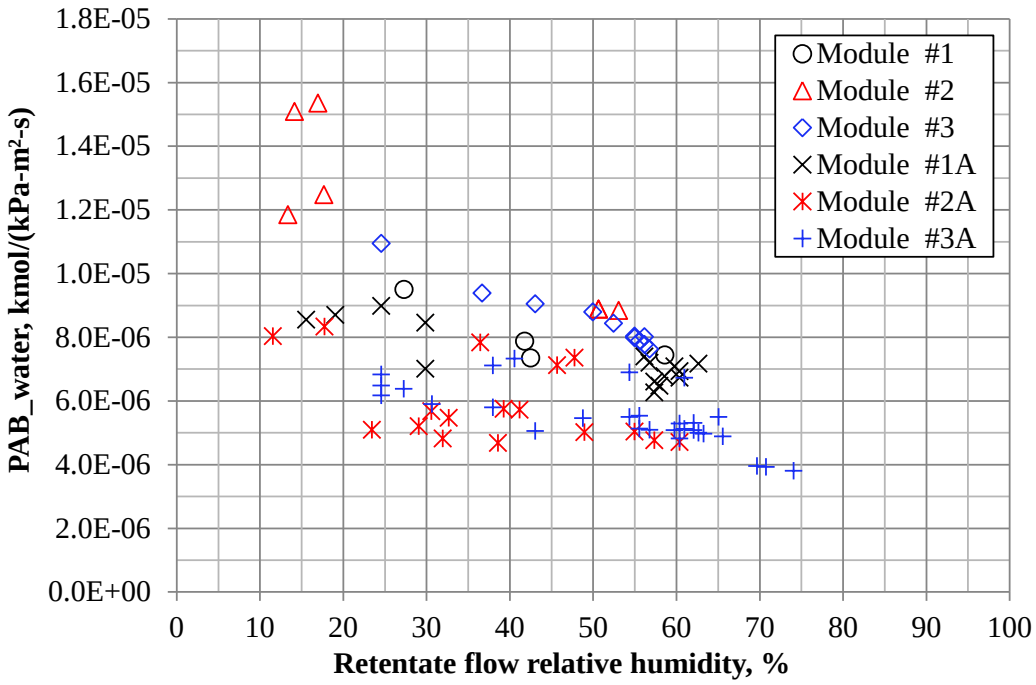

Figure 50. Effective water permeance at various feed flow conditions vs humidity

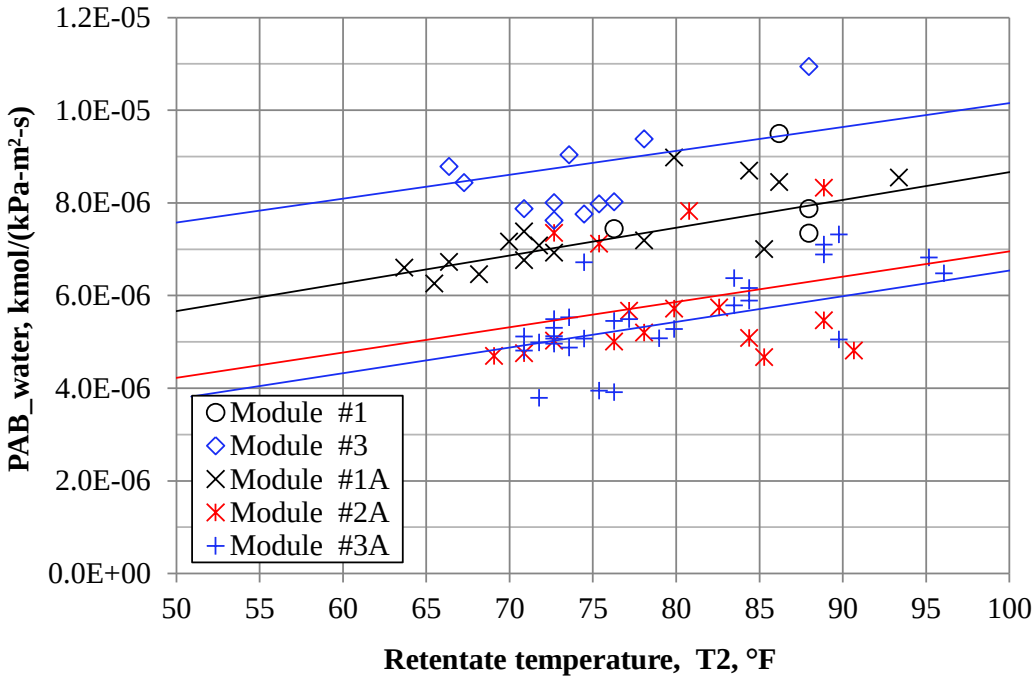

Figure 51. Effective water permeance at various feed flow conditions vs temperature

The effective air permeance has an exponential dependence on a retentate flow relative humidity below 30% and is relatively constant above 30% (Figure 52).

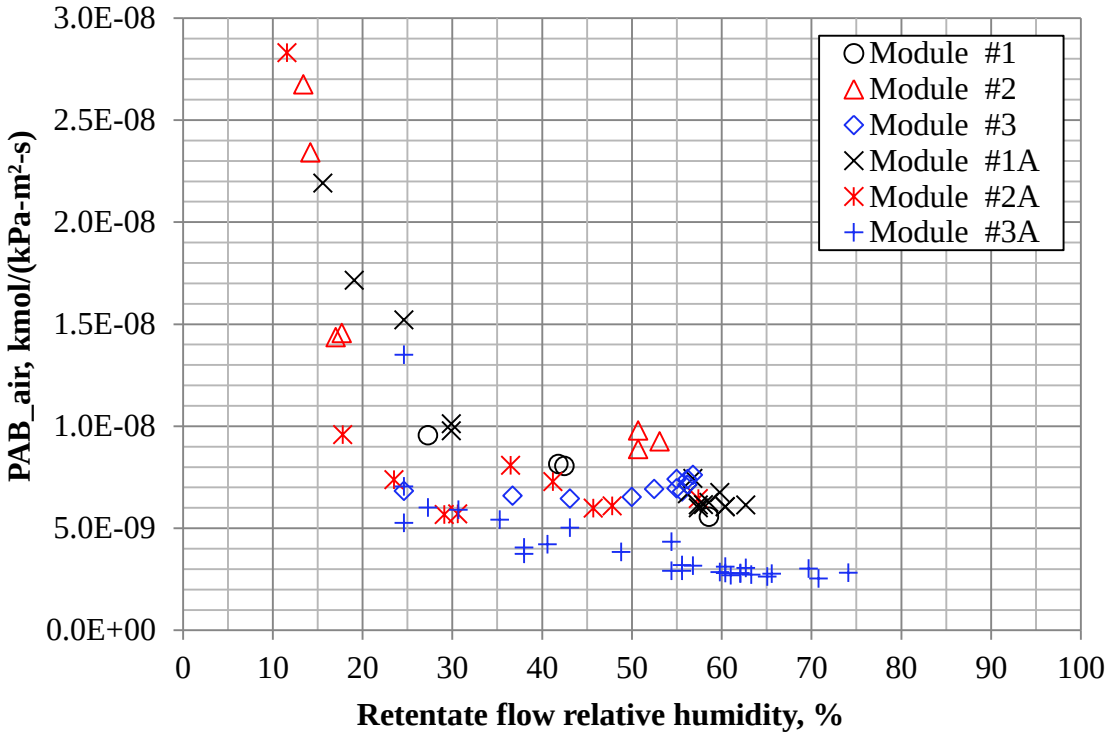

Figure 52. Combined results of effective air permeance at various flow conditions

These two dependences on effective air and water permeance on retentate flow relative humidity provide an average membrane separation factor of 600 (Figure 53) and selectivity coefficient of 1500 (Figure 54) at a retentate flow relative humidity of 50% for the samples tested.

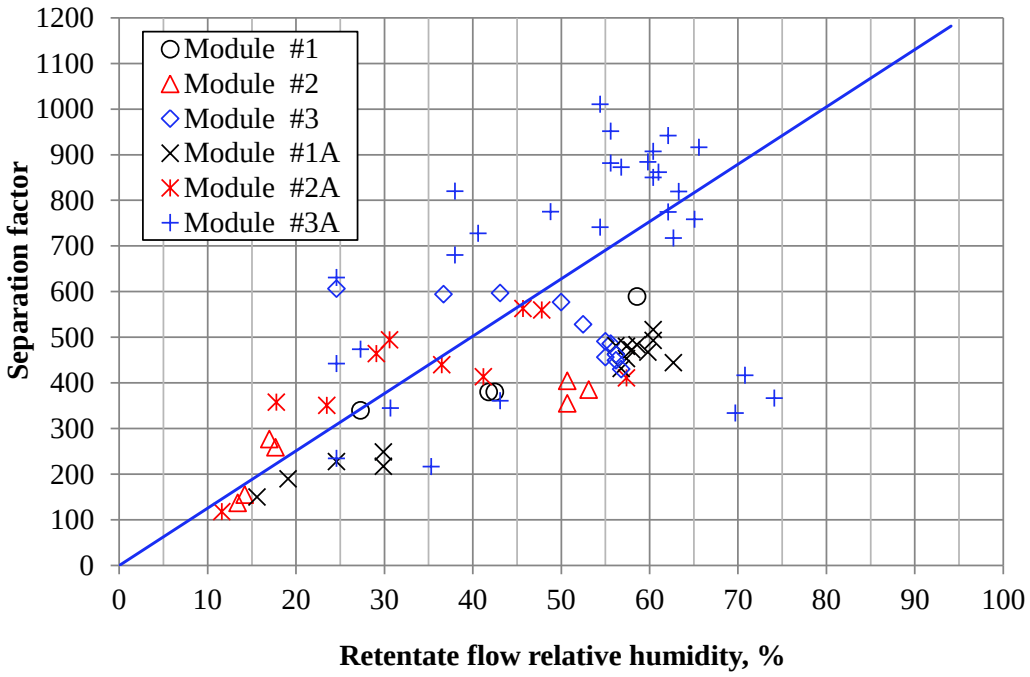

Figure 53. Combined results of the separation factor at various feed flow conditions

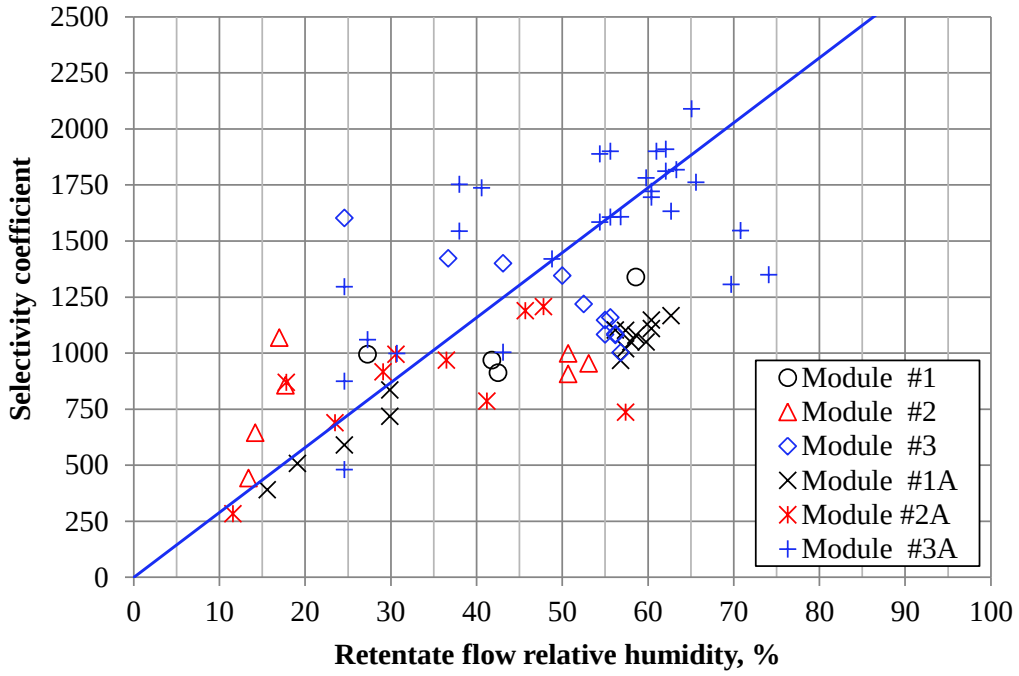

Figure 54. Combined results of selectivity coefficient at various feed flow conditions

Combined experimental results show that it is possible to achieve at least an effective air permeance of 3E-9 kmol/(kPa-m²-s) and effective water permeance of 9E-6 kmol/(kPa-m²-s) for retentate airflow relative humidity above 40%.

Additional experimental results are described in Appendix B-F.

4.5 Single stage system experimental performance at the design conditions

The membrane dehumidification system operation was tested with the different membrane modules. Experimental tests had two major goals: to obtain the required airflow dehumidification level, and reach a separation factor level above 200 at the design conditions.

During the test, a steady state (temperature, humidity) and steady flow of feed airflow were obtained during a two hour initial interval with a vacuum system kept off at a pressure level of 101 kPa. After the supply airflow properties were at the required steady state conditions, the vacuum system was enabled and operated for 30 minutes to obtain steady state operation in the vacuum system. After the steady state conditions in the vacuum system were obtained, parameters were monitored for 20 minutes and a data point was recorded.

Numerous experiments were conducted under the system design conditions. System performance at the design condition can be illustrated using two experimental tests. Experiment Test #10 was conducted at the airflow rate of 4 cfm; the inlet temperature and humidity ratio were both higher than the design values and both the outlet humidity ratio and temperature were slightly lower than the design values (Figure 55). The other experiment (Test #AB-1) was conducted at a higher airflow rate of 9 cfm. The airflow cooling and dehumidification load under these conditions exceeded the capacity of both the sensible and latent cooling systems. As a result outlet relative humidity was 10% above the design value and the temperature was 3°F above the design value (Figure 56) than the design conditions. Nevertheless, this change had a positive effect on the membrane selectivity coefficient by increasing it from 61 to 1038.

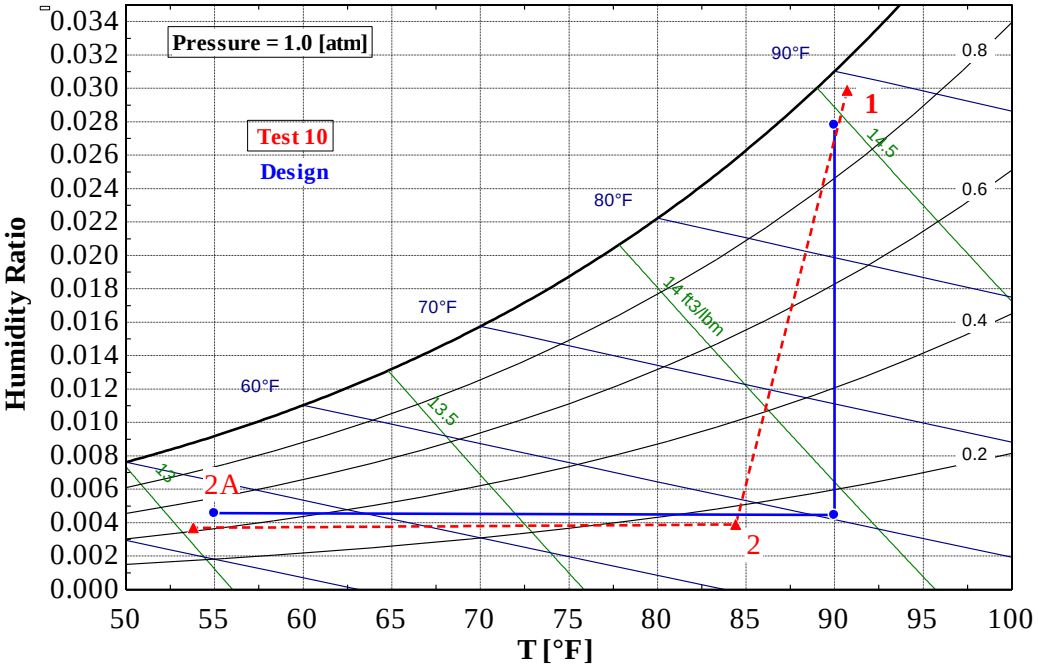

Figure 55. Dehumidification system operations at 4 cfm (113 lpm) (Test 10)

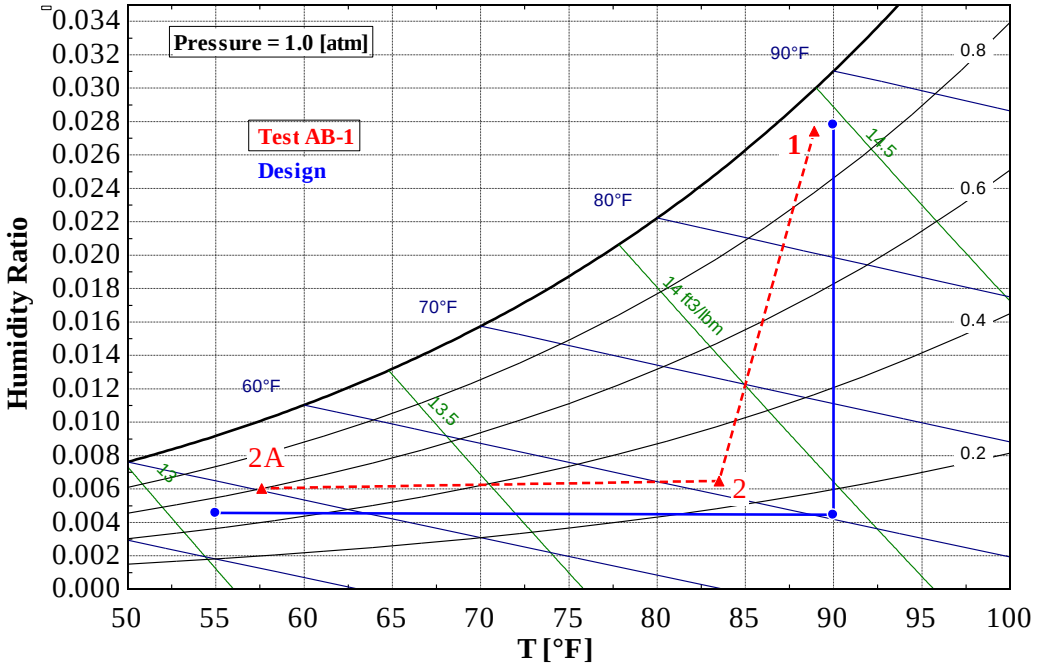

Figure 56. Dehumidification system operations at 9 cfm (255 lpm) (Test AB-1)

Both experiments had effective water permeance lower than the assumptions used in the design. The effective air permeance of Test AB-1 was also lower than value used in the design assumptions. The effective coefficient of performance of the actual experimental system was also lower than the design value of 3.68 (Table 11).

Table 11. Single stage system performance at the design conditions

Test #	Design 4 cfm	10	AB-1
Module #	0	2	3A
Feed airflow rate, cfm	4	4	9
Feed airflow temperature, T1, °F	90.0	90.7	88.9
Feed airflow relative humidity, RH1, %	90.0	94.3	91.9
Feed airflow humidity ratio, ω1	0.027812	0.029960	0.026920
Retentate airflow temperature, T2, °F	90.0	84.4	83.5
Retentate airflow relative humidity, RH2, %	15.4	15.6	26.6
Retentate airflow humidity ratio, ω2	0.004589	0.003897	0.006482
Supply airflow temperature, T2A, °F	55.0	53.8	57.6
Supply airflow relative humidity, RH2A, %	50.0	42.2	60.1
Supply airflow humidity ratio, ω2A	0.004589	0.003691	0.006052
Permeate flow pressure, P3, kPa	0.888	1.200	0.694
Permeate flow temperature, T3,°C	32.2	26.5	25.5
Permeate mass flow of air, m_air3, kg/s-m²	15.4E-6	116.1E-6	9.8E-6
Permeate mass flow of water, m_w3, kg/s-m²	47.7E-6	52.0E-6	92.6E-6
PAB_air, kmol/(kPa-m²-s)	7.5E-9	57.0E-9	4.8E-9
PAB_water, kmol/(kPa-m²-s)	8.0E-6	3.5E-6	5.0E-6
Separation factor	112.2	15	350
Feed mass flow of water, m_w1, kg/s-m²	57.1E-6	59.3E-6	121.9E-6
Percent water removed	83.5%	88%	76%
Selectivity coefficient	1067	61	1038
Cooling provided, kW	0.124	0.1457	0.254
COP ideal	4.595	1.635	3.491
COP effective	3.676	0.892	1.904
COP actual	NA	0.1	0.1

The reduction of the system energy efficiency below the design value was a result of effective air permeance dependence from retentate airflow relative humidity (membrane crystals swelling expansion). In the experimental Test 10 retentate airflow relative humidity was below 16% that increased effective air permeance to 57E-9 kmol/(kPa-m²-s) and caused an increase of the permeate pressure to 1.2 kPa. This

change reduced effective COP of the system to 0.9. To provide low permeate pressure condenser pressure was also lower than the optimum.

The energy efficiency was improved in Test AB-1, where the retentate humidity ratio was above 26%. Higher relative humidity decreased effective air permeance and as a result permeate flow pressure increased to 0.69 kPa, and effective water permeance increased from 3.5E-6 kmol/(kPa-m²-s) to 5.0E-6 kmol/(kPa-m²-s). This change provided an increase of the separation factor from 15 to 350. Effective COP also increased to 1.9.

4.6 Dual stages system experimental performance at the design conditions

The single stage membrane dehumidification system was modified to increase dehumidification capacity of the system. The modified system includes two membrane modules connected in a series relative to the feed airflow. The vacuum side of the system was modified, so each membrane module was equipped with a dedicated intermediate compressor. Vacuum flow from both intermediate compressors was rejected to the same condenser as in the single stage system.

Experiments were conducted with Module #3A, which was used in the first dehumidification stage and Module #1A in the second stage. Temperature and relative humidity of feed and retentate flow for each module were measured simultaneously (Figure 57).

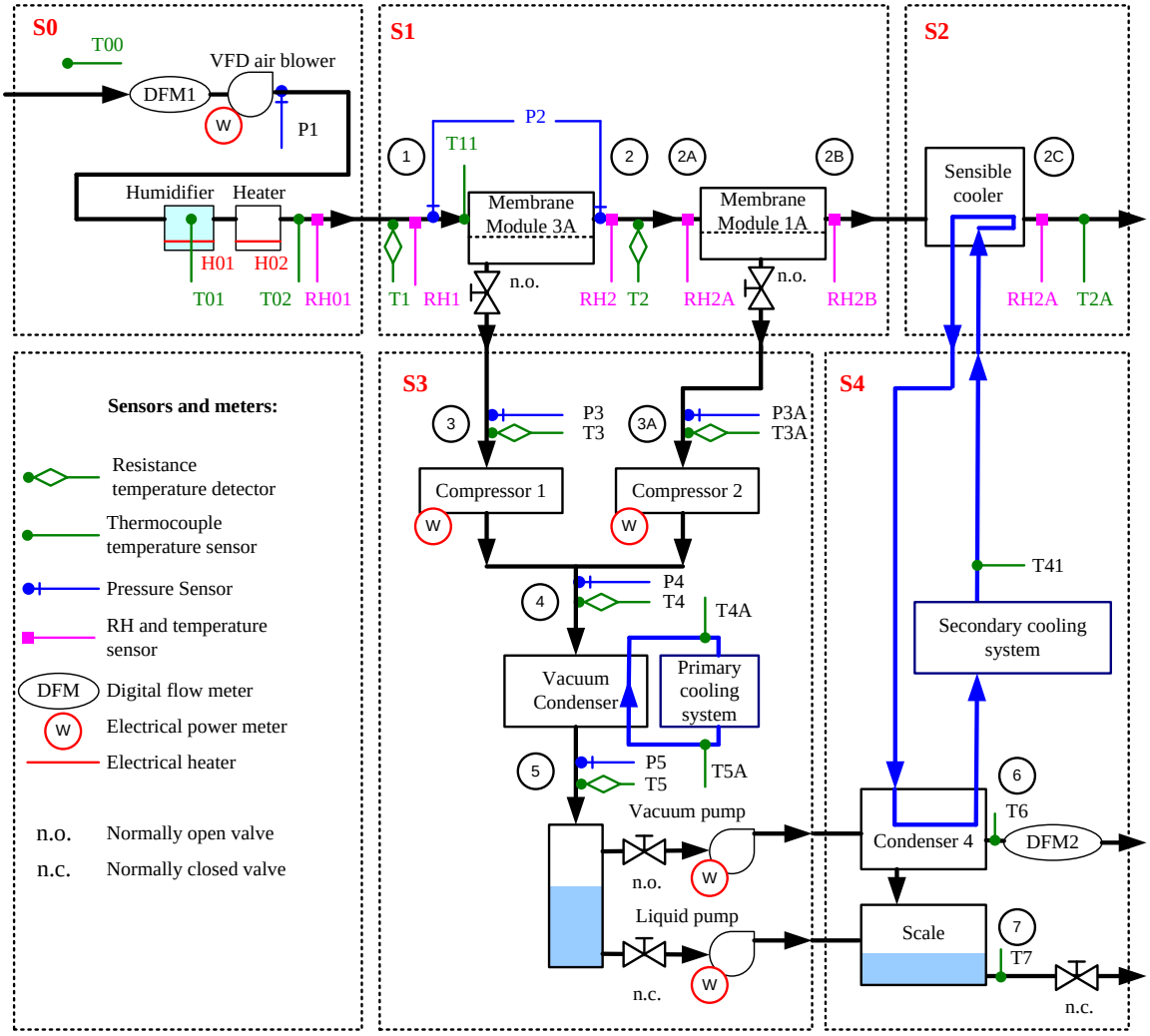

Figure 57. Dual stage system experimental configuration

Multiple experiments were conducted. The main results can be illustrated based on two experiments. The first experiment (Test 2M-7) was conducted with a feed airflow rate of 30 cfm (51 m³/h) at the design feed conditions of 90°F and relative humidity of 90% (Figure 58).

The second experiment (Test 2M-8) was conducted with the reduced airflow rate of 13 cfm. The combined dehumidification capacity of two membrane modules was sufficient to dehumidify feed airflow to the design outlet humidity ratio, and sensible cooling system capacity was sufficient for airflow cooling below the design setpoint at 12.8°C (55°F) (Figure 59).

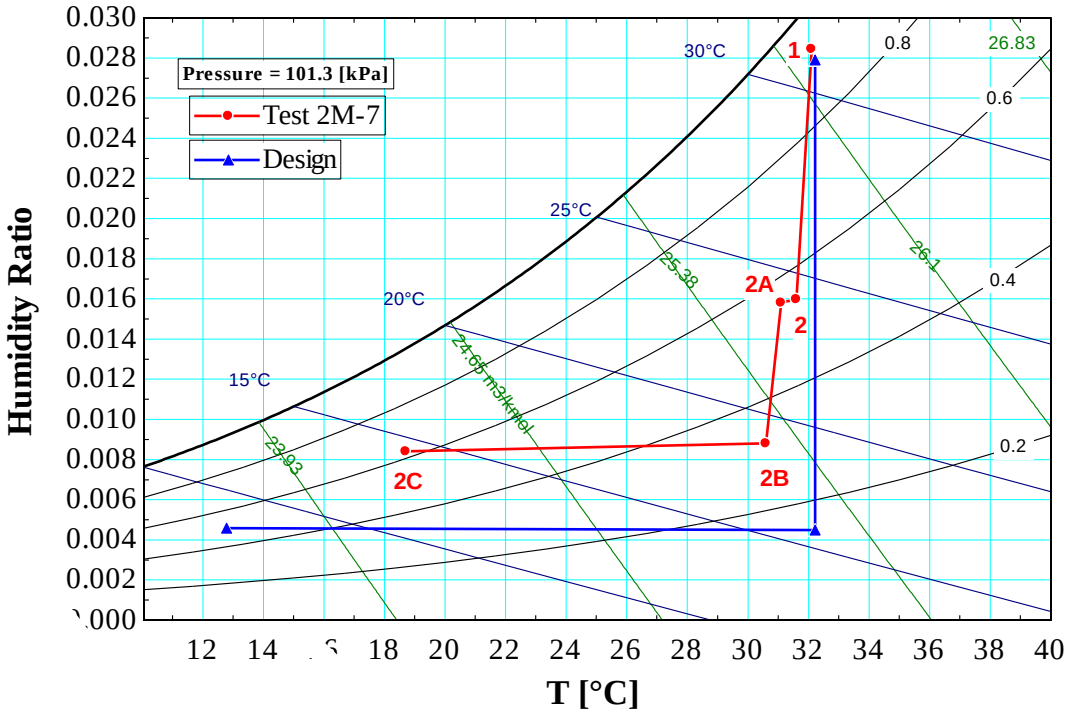

Figure 58. Two stage dehumidification system operations at 30 cfm (Test 2M-7)

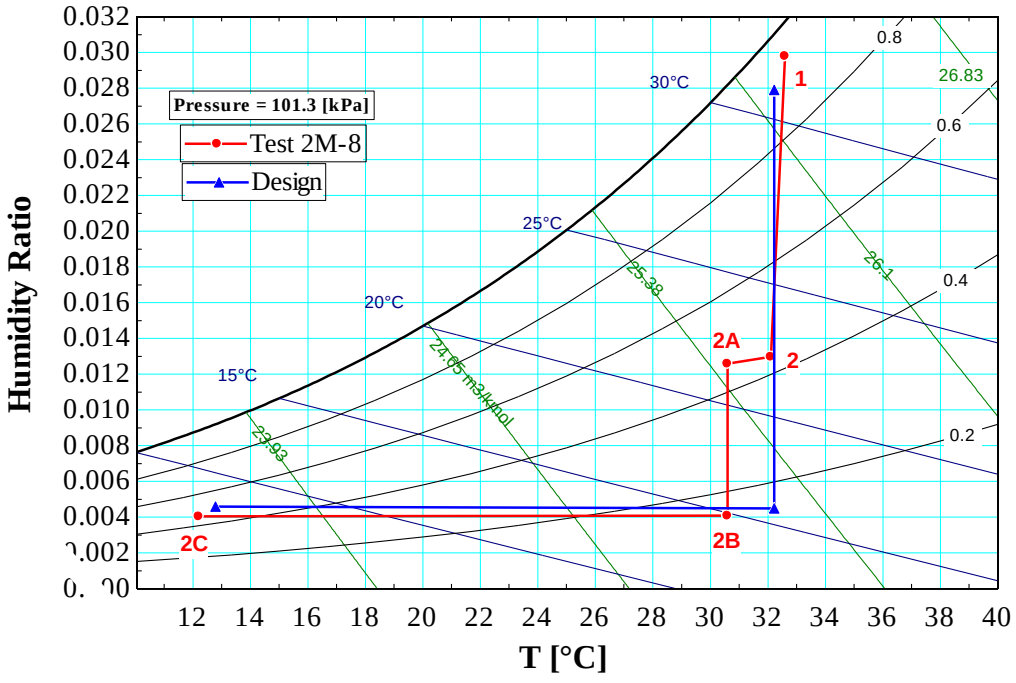

Figure 59. Two stage dehumidification system operations at 13 cfm (Test 2M-8)

The estimated dual stage system separation factor showed similar dependence on relative humidity and temperature as in the single stage system experiments. In both described experiments, the permeate pressure of the first stage membrane module was higher than that of the second stage (Table 12). This effect is described in more details in Section 5.4.

Table 12. Dual stage membrane dehumidification system performance

Test #	2M-7	2M-8
Module #	3A-1A	3A-1A
Feed airflow rate, cfm	30	13
Stage 1 Feed airflow temperature, T1, °F	90	91
Stage 1 Feed airflow relative humidity, RH1, %	92	94
Stage 1Feed airflow humidity ratio, ω1	0.028440	0.029800
Stage 1 Retentate airflow temperature, T2, °F	89	90
Stage 1 Retentate airflow relative humidity, RH2, %	54	43
Stage 1 Retentate airflow humidity ratio, ω2	0.015980	0.012970
Stage 2 Feed airflow temperature, T2A, °F	88	87
Stage 2 Feed airflow relative humidity, RH2A, %	55	46
Stage 2Feed airflow humidity ratio, ω2A	0.015820	0.012590
Stage 2 Retentate airflow temperature, T2B, °F	87	87
Stage 2 Retentate airflow relative humidity, RH2B, %	32	15
Stage 2 Retentate airflow humidity ratio, ω2B	0.008810	0.004086
Permeate mass flow of air, m_air3, kg/s-m²	26.5E-6	117.4E-6
Permeate mass flow of water, m_w3, kg/s-m²	293.3E-6	168.4E-6
Separation factor	389	48
System feed mass flow of water, m_w1, kg/s-m²	424.6E-6	194.6E-6
Dehumidification provided, kW	0.809	0.464
COP ideal	7.971	3.745
COP effective	2.934	1.628
COP actual	0.328	0.180

The first dehumidification stage in both experiments had an exit relative humidity above 30%. That provided a membrane separation factor above 360 and a selectivity coefficient above 1000 (Table 13).

Table 13. First dehumidification stage membrane module properties (Module#3A)

Test #	2M-7	2M-8
Stage 1 Retentate airflow temperature, T2, °C	31.6	32.1
Stage 1 Retentate airflow relative humidity, RH2, %	54.4	43.1
Stage 1 Retentate airflow humidity ratio, ω2	0.015980	0.012970
Permeate flow pressure, P3, kPa	1.286	1.426
Permeate mass flow of air, m_air3, kg/s-m²	8.8E-6	10.2E-6
Permeate mass flow of water, m_w3, kg/s-m²	186.1E-6	110.0E-6
PAB_air, kmol/(kPa-m²-s)	4.3E-9	5.0E-9
PAB_water, kmol/(kPa-m²-s)	6.9E-6	5.0E-6
Separation factor	741	361
Selectivity coefficient	1584	1003

Operation of the second dehumidification stage was at a lower exit relative humidity in comparison to the first stage. The lower exit relative humidity increased the second stage effective air permeance and reduced the separation factor to 44 for Experiment 2M-8 (Table 14).

Table 14. Second dehumidification stage membrane module properties (Module#1A)

Test #	2M-7	2M-8
Stage 2 Retentate airflow temperature, T2B, °C	30.6	30.6
Stage 2 Retentate airflow relative humidity, RH2B, %	32.1	15.0
Stage 2 Retentate airflow humidity ratio, ω2B	0.008810	0.004086
Permeate flow pressure, P3A, kPa	0.839	0.830
Permeate mass flow of air, m_air3, kg/s-m²	17.7E-6	107.1E-6
Permeate mass flow of water, m_w3, kg/s-m²	109.3E-6	59.4E-6
PAB_air, kmol/(kPa-m²-s)	8.6E-9	51.9E-9
PAB_water, kmol/(kPa-m²-s)	13.1E-6	15.8E-6
Separation factor	391	44
Selectivity coefficient	1533	305

An overall separation factor of 48 was obtained for the design inlet and outlet conditions in the dual stage membrane dehumidification system in Experiment 2M-8. This value is better than the single stage system with a separation factor of 15 obtained in Experiment 10. Further investigation of the dual stage system energy efficiency operation advantages is presented in Section 5.4.

4.7 Uncertainty of single stage dehumidification system experimental results

Uncertainty propagation analysis for results of the single stage experimental system was conducted based on the actual uncertainty of the measurement equipment. The analysis was conducted according to the method described in National Institute of Standards and Technology (NIST) Technical Note 1297 [84] for the system design conditions and selected experimental tests.

With the assumption that the individual measurements are uncorrelated and random, the uncertainty in the calculated quantity can be estimated:

$$U_Y = \sqrt{\sum_i \left(\frac{\partial Y}{\partial X_i}\right)^2 U_{X_i}^2} \tag{77}$$

where: U_Y - uncertainty of the estimated variable;

U_X - uncertainty of the measured variable.

Measured variables of the experimental system include temperature, pressure, humidity, and airflow rate (Table 15).

Table 15. Value and uncertainty of the measured variables at the dehumidification system design conditions

Measured variable	Design value	Uncertainty	Full scale
Nozzle system feed airflow pressure drop, in w.g.	0.6455	±1% FS	3
Membrane module feed airflow pressure drop, in w.g.	2.5	±2% FS	5
Feed airflow temperature, T01, °C	32.2	±1°C	
Feed airflow relative humidity, RH01, %	90	±5% RH	
Feed airflow temperature, T1, °C	32.2	±1°C	
Feed airflow relative humidity, RH1, %	90	±5% RH	
Retentate airflow temperature, T2, °C	32.2	±1°C	
Retentate airflow relative humidity, RH2, %	15.4	±5% RH	
Permeate flow pressure, P3, kPa	0.97	±0.5% FS	2
Permeate flow temperature, T3,°C	32.2	±0.15°C	
Condenser inlet pressure, P4, kPa	6.50	±0.5% FS	14
Condenser inlet temperature, T4, kPa	32.2	±0.15°C	
Condenser outlet pressure, P5, kPa	6.50	±0.5% FS	14
Condenser outlet temperature, T5, kPa	30.8	±0.15°C	
Permeate volumetric airflow rate, lpm	0.672	±3% FS	2
Permeate airflow temperature, T6,°C	18	±1°C	

All uncertainty propagation analysis calculations were done in Engineering Equation Solver. Results show that the membrane effective water permeance has the highest uncertainty and as a result the selectivity coefficient also has a high uncertainty (Table 16).

Detailed analysis of the effective water permeance uncertainty propagation shows that more than 99% of the uncertainty comes from the uncertainty in the retentate airflow relative humidity measurement. The retentate airflow relative humidity measurement was made with a capacitive polymer humidity sensor with sensor accuracy of ±5% RH. The combination of ± 5% RH sensor accuracy and design relative humidity of 15.4% RH results in 54% relative uncertainty in the effective water permeance.

Table 16. Uncertainty of the estimated variables at the system design conditions

Measured variable	Estimated value	±Uncertainty	Relative Uncertainty
Permeate mass flow of air, m_air3, kg/s-m²	13.1E-6	1.2E-6	9%
Permeate mass flow of water, m_w3, kg/s-m²	185.6E-6	18.5E-6	10%
PAB_air, kmol/(kPa-m²-s)	6.4E-9	569.3E-12	9%
PAB_water, kmol/(kPa-m²-s)	11.5E-6	6.2E-6	54%
Separation factor	510	58	11%
Feed mass flow of water, m_w1, kg/s-m²	222.2E-6	14.1E-6	6%
Selectivity coefficient	1814	984	54%
Effective COP	3.936	0.1591	4%
Dehumidification provided, kW	0.4963	0.05237	11%
Feed airflow humidity ratio, ω01	0.027870	0.002307	8%
Feed airflow humidity ratio, ω1	0.027870	0.001815	7%
Retentate airflow humidity ratio, ω2	0.004598	0.001510	33%

The same analysis was repeated for the actual data from Test AB-1 (Table 17). The measured retentate airflow relative humidity in this case was 26.6%, which reduced relative uncertainty to 19%. As a result, effective water permeance relative uncertainty also decreased to 25% and selectivity coefficient relative uncertainty to 28% in comparison to 54% at the system design conditions.

Table 17. Uncertainty of variables for experimental Test AB-1 with Module#3A

Variable	Value	±Uncertainty	Relative Uncertainty
Feed airflow rate, cfm	9	0.691	8%
Feed airflow temperature, T1, °F	88.9	0.9	1%
Feed airflow relative humidity, RH1, %	91.9	5	5%
Retentate airflow temperature, T2, °F	83.5	0.9	1%
Retentate airflow relative humidity, RH2, %	26.6	5	19%
Supply airflow temperature, T2A, °F	57.6	0.9	2%
Supply airflow relative humidity, RH2A, %	60.1	5	8%
Permeate flow pressure, P3, kPa	0.694	0.1	14%
Permeate flow temperature, T3,°C	25.5	0.27	1%
Permeate mass flow of air, m_air3, kg/s-m²	9.6E-6	1.2E-6	12%
Permeate mass flow of water, m_w3, kg/s-m²	88.3E-6	11.0E-6	12%
PAB_air, kmol/(kPa-m²-s)	4.7E-9	576.4E-12	12%
PAB_water, kmol/(kPa-m²-s)	4.7E-6	1.2E-6	25%
Separation factor	340	54	16%
Feed mass flow of water, m_w1, kg/s-m²	116.3E-6	11.3E-6	10%
Selectivity coefficient	1009	284	28%
Effective COP	2.120	0.5612	26%
Dehumidification provided, kW	0.2423	0.03123	13%
System inlet airflow humidity ratio, ω01	0.027490	0.002256	8%
Feed airflow humidity ratio, ω1	0.026920	0.001614	6%
Retentate airflow humidity ratio, ω2	0.006482	0.001246	19%

4.8 Dehumidification system application in a large office building DOAS

Application of the membrane dehumidification system for outside air stream dehumidification in Dedicated Outdoor Air System (DOAS) can reduce HVAC system energy consumption and maintain the building humidity level within the comfort level as required by the ASHRAE Standard 62.1-2013 [85]. To estimate potential energy savings two baseline models were developed. The first model includes an office building HVAC system operating in an ideal situation with outside air ventilation flow rate set at the minimum required level and the minimum supply airflow rate set to the minimum required ventilation flow rate. The second model includes a more typical case where the outside airflow rate is more than twice the minimum requirements, and the minimum supply airflow rate is set to 40% of the maximum supply airflow.

Baseline Model 1 was developed as an idealized case with the assumption that the HVAC system operates at the minimum required OA flow rate all the time. Another assumption is that the minimum supply airflow rate is equal to the minimum required

OA flow rate during the occupied time. Building modeling parameters were developed based on an existing office building (Wisenbaker Engineering Research Center (1983) located on Texas A&M campus in College Station, TX). The net area of the simulated building is 174,016 ft² with four floors. Simulation was made using WinAM v4.3.37 developed by the Texas A&M Engineering Experiment Station. The simulated HVAC system is a Single Duct VAV System with reheat (Figure 60).

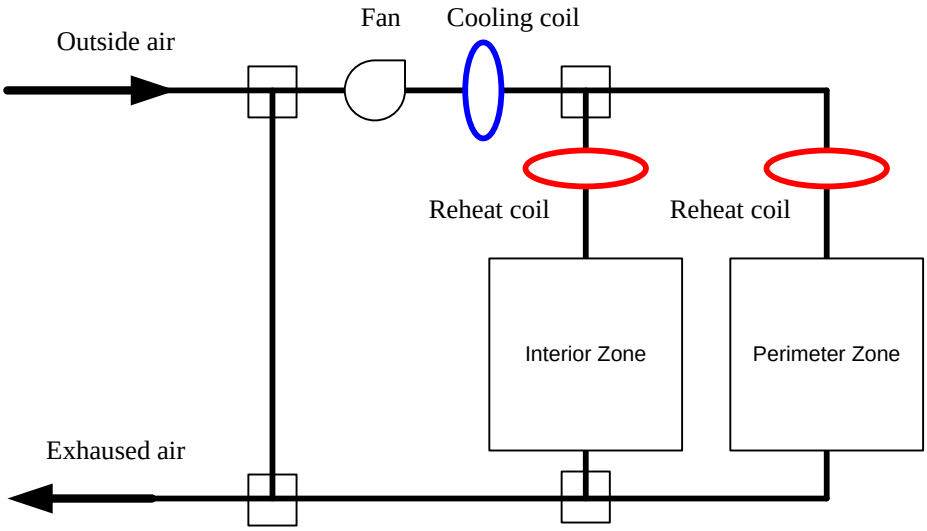

Figure 60. Configuration of Single Duct VAV System with reheat

The operation schedule of the HVAC system is 24/7 during the whole year. The simulation used actual local weather data for College Station, Texas (12/11/2012 to 12/10/2013) was used. The climate of College Station, Texas has outside weather conditions within the ASHRAE 55-2004 predicted mean vote comfort zone for 7.3% of the time. A direct evaporative cooling system can increase comfort an additional 0.8% of the time and natural ventilation for 0.7% so operation of a mechanical HVAC system is required over 90% of the time.

The main design parameters of the baseline model are summarized in Table 18.

Table 18. Model 1 baseline case main parameters

Name	Units	Value
Conditioned floor area	ft²	174,016
Interior zone percentage	%	70
Exterior surface (wall and window) area	ft²	36,158
Window percentage	%	0.39
Roof area	ft²	57,600
Exterior walls conductivity	Btu/ft²-h-°F	0.105
Exterior window conductivity	Btu/ft²-h-°F	1.142
Exterior roof conductivity	Btu/ft²-h-°F	0.194
Weekday occupancy time	h	7:00-18:00
Saturday occupancy time	h	10:00-16:00
Sunday occupancy time	h	None
Primary min occupied airflow	cfm/ft²	0.085
Primary min unoccupied airflow	cfm/ft²	0
Primary max Airflow	cfm/ft²	0.73
Space temperature setpoint	°F	72
Minimum occupied outside airflow	cfm/ft²	0.085
Minimum unoccupied outside airflow	cfm/ft²	0
Outside air control method		No economizer or ERV/HRV
Cooling coil temperature setpoint	°F	55
Peak lighting loads	W/ft²	1.2
Peak plug loads	W/ft²	0.8
Occupancy	ft²/person	200
Sensible heat load per person	Btu/h	250
Latent heat load per person	Btu/h	200
Supply Air Fan power	hp/1000cfm	0.752
Supply Air Fan type		Variable Frequency Drive
Peak electric weekdays load ratio		1
Nighttime Lighting and Plug load ratio		0.6
Electric load Ramp up weekdays start time		6:00
Electric load Ramp down weekdays end time		19:00
Electric load Weekdays Ramp up hours	h	2
Electric load Weekdays Ramp down hours	h	2
Peak electric weekend load ratio		0.6

In this simulation, building occupancy was assumed to be 200 ft²/person. According to the ASHRAE Standard 62.1-2013 [85], the amount of required outside air can be calculated as follows:

Breathing zone Outdoor Airflow:

$$V_{bz} = R_p \cdot P_z + R_a \cdot A_z; \tag{78}$$

where:

R_p – required outdoor airflow rate per person;

P_z – zone population, the number of people in the ventilation zone during typical usage;

R_a – outdoor airflow rate required per unit area;

A_z – zone floor area, the net occupiable floor area of the ventilation zone, ft²;

For office space in the office building: $R_p = 5\frac{\text{cfm}}{\text{person}}$, $R_a = 0.06\frac{\text{cfm}}{\text{ft}^2}$.

$$V_{bz} = 5\frac{cfm}{person} \cdot 870person + 0.06\frac{cfm}{ft^2} \cdot 174{,}016\text{ft}^2 = 14{,}791cfm \tag{79}$$

Zone outdoor airflow can be obtained:

$$V_{oz} = V_{bz}/E_z \tag{80}$$

where:

E_z – zone air distribution effectiveness, for celling supply of cool air $E_z = 1.0$.

$$V_{oz} = \frac{14{,}791cfm}{1} = 14{,}791cfm \tag{81}$$

Required outdoor airflow per unit area:

$$v_{oz} = \frac{14791\text{cfm}}{174{,}016\text{ft}^2} = 0.085\text{cfm/ft}^2 \tag{82}$$

Building lighting and plug maximum electric loads for the simulation are based on the actual measured data. The electrical diversity profile used in the simulation is based on the Research Project 1093-RP electrical diversity profile for lighting and receptacle loads in large office buildings [86]. These diversity profiles are close to actual measured energy consumption profiles in the building.

Table 19. Electrical diversity profile of a large office building

Time	**1**	**2**	**3**	**4**	**5**	**6**	**7**	**8**	**9**	**10**	**11**	**12**
Load ratio	0.54	0.51	0.49	0.49	0.48	0.53	0.6	0.74	0.89	0.92	0.93	0.92
Time	13	14	15	16	17	18	19	20	21	22	23	24
Load ratio	0.91	0.91	0.91	0.91	0.87	0.76	0.69	0.67	0.66	0.63	0.6	0.57

The baseline Model 1 maximum required airflow is estimated from the hourly simulation to be 0.582 cfm/ft². We assume that airflow pressure rise across the fan is 3 in w.g. or (747 Pa), 30% fan design oversize, fan efficiency 65% and motor efficiency 95%. In this case maximum required fan power can be estimated to be:

$$\mathrm{P_{Fan_{max}}} = \frac{1.25 \cdot \dot{\mathrm{V}} \cdot \Delta \mathrm{P}}{\eta_{\mathrm{fan}} \cdot \eta_{\mathrm{motor}}} \tag{83}$$

$$\mathrm{P_{Fan_{max}}} = \frac{1.25 \cdot \left(0.582 \frac{\mathrm{cfm}}{\mathrm{ft^2}} \cdot 174{,}016 \mathrm{ft^2}\right) \cdot \frac{\frac{1.669 \mathrm{m^3}}{3600 \mathrm{s}}}{\mathrm{cfm}} \cdot 747 \mathrm{Pa}}{0.65 \cdot 0.95} = 71.0 \mathrm{kW} \tag{84}$$

$$\mathrm{p_{Fan_{max}}} = \frac{\mathrm{P_{Fan_{max}}}}{\dot{\mathrm{V}}_{\mathrm{max}}} = \frac{71.0 \mathrm{kW} \cdot \frac{1.34 \mathrm{hp}}{\mathrm{kW}}}{1.25 \cdot \left(0.582 \frac{\mathrm{cfm}}{\mathrm{ft^2}} \cdot 174{,}016 \mathrm{ft^2}\right)} = 0.752 \frac{\mathrm{hp}}{1000 \mathrm{cfm}} \tag{85}$$

Part load fan power can be estimated for a variable speed drive based on the following equation [87]:

$$\mathrm{W} = (0.00153 + 0.0052 \cdot \mathrm{PLR} + 1.1086 \cdot \mathrm{PLR^2} - 0.1164 \cdot \mathrm{PLR^3}) \cdot \mathrm{P_{Fan_{max}}} \tag{86}$$

where:

$$PLR = V/\dot{V}_{max} \quad (87)$$

The hourly simulation was performed to estimate annual cooling and heating loads (Table 20). Simulation was made based on the following assumptions:

- Rated capacity is 125% of the maximum cooling load (306 TR);
- Rated effectiveness is 0.5 kW/TR;
- Minimum capacity control is 25% of the rated capacity;
- Nominal leaving chilled water temperature is 15°F below the design cooling coil leaving air temperature;
- Head pressure control is available;
- Nominal head pressure set for 70°F condenser entering water temperature;
- The cooling tower approach is 5°F.

These assumptions result in a chiller with rated power of 153 kW and capacity of 306 TR.

Energy consumption by chilled water and hot water pumps, cooling tower fans and pumps as well as other supplemental systems was not modelled, since application of membrane dehumidification system for outside air stream dehumidification has minimal effect on these systems. The simulation results show the energy consumption of the HVAC system Model 1 Baseline case to be 3.348 kWh/ft²-year.

Table 20. Model 1 baseline case energy consumption

Parameter	Units	Value
Sensible primary cooling	kBtu/ft²-year	45.877840
Latent primary cooling	kBtu/ft²-year	5.846659
Reheat	kBtu/ft²-year	0.166580
Total lighting electric	kWh/ft²-year	7.685280
Total plug electric	kWh/ft²-year	5.123520
Supply air fan electric	kWh/ft²-year	0.436300
Chiller electric	kWh/ft²-year	2.912081
Total HVAC electric	kWh/ft²-year	3.348381

Application of the outside air stream membrane dehumidification system for Model 1 increases the outside airflow pressure drop by 0.5 in. w.g. Operational energy efficiency of the membrane dehumidification system is based on the assumption that 1 m² of membrane area is required for 35 cfm (59.5 m³/h) of the design flow. The simulated dehumidification model membrane has an effective water vapor permeance of 8E-6 kmol/(kPa-m²-s) and effective air permeance of 6E-10 kmol/(kPa-m²-s). Based on these properties, operation of an idealized membrane system was estimated to reach an outlet humidity setpoint of 0.00800 with 35 cfm/m² airflow rate across the membrane surface (Table 21).

Table 21. Ideal membrane dehumidification system operation efficiency

Inlet temperature, F	Inlet RH, %	Condenser Pressure	Inlet humidity ratio	Effective COP
90	90	5	0.02781	2.239
80	90	4	0.01995	5.522
70	90	2.8	0.01415	8.736
60	90	2.4	0.00992	10.801
90	80	4.5	0.02460	3.828
80	80	3.5	0.01767	6.542
70	80	2.8	0.01255	9.528
90	70	4.3	0.02142	4.919
80	70	3.3	0.01540	7.544
70	70	2.7	0.01095	9.998
90	60	3.8	0.01827	6.051
80	60	3.0	0.01316	8.546

Maximum membrane dehumidification effective system COP can be modeled based on the regression fit from Table 21 by formula:

$$\mathrm{COP} = 6{,}971.10 \cdot \omega^2 - 729.67 \cdot \omega + 17.29. \quad (88)$$

This equation is valid in the range of humidity ratio 0.008 to 0.028 to achieve an outlet humidity ratio of 0.008 (Figure 61).

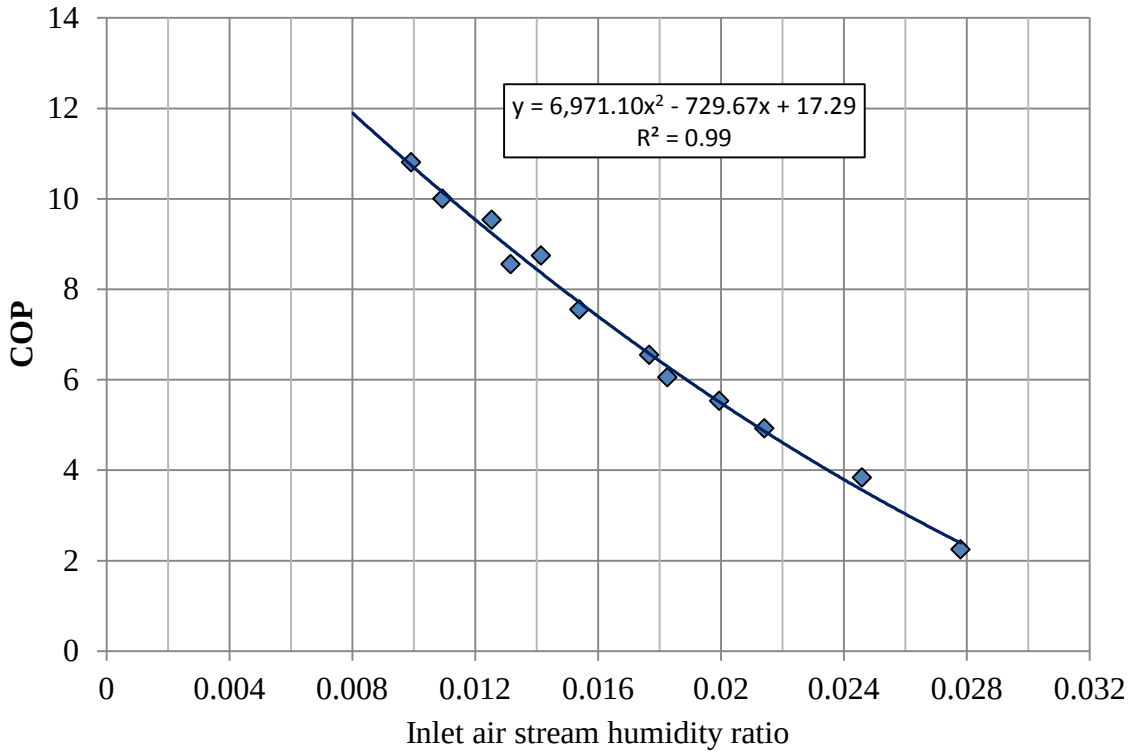

Figure 61. Dehumidification membrane system maximum effective COP

Application of the membrane dehumidification system separates sensible and latent cooling loads. That eliminates the supply air temperature requirement of 55°F. Increasing the supply air temperature decreases chiller energy consumption, but increases the supply airflow rate and requires additional supply air fan energy consumption (Table 22).

The simulation data show that the increasing supply air temperature from 55°F to 56.5°F will result in decrease of the total HVAC system energy consumption. Application of a membrane dehumidification system for outside air dehumidification in Model 1 will reduce HVAC system energy consumption from 3.348 to 3.133 kWh/ft²-year or 6.4% of HVAC energy.

Table 22. Membrane dehumidification HVAC System energy consumption of Model 1

Cooling coil temperature	**°F**	**55**	**56**	**56.5**	**57**	**58**
Chiller rated capacity	ton/1000ft²	1.533	1.526	1.521	1.513	1.501
Chiller rated power	W/ft²	0.767	0.763	0.761	0.756	0.751
Chiller average efficiency	kW/TR	0.865	0.775	0.770	0.763	0.754
Chiller average COP	kW/kW	4.066	4.541	4.567	4.607	4.665
Sensible primary cooling usage	kBtu/ft²-year	45.878	46.068	46.177	46.297	46.576
Latent primary cooling usage	kBtu/ft²-year	0.680	0.435	0.328	0.222	0.128
Reheat usage	kBtu/ft²-year	0.167	0.164	0.163	0.163	0.161
Total lighting electric usage	kWh/ft²-year	7.685	7.685	7.685	7.685	7.685
Total plug electric usage	kWh/ft²-year	5.124	5.124	5.124	5.124	5.124
Supply fan electric usage	kWh/ft²-year	0.436	0.493	0.525	0.560	0.643
Chiller electric usage	kWh/ft²-year	2.637	2.368	2.354	2.335	2.311
Total Primary HVAC system energy	kWh/ft²-year	3.074	2.861	2.879	2.895	2.954
OA supply fan energy	kWh/ft²-year	0.032	0.032	0.032	0.032	0.032
Membrane system energy	kWh/ft²-year	0.240	0.240	0.240	0.240	0.240
Membrane system COP	kW/kW	7.445	7.445	7.445	7.445	7.445
Total HVAC system energy	kWh/ft²-year	3.346	**3.133**	3.151	3.167	3.226

Baseline Model 2 was developed with assumptions of a more typical case. This time OA flow rate is twice the minimum required value and the minimum supply flow rate is equal to 40% of the maximum supply airflow during the occupied time (Table 23).

Table 23. Baseline Model 2 (realistic building) main design parameters

Parameter	Units	Value
Conditioned floor area	ft²	174,016
Interior zone percentage	%	70
Exterior surface (wall and window) area	ft²	36,158
Window percentage	%	0.39
Roof area	ft²	57,600
Exterior walls conductivity	Btu/ft²-h-°F	0.105
Exterior window conductivity	Btu/ft²-h-°F	1.142
Exterior roof conductivity	Btu/ft²-h-°F	0.194
Weekday occupancy time	h	7:00-18:00
Saturday occupancy time	h	10:00-16:00
Sunday occupancy time	h	none
Primary min occupied airflow	cfm/ft²	0.232
Primary min unoccupied airflow	cfm/ft²	0
Primary max Airflow	cfm/ft²	0.58
Space temperature setpoint	°F	72
*Minimum occupied outside airflow	cfm/ft²	0.17
Minimum unoccupied outside airflow	cfm/ft²	0
Outside air control method		No economizer or ERV/HRV
Cooling coil temperature setpoint	°F	55
Peak lighting loads	W/ft²	1.2
Peak plug loads	W/ft²	0.8
Occupancy	ft²/person	200
Sensible heat load per person	Btu/h	250
Latent heat load per person	Btu/h	200
Supply Air Fan power	hp/1000cfm	0.752
Supply Air Fan type		Variable Frequency Drive
Peak electric weekdays load ratio		1
Nighttime Lighting and Plug load ratio		0.6
Electric load Ramp up weekdays start time		6:00
Electric load Ramp down weekdays end time		19:00
Electric load Weekdays Ramp up hours	hr	2
Electric load Weekdays Ramp down hours	hr	2
Peak electric weekend load ratio		0.6

Based on these assumptions, required chiller maximum power is 197 kW and nominal capacity is 394 TR. The annual building total HVAC energy consumption is 4.16 kWh/ft²-year (Table 24).

Table 24. Baseline Model 2 (realistic building) energy consumption

Parameter	Units	Value
Sensible Primary Cooling	kBtu/ft²-year	46.198863
Latent Primary Cooling	kBtu/ft²-year	9.751089
Reheat	kBtu/ft²-year	0.636742
Total Lighting Electric	kWh/ft²-year	7.685280
Total Plug Electric	kWh/ft²-year	5.123520
Supply Fan Electric	kWh/ft²-year	0.568359
Chiller Electric	kWh/ft²-year	3.594033
Total HVAC electric Energy	kWh/ft²-year	4.162392

Installation of the membrane dehumidification system allows an increase of supply air temperature to decrease the combined energy consumption of the chiller and the supply air fan. Simulation results are given in Table 25.

Table 25. Membrane dehumidification HVAC System energy consumption of Model 2

Cooling coil temperature	°F	55	56	57	58
Chiller rated capacity	ton/1000ft²	1.741	1.724	1.718	1.689
Chiller rated power	W/ft²	0.632	0.615	0.601	0.583
Chiller average efficiency	kW/TR	0.867	0.856	0.848	0.833
Chiller average COP	kW/kW	4.059	4.110	4.145	4.220
Sensible primary cooling usage	kBtu/ft²-year	46.199	46.368	46.561	46.720
Latent primary cooling usage	kBtu/ft²-year	0.129	0.129	0.128	0.128
Reheat usage	kBtu/ft²-year	0.637	0.597	0.567	0.543
Total lighting electric usage	kWh/ft²-year	7.685	7.685	7.685	7.685
Total plug electric usage	kWh/ft²-year	5.124	5.124	5.124	5.124
Supply fan electric usage	kWh/ft²-year	0.568	0.638	0.718	0.807
Chiller electric usage	kWh/ft²-year	2.607	2.576	2.556	2.512
Total Primary HVAC system energy	kWh/ft²-year	3.175	3.213	3.274	3.319
OA supply fan energy	kWh/ft²-year	0.063	0.063	0.063	0.063
Membrane system energy	kWh/ft²-year	0.479	0.479	0.479	0.479
Membrane system COP	kW/kW	7.445	7.445	7.445	7.445
Total HVAC system energy	kWh/ft²-year	**3.717**	3.755	3.816	3.861

Simulation shows that the membrane dehumidification system with AHU supply air temperature of 55°F will provide energy consumption reduction of the HVAC system to 3.717 kWh/ft²-year. Application of a membrane dehumidification system in this condition will reduce energy consumption from 4.162 to 3.717 kWh/ft²-year or 10.7% of HVAC system consumption.

Application of the membrane dehumidification system for outside air stream dehumidification in a typical office building located in a hot and humid climate can reduce energy consumption of the HVAC system by at least 6-10% for the cases examined. This value is relatively small in comparison with the difference between the potential membrane dehumidification system COP of 7.4 and the chiller average operation COP of 4.1. The main reason for this small effect is dominance by a factor of five of the sensible cooling load above the building latent cooling load.

4.9 Conclusions

The experimental dehumidification system was designed and constructed to test application of the membrane separation process using zeolite membranes. More than one hundred experiments were conducted under different operating conditions using six zeolite membrane modules built to the same specification.

At the design airflow rate of 30 cfm (850 lpm), the static pressure drop across the tested modules was above 3 in w.g. (750 Pa). It appears that the design static pressure drop of 1 in w.g. (249 Pa) can be reached with further modification of the membrane module construction.

Experimental results showed that the decrease of feed airflow rate at a constant permeate pressure will cause a reduction of the retentate relative humidity, and as a result, a decrease of the membrane selectivity. To provide higher selectivity, when feed airflow rate is reduced, dehumidification system control should increase permeate pressure and keep retentate relative humidity constant at the setpoint level above 30% for the current level of membrane development.

Changing total permeate pressure in the membrane module has twice as much effect on effective water permeance as on the effective air permeance. Reduction of permeate pressure has a relatively small effect on the selectivity coefficient but a large impact on the separation factor.

The effective water permeance does not depend on humidity when the retentate flow relative humidity is above 30%. The effective water permeance has a temperature

dependence and increases with the increase of temperature from 6E-6 to 8E-6 kmol/(kPa-m²-s), when temperature increases from 65°F to 90°F.

The effective air permeance has an exponential dependence on the retentate flow relative humidity below 30% and is relatively constant at 5E-9 kmol/(kPa-m²-s) when retentate airflow relative humidity is above 30%.

It is possible to achieve an effective air permeance of 3E-9 kmol/(kPa-m²-s) and an effective water permeance of 9E-6 kmol/(kPa-m²-s) for retentate airflow relative humidity above 40%.

A membrane separation factor of 600 and the selectivity coefficient of 1,500 were achieved at retentate flow relative humidity above 50%.

Experimental system effective COP for the design conditions was 1.9, which is much lower than the goal value of 3.6. The main reason for this reduction is the dependence of effective air permeance on the retentate relative humidity. Effective system COP can be greatly improved if the membrane module retentate relative humidity is increased from 15% to 30% or the membrane formation technology is improved.

The experimental system configuration with two modules demonstrated that the effective system COP can be increased to 3.1, if the retentate airflow relative humidity is above 30%.

The dual stage dehumidification system experimental results showed some improvement in the system performance. The dual stage configuration is further investigated in the membrane air-conditioning system tests.

The uncertainty of the analysis shows that, for the design conditions, effective water permeance and selectivity coefficient uncertainty is above 50% due to the low retentate design relative humidity of 15.4% and sensor measurement limitation.

The uncertainty of the analysis of the actual experiments shows that effective water permeance and effective COP relative uncertainty is below 30%.

Application of the membrane dehumidification system can provide potential energy savings in the range of 6-10% for typical office building located in hot and humid climate operating at standard ventilation rates.

Application of the membrane dehumidification system in DOAS increased energy efficiency of the dehumidification process from COP of 4.1 (with a chiller) to 7.4 (with the membrane dehumidification system) that provided 10% savings of total HVAC system energy consumption.

5 MEMBRANE AIR-CONDITIONING SYSTEM

The modification to the membrane dehumidification system described in Section 4.1 was made by replacing the vapor-compression cooling component with two evaporative coolers (direct adiabatic cooling systems). Water evaporation cooling is a common and widely used technology in arid regions. This technology cools incoming hot, dry air by evaporating water into the airflow. When water evaporates it absorbs energy (latent heat of vaporization). This process provides cooling to the airflow while humidifying it. Application of evaporative cooling systems is limited to dry climate zones, where airflow can be humidified to the relative humidity that does not exceed the maximum limit of the building occupant comfort. Combination of the membrane dehumidification process with direct evaporative cooling can increase application of this process to other climate zones and systems with a low outside air fraction (e.g. office buildings).

After the system modification, cooling of the airstream is provided in the adiabatic evaporation cooling process from the enthalpy of water vaporization. Multiple stages of the evaporative cooling and membrane dehumidification process can provide required conditions of supply airflow regardless of feed air humidity and temperature.

The experimental system was tested with two configurations. The first configuration includes only one membrane module. The second configuration includes two membrane modules operating at different permeate pressure levels. The goal of the second configuration of experiments was to investigate the advantage of a two stage permeate pressure control strategy on energy consumption of the experimental system.

The design inlet condition of the experimental system was chosen to be an extreme condition with a dry-bulb temperature of 90°F (32.2°C) and a relative humidity of 50% at airflow rate of 30 cfm. The target design outlet conditions were at a dry-bulb temperature of 70°F (21°C) and 80% RH. A parametric experimental study was conducted to determine system performance at various conditions.

In the experimental system setup feed airflow is first cooled with the evaporative cooling system to a temperature approaching the wet-bulb temperature of the feed air. After that, the airflow is dehumidified in the membrane module with further cooling by the second stage of the evaporative cooler.

5.1 Single stage system design

The experimental setup is separated into five major subsystems with their respective components being the inlet-air conditioning component (S0), the membrane module component (S1), the evaporative cooling component (S2), the vacuum system component (S3), and the water rejection measurement component (S4). The diagram with the individual subsystems and components is shown in Figure 62.

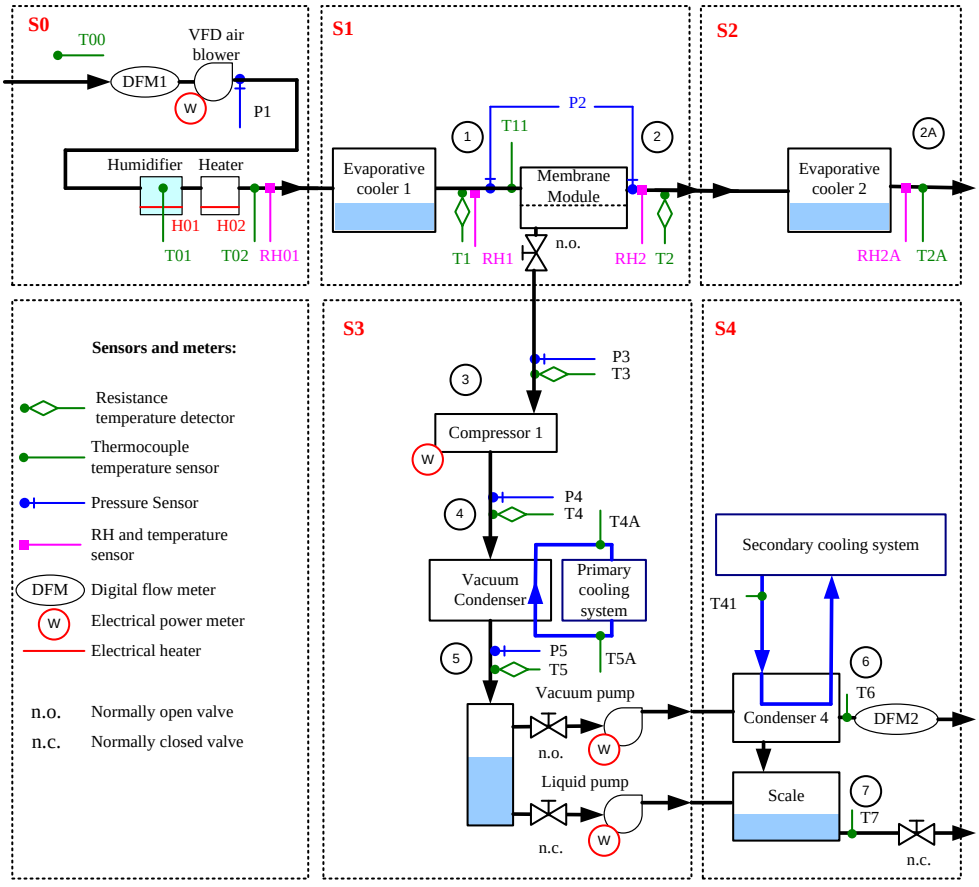

Figure 62. Membrane air-conditioning system configuration

The major subsystems described above were designed to be isolated from the overall system for individual testing with their own control and measurement locations, which ensured that each subsystem was working appropriately and accurately throughout operation. A brief description of each subsystem, referred to by a section number, is presented below.

Section S0 is used to condition the inlet air stream of the membrane air-conditioning system to achieve the required supply airflow rate, dry-bulb temperature of supply air, and supply air relative humidity.

Section S1 is designed to provide evaporative cooling to the feed air stream and subsequent dehumidification of the airflow.

Section S2 includes the membrane outlet evaporative cooler and measurement station for monitoring the outlet temperature and humidity of the supply airflow.

Section S3 is designed to provide the required dehumidification in Section S1. The first element is an intermediate compressor designed to increase the permeate pressure of the dehumidification system from the range of 0.5-2 kPa (based on the required dehumidification) to a pressure of 4-8 kPa corresponding to the water-vapor saturation pressure at a condenser temperature and air to water molar fraction in the permeate flow. After the intermediate compressor the permeate gas flow is cooled in the vacuum condenser by using the cooling water with temperature that is maintained 5°F above the inlet airflow wet-bulb temperature. Condensed water is rejected to the ambient with a liquid pump while the vacuum pump rejects the rest of the noncondensable gas to the ambient.

Section S4 is designed to provide measurements of the extracted water during the dehumidification process and the permeate airflow.

The changes in the design airflow properties during the membrane air-conditioning system operation process are shown on the psychrometric diagram (Figure 63). System inlet airflow design condition dry-bulb temperature is 90°F and relative humidity is 50% (Point 01). This value corresponds to system design outdoor weather conditions. In the first stage, the membrane air-conditioning system humidifies the

airstream to achieve a relative humidity approaching 100% with simultaneous reduction of air dry-bulb temperature due to energy absorbed during water evaporation in the evaporative cooler (Process 01-1). The second stage dehumidifies air at constant temperature with the membrane separation process (Process 1-2). The third process consists of further cooling of airflow with evaporative cooling (Process 2-2A). With the addition of the second membrane module and one more evaporative cooler, further cooling can be achieved.

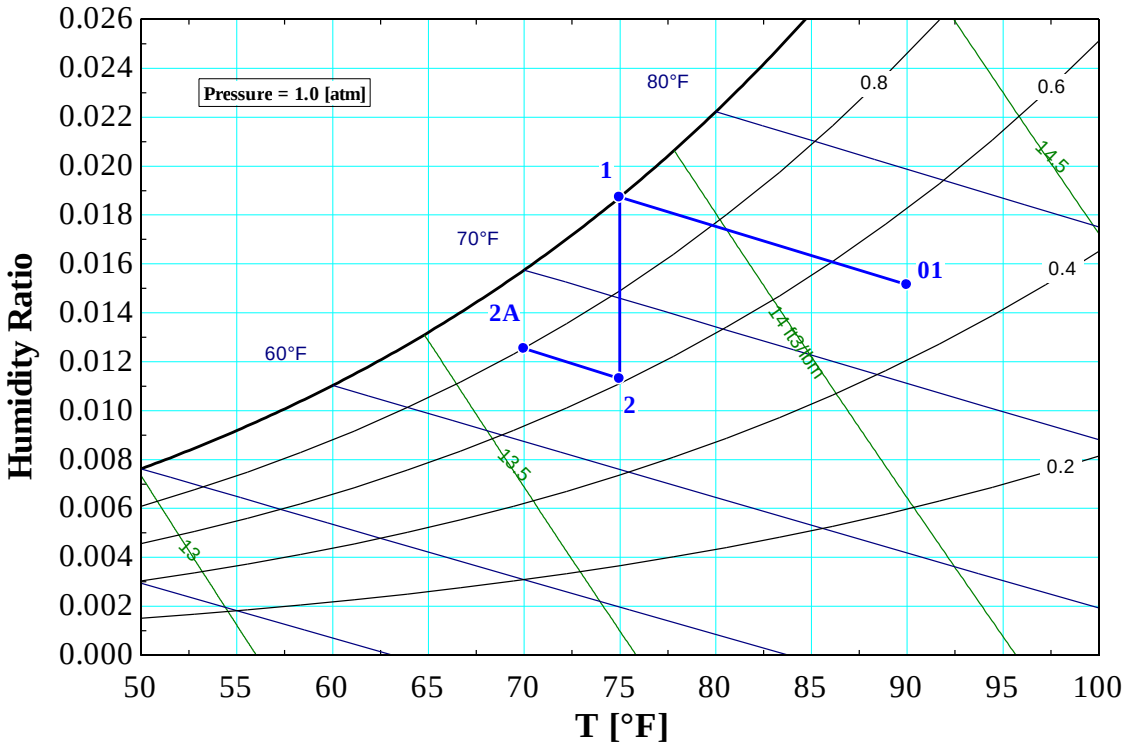

Figure 63. Membrane air-conditioning system operation at the design conditions

Major parts of the membrane air-conditioning experimental system are the same as in the membrane dehumidification experimental system and can be found in its description (Section 4.2). The difference is two additional custom design evaporative coolers. Evaporative coolers used in the experiments were designed using the same principle as conventional evaporative cooling systems. In evaporative coolers the airflow

is passed through porous materials (honeycomb paper) and wetted by an intermittent duty water recirculation system.

5.2 Single stage system performance at the design conditions

Multiple experimental tests were conducted with the single membrane module air-conditioning system at the design inlet conditions and design air-flow rate of 30 cfm. All six available membrane dehumidification modules were used in the experimental setup during the course of this study. Inlet air-stream properties during these experiments were close to the design conditions (90°F, 50% RH), while the outlet air-stream conditions achieved had lower temperatures and humidity ratio than the design values (70°F, 80% RH). To illustrate the experimental results, data obtained for three experiments with different membrane modules are provided in Table 26.

Table 26. Single stage membrane air-conditioning system experimental data at the design conditions

Test#	**Design**	**N2**	**N5**	**N15**
Membrane Module #	NA	3	1A	3A
Feed air flow rate, cfm	30.0	30.0	30.2	30.1
System inlet temperature, T01, °F	90	89	89	89.8
System inlet relative humidity, RH 01, %	50	52	49	52.7
System inlet humidity ratio, ω01	0.01518	0.01511	0.01439	0.01593
Membrane feed temperature, T1, °F	75	74	73	74
Membrane feed relative humidity, RH 1, %	100	100	100	99
Membrane feed humidity ratio, ω1	0.01881	0.01790	0.01728	0.01819
Membrane retentate temperature, T2, °F	75	74	73	74
Membrane retentate relative humidity, RH 2, %	61	56	60	61
Membrane retentate humidity ratio, ω2	0.01143	0.01025	0.01037	0.01114
System outlet temperature, T2A, °F	70	65	64	66
System outlet relative humidity, RH 2A, %	80	93	93	96
System outlet humidity ratio, ω2A	0.01258	0.01251	0.01180	0.01298
Permeate flow pressure, P3, kPa	1.600	0.997	0.943	0.974
Permeate air flow volume at ambient pressure, lpm	0.659	0.750	0.635	0.13
Intermediate compressor power consumption, W	20	660	690	618

In all three experimental results a deeper membrane dehumidification process was achieved with following evaporative cooling to airflow temperatures below system design setpoint (Figure 64). In all tests, cooling performance exceeded the design

requirements (outlet air-stream temperature 66 °F for N15 is 4 °F below the design conditions) and provided comparable humidity ratio 0.01298 (design condition 0.01258).

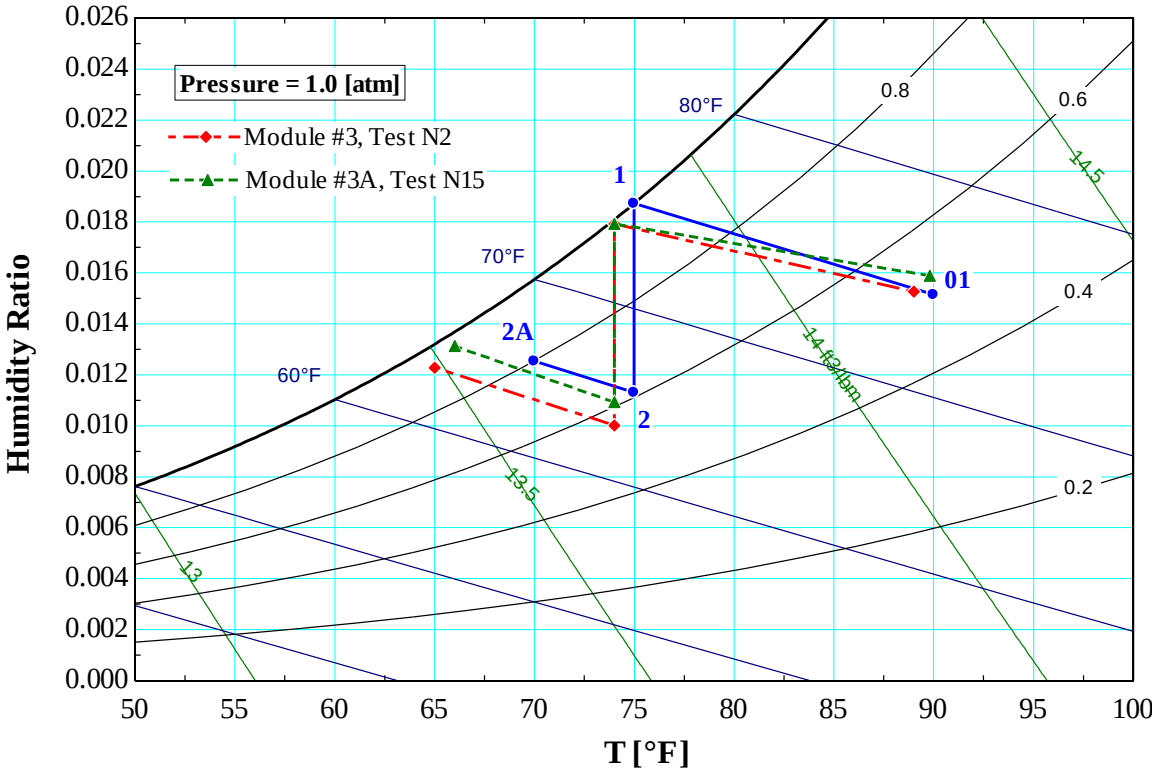

Figure 64. Single stage membrane air-conditioning system performance at the design conditions

Analysis of Test N15 (Table 27) shows the lowest effective air permeation rate achieved of 1.5E-9 kmol/(kPa-m²-s) that increased the membrane separation factor to 2400.

All three experimental results show the same effective water permeance (within measurement uncertainty) at 7E-6 kmol/(kPa-m²-s). Experimental results for Experiment N15 show an effective COP above 5.5 that greatly exceeds the design value of 4. The increase of effective COP for Test N15 is caused by the reduction of the membrane module effective air permeance.

Table 27. Single stage membrane air-conditioning system estimated parameters

Test #	DESIGN	Test N2	Test N5	Test N15
Membrane Module #		3	1A	3A
Permeate air flow, m_air3, kg/s-m²	17.9E-6	20.4E-6	17.3E-6	2.6E-6
Permeate water flow, m_w3, kg/s-m²	162.2E-6	168.9E-6	153.1E-6	112.2E-6
Feed water flow, m_w1, kg/s-m²	412.9E-6	395.0E-6	382.8E-6	289.3E-6
PAB_air, kmol/(kPa-m²-s)	6.3E-9	7.1E-9	6.0E-9	1.25E-9
PAB_water, kmol/(kPa-m²-s)	11.9E-6	7.8E-6	6.9E-6	6.7E-6
Cooling provided, TR	83.7E-3	93.2E-3	98.7E-3	99.5E-3
Effective COP	4.136	2.392	2.332	5.534
Separation factor	481	462	516	2403
Selectivity coefficient	1889	1086	1147	5387

5.3 Single stage system performance at various inlet airstream conditions

To evaluate the membrane air-conditioning system performance at various inlet air-stream conditions, a series of experiments was performed with a design inlet airflow rate of 30 cfm, inlet air temperature between 66-116 °F (19-47 °C), and relative humidity between 9-95% (Figure 65). Experiments shown on Figure 65 were conducted at two levels of humidity ratio, below and above the building design supply airflow humidity ratio setpoint of 0.009.

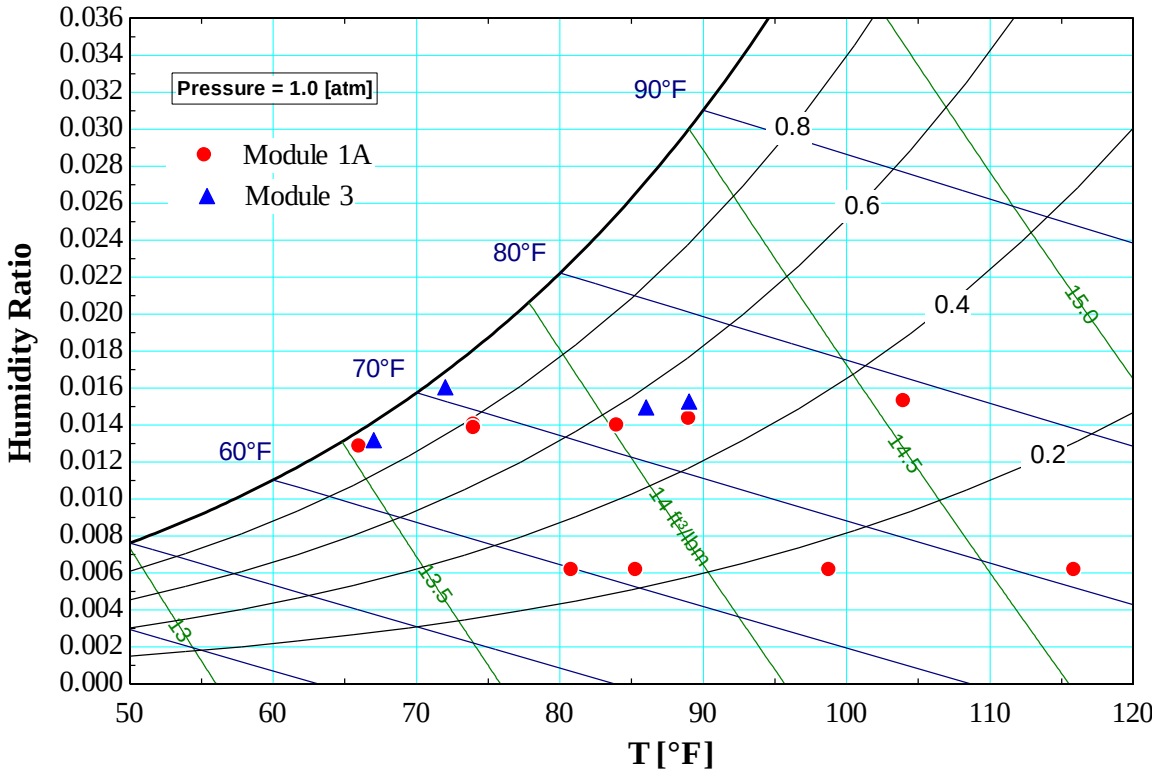

Figure 65. Membrane air-conditioning system inlet airflow test conditions

During the tests, the feed air stream steady state (temperature, humidity) and steady flow were obtained over a two hour interval, while the permeate side was maintained at the atmospheric pressure. Once the supply air and system properties were at the required steady-state condition, the vacuum system was enabled and operated for 20-30 minutes to obtain a steady-state operation in the vacuum system. After steady-state conditions in the vacuum system were obtained, the test parameters were monitored for stability over a 20 minute interval, and the data points were recorded. The experimentally measured data for Module#3 and Module#1A are summarized in Table 28 and Table 29.

Table 28. Membrane air-conditioning system measured data (Test N1-N7)

Test#	N1	N2	N3	N4	N5	N6	N7
Module #	3	3	3	3	1A	1A	1A
Ambient air temperature, T_OA, °C	23.9	21.8	21.2	24.7	20.4	24.3	21.7
Feed air flow rate, cfm	30.0	30.0	30.1	30.0	30.2	30.3	30.1
Membrane module static pressure drop, ΔP, in w.g.	2.6	2.6	2.6	2.6	2.8	2.8	2.8
System inlet temperature, T01, °C	19.6	31.6	30.1	22.1	31.6	40.1	19.1
System inlet relative humidity, RH01, %	93.3	51.5	55.8	95.3	49.1	32.5	94.3
Membrane feed temperature, T1, °C	19.1	23.1	22.1	22.1	22.6	26.1	18.6
Membrane feed relative humidity, RH1, %	99.9	99.9	99.9	99.9	99.5	93.3	99.0
Membrane retentate temperature, T2, °C	19.6	23.6	22.6	22.6	22.6	25.6	19.1
Membrane retentate relative humidity, RH2, %	52.5	56.2	56.2	56.8	60.4	56.8	60.4
System outlet temperature, T2A, °C	15.6	18.6	18.1	18.1	17.6	19.6	15.1
System outlet relative humidity, RH2A, %	90.4	92.9	94.4	90.4	93.4	97.4	92.4
Permeate flow pressure, P3, kPa	0.710	0.997	0.972	0.952	0.943	1.070	0.799
Permeate flow temperature, T3, °C	23.8	22.0	21.8	24.4	21.6	23.9	21.9
Vacuum condenser inlet pressure, P4, kPa	2.250	3.630	3.580	3.740	3.530	3.730	3.420
Vacuum condenser inlet temperature, T4, °C	24.7	26.7	26.0	30.7	25.8	26.9	25.0
Vacuum condenser outlet pressure, P5, kPa	2.110	3.420	3.390	3.380	3.340	3.420	3.270
Vacuum condenser outlet temperature, T5, °C	19.6	24.3	24.2	24.2	24.5	24.6	24.1
Permeate air flow volume at ambient pressure, lpm	0.720	0.750	0.780	0.800	0.635	0.780	0.640
Intermediate compressor power consumption, W	531	660	635	587	690	650	676

Table 29. Membrane air-conditioning system measured data (Test N8-N15)

Test#	N8	N9	N10	N11	N12	N13	N14	N15
Module #	1A	1A	1A	1A	1A	1A	1A	3A
Ambient air temperature, T_OA, °C	24.4	24.8	25.0	23.7	23.0	23.2	23.6	22.9
Feed air flow rate, cfm	30.0	30.0	30.1	30.0	30.0	30.1	30.0	30.1
Membrane module static pressure drop, ΔP, in w.g.	2.8	2.8	2.8	2.8	2.8	2.8	2.8	2.5
System inlet temperature, T01, °C	29.1	23.6	23.6	27.1	29.6	37.1	46.6	32.1
System inlet relative humidity, RH01, %	56.3	77.9	77.4	27.8	24.4	16.2	9.1	52.7
Membrane feed temperature, T1, °C	22.1	21.1	20.6	16.6	17.6	19.6	21.6	23.6
Membrane feed relative humidity, RH1, %	99.5	97.6	98.1	94.8	93.3	93.8	94.8	98.5
Membrane retentate temperature, T2, °C	22.1	21.6	21.1	17.6	18.6	20.1	21.6	23.6
Membrane retentate relative humidity, RH2, %	59.8	56.2	62.7	57.4	57.4	58.0	58.6	61.0
System outlet temperature, T2A, °C	17.1	16.6	17.1	14.1	14.6	15.1	16.6	18.7
System outlet relative humidity, RH2A, %	93.9	92.4	92.4	93.4	91.9	94.9	94.9	95.7
Permeate flow pressure, P3, kPa	0.926	0.867	1.100	0.723	0.754	0.807	0.883	0.974
Permeate flow temperature, T3, °C	23.8	25.0	25.6	23.0	23.2	23.4	23.4	23.1
Vacuum condenser inlet pressure, P4, kPa	3.520	3.470	5.150	3.350	3.420	3.460	3.500	3.670
Vacuum condenser inlet temperature, T4, °C	27.0	26.9	32.2	24.7	24.9	25.5	25.4	27.0
Vacuum condenser outlet pressure, P5, kPa	3.350	3.320	5.170	3.250	3.250	3.280	3.300	3.480
Vacuum condenser outlet temperature, T5, °C	24.4	24.5	25.0	24.0	24.1	24.1	24.2	23.3
Permeate air flow volume at ambient pressure, lpm	0.710	0.704	0.647	0.640	0.650	0.652	0.660	0.153
Intermediate compressor power consumption, W	630	619	720	616	613	602	616	618

For all experiments, the air-conditioning system outlet airflow properties were at temperatures of 55-65 °F (13-18 °C) and relative humidity levels of 90-100% (Figure 66). Two examples of the air-conditioning system operation at the extreme conditions are shown in Figure 67.

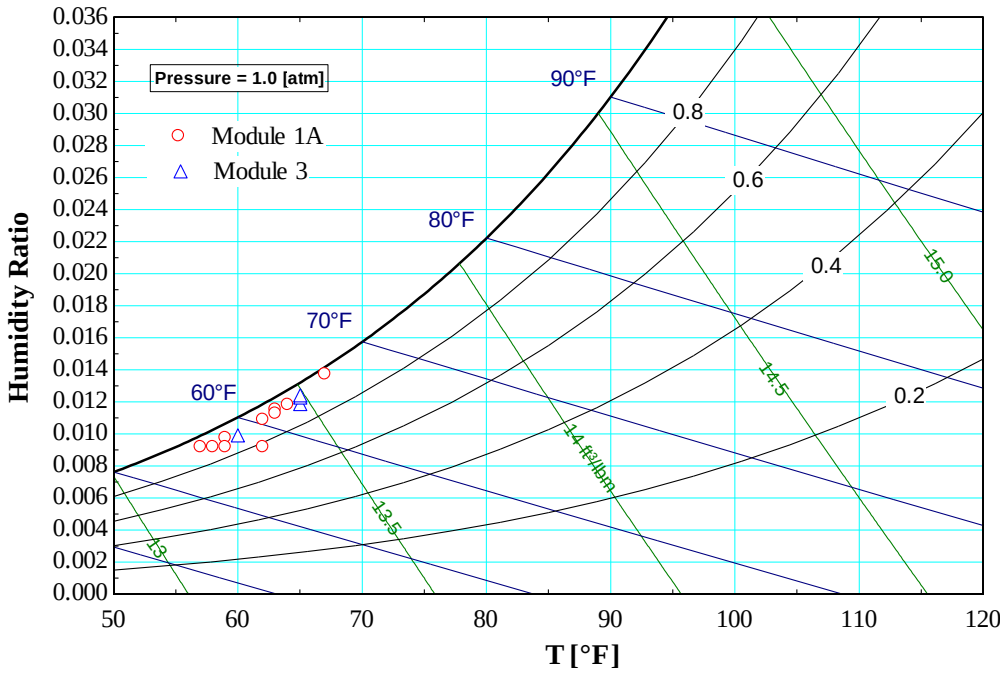

Figure 66. Membrane air-conditioning system outlet airflow test conditions

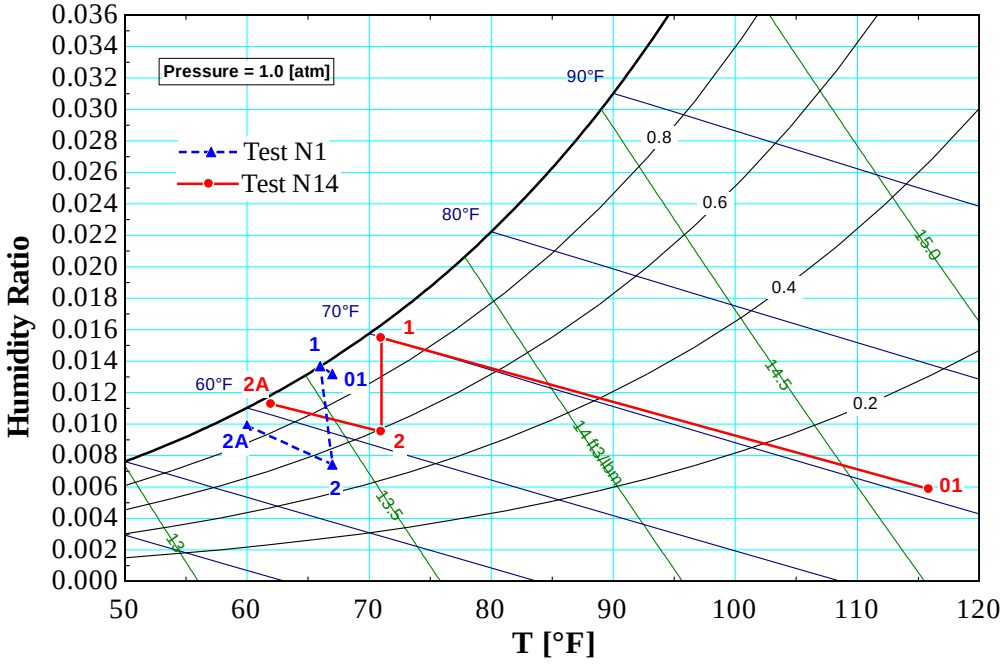

Figure 67. Membrane air-conditioning system airflow property changes

For all experiments conducted at a high feed relative humidity (90%-100%), the membrane permeate airflow rate showed a direct linear dependence on the feed airflow temperature in the experimental range (Figure 68). The membrane permeate airflow rate is proportional to the effective membrane permeance that also linearly increases with temperature (Figure 69). Comparison of previously described results with data for Module #3A at high feed relative humidity (Tests S1-S13 and Test 14-20) shows similar temperature dependence.

Since the maximum operating temperature during the dehumidification process is limited by the maximum wet-bulb temperature of 85°F (30°C) for the feed air, expected average effective air permeance during the system operation should not exceed 3E-9 kmol/(kPa-m²-s).

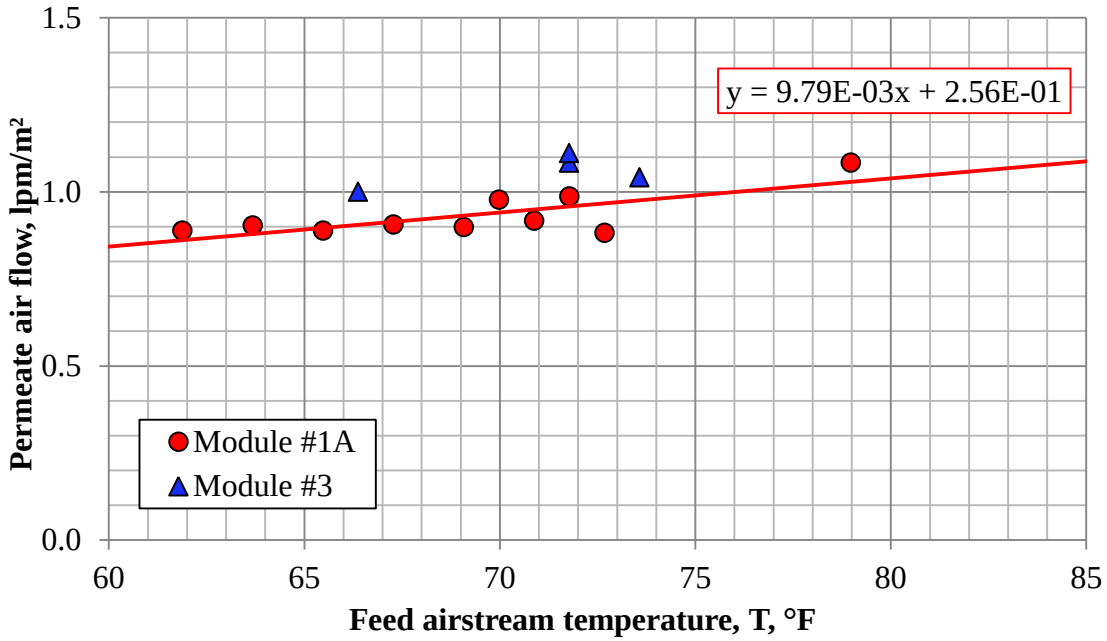

Figure 68. Permeate airflow rate at saturated feed airstream as a function of feed temperature

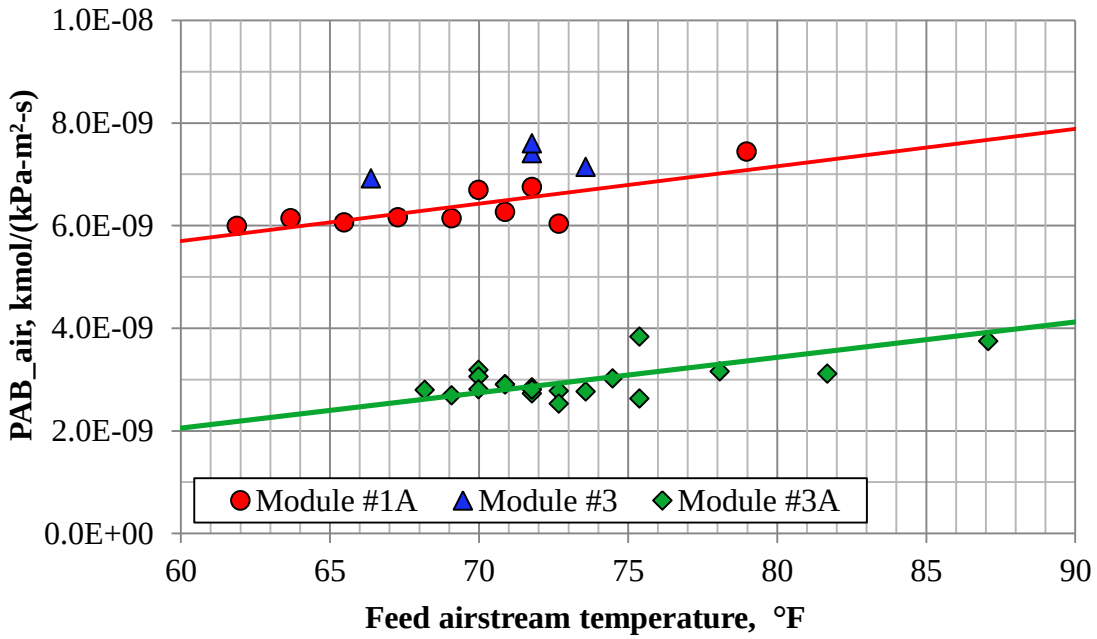

Figure 69. Effective membrane air permeance at saturated feed air stream

Similar dependence exists for the effective water permeance (Figure 70). Analysis of the effective water permeance for three membrane modules showed higher values for Module #1A and Module #3 relative to Module #3A.

With the same assumption, that the air-conditioning system operates at a wet-bulb temperature 60-85 °F (16-30 °C), which is the temperature of the membrane surface, expected average effective water permeance should be at least 5E-6 kmol/kPa-m²-s.

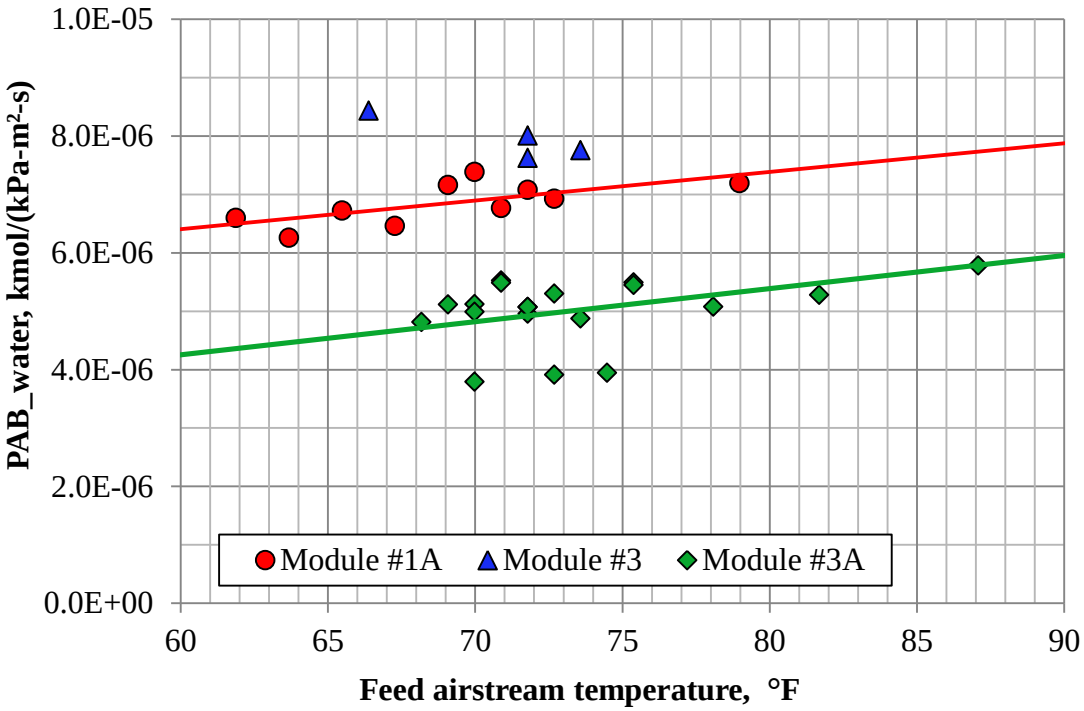

Figure 70. Effective membrane water permeance at saturated feed air stream

The temperature dependence of the effective air and water permeances shown previously correspond to independent selectivity coefficients for a feed airflow temperature near 65°F of about 1100 for Module #1A and Module #3, and 1800 for Module #3A (Figure 71).

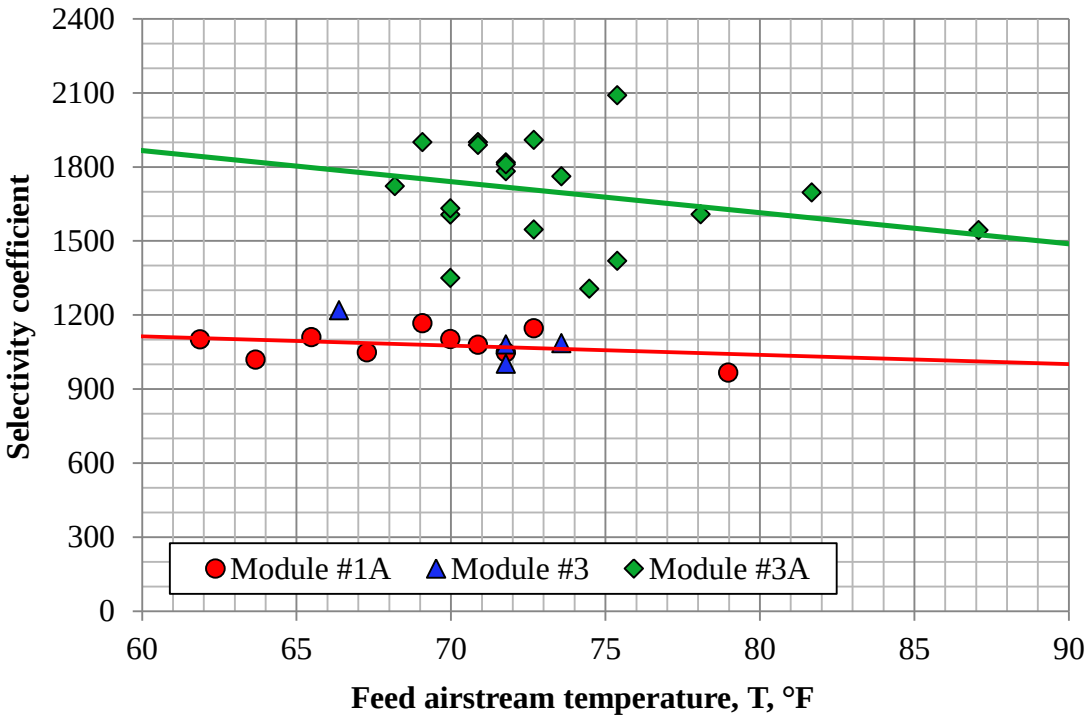

Figure 71. Membrane selectivity coefficient at saturated feed air stream conditions

Additional information about the system operations is given in Table 30 and Table 31. For all experiments with Module #1A and Module #3, the separation factor was between 430 and 528. Module #3A, used for comparison on several previous plots, had a separation factors between 330 and 1010.

Effective COP values with the assumptions discussed in Section 4.3 are provided in Table 30 and Table 31. Calculations were done based on the actual system operation parameters without energy efficiency optimization of a control system. One of the most important factors that need to be adjusted to improve system efficiency is total pressure of the vacuum condenser. Reductions of condenser pressure decreases permeate pressure at a constant power input by the intermediate compressor. As a result, the reduction of permeate pressure creates a higher water concentration gradient between the feed airflow

and permeate flow. The reduction of permeate pressure increases the membrane air-conditioning system capacity as well as the effective water permeance.

Table 30. Membrane air-conditioning system analysis (Test N1-N7)

Test#	N1	N2	N3	N4	N5	N6	N7
Module #	3	3	3	3	1A	1A	1A
Feed air flow rate, cfm	30.0	30.0	30.1	30.0	30.2	30.3	30.1
System inlet temperature, T01, °F	67	89	86	72	89	104	66
System inlet relative humidity, RH01, %	93	52	56	95	49	33	94
System inlet humidity ratio, ω01	0.01339	0.01511	0.01503	0.01602	0.01439	0.01522	0.01311
Membrane feed temperature, T1, °F	66	74	72	72	73	79	65
Membrane feed relative humidity, RH1, %	100	100	100	100	100	93	99
Membrane feed humidity ratio, ω1	0.01391	0.01790	0.01681	0.01681	0.01728	0.02006	0.01335
Membrane retentate temperature, T2, °F	67	74	73	73	73	78	66
Membrane retentate relative humidity, RH2, %	53	56	56	57	60	57	60
Membrane retentate humidity ratio, ω2	0.00747	0.01025	0.00964	0.00975	0.01037	0.01170	0.00834
System outlet temperature, T2A, °F	60	65	65	65	64	67	59
System outlet relative humidity, RH2A, %	90	93	94	90	93	97	92
Membrane retentate humidity ratio, ω2A	0.01003	0.01251	0.01232	0.01178	0.01180	0.01399	0.00992
Feed water flow, m_w1, kg/s-m²	315.1E-6	395.0E-6	374.9E-6	373.6E-6	385.3E-6	439.9E-6	304.4E-6
Permeate air flow, m_air3, kg/s-m²	19.9E-6	20.4E-6	21.2E-6	21.8E-6	17.3E-6	21.2E-6	17.4E-6
Permeate water flow, m_w3, kg/s-m²	146.1E-6	168.9E-6	160.1E-6	157.2E-6	154.0E-6	183.5E-6	114.5E-6
PAB_air, kmol/(kPa-m²-s)	6.9E-9	7.1E-9	7.4E-9	7.6E-9	6.0E-9	7.4E-9	6.1E-9
PAB_water, kmol/(kPa-m²-s)	8.4E-6	7.8E-6	8.0E-6	7.6E-6	6.9E-6	7.2E-6	6.7E-6
Separation factor	528	462	449	430	516	431	493
Selectivity coefficient	1219	1086	1080	1003	1147	966	1109
Percent water removed from the feed flow	46%	43%	43%	42%	40%	42%	38%
Cooling provided, TR	59.9E-3	93.2E-3	90.4E-3	69.5E-3	98.7E-3	112.7E-3	58.2E-3
Effective COP	1.23	2.39	2.27	1.67	2.33	2.64	1.51
Percent of water condensed in condenser	0%	40%	32%	27%	19%	32%	0%

Table 31. Membrane air-conditioning system results analysis (Test N8-N15)

Test#	N8	N9	N10	N11	N12	N13	N14	N15
Module #	1A	1A	1A	1A	1A	1A	1A	3A
Feed air flow rate, cfm	30.0	30.0	30.1	30.0	30.0	30.1	30.0	30.1
System inlet temperature, T01, °F	84	74	74	80.8	85.3	98.8	115.9	89.8
System inlet relative humidity, RH01, %	56	78	77	27.8	24.4	16.2	9.1	52.7
System inlet humidity ratio, ω01	0.01430	0.01430	0.01421	0.00620	0.00630	0.00637	0.00589	0.01593
Membrane feed temperature, T1, °F	72	70	69	62	64	67	71	74
Membrane feed relative humidity, RH1, %	100	98	98	95	93	94	95	99
Membrane feed humidity ratio, ω1	0.01674	0.01542	0.01502	0.01123	0.01178	0.01346	0.01544	0.01819
Membrane retentate temperature, T2, °F	72	71	70	64	65	68	71	74
Membrane retentate relative humidity, RH2, %	60	56	63	57	57	58	59	61
Membrane retentate humidity ratio, ω2	0.00996	0.00906	0.00982	0.00720	0.00767	0.00852	0.00946	0.01114
System outlet temperature, T2A, °F	63	62	63	57	58	59	62	66
System outlet relative humidity, RH2A, %	94	92	92	93	92	95	95	96
Membrane retentate humidity ratio, ω2A	0.01149	0.01094	0.01130	0.00940	0.00955	0.01020	0.01124	0.01298
Feed water flow, m_w1, kg/s-m²	372E-6	345E-6	338E-6	259E-6	270E-6	306E-6	345E-6	402E-6
Permeate air flow, m_air3, kg/s-m²	19E-6	19E-6	18E-6	17E-6	18E-6	18E-6	18E-6	4E-6
Permeate water flow, m_w3, kg/s-m²	151E-6	143E-6	117E-6	93E-6	94E-6	112E-6	134E-6	156E-6
PAB_air, kmol/(kPa-m²-s)	6.7E-9	6.7E-9	6.1E-9	6.0E-9	6.1E-9	6.2E-9	6.3E-9	1.2E-9
PAB_water, kmol/(kPa-m²-s)	7.1E-6	7.4E-6	7.2E-6	6.6E-6	6.3E-6	6.5E-6	6.8E-6	6.7E-6
Separation factor	467	482	444	480	453	472	483	2403
Selectivity coefficient	1049	1103	1166	1101	1019	1049	1079	5388
Percent water removed from the feed flow	41%	41%	35%	36%	35%	37%	39%	39%
Cooling Provided, TR	91.2E-3	74.0E-3	66.5E-3	24.9E-3	33.7E-3	60.5E-3	79.7E-3	99.5E-3
Effective COP	2.13	1.62	3.17	0.74	1.00	1.58	1.95	5.53
Percent of water condensed in condenser	17%	0%	85%	0%	0%	0%	9%	93%

At the same time reductions of condenser pressure reduce the fraction of water that condenses in the vacuum condenser up to the point that no water is condensed at the given vacuum condenser cooling water temperature. In this case, water that should be rejected with a liquid pump as an incompressible liquid, is rejected with a vacuum pump as a compressible gas. Rejection of water flow from medium vacuum to the atmosphere pressure in a gas phase requires increased energy consumption by the air-conditioning system.

The impact of condenser pressure on system effective COP is clear from the comparison of energy efficiency between Test N9 and Test N10 (Table 31). The difference between two tests is in the higher vacuum condenser inlet pressure in Test N10 (5.17 kPa) vs. Test 9 (3.32 kPa) (Table 29). The vacuum condenser pressure in Test 9 was so low that water condensation did not occur (Table 31). The increase of condenser pressure also increased permeate pressure. This change caused reduction of the air-conditioning system capacity by 10% (Figure 72).

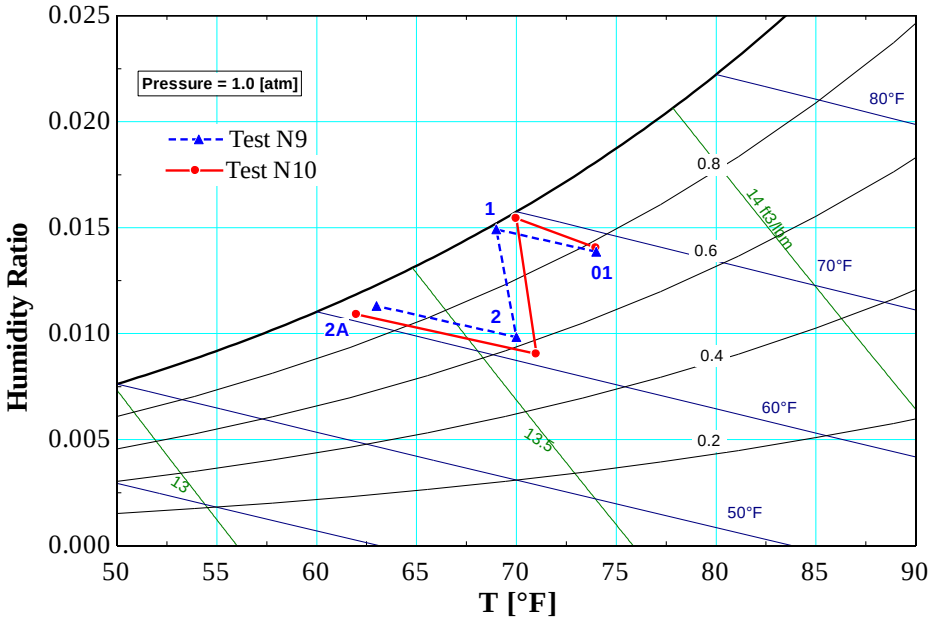

Figure 72. Membrane air-conditioning system airflow properties change for two experimental tests (N9 and N10)

At the same time increase of the condenser pressure in Test N10 caused condensation of 85% of water vapor in a permeate flow. This change increased the effective system COP from 1.62 (Test N9) to 3.17 (Test N10).

The air-conditioning system design conditions have 90% of the permeate water flow condensed in the vacuum condenser. Experimental Test N15 had condensation of 93% of water vapor. A higher condensation fraction in combination with a lower effective air permeance increased effective system COP for Test N15 above five.

5.4 Dual stage system performance at the design conditions

To reduce energy consumption required for the operation of a membrane air-conditioning system, an alternative system configuration was tested (Figure 73). In this configuration, the dehumidification process occurs in two stages. The first stage (Module A) provides partial dehumidification of the feed air stream with relatively high permeate pressure in the membrane module (1-3 kPa). The second stage membrane module permeate side pressure (Module B) is lower and defined by the required outlet humidity ratio and the available area of the membrane surface. The combination of two stages reduces compression energy of the intermediate compressor and increases system operation efficiency.

The minimum energy required for compression of an ideal gas in an isothermal internally reversible process between state 1 and state 3 can be determined by:

$$\mathbf{w}_{comp,in_1} = \mathbf{R} \cdot \mathbf{T} \cdot \mathbf{ln}\left(\frac{P_3}{P_1}\right). \quad (89)$$

A dual stage membrane module system can provide the same dehumidification with lower energy consumption. The first vacuum stage operates with a higher inlet water vapor pressure than the second stage. With the assumption that permeate water mass flow will be equally distributed between two stages, required energy for isothermal compression of an ideal gas by intermediate compressors can be found with:

$$\mathbf{w}_{comp,in_2} = \mathbf{0.5} \cdot \mathbf{RT} \cdot \mathbf{ln}\left(\frac{P_3}{P_1}\right) + \mathbf{0.5} \cdot RT \cdot \mathbf{ln}\left(\frac{P_3}{P_2}\right). \quad (90)$$

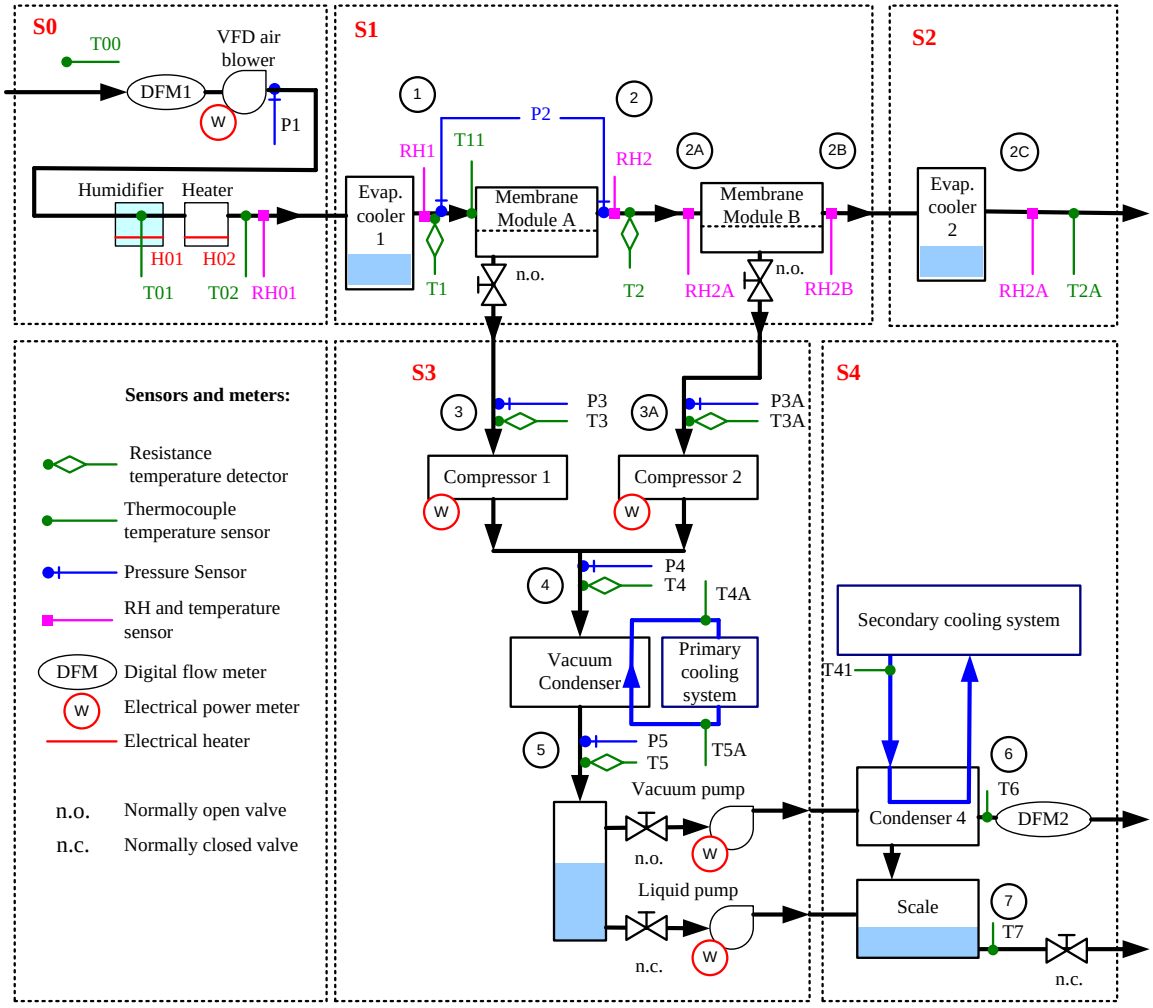

Figure 73. Dual stage membrane air-conditioning system configuration

Assume that the dual stage system needs to provide dehumidification of an airstream from a water vapor feed partial pressure of 3 kPa to retentate water vapor partial pressure of 1 kPa in the isothermal process. In this case the first membrane module can operate at a permeate pressure of 2 kPa and the second at 1 kPa instead of

both of them operating at 1 kPa. The required vacuum condenser pressure to condense water vapor should be at least 5 kPa for condensation at the vacuum condenser surface temperature of 90 °F (32 °C).

$$\frac{w_{comp,in_2}}{w_{comp,in_1}} = \frac{\left[0.5 \cdot RT \cdot \ln\left(\frac{P_3}{P_1}\right) + 0.5 \cdot RT \cdot \ln\left(\frac{P_3}{P_2}\right)\right]}{RT \cdot \ln\left(\frac{P_3}{P_1}\right)}. \quad (91)$$

$$\frac{w_{comp,in_2}}{w_{comp,in_1}} = \frac{\left[0.5 \cdot \ln\left(\frac{5}{2}\right) + 0.5 \cdot \ln\left(\frac{5}{1}\right)\right]}{\ln\left(\frac{5}{1}\right)} = 0.78. \quad (92)$$

Based on this assumptions application of a dual stage system will reduce energy consumption to 78% of the similar single stage system or by more than 20%.

To demonstrate the energy efficiency advantage of a dual stage system, configuration, pairs of experimental tests were conducted. Each pair had the first test conducted at equal permeate pressure in the membrane modules. The second test was conducted with lower permeate pressure in the second membrane module. The rest of the variables were not changed. In both experiments, inlet and outlet humidity were the same. The ratio of two permeate pressures can be referenced as a dual stage system permeate side pressure ratio.

The reduction of energy consumption can be illustrated based on two experimental tests, NB1 and NB2. In the first experiment (Test NB1) the permeate side pressure ratio was 1.7 (2.260 kPa and 1.360 kPa). In the second case, permeate pressure of both modules was equal to 1.720 kPa (Figure 74).

The change from a pressure ratio of 1.0 to 1.7 decreased system energy consumption by 8% (Table 32) and increased system actual COP from 0.26 to 0.32.

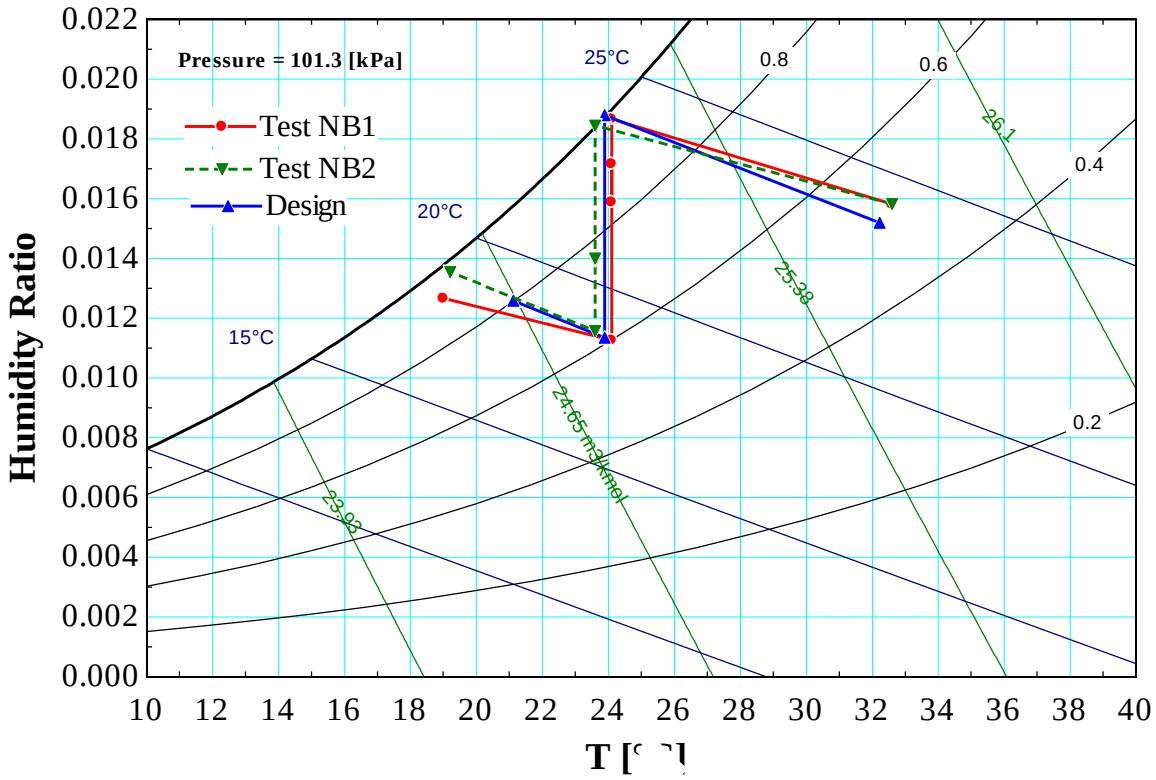

Figure 74. Dual membrane module air-conditioning system operation with pressure ratio 1.7 (Test NB1) and 1.0 (Test NB2)

Table 32. Comparison of the experimental results for Test NB1 and NB2

Parameter	Unit	Test NB1	Test NB2
Average separation factor	-	192	180
Cooling provided	TR	0.1026	0.0912
Permeate airflow	lpm	1.70	1.67
Intermediate compressor total power consumption	W	1132	1237
Permeate side pressure ratio		1.7	1.0
Actual system COP		0.319	0.259

The energy efficiency improvement of the dual stage system configuration compared to the single stage system in Table 32 is consistent with the theoretical estimate of Eq. 92.

5.5 Experimental uncertainty of the single stage air-conditioning system

Error propagation analysis for the single stage air-conditioning system was made based on the uncertainty of the experimental measurements. The error propagation analysis was conducted according to the method described in NIST Technical Note 1297 [84] for the air-conditioning system design conditions and the experimental results described in Section 5.2.

Experimentally measured variables include temperature, pressure, humidity, and volumetric airflow rate (Table 33).

Table 33. Membrane air-conditioning system measured parameters and corresponding measurement uncertainties at the design conditions

Measured variable	Value	Uncertainty	Sensor full scale (FS)
Nozzle system feed airflow pressure drop, in w.g.	2.22	±1% FS	3
Membrane module feed airflow pressure drop, in w.g.	2.5	±2% FS	5
System inlet airflow temperature, T01, °C	32.2	±1°C	NA
System inlet relative humidity, RH01, %	50	±5% RH	100
Feed airflow temperature, T1, °C	23.9	±1°C	NA
Feed airflow relative humidity, RH1, %	100	±5% RH	100
Retentate airflow temperature, T2, °C	23.9	±1°C	NA
Retentate airflow relative humidity, RH2, %	61.4	±5% RH	100
System outlet temperature, T2A, °C	21.1	±1°C	NA
System outlet relative humidity, RH 2A, %	80	±5% RH	100
Permeate flow pressure, P3, kPa	1.600	±0.5% FS	2
Permeate flow temperature, T3,°C	23.9	±0.15°C	NA
Condenser inlet pressure, P4, kPa	5.0	±0.5% FS	14
Condenser inlet temperature, T4, kPa	23.9	±0.15°C	NA
Condenser outlet pressure, P5, kPa	5.0	±0.5% FS	14
Condenser outlet temperature, T5, kPa	23.9	±0.15°C	NA
Permeate volumetric airflow rate, lpm	0.659	±3% FS	2
Permeate airflow temperature, T6,°C	16	±1°C	NA

Based on the design parameters and corresponding measurement uncertainty, the uncertainty of the estimated parameters was determined. The membrane effective water permeance had the highest relative uncertainty of individual parameters, resulting in an even higher relative uncertainty for the selectivity coefficient (Table 34) since it has additional uncertainty due to that of the air permeance.

Table 34. Value and uncertainty of the estimated variables at the air-conditioning system design conditions

	Estimated value	Uncertainty	Relative Uncertainty, %
Permeate mass flow of air, m_air3, kg/s-m²	17.9E-6	±1.6E-6	9%
Permeate mass flow of water, m_w3, kg/s-m²	162.2E-6	±32.3E-6	20%
PAB_air, kmol/(kPa-m²-s)	6.3E-9	±574.3E-12	9%
PAB_water, kmol/(kPa-m²-s)	11.9E-6	±4.3E-6	36%
Separation factor	481	±90	19%
Feed mass flow of water, m_w1, kg/s-m²	412.9E-6	±22.5E-6	5%
Selectivity coefficient	1889	±713	38%
Effective COP	4.157	±1.387	33%
Cooling provided, kW	0.294600	±0.093690	32%
System inlet humidity ratio, ω01	0.015180	±0.001786	12%
Feed airflow humidity ratio, ω1	0.018810	±0.001098	6%
Retentate airflow humidity ratio, ω2	0.011430	±0.001010	9%
System outlet humidity ratio, ω2A	0.012580	±0.000894	7%

The main components of the uncertainty of the effective water permeance across the membrane are measurement uncertainty of the retentate airflow relative humidity (82%) and retentate airflow temperature uncertainty (11%). This percent of uncertainty value is calculated as the ratio of the square of the product of the partial derivative and uncertainty of each measured variable to the square of the uncertainty in the calculated variable. For humidity measurement a capacitive polymer humidity sensor was used with a measurement accuracy of ±5% RH. The combination of a sensor accuracy of ±5% RH and the design retentate relative humidity of 61.4% RH provides 36% relative uncertainty in the water permeance.

The same analysis was repeated for the data obtained from Tests N2, N5 and N15 (Table 35). For these measurements the same equipment was used as described in Table 33. The effective air permeance uncertainty was within 10% for all analyzed experiments except N15 where it increased to 40% due to a low permeate airflow rate. Improvement in Module #3A decreased effective air permeance to (1.5±0.5)E-9 kmol/(kPa-m²-s) keeping the same estimated uncertainty as in other experiments. Effective water permeance for all experiments was constant and independent of the membrane module used in the experiment. Effective water permeance can be estimated to have an average value of (7±2)E-6 kmol/(kPa-m²-s).

Table 35. Estimated values and their uncertainty for experimental Test N2, N5, N15

Test#	**N2**		**N5**		**N15**	
Membrane Module #	3		1A		3A	
	Estimated value	Uncertainty	Estimated value	Uncertainty	Estimated value	Uncertainty
Feed airflow rate, cfm	30.0	0.2	30.0	0.2	30.1	0.2
Feed mass flow of water, m_w1, kg/s-m²	395E-6	22E-6	383E-6	21E-6	289E-6	16E-6
Permeate mass flow of water, m_w3, kg/s-m²	169E-6	31E-6	153E-6	30E-6	156E-6	32E-6
Permeate mass flow of air, m_air3, kg/s-m²	20.4E-6	1.6E-6	17.3E-6	1.6E-6	4.2E-6	1.6E-6
PAB_air, kmol/(kPa-m²-s)	7.1E-9	573E-12	6.0E-9	572E-12	1.25E-9	575E-12
PAB_water, kmol/(kPa-m²-s)	8E-6	2E-6	7E-6	2E-6	6.7E-6	1.6E-6
Separation factor	462	78	513	95	2401	1238
Selectivity coefficient	1086	282	1139	302	5383	2968
Effective COP	2.393	0.725	2.343	0.736	5.477	1.663
Cooling provided, W	328	91	345	89	350	94
System inlet humidity ratio, ω01	0.01511	0.00174	0.01439	0.00172	0.01593	0.00180
Feed humidity ratio, ω1	0.01790	0.00105	0.01728	0.00102	0.01819	0.00109
Retentate humidity ratio, ω2	0.01025	0.00098	0.01037	0.00093	0.01114	0.00099
System outlet humidity ratio, ω2A	0.01251	0.00079	0.01180	0.00075	0.01298	0.00081

The selectivity coefficient (up to 50% uncertainty) and the effective COP (32% uncertainty) have the highest uncertainty values among the other estimated parameters. Uncertainty of the COP estimation in the experiments analyzed was below uncertainty at the design conditions (34%). Experimental data showed that the highest effective COP obtained was 5.8±1.8 for Test N15. In all experiments at the design conditions, the membrane air-conditioning system provided a cooling capacity of 350±100 W (Table 33).

5.6 The membrane air-conditioning system application

Application of the membrane air-conditioning system, as an alternative to a conventional vapor compression system, with a water-cooled condenser can reduce HVAC system energy consumption and maintain indoor building temperature and humidity level within the comfort level as required by the ASHRAE Standard 62.1-2013 [85].

To estimate potential energy savings, which can be achieved by substituting the membrane air-conditioning system for a conventional system, a baseline model, as described in Section 4.8, was developed. The first baseline model, where the HVAC system operates in an ideal situation with the outside air ventilation flow rate set at the minimum required level and the minimum supply airflow rate set to the minimum required ventilation flow rate is used for the comparison. The baseline HVAC system model is a Single Duct Variable Air Volume System with reheat (Figure 60). A more detailed description of the baseline system is given in Section 4.8. The baseline model chiller average annual energy efficiency is 0.6 kW/TR and the equivalent average COP is 5.9.

5.6.1 Simplified analysis at the design conditions

The membrane air-conditioning system has the water cooled cooling coil of a conventional system replaced with two evaporative coolers and the membrane module (Figure 75). The average mixed airflow humidity ratio of the baseline module is 0.00827 with a maximum value of 0.01248. To evaluate the membrane air-conditioning system efficiency the design mixed airflow humidity ratio can be assumed to be 0.01093. These values define the design mixed airflow conditions at dry-bulb temperature of 80 °F and relative humidity of 50% (Point 1 on Figure 76). ASHRAE Standard 55-2004 [88] predicted mean vote comfort zone is also shown on Figure 76.

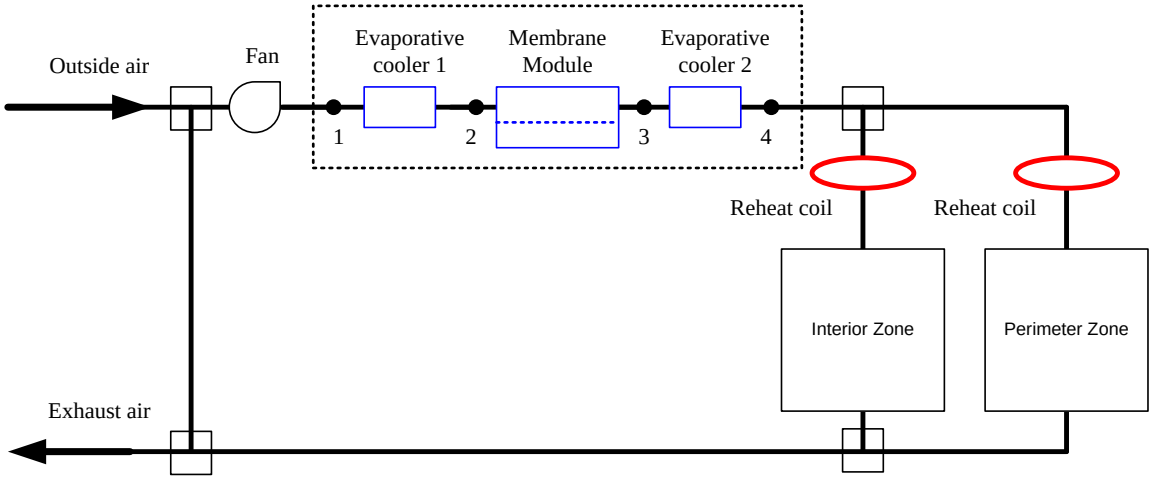

Figure 75. Building membrane air-conditioning system configuration

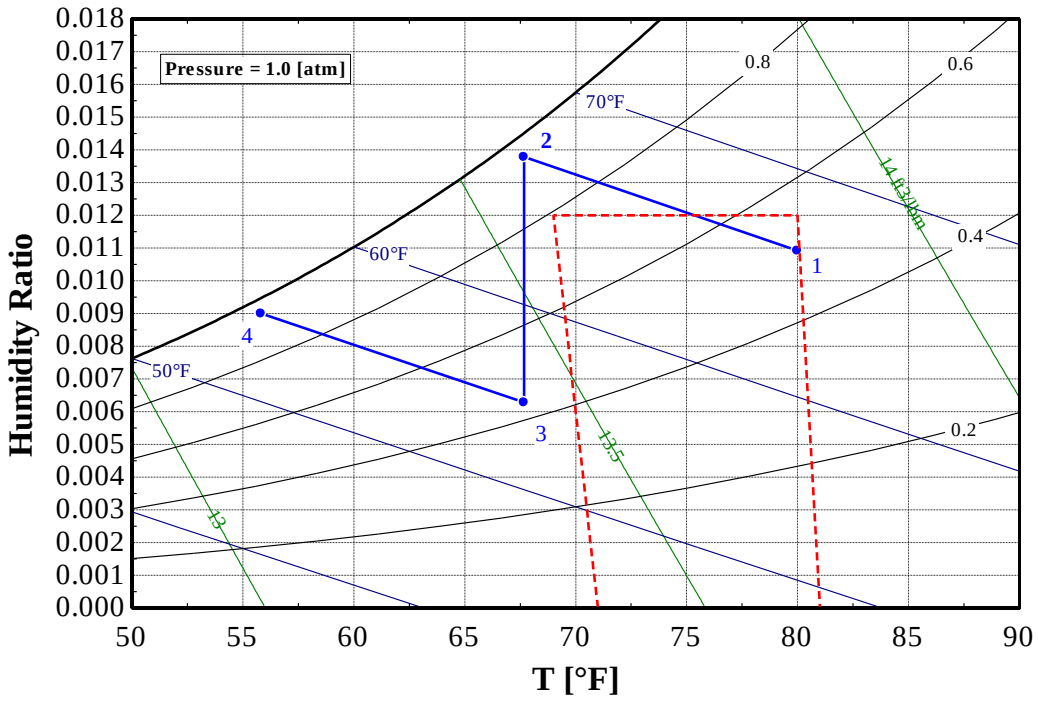

Figure 76. Building membrane air-conditioning system operation process and ASHRAE Standard 55-2004 predicted mean vote comfort zone

The first step of the membrane air-conditioning system operation is evaporative cooling of the mixed airflow from the design conditions, with constant wet-bulb temperature of 66.7 °F (19.3 °C), to relative humidity of 95% (Point 2). Point 2 corresponds to a dry-bulb temperature of 67.7 °F (19.8 °C).

The second step of the system operation is an airflow dehumidification process to the wet-bulb temperature of 55 °F (Point 3). This is an isothermal process at a dry-bulb temperature of 67.7 °F (19.8 °C) from relative humidity of 95% to 44%.

The third step is an airflow evaporative cooling from 67.7 °F (19.8 °C) and relative humidity of 44% along the 55 °F wet-bulb temperature line to the system design outlet dry-bulb temperature of 55.8 °F (13.2 °C) and relative humidity of 95% (Point 4). With this supply condition, the membrane air-conditioning system will provide a supply airflow humidity ratio of 0.009 that corresponds to 54% RH at the design zone temperature of 72 °F (22.2 °C).

The baseline vapor compression system used for this comparison is designed to operate with the constant cooling coil leaving air temperature of 55 °F and maximum hourly cooling coil leaving air humidity ratio of 0.00920.

One of the important differences between two systems is a higher static pressure drop in the membrane air-conditioning system in comparison to the baseline system cooling coil air pressure drop. It is assumed that the change to the new system will increase airflow static pressure drop by 1 in w.g. in addition to the baseline cooling coil static pressure drop.

In actual system operation, the mixed air stream temperature and humidity ratio can be different but it is unlikely that they will exceed the design wet-bulb temperature line since the design point is chosen on the right border of the ASHRAE Standard 55-2004 Predicted Mean Vote comfort zone (Figure 76). In case the mixed air stream wet-bulb temperature is lower than the design value, less dehumidification will be required and system efficiency will increase.

The membrane surface temperature during the dehumidification process should be below 70 °F as defined by operation wet-bulb temperature (Figure 76).

Based on the temperature dependence obtained from the experimental data of Module#3A (described in Section 5.3) the average effective membrane air permeance average value is 3E-9 kmol/kPa-m²-s and average effective membrane water permeance is 5E-6 kmol/kPa-m²-s at the total absolute permeate pressure of 0.9 kPa.

The analysis described in Section 4.4.4 shows that the effective permeance is also a function of a permeate pressure in addition to the temperature and relative humidity. To take this pressure dependence into account, a linear approximation of permeance dependence as a function of the permeate pressure was derived in the range 0.1 – 5 kPa.

$$P_{AB_{Air}} = 3 \cdot 10^{-9} - 0.3 \cdot 10^{-9} \cdot P_3 \quad (93)$$

$$P_{AB_{water}} = 6 \cdot 10^{-6} - 1 \cdot 10^{-6} \cdot P_3 \quad (94)$$

where: P_3 – absolute total permeate pressure, kPa.

The first design parameter that needs to be defined is the membrane area required for the feed airflow dehumidification to provide the maximum system efficiency in operation. To establish this dependence, a parametric study was conducted at the design system conditions and outside air wet-bulb temperature of 70 °F (Table 36).

Table 36. Parametric study of the membrane area performance impact on the system efficiency at design conditions with the actual membrane properties

Membrane area, m²/1000cfm	Required permeate pressure, kPa	PAB_air, kmol/(kPa-m²-s)	PAB_water, kmol/(kPa-m²-s)	Optimum vacuum condenser pressure, kPa	COP ideal	COP effective
144	1.14	2.7E-09	4.8E-06	7.0	5.869	3.199
103	1.03	2.7E-09	5.0E-06	6.3	6.459	3.523
80	0.93	2.7E-09	5.1E-06	5.6	6.781	3.699
72	0.87	2.7E-09	5.1E-06	5.4	6.844	3.733
60	**0.78**	**2.8E-09**	**5.3E-06**	**5.0**	**6.853**	**3.738**
48	0.62	2.8E-09	5.4E-06	4.9	6.670	3.639
40	0.49	2.9E-09	5.6E-06	4.7	6.312	3.443
36	0.42	2.9E-09	5.8E-06	4.5	6.097	3.326
30	0.25	3.0E-09	6.0E-06	4.4	5.280	2.880
26	0.04	3.0E-09	6.0E-06	3.4	3.220	1.760

Simulation results show that changing membrane area, at fixed inlet and outlet conditions, will require changing the total permeate pressure to provide the same dehumidification of the supply airflow stream (Figure 77).

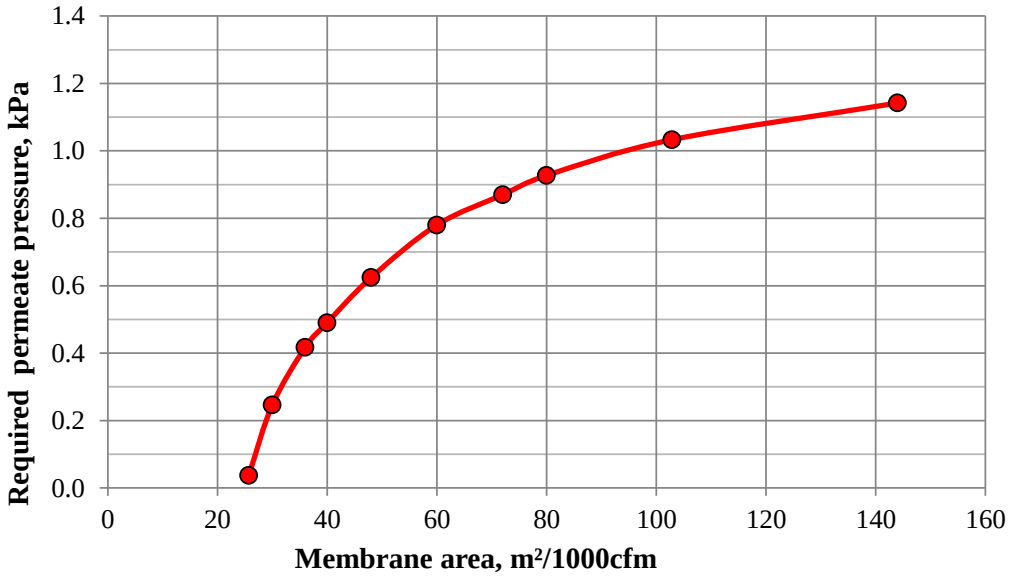

Figure 77. Required membrane total permeate pressure at the design conditions

As a result of the membrane permeate pressure change the maximum effective COP of the system will also change (Figure 78). Simulation results shown in Figure 78 include optimization of vacuum condenser pressure to maximize overall system performance.

A parametric study conducted based on the effective membrane permeance temperature and pressure dependences shows that optimum performance will be achieved at a membrane surface area of 60 m²/1000 cfm (Figure 79).

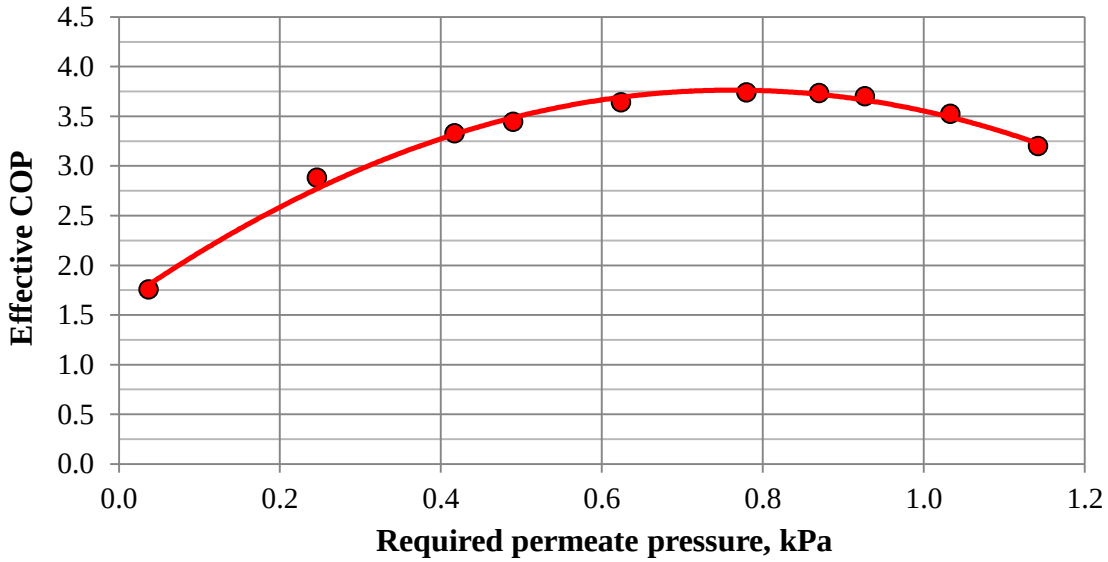

Figure 78. Membrane air-conditioning system energy efficiency as a function of membrane permeate pressure

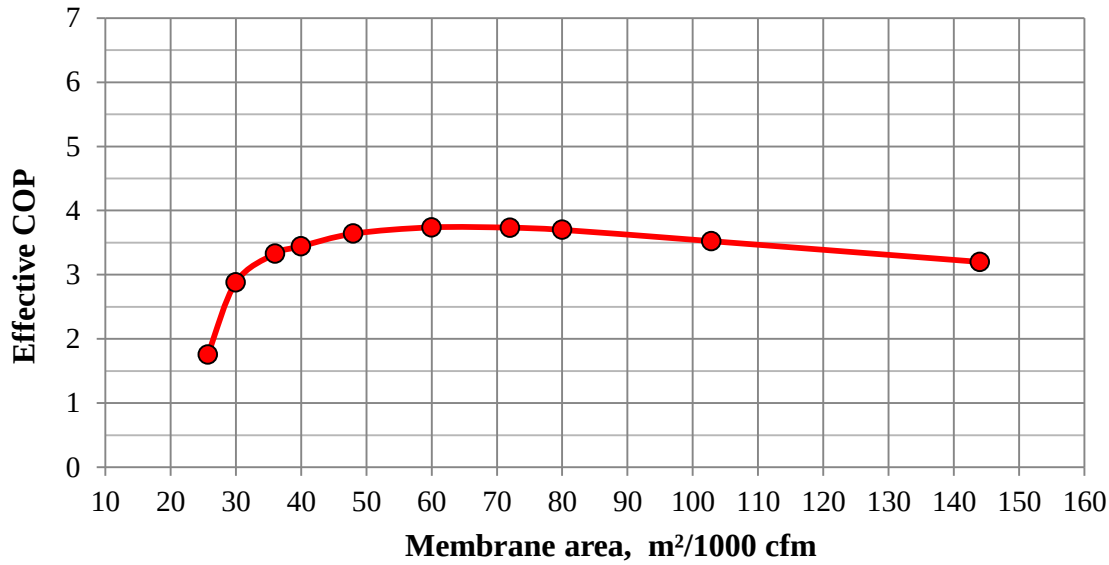

Figure 79. Effective energy efficiency of the membrane air-conditioning system as a function of available membrane area with the actual membrane properties

The same analysis was conducted for another case with the target constant membrane effective water vapor permeance of 8E-6 kmol/kPa-m²-s and effective air permeance 6E-10 kmol/kPa-m²-s (Table 37). This parametric study shows a maximum COP almost twice as high as with the membrane properties of Table 36, with maximum COP at the same membrane area of 60 m²/1000cfm (Figure 80). Both results were obtained for a fixed inlet and outlet conditions.

Table 37. Parametric study of the membrane area impact on performance at the system design conditions (target membrane properties)

Membrane area, m²/1000cfm	Required Permeate pressure, kPa	Optimum vacuum condenser pressure, kPa	COP ideal	COP effective
144	1.05	4.3	9.49	5.18
103	1.02	4.2	10.13	5.52
80	0.99	3.9	10.50	5.73
72	0.97	3.9	10.58	5.77
60	0.92	3.8	10.62	5.79
48	0.83	3.7	10.40	5.68
40	0.74	3.6	9.97	5.44
36	0.67	3.6	9.60	5.24
30	0.53	3.5	8.70	4.75
25	0.36	3.5	7.41	4.04
20	0.09	3.5	4.74	2.59

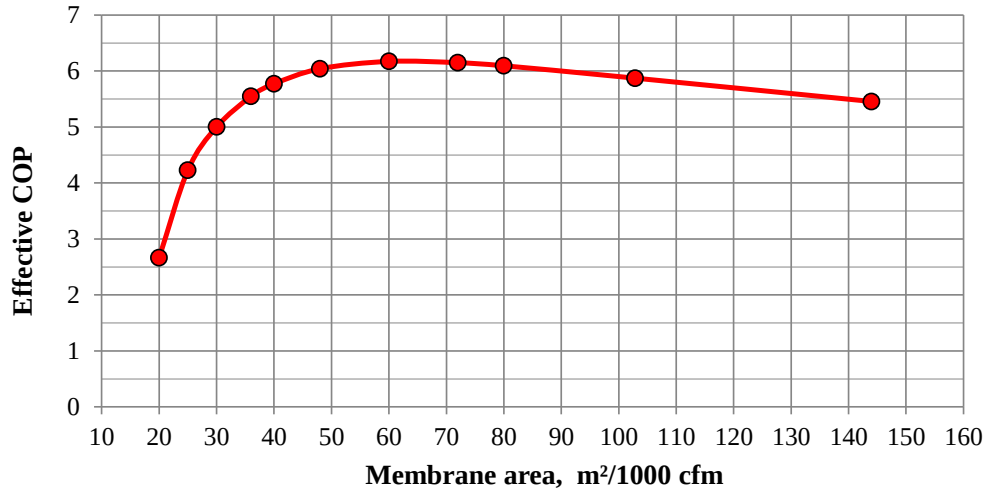

Figure 80. Effective energy efficiency of the membrane air-conditioning system as a function of membrane area with the target membrane properties

The other factor that needs to be considered in the system design is the cost of the membrane material. With this consideration and the results of the previous parametric study, the optimum membrane area was chosen as 40 m^2/1000 cfm or 85 m^2 for every m^3/s of the maximum airflow rate.

With the fixed membrane area and design inlet and outlet conditions of the membrane air-conditioning system the main parameter that influences system COP is the outside air wet-bulb temperature. Membrane air-conditioning system operation requires cooling of the vacuum condenser with the cooling water supplied by the cooling tower. The baseline and the membrane air-conditioning system models assume the same cooling tower approach of 5 °F. Cooling tower pump and fans energy consumption is also assumed the same.

Analysis of the global weather data showed that some of the most extreme humid climates are: Abu Dhabi (United Arab Emirates), Caracas (Venezuela), and Singapore. In all of them the maximum outside air wet-bulb temperature does not exceed 85 °F (29.4 °C). This limit was chosen as the maximum potential operation limit of the membrane air-conditioning system. The low wet-bulb temperature limit is defined at 55 °F (12.8 °C).

Energy efficiency analysis was conducted for two systems with different membrane areas of 40 m^2/1000cfm (optimized for membrane material cost) and 60 m^2/1000cfm (optimized for maximum performance).

The first series of simulations describes a realistic system with a membrane area of 40 m^2/1000 cfm that will require total permeate pressure of 0.49 kPa for air dehumidification to the design conditions. At this permeate pressure, membrane effective air permeance is 2.9E-9 kmol/(kPa-m^2-s) and effective water permeance is 5.6E-6 kmol/(kPa-m^2-s). Parametric study of the system performance at different outdoor air wet-bulb temperatures is summarized in Table 38.

Table 38. Membrane air-conditioning system performance as a function of outdoor air wet-bulb temperature for system with membrane area of 40 m²/1000 cfm (actual membrane properties)

Outdoor air wet-bulb temperature		Optimum vacuum condenser pressure	COP ideal	COP effective
°F	°C	kPa	-	-
55	12.8	2.8	7.60	4.14
60	15.6	3.4	7.10	3.87
65	18.3	3.9	6.68	3.64
70	21.1	4.7	6.31	3.44
75	23.9	5.4	5.99	3.27
80	26.7	6.3	5.71	3.12
85	29.4	7.3	5.46	2.98

Analysis of the realistic system shows that effective system COP decreases between 4 and 3 when outdoor air wet-bulb temperature increases (Figure 81).

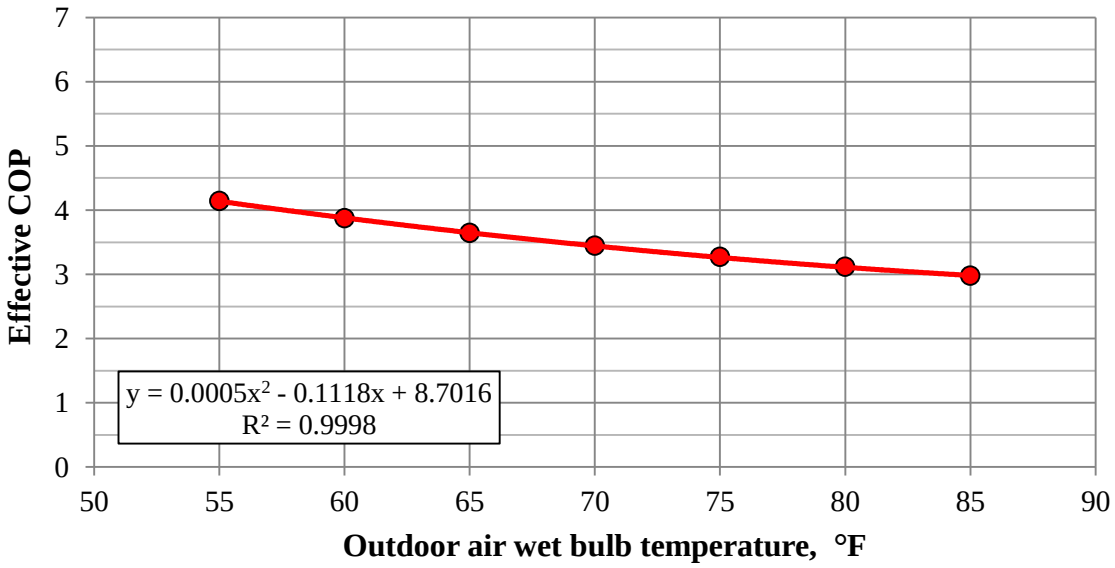

Figure 81. Effective energy efficiency of realistic system as a function of outdoor air wet-bulb temperature

The second simulation describes system operating at the maximum efficiency with the membrane that has target effective air and water permeances. Parametric study results of this system are given in Table 39.

Table 39. Membrane air-conditioning system performance as a function of outdoor air wet-bulb temperature for target membrane properties and area of 60 m²/1000 cfm

Outdoor air wet-bulb temperature		Optimum vacuum condenser pressure	COP ideal	COP effective
°F	°C	kPa	-	-
55	12.8	2.3	14.94	8.15
60	15.6	2.7	13.12	7.16
65	18.3	3.2	11.72	6.39
70	21.1	3.8	10.62	5.79
75	23.9	4.5	9.72	5.30
80	26.7	5.2	8.98	4.90
85	29.4	6.3	8.34	4.55

Simulation results show that the system ideal COP is changing between 15 and 8 and more than three times exceeds performance of the realistic system (Figure 82). This corresponds to an annual energy efficiency of the membrane air-conditioning system between 0.23 kW/TR and 0.44 kW/TR.

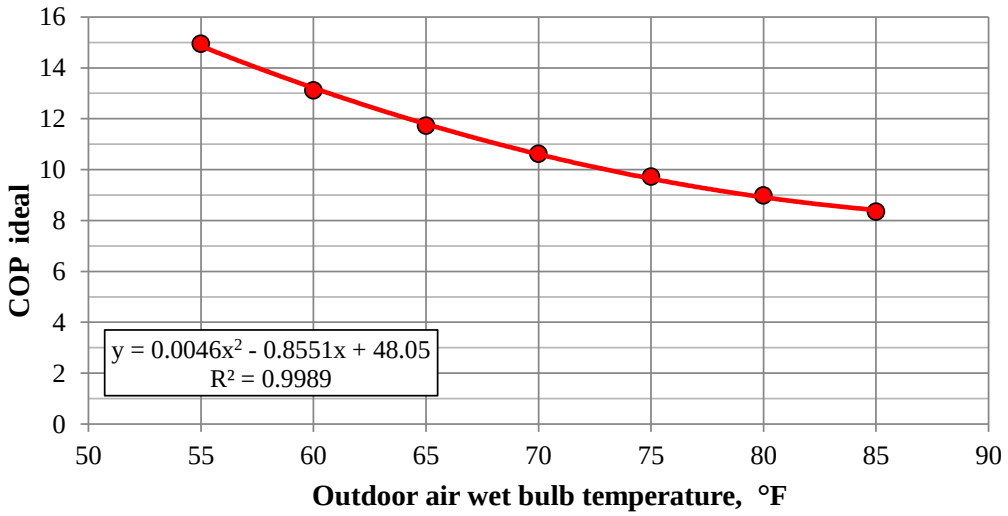

Figure 82. Energy efficiency of the ideal air-conditioning system with the membrane that has target effective air and water permeances

The simplified analysis results show that the effective system coefficient of performance is decreasing with the outside air wet-bulb temperature from 4 to 3 while the ideal COP is decreasing from 15 to 8.

5.6.2 Constant area system energy efficiency analysis (actual properties)

To evaluate annual system performance hourly analysis was conducted for the same weather conditions as described in Section 4.8. The membrane air-conditioning system was enabled when mixed air temperature was above the cooling coil leaving air temperature setpoint of 55 °F. During the analyzed interval of 8,765 hours the membrane air-conditioning system was in operation for 5,883 hours.

Independent simulation was conducted for each hourly interval. Due to the change of building cooling load, the required ventilation airflow rate was not constant and system performance changed with the required airflow rate and dehumidification requirements. To make analysis comparable to the baseline model, the membrane air-conditioning system had to dehumidify the same airflow rate from the same inlet temperature and humidity and to the same outlet conditions as in the baseline model. Optimization of the airflow rate and supply airflow temperature was not considered.

The simulation model input parameters were taken from the baseline model: outside air wet-bulb temperature, system inlet (mixed air temperature, mixed air humidity ratio), system outlet (cooling coil leaving air temperature, cooling coil leaving air humidity ratio), and supply air flow fraction.

A parametric study was conducted for membrane units with different membrane surface areas. The lower area limit was defined by the maximum system dehumidification load at 22.5 m² per 1000 cfm of maximum airflow rate, when total permeate pressure had to be reduced to 95 Pa to provide required dehumidification. The upper limit was 48 m² per 1000 cfm of maximum airflow rate where reduction of energy efficiency was observed due to a large permeate airflow rate (Table 40). The change in the system load (feed airflow rate and dehumidification requirements) caused large difference between average and minimum total permeate pressure that also affected energy efficiency. During the annual system operation retentate relative humidity was always above 43%.

Table 40. Energy performance of basic membrane air-conditioning system

Membrane area per 1000cfm of the design maximum supply airflow rate	**m^2/1000cfm**	**22.5**	**24.0**	**25.7**	**27.7**	**30.0**	**40.0**	**48.0**
Membrane air-conditioning system energy consumption (fan power not included)	kWh/ft^2-year	3.92	3.83	3.79	3.78	3.80	4.08	4.39
Minimum permeate pressure	kPa	0.10	0.18	0.27	0.36	0.45	0.72	0.77
Average permeate pressure	kPa	0.91	0.95	1.00	1.04	1.09	1.24	1.33
Effective coefficient of performance (COP) (kW/kW)	-	3.27	3.34	3.37	3.38	3.36	3.13	2.91
Energy efficiency	kW/TR	1.08	1.05	1.04	1.04	1.05	1.12	1.21

Simulation results show that the maximum efficiency is achieved at 26 m^2 of the membrane surface area per 1000 cfm of maximum airflow rate that is much lower number in comparison to the results of simplified analysis for constant airflow rate system (Figure 83).

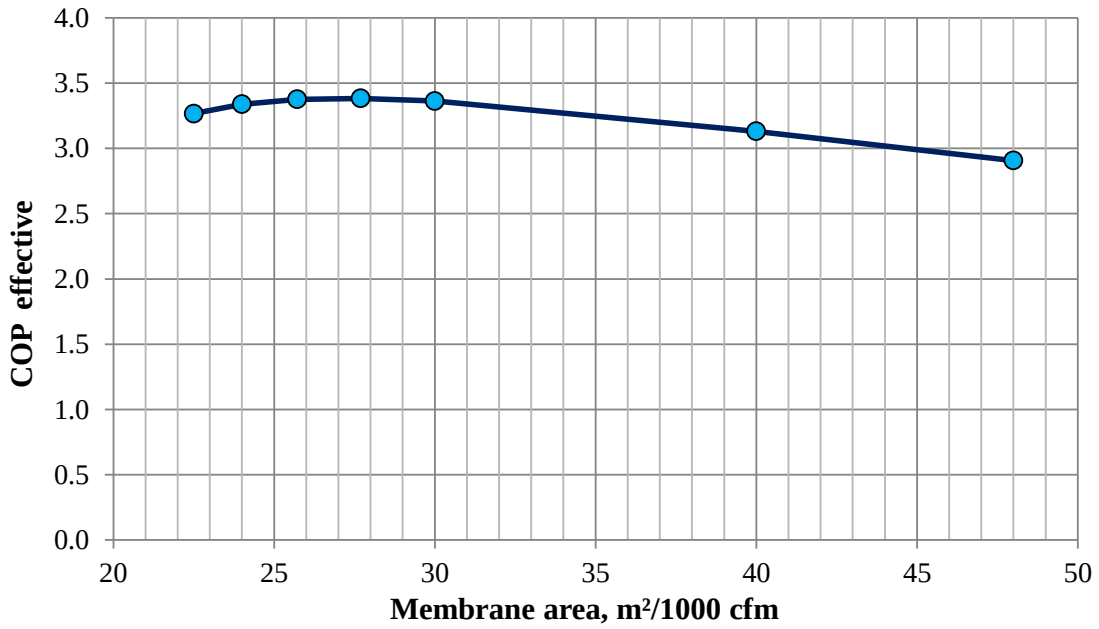

Figure 83. Membrane air-conditioning system performance as a function of the membrane area (actual membrane properties) per 1000 cfm of the maximum airflow rate

The membrane air-conditioning system efficiency hourly analysis shows dependence on the building cooling load with the maximum COP corresponding to a building cooling load of 2.2 W/ft² (Figure 84). A large reduction of the system energy efficiency occurs when the cooling load is above or below the optimum operation zone.

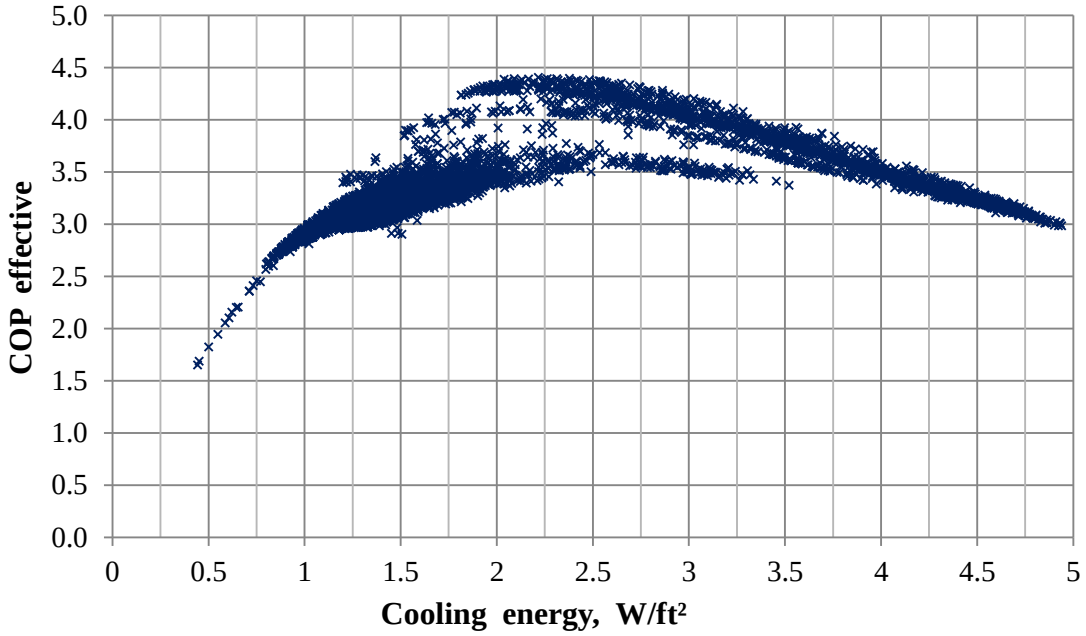

Figure 84. Constant membrane area air-conditioning system efficiency as a function of a cooling load

The minimum membrane air-conditioning system energy consumption (without supply air fan energy) corresponds to a membrane surface of 28 m² per 1000 cfm of maximum airflow rate. In the baseline model, chiller energy consumption was estimated at 2.63 kWh/ft²-year or 0.6 kW/TR. The basic membrane air-conditioning system energy consumption (3.61 kWh/ft²-year or 1.04 kW/TR) was above the baseline level and does not provide an energy efficiency advantage over the baseline system without changes to the design or control strategy. The main cause for the system inefficiency is a large variability in the system cooling load.

5.6.3 Three stage system energy efficiency analysis (actual properties)

Modifications to the system design were made based on the simulation results from the basic membrane dehumidification system. The total system membrane area should be 30 m²/1000cfm (in total 3030 m² per 860 kW of maximum system cooling load) to provide required dehumidification capacity at the analyzed condition as shown in Section 5.6.2. The membrane area per unit of cooling provided is 25% higher than was estimated in [12] as 10m² per 3.5 kW of maximum cooling load. At the same time at a lower dehumidification load, the larger area decreases system efficiency due to additional air permeation.

To prevent reduction of the system efficiency at a lower dehumidification load the membrane module was divided into three equal parts (10m²/1000cfm each) connected in series to one another for dehumidification of the feed airflow. Each section is connected to the same intermediate compressor with vacuum valves that connect and disconnect the membrane sections as needed based on a signal from a control system.

System operation was divided in three stages. The first stage has a membrane area of 10 m²/1000 cfm, and operates during the minimum dehumidification load. The second stage enables first and second membrane dehumidification sections with total area of 20 m²/1000 cfm. The third stage enables all available membrane area of 30 m²/1000cfm and is used for the maximum dehumidification load.

Table 41. Three stage membrane air-conditioning system energy efficiency (actual membrane properties)

Parameter	Constant membrane area system	Variable membrane area system
Number of the membrane module sections	1	3
Membrane section area m² per 1000 cfm of maximum airflow rate	30.0	10.0
Membrane air-conditioning system energy consumption (fan power not included) (kWh/ft²-year)	3.78	3.57
Effective coefficient of performance (kW/kW)	3.383	3.58
Average permeate pressure	1.044	0.78
Minimum permeate pressure	0.36	0.29
Effective energy efficiency (kW/TR)	1.04	0.98

Modifications of the system design provided improvement of annual energy efficiency from 1.04 to 0.98 kW/TR by improvement of the system operation during cooling loads that are above or below the optimum range.

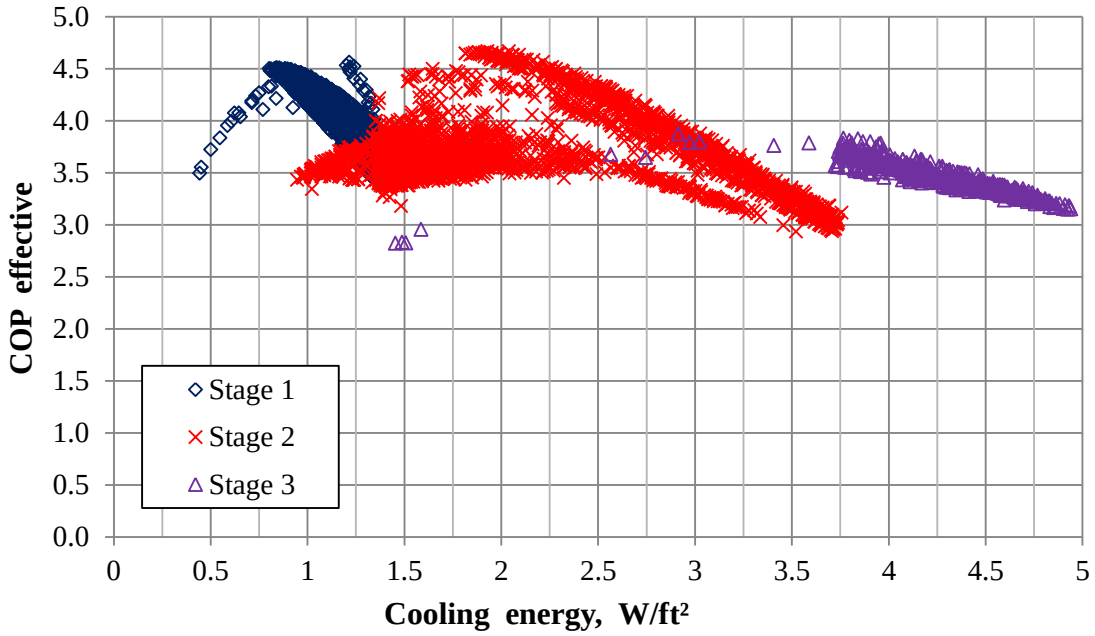

Figure 85. Variable membrane area air-conditioning system efficiency as a function of a cooling load (actual membrane properties)

The proposed modification improved system performance to an average value of 0.98 kW/TR but did not exceed baseline system chiller energy efficiency of 0.6 kW/TR.

5.6.4 Three stage system efficiency analysis (design properties)

The same membrane air-conditioning system as in Section 5.6.3 was analyzed with the only difference that the membrane with the target properties is used. The target constant membrane effective water vapor permeance is 8 E-6 kmol/kPa-m²-s and the effective air permeance is 6 E-10 kmol/kPa-m²-s.

Table 42. Three stage membrane air-conditioning system energy efficiency comparison

Parameter	Target membrane	Actual membrane
Selectivity coefficient	13,333	1,931
PAB_air, kmol/(kPa-m²-s)	0.6 E-9	2.9E-9
PAB_water, kmol/(kPa-m²-s)	8.0 E-6	5.6E-6
Number of the membrane module sections	3	3
Membrane section area, m² per 1000 cfm of maximum airflow rate	10.0	10.0
Membrane air-conditioning system energy consumption (fan power not included), kWh/ft²-year	2.24	3.57
Average permeate pressure, kPa	0.94	0.78
Minimum permeate pressure, kPa	0.59	0.29
Effective coefficient of performance, kW/kW	5.71	3.58
Effective energy efficiency, kW/TR	0.62	0.98

Analysis of the three stage membrane air-conditioning system shows that the effective coefficient of performance is changing between 5 and 8 (Figure 86). Energy efficiency can be further optimized with improvement of the membrane material properties. An air-conditioning system that uses the membrane material with the target properties can achieve energy efficiency of 0.62 kW/TR comparable to the baseline annual average chiller energy efficiency of 0.6 kW/TR.

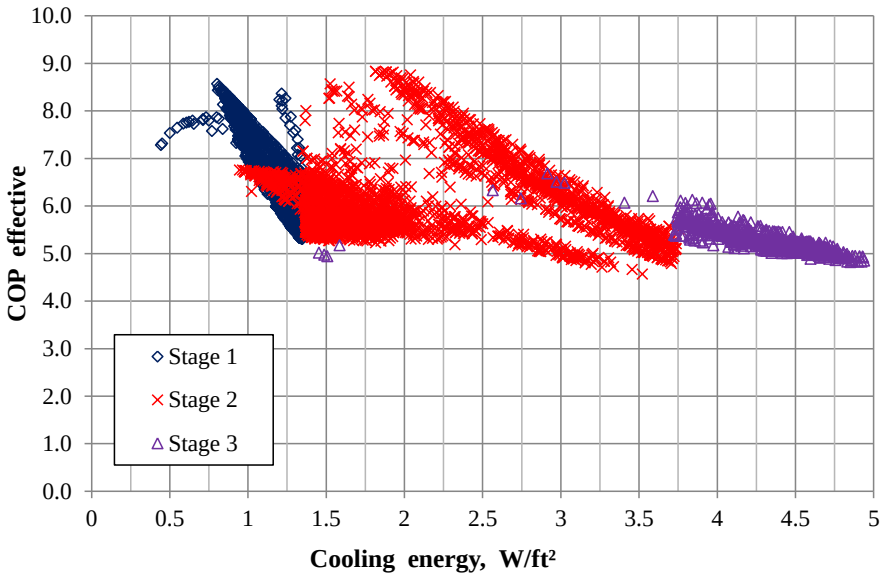

Figure 86. Variable membrane area air-conditioning system efficiency as a function of a cooling load (target membrane properties)

5.7 Conclusions

The membrane operating temperature during the dehumidification process is between 60 °F and 85 °F (16-30 °C) and is limited by the outside air maximum wet-bulb temperature. In this temperature range, the average effective air permeance should not exceed (3±0.5)E-9 kmol/(kPa-m²-s) and average effective water permeance should be at least (5±2)E-6 kmol/kPa-m²-s.

Application of a dual stage membrane dehumidification system will reduce membrane air-conditioning system energy consumption to 78% of the single stage system or by more than 20%.

Changing the membrane area, at fixed inlet and outlet conditions, will require change of the total permeate pressure to provide the same dehumidification of the supply airflow stream. As a result of the membrane permeate pressure change the maximum effective COP of the system will also change.

The membrane air-conditioning system operating at a constant airflow rate and tested membrane material properties will require 60 m²/1000cfm of the membrane surface to obtain maximum efficiency (COP 3.74 or 0.94 kW/TR). With the consideration of the membrane material cost, the area can be reduced to 40 m²/1000cfm that provides a COP 3.44 and energy efficiency of 1.02 kW/TR for the design conditions.

Increasing the outdoor air wet-bulb temperature decreases the effective system coefficient of performance. For the membrane with tested membrane material properties the reduction of COP is from 4 to 3 when outdoor air wet-bulb temperature increases from 55°F to 85°F. The ideal system with the target membrane material can provide a COP between 15 and 8 or energy efficiency between 0.23 kW/TR and 0.44 kW/TR.

The annual hourly simulation for the actual membrane air-conditioning system shows that the optimum membrane area is 26 m² per 1000 cfm of the maximum airflow rate. The reduction of the optimum membrane area can be explained by the fact that the air-conditioning system operates most of the time with an airflow rate that is much below the design value.

The membrane air-conditioning system efficiency is a function of the dehumidification load. Reduction of the load or increase above the optimum level will cause reduction of system energy efficiency. At the optimum system load of 2.2 W/ft² of the building area, the system COP increased to the maximum level 4.4 (0.8 kW/TR).

To minimize effect of building cooling load changes, the membrane module can be separated in three equal area sections connected in parallel. This modification increases annual average effective energy efficiency for the actual membrane from 1.04 to 0.98 kW/TR.

Separation of the membrane module into three sections and application of the membrane material with the target properties provides system annual operation energy efficiency of 0.62 kW/TR. The effective coefficient of performance obtained for the target membrane air-conditioning system shows that the proposed system can be competitive with existing water cooled chiller systems based on the annual energy efficiency.

6 SUMMARY AND CONCLUSIONS

6.1 Summary

The goal of this research is to investigate the opportunity for application of the membrane separation process based on inorganic zeolite membrane material for dehumidification in building air-conditioning and ventilation system. The investigation of different systems based on the membrane dehumidification process was made for conditions of warm and hot climates.

Three main applications targets for zeolite membrane building dehumidification process were studied: flat plate membrane energy recovery ventilation; outdoor air dehumidification, as part of a dedicated outdoor air system (DOAS); and an air-conditioning system, that combines evaporative cooling with the membrane dehumidification system.

Theoretical thermodynamic and heat transfer analytical models of a zeolite membrane ERV device were developed. Two configurations (counter-flow and cross-flow) of unmixed fluids single pass flat plate ERV systems were analyzed. Based on these models, theoretical energy effectiveness of energy recovery ventilation system was estimated as the ratio of the airflow rate and available membrane area.

A single stage experimental dehumidification system was designed and built to test application of the membrane separation process using a zeolite membrane for a building DOAS operating in a hot and humid climate. In this study, six zeolite membrane modules were used. This experimental system combines a membrane dehumidification unit with a conventional chilled water cooling coil that received chilled water from a direct expansion refrigeration system to provide sensible cooling.

The membrane dehumidification unit operated at a medium vacuum with a total pressure of 0.5-2 kPa on a permeate side of the membrane. Several hundred experiments were conducted for the system design conditions as well as for variable inlet air stream conditions (volumetric flow, relative humidity, and temperature), variable permeate total

pressure, and variable vacuum condenser pressure. The goal of these experiments was to investigate membrane properties and system energy efficiency at different operation conditions.

The single stage membrane dehumidification system was modified to increase dehumidification capacity and energy efficiency of the membrane dehumidification system. The modified system includes two membrane modules connected in series relative to the feed airflow. The vacuum side of the system was modified, so each membrane module was equipped with a dedicated intermediate compressor.

The annual energy performance of a membrane dehumidification system incorporated in a dedicated outside air system for outside air stream dehumidification was simulated for an actual building located in College Station, Texas based on the previously obtained experimental results and actual weather data.

A further modification to the experimental membrane dehumidification system was made by replacing the vapor-compression cooling component with two evaporative coolers (direct adiabatic cooling systems) to provide system operation without fluorocarbon gases (refrigerants). With this modification, multiple experimental tests were conducted to investigate effective air and water permeance as a function of feed airstream temperature and its impact on the system energy efficiency.

To reduce the energy consumption required for the operation of a membrane module air-conditioning system, an alternative system configuration was tested with two membrane modules. Each module had independent pressure control that allow the permeate pressure of the first stage to be increased in comparison to the second stage that increased actual COP by 20%.

The experimental results obtained were used to analyze performance of the membrane air-conditioning system application in a large office building located in College Station, Texas. The annual energy efficiency analysis of the proposed system was conducted for membranes with actual and target properties. The result shows that the proposed system can be competitive with conventional refrigerant compression water cooled chiller systems.

6.2 Conclusions

This work studies the membrane separation process for building dehumidification in three main applications: an energy recovery ventilation (ERV) system; outdoor air dehumidification, as part of a dedicated outdoor air system (DOAS); and an air-conditioning system that combines evaporative cooling and the membrane dehumidification system. In this study, six membrane modules were used with microporous molecular sieve non-organic zeolite composite membrane material with Ni-support and a medium vacuum on the permeate side of the membrane. The main conclusions drawn from the analytical and experimental results are:

- The membrane ERV system with a channel height of 2 mm and cross-flow operation constructed from the membrane material with water permeance of 8E-6 kmol/(kPa·m²·s) can operate with a combined heat and mass transfer effectiveness of 0.8 for a membrane area of 0.25 m²/cfm of airflow.
- The diffusion resistance and the membrane resistance are approximately equal for a flow velocity of 1 m/s when the membrane permeance to water vapor is 8E-6 kmol/(kPa·m²·s).
- A 2 mm channel spacing normal to the membrane was determined to be the optimum spacing to maximize measurable mass and heat transfer through the membrane while not creating excessive pressure drops.
- Experimental test results of membrane dehumidification system at the design airflow rate of 30 cfm (850 lpm) showed that the static pressure drop across membrane module is above 3 in w.g. (750 Pa). The design static pressure drop of 1 in w.g. (249 Pa) can be reached with further modification of the membrane module construction.
- Decreasing the feed airflow rate at a constant permeate pressure will reduce the retentate relative humidity, and as a result, decrease the membrane selectivity due to a decrease of adsorption-induced expansion of the crystals that block non-zeolite pores.

- To provide higher selectivity, when feed airflow rate is reduced, dehumidification system control should increase permeate pressure or use sectioning of the membrane module to keep retentate relative humidity constant at the setpoint level above 30% RH for the current level of membrane development.
- Changing the total permeate pressure of the membrane module has twice as much effect on effective water permeance as on effective air permeance. Reduction of permeate pressure has a relatively small effect on selectivity coefficient but a large impact on separation factor.
- The effective water permeance does not depend on humidity when relative humidity is above 30%. Effective water permeance has a temperature dependence and increases with increase of temperature from 6E-6 to 8E-6 kmol/(kPa-m²-s), when temperature increases from 65°F to 90°F.
- The effective air permeance has an exponential dependence on retentate flow relative humidity below 30% and is relatively constant near 5E-9 kmol/(kPa-m²-s) when retentate airflow relative humidity is above 30%.
- An experimental dehumidification system configuration with two modules demonstrated that effective system COP can be increased to 3.1 if retentate airflow relative humidity is above 30%. This is 20% energy savings in comparison to the single stage system.
- Application of the membrane dehumidification system in a DOAS increased COP of the dehumidification process from 4.1 (chiller) to 7.4 (membrane dehumidification system) that provided 6-10% savings of HVAC energy consumption due to the small fraction of dehumidification load in the typical office building.
- Membrane air-conditioning system tests show that with the existing technology, zeolite membrane average effective air permeance should not exceed (3±0.5)E-9 kmol/(kPa-m²-s) and average effective water permeance

should be at least (5±2)E-6 kmol/kPa-m²-s that provides selectivity above 1500 and can be further improved.

- Changing the membrane area, at fixed inlet and outlet conditions, requires changing the total permeate pressure to provide the same dehumidification of the supply airflow stream. As a result of the membrane permeate pressure change, the maximum effective COP of the system will also change.
- The annual hourly simulation for the actual membrane air-conditioning system shows that the optimum membrane area is 26 m² per 1000 cfm of the maximum airflow rate.
- To minimize effect of building cooling load changes, the membrane module can be separated into three equal area sections connected in parallel. This modification increases annual average effective energy efficiency for the actual membrane from 1.04 to 0.98 kW/TR.
- Separation of the membrane module into three sections and application of the membrane material with the target properties provides system annual operation energy efficiency of 0.62 kW/TR. The effective coefficient of performance obtained for the target membrane air-conditioning system shows that the proposed system can be competitive with the existing water cooled chiller systems based on the estimated annual energy efficiency.

REFERENCES

[1] Bernardo, P., Drioli, E., and Golemme, G., 2009, "Membrane Gas Separation: A Review/State of the Art," Ind Eng Chem Res, 48(10), pp. 4638-4663.

[2] Tanskyi, O., and Claridge, D. E., 2011, "Theoretical Minimum Energy Use of a Building HVAC System," Proc. 11th International Conference for Enhanced Building Operation Brooklyn, New York, USA.

[3] Bynum, J., 2012, "Thermodynamic Modeling of a Membrane Dehumidification System," Ph.D. Dissertation, Texas A&M University.

[4] Liu, W., 2010, "High Efficiency, on-Line Membrane Air Dehumidifier Enabling Sensible Cooling for Warm and Humid Climates," ARPA-E Control Number 0289-1530.

[5] Shimekit, B., and Mukhtar, H., 2012, "Natural Gas Purification Technologies - Major Advances for CO2 Separation and Future Directions," Advances in Natural Gas Technology, pp. 235-271.

[6] Nenoff, T. M., and Dong, J., 2009, "Highly Selective Zeolite Membranes," Ordered Porous Solids. Recent Advances and Prospects, V. Valtchev, S. Mintova, and M. Tsapatsis, eds., Elsevier, Amsterdam, pp. 365-386.

[7] Ockwig, N. W., and Nenoff, T. M., 2007, "Membranes for hydrogen separation," Chem Rev, 107(10), pp. 4078-4110.

[8] Van de Graaf, J. M., Kapteijn, F., and Moulijn, J. A., 1999, "Modeling permeation of binary mixtures through zeolite membranes," Aiche J, 45(3), pp. 497-511.

[9] Van de Graaf, J. M., Van der Bijl, E., Stol, A., Kapteijn, F., and Moulijn, J. A., 1998, "Effect of operating conditions and membrane quality on the separation performance of composite silicalite-1 membranes," Ind Eng Chem Res, 37(10), pp. 4071-4083.

[10] Caro, J., Noack, M., Kolsch, P., and Schafer, R., 2000, "Zeolite membranes - state of their development and perspective," Micropor Mesopor Mat, 38(1), pp. 3-24.

[11] Yang, M., Crittenden, B. D., Perera, S. P., Moueddeb, H., and Dalmon, J. A., 1999, "The hindering effect of adsorbed components on the permeation of a non-adsorbing component through a microporous silicalite membrane: The potential barrier theory," J Membrane Sci, 156(1), pp. 1-9.

[12] Xing, R., Rao, Y. X., TeGrotenhuis, W., Canfield, N., Zheng, F., Winiarski, D. W., and Liu, W., 2013, "Advanced thin zeolite/metal flat sheet membrane for energy efficient air dehumidification and conditioning," Chem Eng Sci, 104, pp. 596-609.

[13] Arruebo, M., Mallada, R., and Pina, M. P., 2008, "Zeolite Membranes," Handbook of Membrane Separations, CRC Press, Boca Raton, Florida, pp. 269-323.

[14] Miachon, S., Landrivon, E., Aouine, M., Sun, Y., Kumakiri, I., Li, Y., Prokopova, O. P., Guilhaume, N., Giroir-Fendler, A., Mozzanega, H., and Dalmon, J. A., 2006, "Nanocomposite MFI-alumina membranes via pore-plugging synthesis - Preparation and morphological characterisation," J Membrane Sci, 281(1-2), pp. 228-238.

[15] Pabby, A. K., Rizvi, S. S. H., and Sastre, A. M., 2009, Handbook of membrane separations: chemical, pharmaceutical, food, and biotechnological applications, CRC Press, Boca Raton, Florida.

[16] Lovallo, M. C., Gouzinis, A., and Tsapatsis, M., 1998, "Synthesis and characterization of oriented MFI membranes prepared by secondary growth," Aiche J, 44(8), pp. 1903-1913.

[17] Lai, Z. P., Bonilla, G., Diaz, I., Nery, J. G., Sujaoti, K., Amat, M. A., Kokkoli, E., Terasaki, O., Thompson, R. W., Tsapatsis, M., and Vlachos, D. G., 2003, "Microstructural optimization of a zeolite membrane for organic vapor separation," Science, 300(5618), pp. 456-460.

[18] Gibbons, W. T., Zhang, Y. F., Falconer, J. L., and Noble, R. D., 2010, "Inhibiting crystal swelling in MFI zeolite membranes," J Membrane Sci, 357(1-2), pp. 54-61.

[19] Lee, J. B., Funke, H. H., Noble, R. D., and Falconer, J. L., 2008, "High selectivities in defective MFI membranes," J Membrane Sci, 321(2), pp. 309-315.

[20] Chen, Y. D., and Yang, R. T., 1992, "Predicting binary Fickian diffusivities from pure-component Fickian diffusivities for surface-diffusion," Chem Eng Sci, 47(15-16), pp. 3895-3905.

[21] Johnson, J. E., 1997, "Heat and mass transfer between two fluid streams separated by a thin, permeable barrier," Ph.D. Dissertation, University of Minnesota.

[22] Zhang, L. Z., and Niu, J. L., 2001, "Energy requirements for conditioning fresh air and the long-term savings with a membrane-based energy recovery ventilator in Hong Kong," Energy, 26(2), pp. 119-135.

[23] Air Products and Chemicals, I., 2014, "Air Products PRISM Membranes. Frequently Asked Questions."

[24] Auvil, S. R., Choe, J. S., and Kellogg, L. J., 1993, "Use of membrane separation to dry gas streams containing water vapor. United States Patent: 5259869," U. S. Patent, ed.United States.

[25] El-Dessouky, H. T., Ettouney, H. M., and Bouhamra, W., 2000, "A novel air conditioning system - Membrane air drying and evaporative cooling," Chem Eng Res Des, 78(A7), pp. 999-1009.

[26] Wang, K. L., Mccray, S. H., Newbold, D. D., and Cussler, E. L., 1992, "Hollow Fiber Air Drying," J Membrane Sci, 72(3), pp. 231-244.

[27] Asaeda, M., Du, L. D., and Ikeda, K., 1986, "Experimental Studies of Dehumidification of Air by an Improved Ceramic Membrane," J Chem Eng Jpn, 19(3), pp. 238-240.

[28] Isetti, C., Nannei, E., and Magrini, A., 1997, "On the application of a membrane air-liquid contactor for air dehumidification," Energ Buildings, 25(3), pp. 185-193.

[29] Ray, R., Newbold, D. D., McCray, S. B., Friesen, D. T., and Kliss, M., 1992, "A novel membrane device for the removal of water vapor and water droplets from air," SAE technical paper series (921322).

[30] Zhang, L. Z., Zhu, D. S., Deng, X. H., and Hua, B., 2005, "Thermodynamic modeling of a novel air dehumidification system," Energ Buildings, 37(3), pp. 279-286.

[31] Woods, J., 2014, "Membrane processes for heating, ventilation, and air conditioning," Renew Sust Energ Rev, 33, pp. 290-304.

[32] Bonne, U., Deetz, D. W., Lai, J. H., Odde, D. J., and Zook, J. D., 1990, "Membrane dehumidification. United States Patent: 4900448," U. S. Patent, ed., Honeywell Inc., United States.

[33] DiMartino, S. P., 1990, "Membrane drying of gas feeds to low temperature units. United States Patent: 4952219," U. S. Patent, ed., Air Products and Chemicals, Inc., United States.

[34] Culp, C. H., and Claridge, D. E., 2013, "Systems and methods for air dehumidification and sensible cooling using a multiple stage pump. United States Patent: 8496732," U. S. Patent, ed., The Texas A&M University System, United States.

[35] Claridge, D. E., and Culp, C. H., 2013, "Systems and methods for air dehumidification and cooling with membrane water vapor rejection.United States Patent: 8500848," U. S. Patent, ed., The Texas A&M University System, United States.

[36] Claridge, D. E., and Culp, C. H., 2014, "Systems and methods for multi-stage air dehumidification and cooling. United States Patent: 8641806," U. S. Patent, ed., The Texas A&M University System, United States.

[37] Ito, A., 2000, "Dehumidification of air by a hygroscopic liquid membrane supported on surface of a hydrophobic microporous membrane," J Membrane Sci, 175(1), pp. 35-42.

[38] Zhang, L. Z., Liang, C. H., and Pei, L. X., 2008, "Heat and moisture transfer in application scale parallel-plates enthalpy exchangers with novel membrane materials," J Membrane Sci, 325(2), pp. 672-682.

[39] Fehrm, M., Reiners, W., and Ungemach, M., 2002, "Exhaust air heat recovery in buildings," Int J Refrig, 25(4), pp. 439-449.

[40] Christman, K. D., Haberl, J. S., and Claridge, D. E., 2009, "Analysis of energy recovery ventilator savings for Texas buildings," Proceedings of the Ninth International Conference for Enhanced Building Operations, Energy Systems Laboratory, Texas A&M University, College Station, Texas, Austin, Texas.

[41] Min, J. C., and Su, M., 2010, "Performance analysis of a membrane-based enthalpy exchanger: Effects of the membrane properties on the exchanger performance," J Membrane Sci, 348(1-2), pp. 376-382.

[42] Min, J. C., Hu, T., and Song, Y. Z., 2011, "Experimental and numerical investigations of moisture permeation through membranes," J Membrane Sci, 367(1-2), pp. 174-181.

[43] Nasif, M., Al-Waked, R., Morrison, G., and Behnia, M., 2010, "Membrane heat exchanger in HVAC energy recovery systems, systems energy analysis," Energ Buildings, 42(10), pp. 1833-1840.

[44] Zhou, Y. P., Wu, J. Y., and Wang, R. Z., 2007, "Performance of energy recovery ventilator with various weathers and temperature set-points," Energ Buildings, 39(12), pp. 1202-1210.

[45] Kistler, K. R., and Cussler, E. L., 2002, "Membrane modules for building ventilation," Chem Eng Res Des, 80(A1), pp. 53-64.

[46] Min, J. C., and Su, M., 2010, "Performance analysis of a membrane-based energy recovery ventilator: Effects of membrane spacing and thickness on the ventilator performance," Appl Therm Eng, 30(8-9), pp. 991-997.

[47] Min, J. C., and Su, M., 2011, "Performance analysis of a membrane-based energy recovery ventilator: Effects of outdoor air state," Appl Therm Eng, 31(17-18), pp. 4036-4043.

[48] Kozubal, E., Woods, J., Burch, J., Boranian, A., and Tim, M., 2011, "Desiccant Enhanced Evaporative Air-Conditioning (DEVap): Evaluation of a New Concept in Ultra Efficient Air Conditioning," No. NREL/TP-5500-49722.

[49] Woods, J., and Kozubal, E., 2013, "A desiccant-enhanced evaporative air conditioner: Numerical model and experiments," Energ Convers Manage, 65, pp. 208-220.

[50] Uges, P., 2006, "Air conditioning using R718 (water) as refrigerant," 7th IIR Gustav Lorentzen Conference on Natural Working Fluids (29 - 31 May 2006), Int. Institute of Refrigeration, Trondheim, Norway

[51] Kanoglu, M., Carpinlioglu, M. O., and Yildirim, M., 2004, "Energy and exergy analyses of an experimental open-cycle desiccant cooling system," Appl Therm Eng, 24(5-6), pp. 919-932.

[52] American Water Works Association Research Foundation., Lyonnaise des eaux-Dumez (Firm), and South Africa. Water Research Commission., 1996, Water treatment membrane processes, McGraw-Hill, New York.

[53] Mulder, M., 1991, Basic principles of membrane technology, Kluwer Academic, Dordrecht, Netherlands ; Boston.

[54] Krishna, R., and Wesselingh, J. A., 1997, "Review article number 50 - The Maxwell-Stefan approach to mass transfer," Chem Eng Sci, 52(6), pp. 861-911.

[55] Kapteijn, F., Moulijn, J. A., and Krishna, R., 2000, "The generalized Maxwell-Stefan model for diffusion in zeolites: sorbate molecules with different saturation loadings," Chem Eng Sci, 55(15), pp. 2923-2930.

[56] Bird, R. B., Stewart, W. E., and Lightfoot, E. N., 2007, Transport phenomena, J. Wiley, New York.

[57] Ghoreyshi, A. A., Farhadpour, F. A., and Soltanieh, M., 2004, "A general model for multicomponent transport in nonporous membranes based on Maxwell-Stefan formulation," Chem Eng Commun, 191(4), pp. 460-499.

[58] Madaeni, S. S., Moradi, A., and Kazemi, V., 2009, "PDMS Coated Polyethersulphone Composite Membranes for Separation of Propylene and Nitrogen Gas Mixtures," Iran Polym J, 18(11), pp. 873-879.

[59] Vankelecom, I. F. J., Scheppers, E., Heus, R., and Uytterhoeven, J. B., 1994, "Parameters influencing zeolite incorporation in PDMS membranes," J Phys Chem-Us, 98(47), pp. 12390-12396.

[60] Kesting, R. E., and Fritzsche, A. K., 1993, Polymeric gas separation membranes, Wiley, New York.

[61] Choi, S. H., Kim, J. H., and Lee, S. B., 2007, "Sorption and permeation behaviors of a series of olefins and nitrogen through PDMS membranes," J Membrane Sci, 299(1-2), pp. 54-62.

[62] Lie, J. A., and Hagg, M. B., 2006, "Carbon membranes from cellulose: Synthesis, performance and regeneration," J Membrane Sci, 284(1-2), pp. 79-86.

[63] Stern, S. A., 1968, "The "barrer" permeability unit," Journal of Polymer Science Part A-2: Polymer Physics, 6(11), pp. 1933-1934.

[64] American Society for Testing and Materials International., 1995, "ASTM E96-95. Standard Test Methods for Water Vapor Transmission of Materials," American Society for Testing and Materials International.

[65] DIN, 1991, "DIN 53122. Testing of plastics and elastomer films, paper, board and other sheet materials - Determination of water vapour transmission - Part 1: Gravimetric method.," Deutsches Institut für Normung.

[66] Metz, S. J., 2003, "Water vapor and gas transport through polymeric membranes," PrintPartners Ipskamp B.V., Enschede, The Netherlands, p. 143.

[67] Elshof, J. E., Abadal, C. R., Sekulic, J., Chowdhury, S. R., and Blank, D. H. A., 2003, "Transport mechanisms of water and organic solvents through microporous silica in the pervaporation of binary liquids," Micropor Mesopor Mat, 65(2-3), pp. 197-208.

[68] Venkatesan, R., and Fogler, H. S., 2004, "Comments on analogies for correlated heat and mass transfer in turbulent flow," Aiche J, 50(7), pp. 1623-1626.

[69] Incropera, F. P., and DeWitt, D. P., 2002, Fundamentals of heat and mass transfer, J. Wiley, New York.

[70] Mills, A. F., 1999, Heat transfer, Prentice Hall, Upper Saddle River, New Jersey.

[71] Basmadjian, D., Farnood, R., and Basmadjian, D., 2007, The art of modeling in science and engineering with Mathematica, Chapman & Hall/CRC, Boca Raton, Florida.

[72] Zigrang, D. J., and Sylvester, N. D., 1985, "A review of explicit friction factor equations," Transactions of the ASME. Journal of Energy Resources Technology, 107.

[73] Nellis, G., and Klein, S. A., 2009, Heat transfer, Cambridge University Press, Cambridge ; New York.

[74] Hu, Y., Topolkaraev, V., Hiltner, A., and Baer, E., 2001, "Measurement of water vapor transmission rate in highly permeable films," Journal of Applied Polymer Science, 81(7), pp. 1624-1633.

[75] Kumaran, M. K., 1998, "Interlaboratory comparison of the ASTM Standard Test Methods for Water Vapor Transmission of Materials (E 96-95)," J Test Eval, 26(2), pp. 83-88.

[76] Mukhopadhyaya, P., Kumaran, K., Lackey, J., and van Reenen, D., 2007, "Water vapor transmission measurement and significance of corrections," Am Soc Test Mater, 1495, pp. 21-32.

[77] Çengel, Y. A., 2005, Heat transfer: a practical approach, McGraw-Hill, New Delhi.

[78] American Society of Heating Refrigerating and Air-Conditioning Engineers., 2008, ANSI/ASHRAE Standard 84 - 2008: Method of Testing Air-to-Air Heat/Energy Exchangers American Society of Heating, Refrigerating and Air-Conditioning Engineers, Atlanta, Georgia.

[79] Klein, S. A., and Alvarado, F. L., 2014, "Engineering equation solver (EES), F-Chart Software," http://www.fchart.com/.

[80] Kistler, K. R., 2000, "Membrane modules for building ventilation," Ph.D. Dissertation, University of Minnesota.

[81] Rees, J. A., 2013, "Energy Recovery Ventilator Membrane Efficiency Testing," Master of Science Thesis, Texas A&M University.

[82] Schaff, F. N., 2014, "Design and Development of a Vacuum Dehumidification Test Facility," Master of Science Thesis, Texas A&M University.

[83] American Society of Heating Refrigerating and Air-Conditioning Engineers., 2007, "ANSI/ASHRAE Standard 51 - 2007: Laboratory Methods of Testing Fans for Certified Aerodynamic Performance Rating.," ASHRAE standard, American Society of Heating, Refrigerating and Air-Conditioning Engineers, Atlanta, Georgia.

[84] Taylor, B. N., and Kuyatt, C. E., 1994, Guidelines for evaluating and expressing the uncertainty of NIST measurement results, U.S. Department of Commerce, Technology Administration, National Institute of Standards and Technology, Gaithersburg, Maryland.

[85] American Society of Heating Refrigerating and Air-Conditioning Engineers., and American National Standards Institute., 2013, ANSI/ASHRAE Standard 62.1 - 2013: Ventilation for acceptable indoor air quality, American Society of Heating, Refrigerating and Air-Conditioning Engineers, Atlanta, Georgia.

[86] Abushakra, B., Sreshthaputra, A., Haberl, J. S., and Claridge, D. E., 2001, "Compilation of Diversity Factors and Schedules for Energy and Cooling Load Calculations, ASHRAE Research Project 1093-RP, Final Report," Energy Systems Laboratory, Texas A&M University.

[87] Kreider, J. F., and Rabl, A., 1994, Heating and cooling of buildings: design for efficiency, McGraw-Hill, Dubuque, Iowa.

[88] American Society of Heating Refrigerating and Air-Conditioning Engineers., and American National Standards Institute., 2004, ANSI/ASHRAE Standard 55 - 2004: Thermal environmental conditions for human occupancy, ASHRAE, Atlanta, Georgia.

APPENDIX A

AIRFLOW SENSORS COMPARISON

Three main flow sensors were used during the experiments described in this work : Omega FLR1005-D (0.4 – 2 lpm), Omega FLR1006-D (1.0 - 5.0 lpm) and Agilent ADM2000 (5E-4 - 1.0 lpm). All of them have manufacturer calibration certificates. The main tool for measuring permeate airflow was the Omega FLR1005-D (0.4 – 2 LPM) airflow sensor, so this sensor is compared to the other.

Comparison of the Pelton-type turbine wheel sensor Omega FLR1005-D (0.4-2 lpm) and the Pelton-type turbine wheel sensor Omega FLR1006-D (1.0-5.0 lpm) shows agreement of readings between them within the accuracy of each sensor (Figure 87).

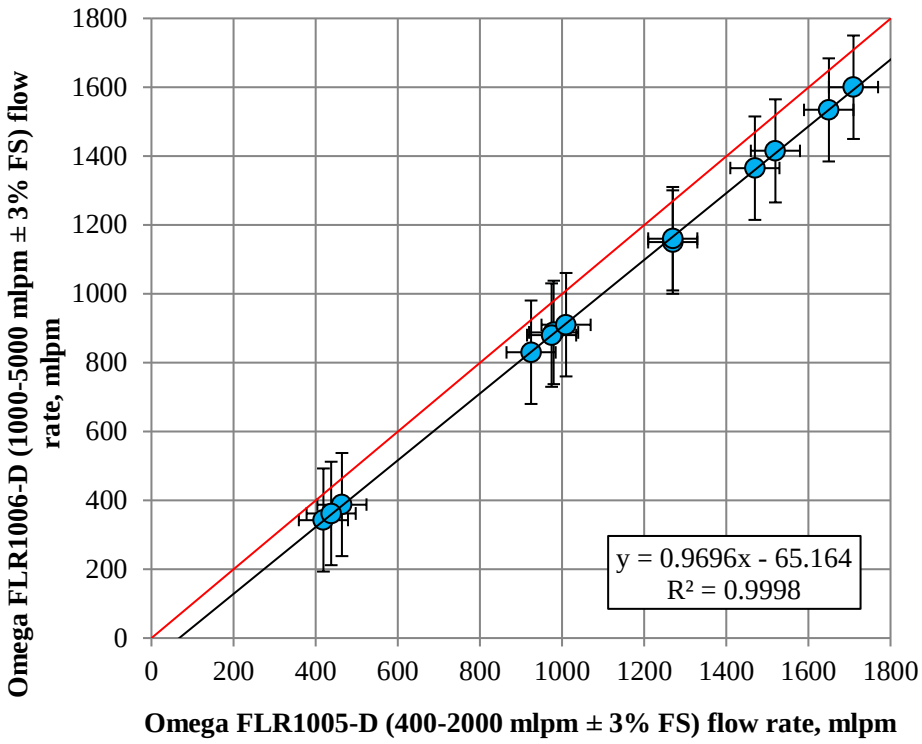

Figure 87. Comparison of airflow sensors Omega FLR1005-D and FLR1006-D

Another series of tests was made to compare FLR1005-D (0.4-2 lpm) with positive displacement volumetric flow sensor Definer 220M. Flow sensor Definer 220M is ISO 17025 traceable and includes integrated temperature sensors and pressure transducers in the flow stream. This sensor provides compensation for standard conditions - allowing traceable verifications of mass flow devices. Although the reading from FLR1005-D is the actual measured flow that is not converted to standard conditions, the difference between recorded values is within the accuracy of the airflow sensors (Figure 88).

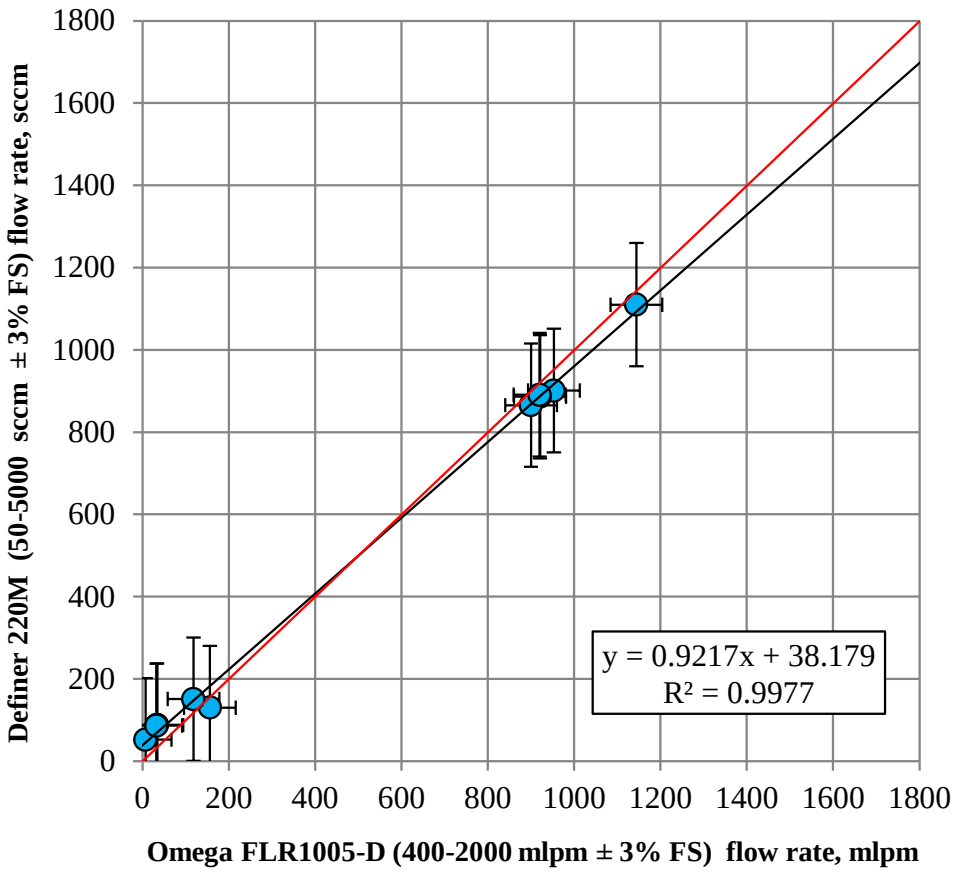

Figure 88. Comparison of airflow sensors Omega FLR1005-D and Definer 220M

The last series of experiments was a comparison of the Omega FLR1005-D Pelton-type turbine wheel sensor with the Agilent ADM2000. The Agilent ADM2000 airflow sensor operation is based on a diaphragm movement proportional to the flow rate. Comparison was made in the lower airflow rate diapason relative to previous tests (Figure 89). Sensor readings agree within the accuracy interval of each sensor.

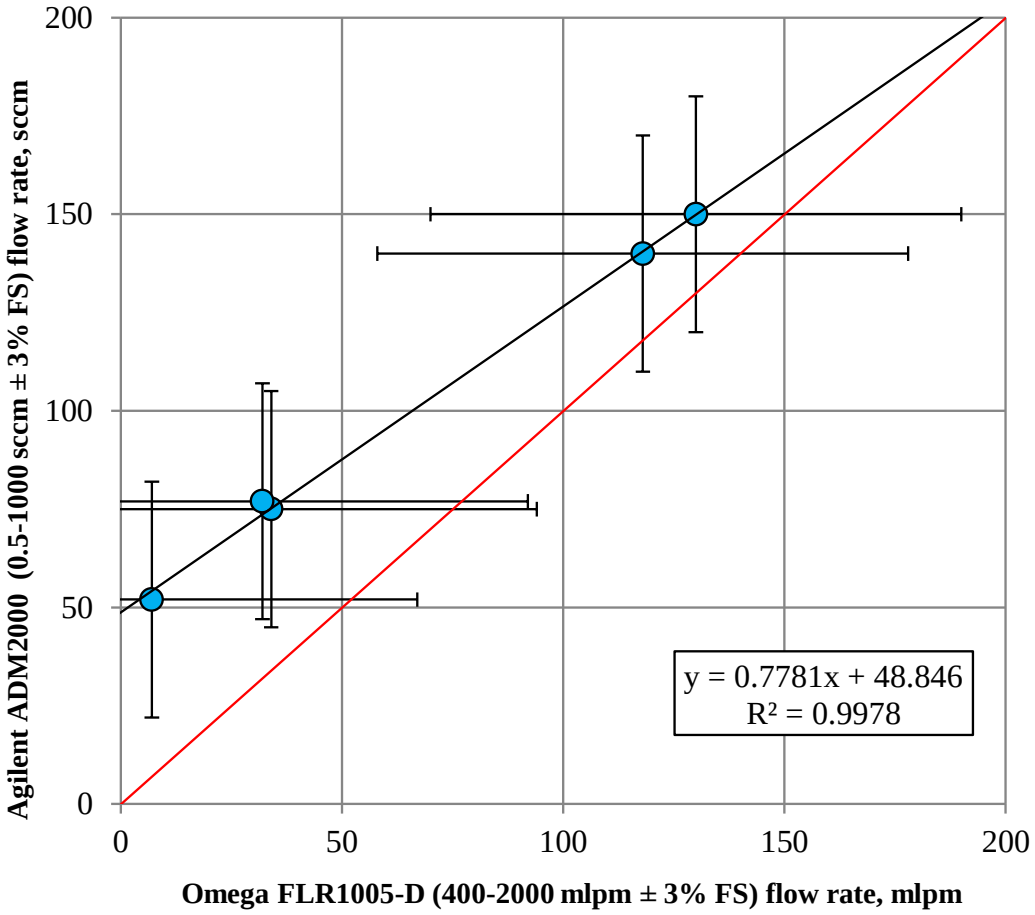

Figure 89. Comparison of airflow sensors Omega FLR1005-D and Agilent ADM2000

Experimental results of all test show agreement between the sensor measurements within the accuracy range defined by the sensor manufacturer.

APPENDIX B
VACUUM SYSTEM LEAK TEST

To estimate system leakage, a series of experiments was made with the vacuum system exhaust airflow measured by four airflow sensors. The membrane module was disconnected from the vacuum system to isolate the air leakage from the vacuum system components. Once the membrane module was disconnected, the KF-40 attachment fittings were clamped together to ensure these components were evaluated for leakage as well, which is shown in Figure 90.

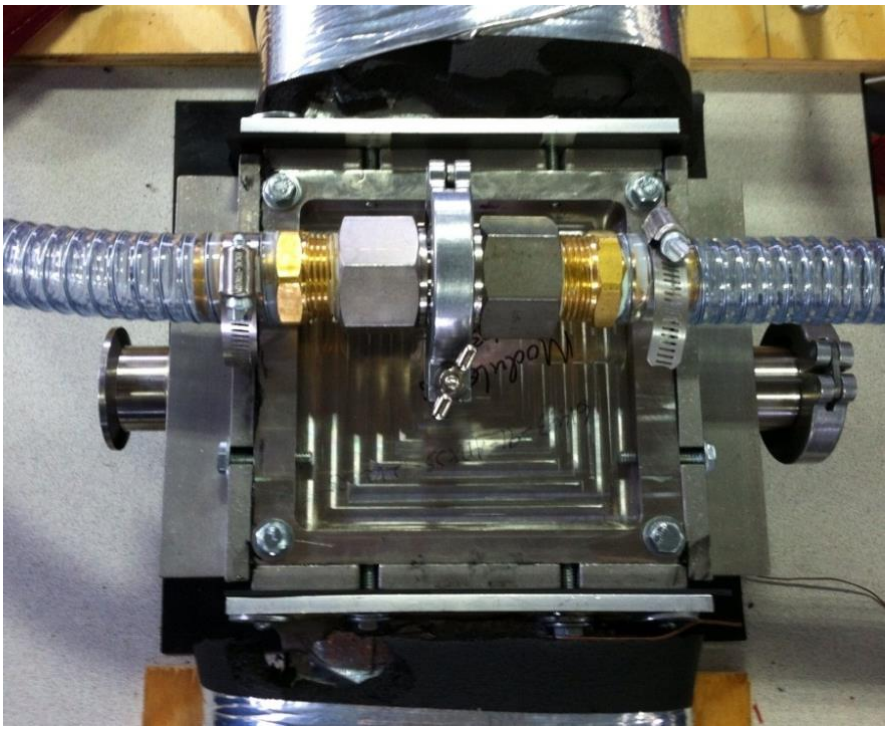

Figure 90. Experimental system vacuum system leak test configuration of the membrane module connection

The normal configuration for these KF-40 fittings is depicted in Figure 91 for comparison.

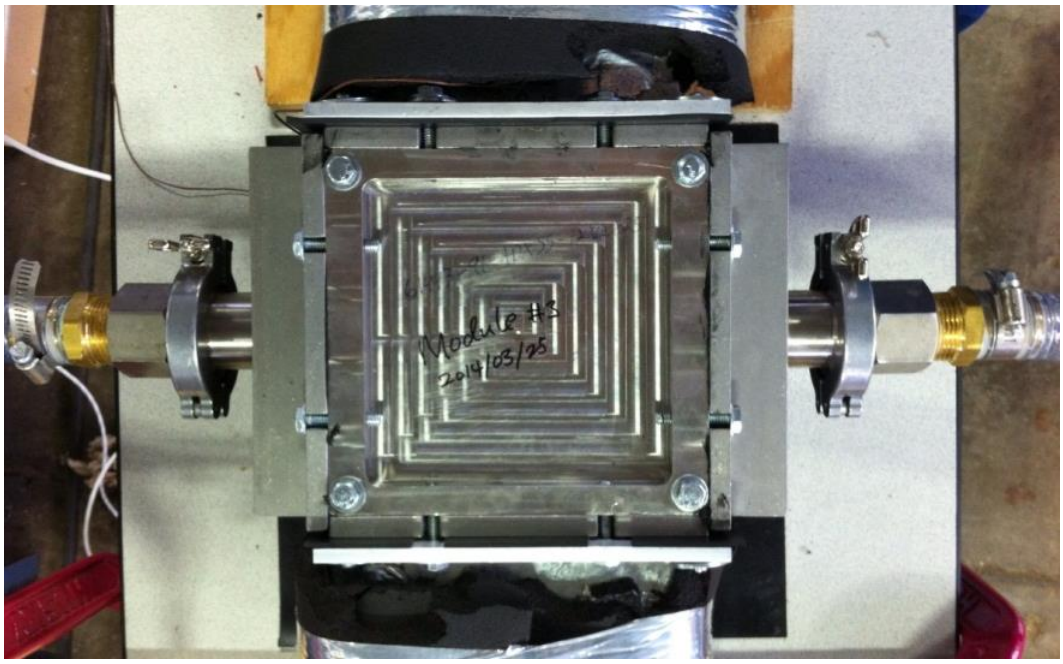

Figure 91. Experimental system normal operation mode membrane module connection

After disconnecting the membrane module and clamping the KF-40 fittings together, the system was evacuated to a pressure level of 108 Pa, and the vacuum pump exhaust flow rate was recorded. The results for this leakage test are shown in Table 43.

Table 43. System leak test measurements

Flow Sensor	Reading correction	Range, mlpm	Sensor Accuracy	Measured Flow, mlpm	Vacuum system pressure, P3, kPa
Omega FLR1005-D	None	400-2000	±3% FS	7	0.945
Omega FLR1006-D	None	1000-5000	±3% FS	17	0.612
Agilent ADM2000	STP	0.5-1000	±3% FS or 0.2mLPM	52	0.568
Definer 220M	STP	50-5000	±1% FS	52	0.520

The airflow rate was in the range of measurement for only two airflow sensors: the Agilent ADM2000 and the Definer 220M. Based on the experimental results, system leakage was estimated to be 52 ±30 sccm.

APPENDIX C
MAXIMUM AIR PERMEATION RATE TEST

To investigate the feed airstream humidity ratio's influence on the membrane air permeance, a series of experiments was conducted. The membrane module was exposed to still ambient air in each of these tests. The experiment was repeated with three different membrane dehumidification modules, and the test results are shown in Table 44.

Table 44. Membrane air permeance test at zero feed airflow rate

	Module 1	Module 2	Module 3
Minimum achieved pressure (P3), kPa	8.0	7.5	7.0
Steady state air permeate flow (DFM2), LPM	24.8	19.7	10.5

The test results suggest that Module 3 had the lowest permeate airflow rate of all the tested membrane modules; it was concluded this is a result of the design improvements for this module assembly. The impact of the feed air-flow rate on a permeate airflow across the membrane can also be seen from the experimental data. The initial conditions of this test were 30 cfm of airflow at 65F and 94% RH. After the feed airflow rate was reduced from 30cfm to 0 cfm, the permeate airflow rate increased from 0.7 LPM to 10.5LPM (as shown in the Figure 92 and Figure 93 time slots). At 16:45, the feed airflow rate was then increased from 0 cfm to 7 cfm, which caused a reduction of the permeate airflow rate. The original increase of the permeate flow rate also affected the system pressure (see Figure 93) and temperature (see Figure 94).

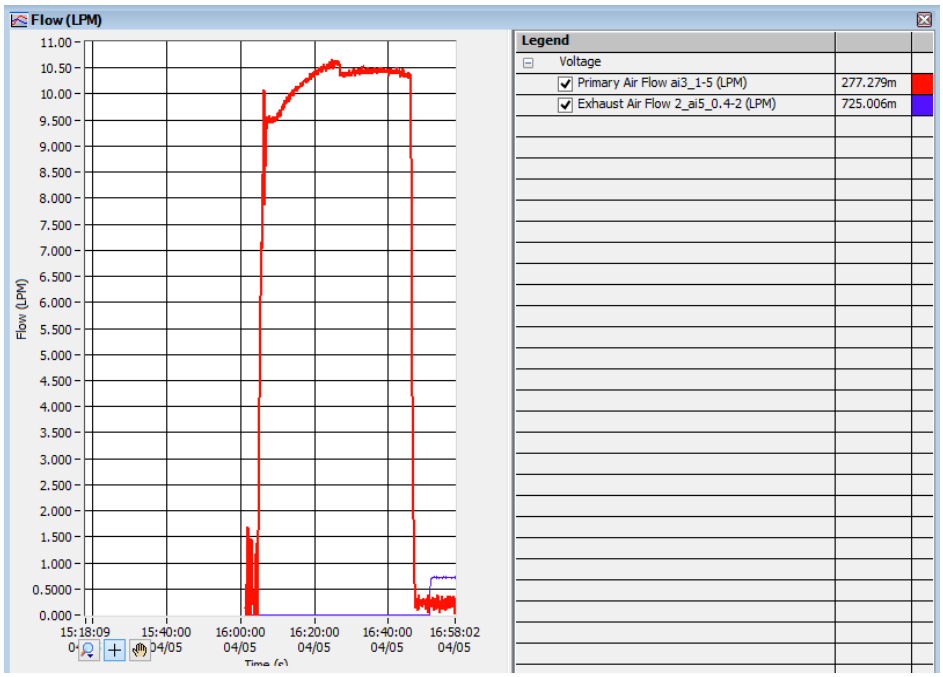

Figure 92. Permeate airflow rate dependence from feed air stream humidity

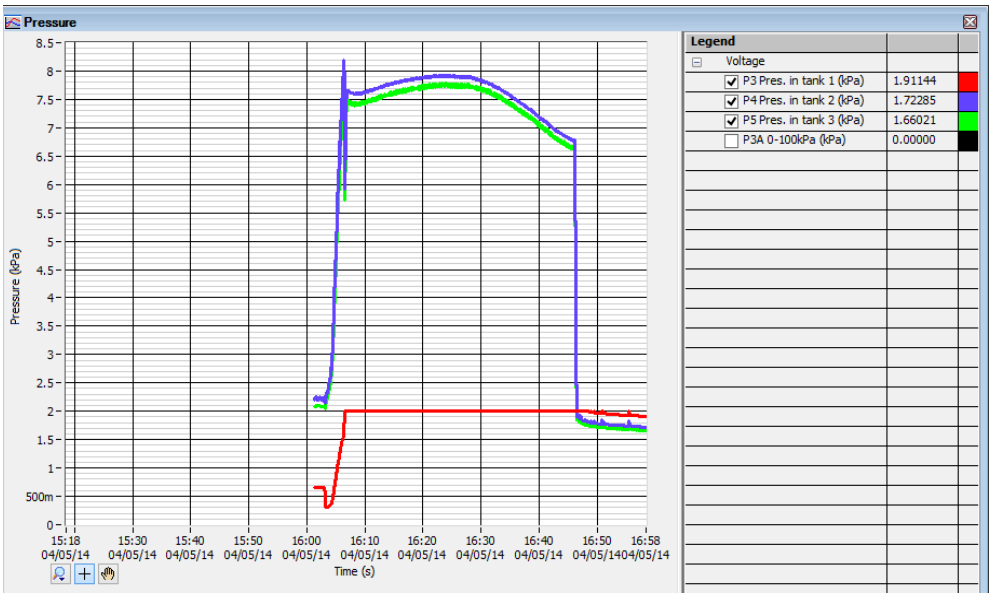

Figure 93. Vacuum system pressure change with time as a function of feed air stream humidity

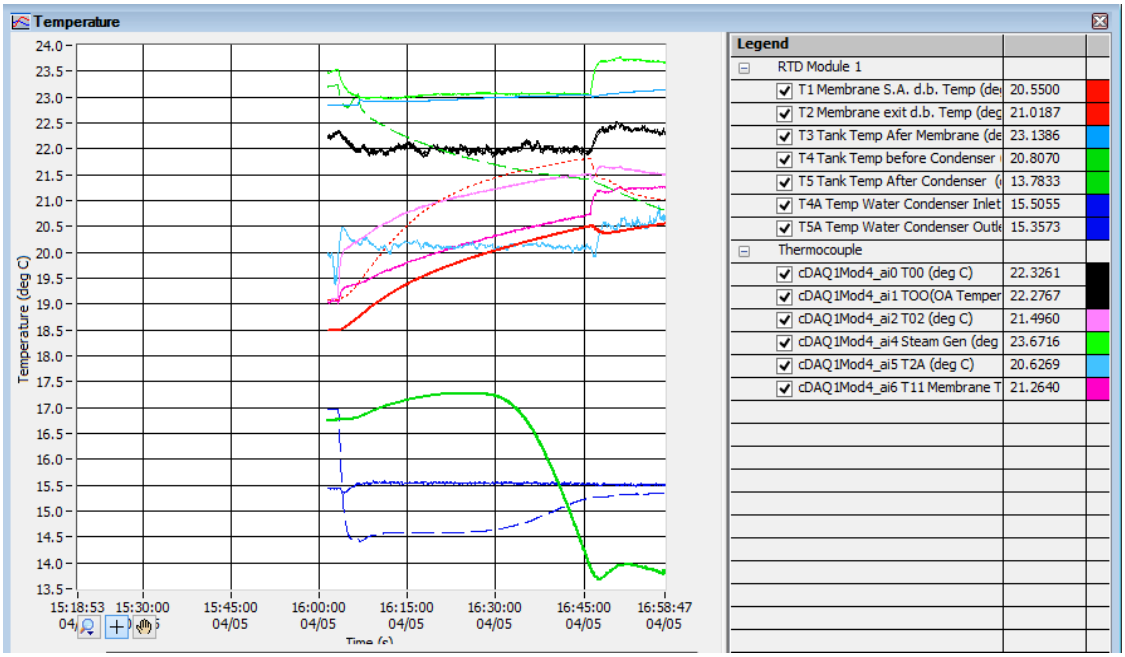

Figure 94. Vacuum system temperature change with time as a function of feed air stream humidity

Finally, this experiment shows an inverse relationship between the feed-side water vapor mass flow rate and permeate airflow rate. This dependence makes the inlet airstream evaporative cooler a critical component for efficient system operation.

APPENDIX D
MEMBRANE CASSETTE #3 TEST

Membrane Cassette #3 was tested at a laboratory air condition to estimate membrane behavior. The first test was made with the membrane surface exposed to still ambient air (T=23.1°C, RH=57.8%). The second test was made when low velocity airflow was applied to the membrane surface. The experimental setup is shown in Figure 95.

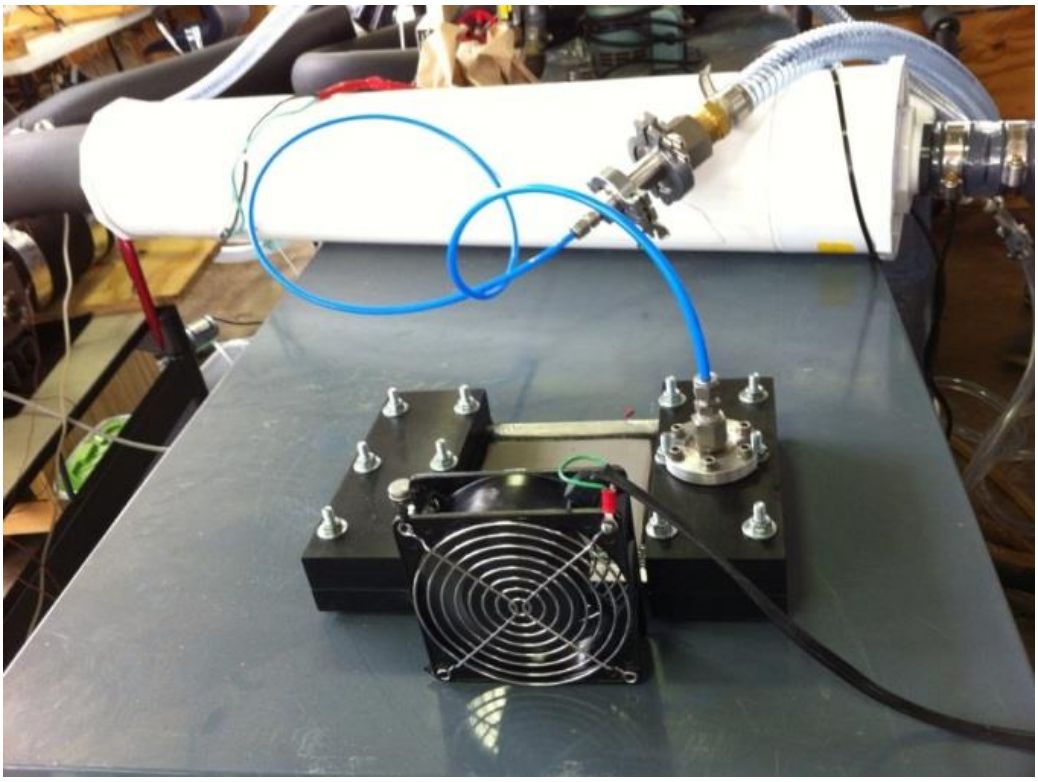

Figure 95. Membrane Cassette #3 test with ¼-inch pipe connection

Experimental results (Table 45) show that the change of the recorded airflow was below the measurement accuracy of the available equipment.

Table 45. Membrane Cassette #3 test with 1/4-inch pipe connection

Flow Sensor	Reading correction	Range, mLPM	Sensor Accuracy	Permeate airflow when membrane exposed to still air, mLPM	Permeate airflow when membrane exposed to moving air, mLPM
Omega FLR1005-D	None	400 - 2000	±3% FS	34	32
Omega FLR1006-D	None	1000 - 5000	±3% FS	11	9
Agilent ADM2000	STP	0.5-1000	±3% FS or 0.2mLPM	75	77
Definer 220M	STP	50-5000	±1% FS	88	86.5

Another set of experiments was performed with the direct connection of the Membrane Cassette #3 to the vacuum system omitting the 1/4-inch pipe connection (Figure 96).

Figure 96. Membrane Cassette #3 water test experimental setup

During the test, Membrane Cassette #3 was gradually submerged in distilled water and permeate airflow rate was recorded during the process (Table 46).

Table 46. Membrane Cassette #3 test with direct connection

Sensor	Flow Sensor	Range, sccm	Sensor Accuracy	Flow, sccm	P3, kPa
Membrane cassette exposed to still air	Definer 220M	50-5000	±1% FS	92	0.425
Membrane cassette lower surface submerged	Definer 220M	50-5000	±1% FS	68	0.586
Membrane cassette completely submerged	Definer 220M	50-5000	±1% FS	57	0.742

Experimental data show that complete submerging the cassette reduced the permeate airflow rate to the leakage level (57 vs 52 sccm), while when both cassette surfaces are open to ambient air permeate airflow rate was 41 sccm above this level.

APPENDIX E

MEMBRANE CASSETTE #4 TEST

Membrane Cassette #4 was tested with laboratory air to estimate membrane behavior. The first test was made with a membrane exposed to the ambient air (T=24.1°C, RH=55.4%). The second test was made when low velocity airflow was applied to the membrane surface (Table 47). The third test was made when a lower surface of the module was submerged in the water. The fourth test was made with the whole membrane submerged in the water. The experimental setup is shown on Figure 97.

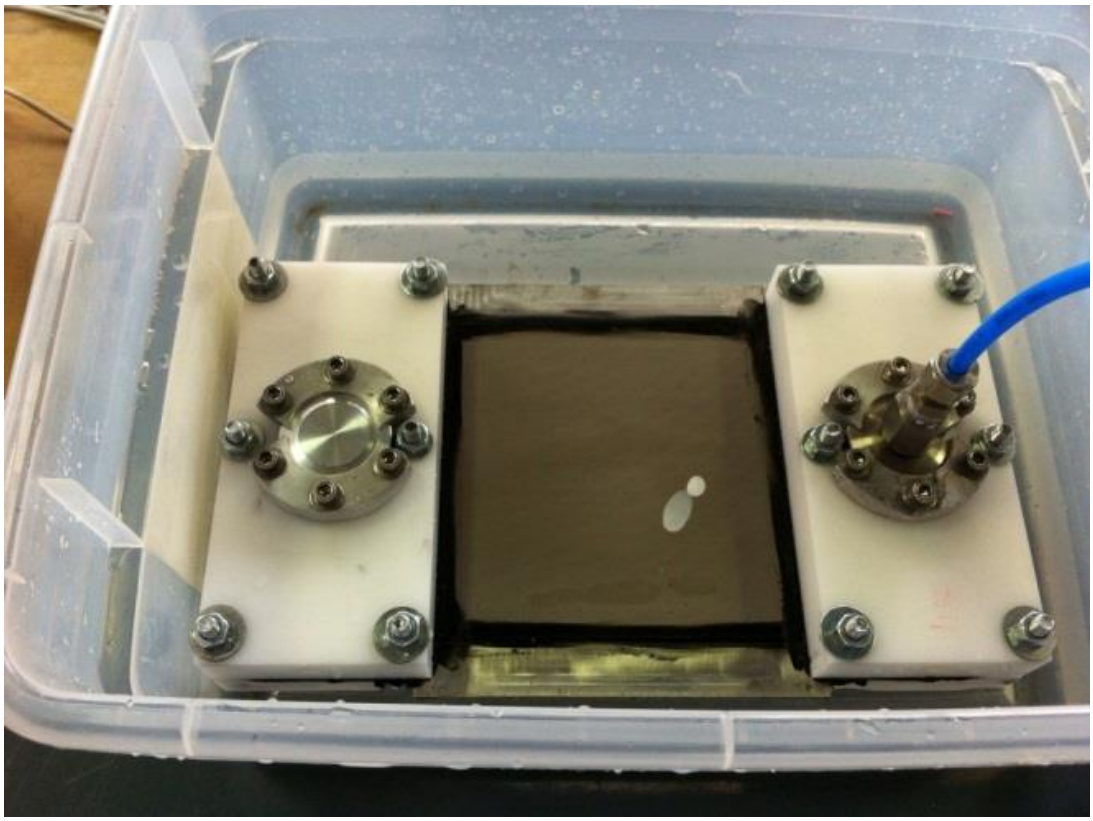

Figure 97. Membrane Cassette #4 water test experimental setup

Table 47. Membrane Cassette #4 permeate airflow test with ¼-inch pipe connection

Flow Sensor	Reading correction	Range, mlpm	Sensor Accuracy	Membrane exposed to still air, mlpm	Membrane exposed to moving air, mlpm	Lower membrane surface submerged, mlpm	Membrane surface completely submerged, mlpm
Omega FLR1005-D	None	400-2000	±3% FS	130	118	NA	NA
Omega FLR1006-D	None	1000-5000	±3% FS	60	50	NA	NA
Agilent ADM2000	STP	0.5-1000	±3% FS or 0.2mLPM	150	140	86	45
Definer 220M	STP	50-5000	±1% FS	156	151	93	52.5

Experimental results show a decrease of permeate airflow when airflow across the membrane surface was increased. Submerging the lower membrane surface decreased permeate airflow by 54 sccm. When the upper membrane surface was submerged, flow was further reduced by 41 sccm. With both membrane surfaces submerged, the exhaust airflow rate from the vacuum system was equal to the system leakage level measured before.

APPENDIX F

MEMBRANE MODULE #3A PRELIMINARY TEST

An experiment was made with the membrane Module # 3 after it was received from PNNL. During the experiment, feed airflow was supplied with a fan located next to the membrane module. The permeate side of the membrane module was connected to the vacuum system and evacuated to a pressure below 1 kPa.

Experimental results show that during all experiments with membrane pressure below 1 kPa and temperature between 20-25°C, the permeate airflow rate was below 0.25 lpm during a three-hour test interval (Figure 98-Figure 100).

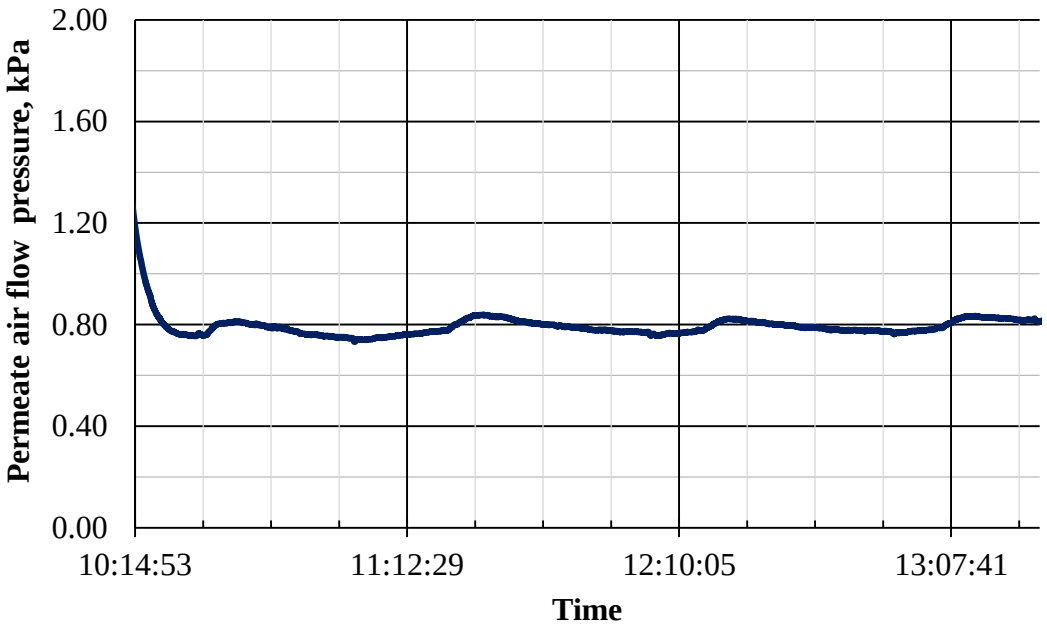

Figure 98. Membrane Module #3A preliminary test pressure change with time

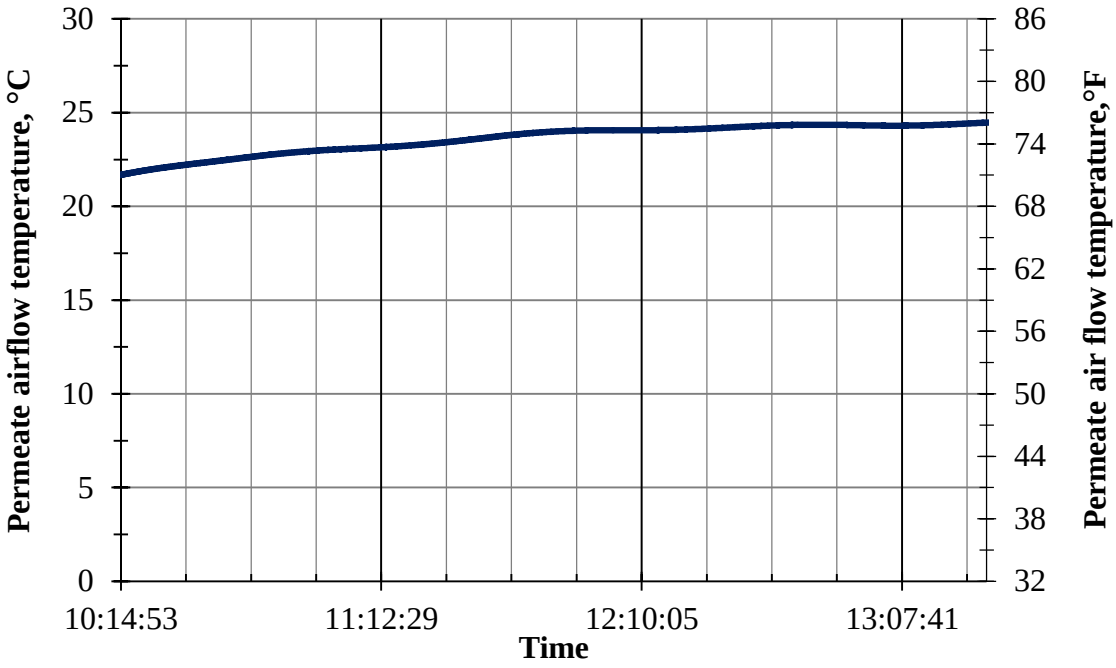

Figure 99. Membrane Module #3A preliminary test temperature change with time

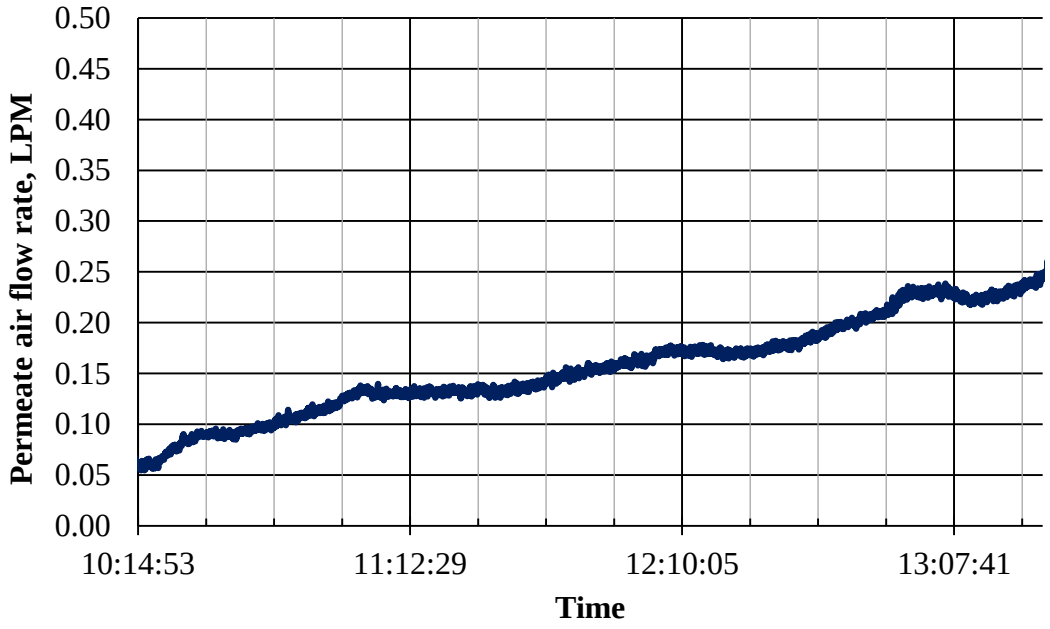

Figure 100. Membrane Module #3A preliminary test airflow rate change with time